BIOPHYSICAL, BIOCHEMICAL AND STRUCTURAL CHARACTERIZATION OF DRUG TARGETS FROM BACTERIA

Ph.D. THESIS

by

ANCHAL SHARMA

DEPARTMENT OF BIOTECHNOLOGY
INDIAN INSTITUTE OF TECHNOLOGY ROORKEE
ROORKEE-247 667 (INDIA)
MAY, 2018


भारतीय प्रौद्योगिकी संस्थान रुड़की
INDIAN INSTITUTE OF TECHNOLOGY ROORKEE

BIOPHYSICAL, BIOCHEMICAL AND STRUCTURAL CHARACTERIZATION OF DRUG TARGETS FROM BACTERIA

A THESIS

Submitted in partial fulfilment of the
Requirements for the award of the degree

of

DOCTOR OF PHILOSOPHY

in

BIOTECHNOLOGY

by

ANCHAL SHARMA

DEPARTMENT OF BIOTECHNOLOGY
INDIAN INSTITUTE OF TECHNOLOGY ROORKEE
ROORKEE-247 667 (INDIA)
MAY, 2018

INDIAN INSTITUTE OF TECHNOLOGY ROORKEE
ROORKEE

CANDIDATE'S DECLARATION

I hereby certify that the work which is being presented in the thesis entitled " **BIOPHYSICAL, BIOCHEMICAL AND STRUCTURAL CHARACTERIZATION OF DRUG TARGETS FROM BACTERIA**" in partial fulfilment of the requirements for the award of the Degree of Doctor of Philosophy and submitted in the Department of Biotechnology of the Indian Institute of Technology Roorkee, Roorkee is an authentic record of my own work carried out during a period from January 2013 to May 2018 under the supervision of Dr. Pravindra Kumar, Associate Professor, Department of Biotechnology, Indian Institute of Technology Roorkee, Roorkee.

The matter presented in this thesis has not been submitted by me for the award of any other degree of this or any other institution.

Signature of the Candidate

This is to certify that the above statement made by the candidate is correct to the best of our knowledge.

Signature of Supervisor (s)

The Ph.D Viva-Voce Examination of Anchal Sharma, Research Scholar has been held on ……………………

Chairman, SRC **Signature of External Examiner**

This is to certify that the student has made all the corrections in the thesis.

Signature of Supervisor (s) **Head of the Department**

Dated:____________


भारतीय प्रौद्योगिकी संस्थान रुड़की
INDIAN INSTITUTE OF TECHNOLOGY ROORKEE

ABSTRACT

The rapid emergence of drug resistance and declining rate of development and approval of novel antimicrobials agents has presented a serious challenge to modern medicine. The increment of drug resistance in bacteria has become a public health concern worldwide but only a few new therapies have been developed. Therefore, the efforts toward the discovery and development of novel molecules/new scaffolds with new action of mechanism are essentially required at this crucial stage to combat the problem. The recent technological advancement in the field of structural genomics opens up the doors toward the identification and characterization of novel and potential drug targets in pathogenic bacteria.

The exploration of essential biosynthetic pathways present in bacteria has drawn the attention of researchers for the expansion of potent inhibitors by targeting the enzymes of these pathways. Shikimate pathway and lipopolysaccharide (LPS) biosynthesis pathway in microbes are essential and attractive pathways for the development of the inhibitors against the pathogenic bacteria. Since these pathways are absent in animals and humans, the enzymes of the pathways are attractive and potential target for the development and designing of novel drug against the resistant bacteria.

This thesis contains two sections, which covers the biochemical, biophysical and structural characterization of a monofunctional 3-deoxy-d-arabino-heptulosonate 7-phosphate synthase (DAH7PS) enzyme from drug-resistant Gram-negative bacteria Providencia alcalifaciens. Additionally, a bifunctional DAH7PS from Bacillus subtilis has also been characterized and its binding and inhibition aspects with polyphenol compounds (Chlorogenic acid, Prephenate, Shikimate, and Ferulate) have determined. In second section, we have characterized LpxC enzyme from a Gram-negative, drug-resistant pathogenic *Moraxella catarrhalis* and analyzed the binding features of Lpxc with the most potent inhibitors (LpxC-4 and LpxC-2).

In first chapter, we have described the general overview of emerging problem of the antibiotic resistance in bacteria. The molecular mechanisms for the acquisition of drug resistance among microbes have been described. Additionally, the potential approaches and efforts made in the direction to overcome the resistance problem have also been discussed. This chapter describes the shikimate pathway and intracellular localization of enzymes of this pathway in different organisms. We have also described the classification, structural characterization and regulation mechanism of microbial DAH7PS. Furthermore, this chapter encompasses the lipid biosynthesis pathway (LPS) along with the structural components of cell envelop present in Gram-negative bacteria. Additionaly, the activation and stimulation of the host innate immune system mediated via Lipid A (Endotoxin) has been elaborated. In last part of the chapter, we have described the structural features and reported inhibitors of LpxC which is a committed enzyme of the LPS pathway.

3-deoxy-d-arabino-heptulosonate 7-phosphate synthase (DAH7PS), the first committed enzyme of the shikimate pathway, catalyzes the condensation reaction of phosphoenolpyruvate (PEP) and D-erythrose 4-phosphate (E4P) to produce DAHP. It further produces a precursor molecule “chorismate” that leads to production of several essential compounds like aromatic amino acids, folates, phylloquinone (vitamin K), ubiquinone, napthoquinone in bacteria, fungi, apicomplexan and plants. Since this pathway is employed only in plants, fungi, microbes, and apicomplexans, enzymes of this pathway are potential targets for the development of drug molecules and herbicides.

In second chapter, the molecular cloning, expression, purification, and characterization of DAH7PS from *Providencia alcalifaciens* (PaDAH7PS) have been described. DAH7PS is a metalloenzyme, which exhibits vulnerability to the oxidative stress and it undergoes inactivation in multiple ways in the presence of redox metal, H_2O_2, and superoxide. We have determined the oligomeric state of PaDAH7PS and the effect of redox metal on its stability through the size exclusion chromatography. The FTIR, MALDI-TOF/TOF-MS studies have revealed that methionine residues of PaDAH7PS were modified to methionine sulfoxide in oxidative stress conditions. During oxidation, PaDAH7PS alters into partially folded and unfolded states and determined by CD and Fluorescence studies. A significant loss in enzymatic activity of PaDAH7PS was determined and the formation of amorphous aggregates was visualized using AFM imaging, further confirmed by ThT binding based assay. This is the first report where we have shown a hexameric DAH7PS and the methionine residues of PaDAH7PS get oxidize in the presence of redox metals. The partially folded and unfolded oligomeric states with high β-content of PaDAH7PS might be the critical precursors for aggregation.

Furthermore, elaboration of the structural characterization of PaDAH7PS has been described in the third chapter. Here, we have determined 3.3 Å crystal structure of PaDAH7PS in apo form. Crystallization of hexameric PaDAH7PS (non-oxidized most active form) was performed in sitting drop trays by the vapor diffusion method. Crystals were grown in the presence of Bis Tris propane buffer, PEG 3350 as the precipitant, 1mM substrate (PEP), 10 mM DTT as a reducing agent at the 293 K. The crystal belongs to *P*1211 space group with unit cell parameters a, b, c = 54.55, 165.46, 77.08 and α, β, γ = 90, 106.5, 90. The structural comparison

of apo PaDAH7PS, with complexed DAH7PS (PEP and metal) of *Escherichia coli* and apo DAH7PS of *Saccahromyces cerevesaeaie* reveals that the PaDAH7PS molecule adopted a typical well conserved $(\beta/\alpha)_8$ TIM-barrel fold and its different type assembly of tetrameric form. In apo PaDAH7PS, loop (L2 and L8) regions associated with the binding of the substrate and catalytic metal ions were found disordered. In future, the optimization and analysis of a high resolution structure of PaDAH7PS could provide more structural insights that will be useful for the rational design of inhibitors.

Recently, our group members have reported a crystal structure of truncated N-terminal chorismate mutase (CM) regulatory domain, complexed with chlorogenic acid, from bifunctional DAH7PS of *Bacillus subtilis*. The structural and biochemical data have evidently shown that chlorogenic acid (a structural analog of chorismic acid) acts as an inhibitor of truncated N-terminal regulatory CM domain (chorismate mutase). We have hypothesized that binding of the substrate, product and their analogs at the active site of CM domain can induce conformational changes in DAH7PS catalytic domain and inhibit its catalytic activity. In this context, chapter fourth describes the cloning, expression, purification and characterization of a full length bifunctional DAH7PS from *Bacillus subtilis* (BsDAH7PS). We have evaluated the binding and inhibition of full length BsDAH7PS, via CM regulatory domain, with the four phenolic compounds (Chlorogenic acid, Prephenate, Ferulate, and Shikimate) using fluorescence and circular dichroism (CD) spectroscopy as well as the molecular docking studies. The fluorescence data suggested the quenching of intrinsic fluorescence of BsDAH7PS via a static mechanism and K_q values (higher than 10^{10}), indicated the ground state complex formation between phenolic compounds and BsDAH7PS. Isothermal titration calorimetry studies have shown that chlorogenic acid has the strongest binding affinity with the BsDAH7PS (K_D = ~10.0 μM). The far-UV CD results have shown the increment in the α-helical content of BsDAH7PS upon ligand binding. Molecular docking studies have predicted that all compounds are interacting with the regulatory CM domain and Arg27 (Chain A) and Arg10* (Chain B) are the critical residues which are forming H-bonding. This study may be helpful for the development and further designing of the more potent multi-targeted antibacterial agents.

Gram-negative bacteria contain an outer membrane which surrounds the cell wall and protects the bacteria from many antimicrobial agents. The outer membrane is composed of lipopolysaccharide molecule which contains three components: O-antigen, a core polysaccharide, and lipid A. Lipid A is mainly responsible for anchoring of the membrane to cell wall and essential for the viability and virulence of the bacteria.

The biosynthesis of Lipid A is catalyzed by nine enzymes, and the committed step of the LPS pathway is catalyzed by a zinc metalloenzyme UDP-3-*O*- [(*R*)-3hydroxymyristoyl]-*N*-acetylglucosamine deacetylase (LpxC). LpxC is conserved and shows no homology to any human enzyme. Thus, LpxC has attracted attention for the new drug development against pathogenic bacteria.

In chapter fifth, we have described the cloning, expression, purification and characterization of the zinc metalloenzyme UDP-3-O-[(*R*)-3-hydroxymyristoyl]-*N*-acetylglucosamine deacetylase (LpxC) from *Moraxella catarrhalis* (McLpxC). Several reported potential compounds against LpxC have shown large variation in their potency and efficacy. The differential susceptibility and selective binding features of these inhibitors against LpxC from numerous drug-resistant bacteria are still unexplored. In this chapter, we have investigated its binding features with potent inhibitors LpxC-2 and LpxC-4 using biochemical, biophysical and *in silico* approaches. The circular dichroism results have revealed the changes in secondary and tertiary structure of McLpxC upon inhibitors binding. The fluorescence quenching mechanism was found to be static with $K_q > 10^{10}$ suggesting a ground state complex formation between the McLpxC and inhibitors. Finally, the overall spectroscopic findings suggest that the interaction of LpxC-4 caused large conformational alterations and significant loss of α-helical content in McLpxC as compared to LpxC-2. In Isothermal titration calorimetry based studies, both inhibitors have shown comparable binding affinities (K_D = ~10.0 μM) and their interactions were exothermic and driven by enthalpy change. Furthermore, the docking studies have shown that Lys239 and Thr191 are the critical residues for binding of the inhibitors. Thus, this study suggests that further optimization and utilization of molecules based on this scaffold will be helpful in designing the new antimicrobial agents targeting LpxC.

Conclusively, the overall findings of our proposed work will enhance the understanding of the potential drug targets (DAH7PS and LpxC) in terms of their structural and inhibition features and could serve as a starting point for the development of new antimicrobial agents against bacteria.

DEDICATION

This thesis work is dedicated to my Late grandmother Smt. Anaro Devi (Maa) she always loved me unconditionally and supported me for my decisions and whose good examples have taught me to work hard for the things that I aspire to achieve.

ACKNOWLEDGEMENTS

This thesis is the culmination of my journey of Ph.D which was just like climbing a high peak step by step accompanied with encouragement, hardship, trust, and frustration. I have been accompanied and supported by many people during this period. They all should be thanked for helping me get here and it is very hard to know where to start. I take this opportunity to express my gratitude to all of them.

First and foremost, I would like to thank almighty God for giving me all the opportunities he has presented to me and giving me patience, strength and warmed my heart during my hard time. I have selfishly prayed so many times for many things and even for experiment to workout in lab, and he answered me for every silent prayer. I will keep on trusting you for my future. Thank you, Lord.

I have no words to express my deep sense of admiration and gratitude to my supervisor "Dr. Pravindra Kumar" for his great enthusiasm, relentless supervision, patience, and motivation. I am really thankful to him for providing me an opportunity to work in his laboratory, enabling me to pursue my research career. His positive outlook and constant enthusiasm has always uplifted my spirits and given me strength to fight all the challenges to accomplish my goals. I am thankful to him for all his constructive criticism and his belief that I can do better still even if nothing is going out to work. He always placed his full faith and trust in me that enabled me to believe in my research goals and instilled self-confidence and determination to achieve them. He has always been like what a best teacher could be to a student or what a parent is to a child. I remain indebted to him for his keen interest in correcting, sculpting and shaping my thesis scientifically.

I would like to express my gratitude to Dr. Shailly Tomar for her understanding, encouragement and personal attention for my work and a very healthy discussion throughout. Her scientific vision and valuable suggestions in the field of molecular biology and biochemistry have played an important role in the quality of my research and its successful completion.

I want to acknowledge to Dr. A. K. Sharma, Head of the Department and an excellent biochemist and X-ray crystallographer. I am much indebted to him for valuable advices and precious time for discussions. I owe thanks to Prof. R. Prasad for allowing me and providing me to use Mass spectrometry facility.

I endowed a sincere thank to my research committee members Dr. Partha Roy (SRC Chairman), Dr. Bijan Choudhary (Internal expert) and Dr. Kaushik Ghosh (External expert) for their encouragement during my research work. I wish to thank to all of them for their constructive inputs and valuable suggestions during my presentations which were helpful for completing my projects. I am very fortunate to have such supportive committee members.

I feel overwhelmed in thanking to Prof. Partha Roy (Ex-Head) and Prof. R. Prasad (Former Head) Department of Biotechnology for providing necessary facilities, support and cooperation in the Department. I am courteous to all the honorable faculty and staff members for their support and encouragement.

I would also like to acknowledge Prof. Ramesh Chandra (Ex-Head) Institute Instrumentation Centre for providing AFM facility. He is extremely understanding and supportive. He has a very positive reflection and highly enthusiastic personality. He has been very friendly with me and always inspired me a lot to maintaining my efficiency at a high level. I express my gratitude to Dr. Kaushik Ghosh (Head of the NMR) for allowing me to use Fluorescence facility at the NMR and FTIR at the Chemistry Department.

I sincerely acknowledge the Ministry of Human Resource Development (MHRD), Government of India, for providing financial assistance during my research tenure.

I owe gratitude to my seniors Dr. Shivendra Pratap, Dr, Aditya Dev, Dr. Pramod Kumar and Dr. Sonali Dhindwal, they all always suggested me good ideas and inspired me and motivated me to work more. They all have discussions with me regarding any problem in my work. I want to be specially acknowledged with love and appreciation in the memorable concern, affection and care from my seniors Dr. Aditya Dev and Dr. Shivendra Pratap because only they have started and generated the ideas about these projects on which I worked during my Ph.D and have learned lot of things. So, today I am at this stage and able to complete my thesis and writing this acknowledgement.

I want to give my warm appreciation and a great thanks to my colleague and good friend Vijay Kumar with whom I worked most of the time of my Ph.D. He was the one in my lab who always there beside me during the happy and hard moments to inspire me and motivate me. He always helped me even though he was not working in any project. We used to do experiments together in a long run and used to skip lunch and that day we usually go to Nescafe together for coffee and snacks. We have learned various laboratory techniques together and really have a great *memorable period of Ph.D. I feel without his help and guidance it would have been very difficult task to finish this long journey on time. We always inspired and motivated to each other whenever we felt low.*

I am in dearth of the words and like to give my heartiest thanks, love, care and affection to Apurva Chatrath for helping me in my very tough time and without her help my work would have been much more difficult to be finished. She is very helping and has good nature and wonderful heart whenever I asked any help and support from her she was always ready and said yes to every work.

I would also like thanks to all my current lab members Madhu, Vijay, Neha, Pooja, Neetu, Poonam, Vikram, Jaikrishna, Monica, Ishaan, Visakha and Dr. Stuti, for their sincere efforts, cooperation and creating a working atmosphere in the laboratory. The atmosphere they helped to create in the lab made it enjoyable to come to work each day. Their thoughts and suggestions were especially useful.

I would like to give heartiest thanks and love to Neetu for all of her good advices and help over the past two years when things were not going to plan. She always helped me to solve many difficulties and provided many things whenever I needed during my experiments at the crucial moments. She also gave me some valuable suggestions and motivated me during my work.

I owe big thanks to Madhu for helping me and providing things whenever I needed anything in lab. Madhu always ready to help me, whenever I faced any difficulty to handle an instrument. I thanks to him for many important discussions and providing good ideas at some crucial stages and maintaining a good harmony in the lab during such a long period of Ph.D.

I would also like to thank the many B.tech and M.Sc students of the MCU lab who have come and gone throughout my Ph.D time here: Nandita, Kanika, Ilu, Ravi, Shubham, Aditya, Ishaan. I spend a very good and memorable time with Kanika and we use to have lot of fun together. I owe thanks to Ravi, we use to have good discussions on scientific idea and always ready to help me whenever I asked him. He always helped me to keeping my experimental things from one temperature to other in the night time. I am really thankful for his support.

I owe thanks to all past and current members of the RL-1 lab and all seniors Dr. Megha Aggarwal, Dr. Manju Narwal, Dr. Monu Batra and Dr. Rajesh Sharma for always providing good suggestions, help and support. I would like to acknowledge Dr. Manju Narwal for me giving valuable suggestions during my very initial and learning phase of the Ph.D. I would like *to thanks Rajat, Ramanjit, Harvijay, Anjali, Benazir, Akshay, Vedita and Supriti for their help, support and good behavior. They all always welcome us very nicely, whenever we went to their lab for any experiments. I warmly thanks to Rajat for his readily extending helping hand whenever I needed his help and always give good and valuable suggestions. My special thanks to Benazir and Harvijay for maintaining a very good working and wonderful environment in the RL-4, whenever we (I and Vijay) went there for experiments we really spend a good time with these peoples.*

I also would like to thanks all past and current members of the Biochemistry lab, my seniors Dr. Anamika Singh, Dr. Prabhat Tomar, Dr. Bibekanand Kar, Dr. Preeti, Dr. Nidhi, Gunjan, Pranav, Deenanath, and Brejesh. All of them always provided their help and support whenever I asked to them during last five years of my Ph.D. I really want to give a heartiest thanks to the Dr. Anamika Singh for giving me good idea and suggestions to solve so many difficulties during my work. I owe special thanks to Pranav he always helped us and give his precious time whenever we asked to him during our CD experiments.

Also to be acknowledged with appreciation in the memorable concern Dr. Rekha Sharma, Somesh Banerjee, Atin Sharma, Poonam Baswan, Rashmi Gangwar, Zia Tariq and many other persons for their help and support whenever I needed. I also would like to thanks Mr. Charan Singh for his help and providing instrument booking whenever we needed in the NMR.

I would like to acknowledge all the teachers I learnt from since my childhood, I would not have been here without their guidance, blessing and support. My special thanks to Dr. D.C. Sharma who inspired me to pursue my research career. He was always to be so inspirational and motivating. He has taught me another aspect of life, that, "Whatever we give to others that will definitely return back to us even with a great amount of interest". I owe a lot of gratitude to him for nurturing my scientific temperament during my master's project and I feel privileged to be associated with a person like him in my life.

It's my fortune to gratefully acknowledge the support of my friends at IITR, Savita, Swati, Jyoti, Richa, Akansha, Sandeep Shukla, Akshay Pandey, Adrish Mullick, Dr. Shoib, and Dr. Suresh for their support and generous care throughout the research tenure. They were always beside me during the happy and hard moments to push me and motivate me.

I appreciate, my Master's seniors Dr. Sujata Rathi, Dr. Akansha Vashitha, Dr. Neha Mittal, Dr. Shalu Singh, and my friends Dr. Vikas Mehashi, Anamika, Supriya, Mahima, Ruchi, and Aijaz for their encuouragement and support.

A Special and big thanks is extended to my best buddy Namitosh for her unconditional love, care, and motivation. She and her family have an important role in my life and always help and support to achieve my goals. I owe thanks to my younger brother Varun Sharma for his help and support to read the final draft of my thesis.

I feel emotional and lack language of expression, in mentioning the sacrifices made by my beloved mother. Today wherever I am are the results of her great efforts, sacrifices and compromises. She is really a role model for me. She developed and nurtured me into a strong person and taught me how to survive and be happy even in worst situations. I am also grateful to my all family members whose unconditional support and encouragement at every step boosted my moral to accomplish my goals. I would never be able to pay back the love and affection showered upon by my family. My heartfelt regard goes to my father in law, mother in law and loving and caring sister in law (Dr. Mala and Preeti) for their patience, love, and moral support.

At last I do not know how to begin with saying thank you to my soul mate, my dearest husband and my best friend Anuj Tiwari. I love you for everything, for being so understanding and for putting up with me through the toughest moments of my life. I greatly value his contribution and deeply appreciate his belief in me. I thank God for enlightening my life with your presence. You are the best thing that has ever happened to me.

(Anchal Sharma)


भारतीय प्रौद्योगिकी संस्थान रुड़की
INDIAN INSTITUTE OF TECHNOLOGY ROORKEE

TABLE OF CONTENT

Page No.

ABSTRACT I

DEDICATION V

ACKNOWLEDGEMENT VII

TABLE OF CONTENT XIII

LIST OF PUBLICATIONS XIX

LIST OF FIGURES XXI

LIST OF TABLES XXV

LIST OF ABBREVIATIONS XXVII

CHAPTER 1 INTRODUCTION AND LITERATURE REVIEW

1.1 Introduction 1
- 1.1.1 Mechanisms of resistance in bacteria 2
  - 1.1.1.1 Horizontal gene transfer 3
  - 1.1.1.2 Mutational resistance 4
- 1.1.2 Strategies to develop new antibiotics 5

1.2 The shikimate pathway 6
- 1.2.1 Biosynthesis of the chorismate 7
- 1.2.2 Molecular organization and intracellular localization of shikimate pathway enzymes 9

1.3 Microbial DAH7PS 9
- 1.3.1 3-Deoxy-D-arabino-heptulosonate-7-phosphate synthase 9
- 1.3.2 Classification of microbial DAH7PS 10
- 1.3.3 Metal activation of the DAH7PS 12
- 1.3.4 Metal catalyzed oxidation of EcDAH7PS (Phe) 13

1.4 Structural features of DAH7PS 14
- 1.4.1 Structural features of the microbial Type Iα DAH7PS 14
- 1.4.2 Structural features of the Type Iβ DAH7PS 16
- 1.4.3 Structural features of the Type II DAH7PS 18
- 1.4.4 Microbial DAH7PS regulation and inhibition 19
- 1.4.5 Chorismate mutase and DAH7PS fusion enzyme 23

1.5 Plant’s DAH7PS and regulation 25

1.6 Lipopolysaccharide (LPS) in Gram-negative bacteria 25
  1.6.1 Structure of lipopolysaccharides 27
    1.6.1.1 Lipid A 27
    1.6.1.2 The core oligosaccharide and O-antigen 29
  1.6.2 Lipid A (Endotoxin) as an activator of innate immune system 29
    1.6.2.1 TLR4 stimulation and signal transduction 30
  1.6.3 LPS biosynthesis and transport 32
  1.6.4 LpxC as an unexploited antibiotic target 35
    1.6.4.1 LpxC a zinc metalloamidases 36
    1.6.4.2 LpxC adopts unique structural fold 37
    1.6.4.3 Sites of LpxC for inhibitors exploitation 38
  1.6.5 LpxC inhibitors 39
    1.6.5.1 Classical LpxC inhibitors 40
    1.6.5.2 Recent LpxC inhibitors 41

CHAPTER 2 BIOPHYSICAL AND BIOCHEMICAL CHARACTERIZATION OF DAH7PS FROM *PROVINDENCIA ALCALIFACIENS* (PaDAH7PS)

2.1 Introduction 43
2.2 Materials and methods 45
  2.2.1 Materials 45
  2.2.2 Methods 45
    2.2.2.1 Molecular cloning and overexpression of recombinant PaDAH7PS 45
    2.2.2.2 Purification and cleavage of His-Tag of PaDAH7PS 46
    2.2.2.3 Size exclusion chromatography 46
    2.2.2.4 Glutaraldehyde cross-linking and Native-PAGE 47
    2.2.2.5 Metal-catalyzed oxidation effect on the oligomeric state of PaDAH7PS 47
    2.2.2.6 FTIR spectroscopy 47
    2.2.2.7 Mass spectrometric analysis 47
    2.2.2.8 Enzymatic activity of PaDAH7PS 48
    2.2.2.9 Atomic force microscopic imaging of 49

PaDAH7PS
2.2.2.10 Circular dichroism spectroscopy 49
2.2.2.11 Fluorescence spectroscopy 49
2.2.2.12 ThT binding assay 50
2.3 Results 50
2.3.1 Cloning, expression, purification, and oligomeric state determination of PaDAH7PS 50
2.3.2 Influence of oxidative condition and redox metal treatment on the PaDAH7PS 54
2.3.3 FTIR spectroscopy analysis 55
2.3.4 Identification of the oxidative modification in PaDAH7PS 56
2.3.5 FTIR spectroscopy analysis 64
2.3.6 Identification of the oxidative modification in PaDAH7PS 65
2.3.7 Enzymatic activity of different oligomeric states of PaDAH7PS 66
2.3.8 Fluorescence spectroscopic characterization of different oligomeric states of PaDAH7PS 69
2.3.9 ThT binding study of different oligomeric states of PaDAH7PS 70
2.4 Discussion 71
2.5 Conclusion and future perspectives 73

CHAPTER 3 STRUCTURAL CHARACTERIZATION OF DAH7PS FROM *PROVINDENCIA ALCALIFACIENS* (PaDAH7PS)

3.1 Introduction 75
3.2 Materials and methods 76
3.2.1 General procedure for crystallization 76
3.2.2 Initial crystallization trials and optimization of crystal conditions 76
3.2.3 Preparation of PaDAH7PS crystals for the data collection 77
3.2.4 X-Ray diffraction data collection and processing 77
3.2.5 Overview of structure modeling and refinement 77
3.2.6 Structure determination of PaDAH7PS 78
3.2.6.1 Matthew’s Coefficient 78
3.2.6.2 Molecular replacement 78

3.2.6.3 Model building and refinement 78
3.2.6.3.1 Refinement process with REFMAC5 79
3.2.6.3.2 Refinement process with Phenix.refine 79
3.2.6.3.3 Model building with Crystallographic Object-Oriented Toolkit (COOT) 80
3.2.7 Structural analysis and validation 80
3.3 Results and discussion 80
3.3.1 Crystallization and structure solution of PaDAH7PS 80
3.3.2 Sequence characteristics of PaDAH7PS 83
3.3.3 Overall structure of PaDAH7PS 84
3.3.4 Quaternary structure of PaDAH7PS 90
3.3.5 Comparison of PaDAH7PS structure 93
3.3.5.1 Comparison of PaDAH7PS with complexed EcDAH7PS 94
3.3.5.2 Comparison of PaDAH7PS with apo ScDAH7PS 96
3.3.5.3 Comparison of the active site 97
3.4 Conclusion and future perspectives 100

CHAPTER 4 BIOCHEMICAL, BIOPHYSICAL AND STRUCTURAL CHARACTERIZATION OF BIFUNCTIONAL DAH7PS FROM *BACILLUS SUBTILIS* (BsDAH7PS)

4.1 Introduction 101
4.2 Materials and methods 104
4.2.1 Materials 104
4.2.2 Molecular cloning and expression of BsDAH7PS 104
4.2.3 BsDAH7PS purification by IMAC 104
4.2.4 Enzymatic activity assay 105
4.2.5 Inhibition studies 105
4.2.6 Circular dichroism measurements 106
4.2.7 Fluorescence measurements 106
4.2.8 Isothermal titration calorimetry 107
4.2.9 Molecular modeling 107
4.2.10 Molecular docking 107
4.2.11 Antibacterial susceptibility assay 108

4.3 Results 108
4.3.1 Molecular cloning, expression and purification of the BsDAH7PS 108
4.3.2 Enzymatic activity 109
4.3.3 CD spectroscopic studies 112
4.3.3.1 Effects of the ligand binding 114
4.3.4 Fluorescence analysis 115
4.3.4.1 Quenching mechanism determination 116
4.3.5 Isothermal titration calorimetry 118
4.3.6 Sequence analysis and molecular modeling 121
4.3.7 Molecular docking 124
4.3.8 Growth inhibition assays 126
4.4 Disussion 126
4.5 Conclusion and future perspectives 128

CHAPTER 5 BIOCHEMICAL, BIOPHYSICAL AND STRUCTURAL CHARACTERIZATION OF LPXC FROM *MORAXELLA CATARRHALIS* (McLpxC)

5.1 Introduction 129
5.2 Materials and methods 131
5.2.1 Reagents and chemicals 131
5.2.2 Cloning and expression of the McLpxC 131
5.2.3 Purification of McLpxC by affinity chromatography 131
5.2.4 Fluorescence-based enzymatic activity assay of McLpxC 132
5.2.5 Kinetic inhibition of McLpxC 132
5.2.6 Antibacterial susceptibility assay 133
5.2.7 Circular dichroism spectroscopy 133
5.2.8 Fluorescence spectroscopy 134
5.2.9 Isothermal titration calorimetry assays 134
5.2.10 Sequence analysis and molecular modeling 135
5.2.11 Molecular docking studies 135
5.3 Results 135
5.3.1 Molecular cloning, expression and purification of the McLpxC 135
5.3.2 Enzymatic activity and inhibition assays 136

5.3.3 CD spectroscopic studies 137

5.3.3.1 CD measurements of the McLpxC 137

5.3.3.2 Effect of the substrate binding 138

5.3.3.3 Effect of the Inhibitors binding 139

5.3.4 Fluorescence quenching mechanism 141

5.3.4.1 Quenching mechanism determination 142

5.3.5 Thermodynamics of inhibitors binding to McLpxC 144

5.3.6 Sequence analysis and molecular modeling of McLpxC 145

5.3.7 Molecular docking 147

5.4 Discussion 149

5.5 Conclusion and future perspectives 152

REFERENCES 153

LIST OF PUBLICATIONS/PUBLISHED/COMMUNICATED

1. **Anchal Sharma,** Vijay Kumar, Apurva Chatrath, Aditya Dev, Ramasare Prasad, Ashwani Kumar Sharma, Shailly Tomar, Pravindra Kumar. *In vitro* metal catalyzed oxidative stress in DAH7PS: Methionine modification leads to structure destabilization and induce amorphous aggregation. **International Journal of Biological Macromolecules** 106 (2018) 1089-1106.

2. **Anchal Sharma,** Pramod Kumar, Pooja, Kesari , Neetu, Madhusudhan Rao Katiki, Mishra Manisha, PK Singh, BR Gurjar, AK Sharma, S Tomar, Pravindra Kumar. Purification and Characterization of 2S Albumin from Seeds of Wrightia tinctoria Exhibiting Antibacterial and DNase Activity. **Protein Peptide Letters** 24 (4) (2017) 368-378.

3. Vijay Kumar, **Anchal Sharma,** Shivendra Pratap, Pravindra Kumar. Characterization of isoflavonoids as inhibitors of β-hydroxyacyl-acyl carrier protein dehydratase (FabZ) from Moraxella catarrhalis: Kinetics, spectroscopic, thermodynamics and in silico studies. **BBA-General Subjects** 1862 (2018) 726-744.

4. Vijay Kumar, **Anchal Sharma,** Shivendra Pratap, Pravindra Kumar. Biophysical and in silico interaction studies of aporphine alkaloids with Malonyl-CoA: ACP transacylase (FabD) from drug resistant *Moraxella catarrhalis*. **Biochimie** 149 (2018) 18-33.

5. Pooja, Kesari , Neetu, **Anchal Sharma,** MadhusudhanRao Katiki, Pramod Kumar, BR Gurjar, AK Sharma, S Tomar, Pravindra Kumar. Structural, Functional and Evolutionary Aspects of Seed Globulins. **Protein Peptide Letters** 24 (3) (2017) 267-277.

6. **Anchal Sharma,** Vijay Kumar, Shivendra Pratap, Pravindra Kumar. The inhibitory and binding studies of methyl-sulfone hydroxamate based inhibitors against LpxC from drug resistant *Moraxella catarrhalis* using biophysical, biochemical and *in silico* approaches. **(Under revision).**

7. **Anchal Sharma,** Vijay Kumar, Shivendra Pratap, Pravindra Kumar. The inhibitory and binding insights of polyphenols with bifunctinonal DAH7PS from *Bacillus subtilis* using biophysical, biochemical and *in silico* approaches. **(In preparation).**

8. Vijay Kumar, **Anchal Sharma,** Shivendra Pratap, Pravindra Kumar, 1,4- Naphthoquinone as multi- targeted dual inhibitors FabD and FabZ enzymes of FAS II pathway from *Moraxella catarrhalis*: Biochemical, biophysical and in silico studies. **(Communicated).**

CONFERENCE ATTENDED AND POSTER PRESENTATION

1. Anchal Sharma, Shivendra Pratap Singh, Pravindra Kumar
"Cloning, Expression and Purification of Lpx-C from *Moraxella catarrhalis*" Recent advances in Structural Biology & Drug Discovery, 54, IIT Roorkee, 2014.

2. Anchal Sharma, Pravindra Kumar
"Biophysical Characterization of *Providencia alcalifaciens* DAH7PS (PaDAH7PS)" Annual Symposium of the Indian Biophysical Society, 254, IISER Mohali, 2017.

BOOK CHAPTER

1. Anchal Sharma, Poonam Dhankar, MadhusudhanRao Katiki, and Pravindra Kumar Structural Characterization of enzymes involved in Pesticides degradation. Bioremediation II. Studium Press LLC, USA (2016) 310-335.

LIST OF FIGURES

Figure No.	Title	Page No.
1.1	Schematic representation of the timeline of antibiotic discovery and resistnace	1
1.2	Acquisition of antibiotic resistance	3
1.3	Schematic representation of the common antibiotics action mechanism and resistance mechanism developed in bacteria.	4
1.4	Schematic representation of the shikimate pathway	8
1.5	Condensation reaction of PEP and E4P catalyzed by DAH7PS synthase.	10
1.6	Classification of microbial DAH7PS.	11
1.7	Monomeric structure of Type Iα DAH7PS	14
1.8	Quaternary structure of EcDAH7PS	15
1.9	(A) The active site architecture and of DAH7PS (B) The metal ion binding site	15
1.10	The allosteric inhibitor binding site.	16
1.11	Monomeric structure of the Type Iβ DAH7PS from TmDAH7PS	17
1.12	Monomeric structure of the Type Iβ DAH7PS (A) PfDAH7PS (B) ApDAH7PS	18
1.13	Monomeric structure of the Type II DAH7PS from MtDAH7PS	18
1.14	The active site architecture of MtDAH7PS	19
1.15	Feedback regulation of the Type Iα DAH7PS	21
1.16	Feedback regulation of the Type Iβ DAH7PS	22
1.17	Feedback regulation of the Type II DAH7PS	23
1.18	Chorismate mutase and DAH7PS fusion enzyme	24
1.19	The cell envelope of Gram-negative bacteria	26
1.20	General structure of the LPS	28
1.21	Schematic representation of the activation of the host innate immune system	30
1.22	Schematic representation of the LPS/TLR4 signal transduction	31
1.23	Lipid A Biosynthesis in *E. coli*	34
1.24	Shmetic representation of LPS transport	35
1.25	Structure of zinc-inhibited LpxC	37

1.26 Three dimensional structure of AaLpxC/TU514 complex 38
1.27 LpxC inhibitors binding sites 39
1.28 The chemical structures of the potent LpxC inhibitors 41
2.1 Purification profile and oligomeric state characterization of PaDAH7PS 51
2.2 (A) MALDI-TOF MS spectrum of His-tagged PaDAH7PS (B) Glutaraldehyde cross-linking profile of PaDAH7PS (C) The native-PAGE profile of PaDAH7PS 53
2.3 Effect of oxidized purification condition and redox metal treatment on the oligomeric state of PaDAH7PS 54
2.4 FTIR absorption spectrum of PaDAH7PS 56
2.5 Mass spectrometric analysis of PaDAH7PS-Hexnox 57
2.6 Mass spectrometric analysis of PaDAH7PS (A) PMF of PaDAH7PS-Tetox (B) PMF of PaDAH7PS-Diox 61
2.7 (A) MS/MS spectrum of 2179.908 Da and 2195.933 Da peptide peptide. 62
2.8 (A) MS/MS spectrum of 3000.426 Da and 3016.454 Da peptide (B) MS/MS spectrum of 3016.454 Da peptide. 63
2.9 (A) Enzyme activity in different oligomeric forms of PaDAH7PS (B & C) Michaelis-Menten kinetic parameters calculated for the both substrates. 65
2.10 Atomic force microscopy profile of PaDAH7PS-Tetox form of protein 66
2.11 Atomic force microscopy 2D image of PaDAH7PS-HOmox* showing the amorphous aggregates 67
2.12 Far-UV CD spectra comparison of different oligomeric states of PaDAH7PS 68
2.13 Intrinsic and extrinsic fluorescence spectra of different oligomeric states of PaDAH7PS 70
2.14 ThT binding assay profile of different oligomeric states of PaDAH7PS 71
3.1 Crystals of PaDAH7PS obtained by the vapor-diffusion method 81
3.2 Primary sequence analysis of PaDAH7PS with structurally related DAH7PS 84

3.3 The structure of apo PaDAH7PS, Type Iα DAH7PS enzyme 85
3.4 Enlarge view of the disordered regions in apo PaDAH7PS structure 86
3.5 Overall structure of PaDAH7PS in apo form. 86
3.6 Topology diagram of PaDAH7PS monomer 87
3.7 Overview of the secondary structures of PaDAH7PS 88
3.8 Comparison of oligomeric states of apoPaDAH7PS 91
3.9 Schematic diagram of interactions between protein chains 92
3.10 Schematic representation of interacting residues at the interfaces. 93
3.11 The superimposition of the apo PaDAH7PS with the complexed EcDAH7PS and apo ScDAH7PS. 94
3.12 Structure of the complexed EcDAH7PS 94
3.13 Comparison of PaDAH7PS with complexed EcDAH7PS 95
3.14 Monomer structure of the apo ScDAH7PS 96
3.15 Comparison of PaDAH7PS with apo ScDAH7PS 97
3.16 Representing the active site architecture of the EcDAH7PS 98
3.17 The active site comparison of PaDAH7PS 99
3.18 The allosteric site comparison of PaDAH7PS 99
4.1 Chemical structures of the inhibitors. 106
4.2 Cloning, expression and purification profile of BsDAH7PS 109
4.3 Biochemical characterization of BsDAH7PS 110
4.4 Kinetic analysis of inhibition mechanism 112
4.5 Circular dichroism spectroscopic studies of BsDAH7PS 113
4.6 Effect of different ligands binding on the BsDAH7PS 114
4.7 Fluorescence based quenching studies of BsDAH7PS 116
4.8 Stern-Volmer plots analysis of BsDAH7PS 118
4.9 ITC profiles of BsDAH7PS describing the binding of ligands 120
4.10 Pairwise sequence alignment of BsDAH7PS 121
4.11 The multiple sequence alignment of BsDAH7PS 122
4.12 Structure validation of the predicted BsDAH7PS model 123
4.13 Molecular modeling of full length BsDAH7PS 124
4.14 Molecular docking studies of BsDAH7PS 126
5.1 Chemical structures of the inhibitors 133
5.2 Cloning, expression and purification profile of McLpxC 136
Biochemical characterization of McLpxC

5.3	Biochemial charactersiation of McLpxC	137
5.4	Circular dichroism measurements of McLpxC	138
5.5	Effect of the inhibitors on the McLpxC	140
5.6	Secondary structure content of McLpxC	141
5.7	Fluorescence based quenching studies of McLpxC	142
5.8	Quenching mechanism studies of the McLpxC	143
5.9	ITC studies of McLpxC describing the thermodynamics parameters	145
5.10	Multiple sequence alignment of McLpxC	146
5.11	Molecular modeling of McLpxC	147
5.12	Molecular docking studies of McLpxC	148

LIST OF TABLES

Table No.	Title	Page No.
1.1	Outline of different biochemically and structurally characterized DAH7PS	12
2.1	Different purification conditions and their effects on the oligomeric state of PaDAH7PS	52
2.2	Effect of redox metal treatment on the oligomeric state of PaDAH7PS in different purification conditions	55
2.3	Methionine residues containing peptides generated by trypsin digestion from different oligomeric states of PaDAH7PS	58
2.4	Comparison of kinetic parameters of PaDAH7PS-Hexnox oligomeric state with its homologs	64
2.5	Secondary structure content of different oligomeric states of PaDAH7PS	68
3.1	Data collection and refinement statistic of PaDAH7PS	82
3.2	Statistics of β-strands of PaDAH7PS structure	88
3.3	Statistics of α-helices of PaDAH7PS structure	89
3.4	Statistics for all the interfaces interactions in PaDAH7PS tetramer	91
4.1	Comparison of the kinetic parameters of full length BsDAH7PS with other homologs DAH7PS (Type Iβ)	110
4.2	Inhibitory activities of chlorogenic acid, prephenate, ferulate, and shikimate against the full length BsDAH7PS	111
4.3	Quenching constants (K_q) and Stern-Volmer constants (K_{SV}) derived from SV equation on the ligands binding with the BsDAH7PS	117
4.4	Thermodynamic parameters of BsDAH7PS	119
4.5	Selective binding interactions of BsDAH7PS with inhibitors	125
5.1	Quenching constants (K_q) and Stern Volmer constants (K_{SV}) derived from SV equation on the inhibitors binding with McLpxC	144
5.2	Thermodynamic parameters of McLpxC	145
5.3	Selective binding interactions of McLpxC with inhibitors	149
5.4	MIC and IC_{50} Values of the inhibitors with Gram negative bacteria	150

LIST OF ABBREVIATIONS

Å	Angstrom
α	Alpha
AFM	Atomic force microscopy
β	Beta
BTP	1, 3 -bis (tris (hydroxymethyl) methylamino) propane
˚C	Degree centigrade
CD	Circular Dichroism
Cfu	Colony forming units
CHL	Chlorogenic acid
cm	Centimeter
CM	Chorismate mutase
DAH7PS	3 -deoxy- D-arabino-heptulosonate 7-phosphate synthase
DTT	Dithiothreitol
DMF	dimethylformamide
DMSO	Dimethyl Sulfoxide
E4P	Erythrose-4-phosphate
ESBLs	Extended spectrum β-lactamases
FER	Ferulate
g	Gram
h	Hours
HCl	Hydrocholride
HTS	High-throughput screening
IC_{50}	The half maximal inhibitory concentration
IFN	Interferon
IKK	IKB kinase
IPTG	Isopropyl β-D-1-thiogalactopyranoside
IRAK	interleukin-1 receptor-associated kinase
IRF3	Interferon response factor 3
ITC	Isothermal titration calorimetry
k_{cat}	Turnover number
Kdo	3-deoxy-D-waw70-oct-2-uiosonic acid
K_D	dissociation constant

K_m	Michaelis constant
LB	Luria Bertani
LBP	LPS-binding protein
LPS	Lipopolysaccharide
LpxC-2	α(R)-N-Hydroxy-α-methyl-α-(methylsulfonyl)-[1,1′-biphenyl]-4-butanamide, (+)-(2R)-4-(Biphenyl-4-yl)-N-hydroxy-2-methyl-2-(methylsulfonyl)butanamide, (2R)-4-Biphenyl-4-yl-N-hydroxy-2-methyl-2-(methylsulfonyl)butanamide
LpxC-4	α(R)-4-(2-Fluoro-4-methoxyphenyl)-N-hydroxy-α-methyl-α-(methylsulfonyl)-2-oxo-1(2H)-pyridinebutanamide, (2R)-4-[4-(2-Fluoro-4-methoxyphenyl)-2-oxo-2H-pyridin-1-yl]-N-hydroxy-2-methyl-2-(methylsulfonyl)butanamide
MaI	MyD88 adaptor-like
MALDI	Matrix Assisted Laser Desorption/Ionization;
MetSO,	Methionine sulfoxide
MIC	Minimum inhibitory concentration
mg	milligram
min	Minute
ml	Millilitre
mM	Millimolar
MRE	Mean residual ellipticity
OD	Optical Density
PCR	Polymerase chain reaction
PDB	Protein Data Bank
PEP	Phosphoenolpyruvate
PRE	Prephenate
rpm	Revolutions per minute
RMSD	Root mean square deviation
s	Seconds
SDS-PAGE	Sodium dodecyl sulfate polyacrylamide gel electrophoresis
SKA	Shikimate
TEV	Tobacco etch virus
ThT	ThioflavinT
TLR4	Toll-like receptor 4

TRAF6	TNF receptor-associated factor 6
TRAM	TRIF-related adaptor molecule
TRIF	Toll-interleukin receptor adaptor protein inducing interferon-β
Tris	tris(hydroxymethyl)aminomethane
UDP	Uridine diphosphate
UDP-GalNAc	UDP-N-acetyl-galactosamine
UDP-GlcNAc	UDP-N-acetyl-glucosamine
Ɛ	Molar extinction coefficient
γ	Gamma
M	Molar
μg	Microgram
μl	Microlitre
μM	Micromolar


भारतीय प्रौद्योगिकी संस्थान रुड़की
INDIAN INSTITUTE OF TECHNOLOGY ROORKEE

CHAPTER 1

INTRODUCTION AND LITERATURE REVIEW

1.1 Introduction

In the golden age (1940-1960s), a remarkable success in the antibiotic drug discovery symbolized a classic victory towards the wellness of human beings. But it generated a misconception that antibiotics could be utilized against all pathogenic bacteria causing the infectious diseases. However, severe health-threatening conditions and serious outbreaks of the bacterial infections are still continuing and increasingly being reported due to the emergence of drug resistance in bacteria and slow development of new antibiotics. Now the emergence of drug resistance in the bacteria has become second-leading cause for the mortality worldwide (Figure 1.1) [1-4].

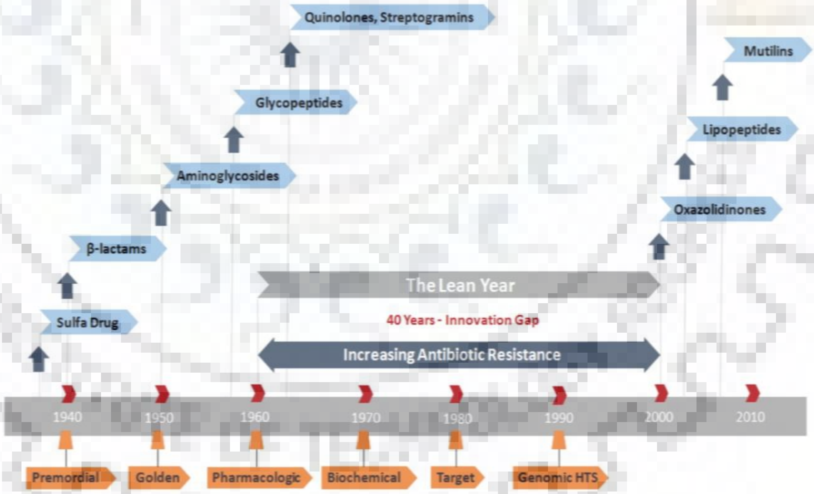

Figure 1.1: Schematic representation of the timeline of antibiotic discovery and concomitant attempts taken to avoid the resistance. In the period of golden era, most of the antibiotics used today were discovered. In the lean year (~ 40 years) there is no new antibiotic discovery and development occurred. In the pharmacologic period, attempts were made to better understanding and improvement the usage of drug likely by dosing and administration. In the biochemical period, knowledge about the biochemical actions of the drugs and their resistance mechanisms led to the several chemical modification studies to overcome the drug resistance. In the target period, several genetic studies and knowledge about the mode of action

led to the efforts to design new compounds. Further, genome sequencing approaches and development of the high-throughput screening (HTS) assays were introduced for the target identification and new drug molecules optimization (Figure modified from Fischbach et al., 2009).

The three classes of the drug resistant bacteria are emerging threat to the public health and results in high health care cost [4]. In the first class, the methicillin-resistant Staphylococcus aureus (MRSA) and the vancomycin-resistant S. aureus (VRSA) are the most prevalent deadly bacteria which causes deaths of thousands of people and adds to billions of health care cost every year [5]. Second class consists of the multidrug-resistant (MDR) and the pan-drug-resistant (PDR) Gram-negative bacteria are associated with the serious threat of infections that are really untreatable and fatal. Moreover, the strains of *Escherichia coli*, *Klebsiella pneumoniae*, *Acinetobacter baumannii*, and *Pseudomonas aeruginosa* have shown resistance to the commonly used antibiotic classes like penicillins, cephalosporins, aminoglycosides, tetracyclines, carbapenems, monobactams, quinolones and polymyxins [6]. Third class includes the MDR and the extensively-drug-resistant (XDR) strains of *Mycobacterium tuberculosis* pathogenic bacteria, which impedes treatment challenges and causes threats to the developing world [7, 8].

Thus, the continuous and rapid growth of the new antibiotic-resistant strains has created a situation in which there is a few or no treatment for certain infections associated with the resistant microorganisms [9]. The emergence of drug resistant bacteria and the dipping in rate of development as well as approval of the new antimicrobials agents have presented a serious challenge to the modern medicine [10].

1.1.1 Mechanisms of resistance in bacteria

Currently, the exorbitant usage of antibiotics in controlling several infectious diseases associated with humans and animals as well as in the agriculture field has created unprecedented conditions for the mobilization of resistance elements among microbes [11, 12]. Microbial world has remarkable genetic plasticity and diverse molecular tools to respond against wide array of environmental threats and to drive resistance in the presence of inhibitory molecules that may risk their survival [13]. Bacteria existing in the same ecological niche as of other antibiotic-producing microbes have evolved various molecular mechanisms to resist the adverse effects of antibiotic molecules. Thus, the intrinsic resistance mechanisms allow the bacteria to survive in the presence of unfavorable conditions.

From the evolutionary viewpoint, bacteria usually utilize two genetic strategies to eliminate the attack of antibiotic molecules viz. (i) by gaining a foreign DNA i.e., code for the resistance mechanism (ii) mutations (Figure 1.2) [14] .

1.1.1.1 Horizontal gene transfer

Horizontal gene transfer (HGT) mechanism is the most frequent mechanism to acquire the foreign DNA. It is also an important driver for magnification and evolution of resistance in bacteria [15]. Naturally, bacteria acquire foreign DNA via three main strategies, (*i*) transformation (incorporation of foreign naked DNA), (ii) conjugation (bacterial "sex") and (*iii*) transduction (mediated through phage) (Figure 1.2) [6]. Transformation is the prevalent mechanism of HGT in many human pathogenic bacteria, including representatives of the genera *Staphylococcus, Streptococcus, Campylobacter, Neisseria, Helicobacter, Haemophilus, and Pseudomonas* [16]. The microbes present in the hospital's environment commonly use cell-to-cell contact strategy (i.e., conjugation) for gene transfer to acquire the resistance. In last, one of the most efficient and simple mechanism for accumulating resistance genes in bacteria is demonstrated by integrons. It is a robust tactic for genetic material interchange and main driver of the bacterial evolution and resistance [14].

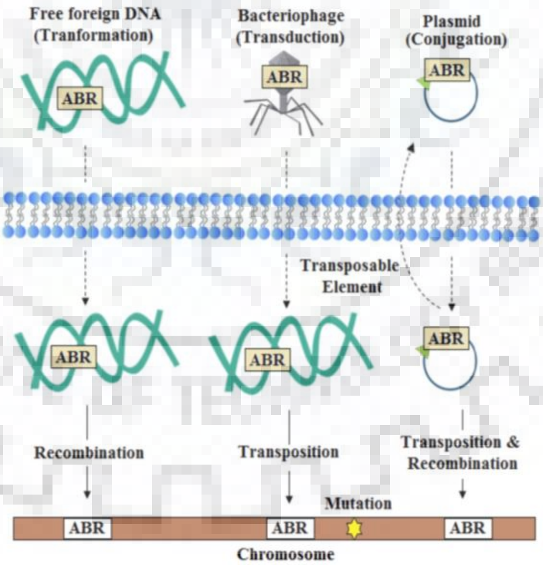

Figure 1.2: Acquisition of antibiotic resistance. Bacteria can acquire the foreign DNA having antibiotic resistance gene (ABR) by the transformation. ABR can also transfer by the transduction process mediated through bacteriophage. ABR can be transferred through through plasmids and conjugative transposons during conjugation process. Bacteria can also become drug resistant on the mutation in the target gene in the chromosome (Figure modified from Alekshun and Levy, 2007).

1.1.1.2 Mutational resistance

In this state, there is a mutation in the gene(s) of the population of susceptible bacterial cells, against an antibiotic, which affects the activity of drug. This results into the survival of the cells even in the presence of an antimicrobial agent and the emergence of the resistant mutant cells. Consequently, the resistant mutant bacterial strains predominate and the susceptible strains eliminate over the time.

The alteration in the activity of drug by bacteria can be done by following several strategies: (i) modifications of the drug target (ii) a decrease in the uptake of the drug (iii) activation of efflux mechanisms to extrude the antibiotics (iv) production of the antibiotic-inactivating enzymes (v) global alterations in important metabolic pathways (Figure 1.3) [17, 18] .

Thus, the resistance developed in bacteria due to the acquired mutation is diverse and also varies in complexity [19, 20]. For example the emergence of the efflux systems in bacteria is responsible for the ineffectiveness of chloramphenicol (targets protein synthesis machinery) against many pathogens and hence chloramphenicol is no longer considered a first line agent [21]. Rifampicin (targets RNA polymerase enzyme) has been shown to be less effective due to the modification of its target [22]. Additionally, bacterial cells can utilize cadre of resistance mechanisms and multiple biochemical pathways for their survival in the presence of antibiotics. Bacteria have exhibited the co-existence of the several biochemical strategies to resist the fluoroquinolone (FQ) such as the over-expression of drug efflux pumps, mutations in the genes encoding the target site and protection of target site by a protein designated Qnr [23].

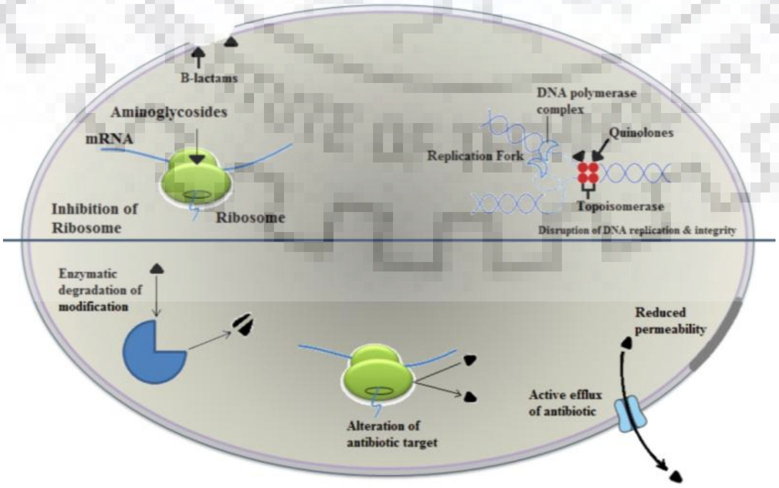

Figure 1.3: Schematic representation of the common antibiotics action mechanism (upper panel) and resistance mechanism develop in bacteria (lower panel) (Figure modified from Crofts et al., 2017).

On the other hand, bacterial species also display the preference for some resistance mechanisms in comparison to the others. For example, Gram-negative bacteria show the resistance to the β-lactams based antibiotics, predominantly by producing the β-lactamases enzymes, whereas Gram-positive bacteria modify the target sites via penicillin-binding protein to become resistant against these compounds [24-26].

Most of the existing antibiotics represent a similar core chemical structure and target the cellular processes such as cell wall biosynthesis, transcription, and translation of the bacterial cell (Figure 1.3) [27]. Hence, bacteria have shown the emergence of the multi-drug resistance against all the currently available antibiotics in the market. Thus, the alarming rate of increment in the antibiotic-resistant bacteria presents a serious threat to the human health. Therefore, the efforts toward the discovery and the development of novel molecules/new scaffolds are essentially required to combat the problem at this crucial stage.

1.1.2 Strategies to develop new antibiotics

Until the beginning of 1990s, the principal strategy was to modify and improve the already existing drugs and make them more efficient against the resistant organisms. For example, glycylcyclines and fluoroquinolones were derived through the modification of the tetracyclines and quinolones, respectively [28, 29].

But, in the 21st century, it has become difficult to deal with the large requirements of the medical community and to provide them with a sufficient coverage. Another approach is to target and inhibit the resistance causing gene products i.e., enzymes which destruct/hydrolyze the antibiotics [30]. Several bacteria produces β-lactamase, which inactivate the drugs of the β-lactam class of the antibiotics (penicillins, cephalosporins, and others), and thus it is the most potential enzyme associated with the resistance mechanism. The problem posed by the β-lactamases can be reduced by introducing the substance, which functions as the inhibitor of β-lactamases, synergistically with the β-lactam antibiotics. Several specific substances including clavam, clavulanic acid, the penicillanic acid sulfones sulbactam and 7-acetylmethylenepenicillanic acid (AMPA) act against the β-lactamases and protect the β-lactamase-susceptible antibiotics. The clavulanic acid is a potent and well known clinically used inhibitor of β-lactamases, which is effective when supplemented with amoxicillin and ticarcillin. The success of clavulanic acid has established that β-lactamase inhibitors can be considered a good solution to the problem of antibiotic resistance [30]. But to keep the pace up with the increasing microbial resistance, additional approaches must be explored and followed to discover and develop the more potential novel classes of the antibacterial molecules.

Now the identification and characterization of unexplored novel cellular functions as the potential targets are preconditions for the development of novel antibiotics. And currently, the extensive success in the field of genomics is providing a wealth of new validated molecular targets information, which is driven by complete genome sequencing of the multiple pathogenic bacteria [31, 32]. For the development of new antimicrobial molecules by applying this strategy, furthermore key steps are required to be followed after the identification and the structural/functional characterization of validated target such as high-throughput screening against different compound collection, structure-activity relationship (SAR) study (narrow down the possible lead molecules) and *in vivo* testing in animal models and finally to the human clinical trials [31].

Although, various novel leads compounds are rising from the genomics-driven and target-based screening approach, but now the major challenge is to optimize and progress these leads molecules towards the clinical trials and made them a part of next generation antibiotics [32, 33]. Hence, selection and characterization of a potential drug target are very crucial steps of this lengthy and expensive process of the drug development.

The present study focuses on biophysical, biochemical and the structural characterization of validated and potential drug targets; DAH7PS and LpxC committed enzymes of the Shikimate and Lipopolysaccharide biosynthesis pathway, respectively present in bacteria. We have characterized a monofunctional DAH7PS from a drug-resistant *Providencia alcalifaciens* and a bifunctional DAH7PS from the *Bacillus subtilis.* Furthermore, we have also characterized LpxC enzyme from a Gram-negative, drug-resistant pathogenic *Moraxella catarrhalis* and binding features with its inhibitors.

1.2 The shikimate pathway

All the living organisms demand a variety of the aromatic compounds such as aromatic amino acids (Phe, Trp, and Tyr), folates, Phylloquinone (vitamin K), ubiquinone, napthoquinones, which are essential for their primary metabolism. In all bacteria, fungi, apicomplexans and plants, the de novo biosynthesis of these aromatic compounds mediates via an essential pathway known as the shikimate pathway [34-37]. All animals and humans, being deficient of the shikimate pathway obtain the above compounds from their dietry sources. Firstly, this pathway was elucidated in bacteria, which were deficient in the growth as a result of mutation until the aromatic supplements were provided to the mutant cells [38]. The shikimate pathway involves seven enzymatic reactions, resulting in the stepwise conversion of the primary carbon metabolites (Erythrose-4-phosphate and Phosphoenolpyruvate) into chorismate (Figure 1.4). The synthesized end product “chorismate” of this pathway aid as a universal precursor molecule for further synthesis of a variety of aromatic compounds [34-37].

Moreover, the secondary metabolites such as lignin, coumarins, indole derivatives, flavonoids, alkaloids, and various other phenolic compounds are also synthesized by the chorismate molecule [34-37]. These compounds are very important for the UV protection, signaling, electron transport, communication, plant defense, and wound response [39]. For the first time in 1885, “shikimic acid”, a central intermediate compound of this pathway was isolated from Japanese plant *Illicium anisatum*, naming the pathway as shikimate pathway [40, 41]. All the enzymes of this pathway have been characterized from different microbes and plants [42]. Moreover, the genes of enzymes involved in the shikimate pathway have been identified from many apicomplexan parasites including *Plasmodium* species and *Toxoplasma gondii* etc [43-47]. The shikimate pathway is absent in both the animals and humans and highly essential for the microbes, fungi, algae and plants. Thus, the enzymes of this pathway have attracted attention and are being exploited as the potential targets for antimicrobial agents and herbicides designing [42, 48-50]. Therefore, the functional and the structural characterization of enzymes involved in the shikimate pathway are very crucial for the designing and development of the broad spectrum inhibitors and herbicides against several pathogenic microbes, fungi, and apicomplexan parasites.

1.2.1 Biosynthesis of the chorismate

Here, we have briefly described all the reactions of shikimate pathway catalyzed by different enzymes during the biosynthesis of the chorismate (Figure 1.4) [51, 52] The first committed reaction catalyzed by DAHP synthase (EC 2.5.1.54) results in the formation of seven carbon 3-deoxy-D-arabino-heptulosonate-7-phosphate (DAH7P) [51, 53-55]. In the second reaction, the formed DAH7P loses its phosphoryl group and cyclizes into the 3-dehydroquinone (DHQ) by 3-dehydroquinone synthase (EC 4.6.1.3) enzyme which utilize the NAD+ as a cofactor [56]. The third enzyme, 3-dehydroquinone dehydratase (EC 4.2.1.10) introduces a double bond in the aromatic ring and leads to the formation of an intermediate 3-dehydroshikimate (DHS). In fourth reaction, DHS transforms into the shikimic acid by shikimate dehydrogenase through NADP reduction. Then shikimic acid phosphorylates to 3-phosphoshikimate and the reaction is catalyzed by shikimate kinase (EC 2.7.1.71) [57, 58]. Afterward, 5-Enolpyruvylshikimate-3-phosphate synthase (EPSP synthase, EC 2.5.1.19), which is also known as 3-phosphoshikimate

1-carboxyvinyltranferase, catalyzes the transfer of the enolpyruvyl moiety of phosphoenolpyruvate to 5-OH position in shikimate 3-phosphate to form EPSP [59]. The formed EPSP loses its phosphoryl group and is subjected to the reduction to produce chorismate by chorismate synthase [60]. The chorismate further serves as a checkpoint in the biosynthesis of phenylalanine and tyrosine/tryptophan. The enzyme 5-enolpyruvylshikimate 3-phosphate (EPSP) synthase of the shikimate pathway is one of the potential target for the development of broad-spectrum herbicide known as glyphosate (N-[phosphonomethyl]-glycine) [61].

Figure 1.4: Schematic representation of the shikimate pathway. The key reactions involved in the synthesis of chorismate prior to branching of the pathway and formation of the several vital amino acids (Tyr, Phe and Trp).

The differences in the structural characteristics of these enzymes among microbes, fungi, and plants, enlighten their differential mode of regulations. Considering such a huge diverse nature of these enzymes, a SKPDB (Shikimate Pathway Database) has been developed to study them. This database contains extensive information on each enzyme from the different sources with a full description of their sequence, function, crystal and NMR structures [62].

1.2.2 Molecular organization and intracellular localization of shikimate pathway enzymes

The shikimate pathway enzymes have shown diversity in their molecular organization. In case of prokaryotes, fungi, and plants, the molecular organization of enzymes is similar and each of these individual enzymes is encoded by an individual gene. However, in plants, the dehydroquinate dehydratase and the shikimate dehydrogenase are exception in a way that these occur as a fused protein [63, 64]. In bacteria and fungi, all the reactions of the pathway operate in the cytoplasm, whereas in plants and algae all enzymes are functional in plastid organelles [65]. In plants the enzymes of shikimate pathway have an N-terminal signal sequence which is mainly responsible for their transport to the plastids [66]. As these enzymes are encoded by the genomic DNA and expressed in the cytoplasm and then localized to the plastids and followed by the cleavage of the signal sequence inside the plastid. In eukaryotic ancestors including fungi, the shikimate pathway enzymes are mainly found in the cytoplasm, and the enzymes starting from 2^{nd} to 6^{th} (DHQS-DHQ-SDH-SK-ESPSPS) of the pathway form AROM complex [35, 63, 67]. Further, in higher organisms, all these enzymes are localized to plastids. However, in some red algae ancestor, the enzymes of the shikimate pathway are found in both cytosol and plastids [68].

1.3 Microbial DAH7PS

1.3.1 3-Deoxy-D-arabino-heptulosonate-7-phosphate synthase

3-deoxy-D-arabino-heptulosonate-7-phosphate (DAH7PS) synthase (EC 2.5.1.54) catalyzes the first committed step in the biosynthesis of the shikimic acid, which further leads to the synthesis of various aromatic compounds. It catalyzes the stereospecific aldol condensation reaction between the phosphoenolpyruvate (PEP) and the erythrose 4-phosphate (E4P) and produces a seven carbon keto acid, 3-deoxy-D-arabinoheptulosonate-7-phosphate (DAH7P) and an inorganic phosphate (*Pi*) (Figure 1.5). During this stereospecific condensation reaction, C-O bond cleavage occurs, instead of the typical P-O bond cleavage, and *si* face of C3 of the PEP attacks on the re face of the aldehyde of E4P [69-71].

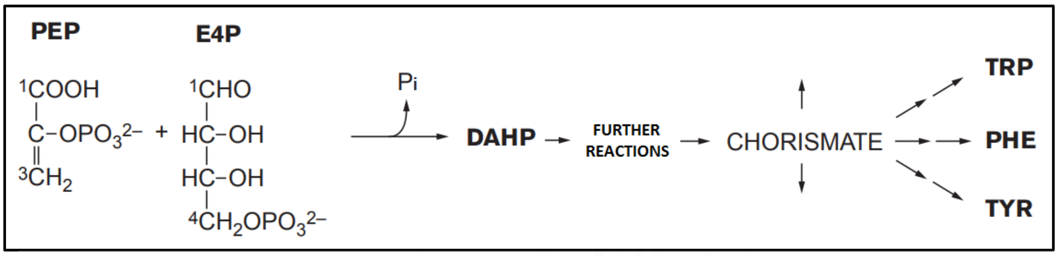

Figure 1.5: Condensation reaction of PEP and E4P catalyzed by DAH7PS synthase.

In most microbes DAH7PS exists mainly in three isoforms; DAH7PS (Phe), DAH7PS (Tyr) and DAH7PS (Trp) [72-74]. Each of the three isoforms of DAH7PS in *E.coli* is feedback regulated by one of the three aromatic amino acids (Phe, Tyr and Trp) fomed by the shikimate pathway. DAH7PS (Phe) is a major isofrom and constitutes ~ 80 % of total cellular DAH7PS activity in *E.coli*, while DAH7PS (Tyr) and DAH7PS (Trp) are less abundant and constitute only 20 % and 1 %, DAH7PS acitivity, respectively [75]. All these isoforms of DAH7PS are metalloenzyme and require a divalent cation for their catalytic activity [76]. But the nature of metal required for their catalytic activity varies among the different microbial species.

1.3.2 Classification of microbial DAH7PS

Primarily on the basis of the sequence similarity, the DAH7PS enzymes have been classified into the Type I and Type II (Figure 1.6). Both types of DAH7PS share < 10 % of the sequence identity and also exhibit the considerable differences in their oligomeric states/quaternary structures. The sequence comparison analysis of the DAH7PS has shown that the isoforms of the DAH7PS only share ~ 41 % sequential identity. The variation in the primary sequences also leads to their differential mode of regulation [4]. Type I DAH7PS are mainly associated with microbes including *E. coli* and *Saccharomyces cerevisiae* [34] whereas Type II DAH7PS are associated with plants [53] and some microbes including *Mycobacterium tuberculosis* [77], *Helicobacter pylori* [78], *Streptomyces sp.*, *Campylobacter jejuni*, *Corynebacterium diphtheriae*, *Agrobacterium tumefaciens*, and *Novosphingobium aromaticivorans* [79]. All these microbes having Type II DAH7PS are found deficient in Type I DAH7PS, which evidently shows the essential role of Type II DAH7PS in the aromatic amino acid biosynthesis. However, the overall monomeric fold, arrangement of the substrate (PEP) and the divalent metal ion interacting key residues are found entirely conserved and situated in almost an identical way in both types (I & II) DAH7PS enzymes [78]. Additionally, in *Bacillus subtilis* a bifunctional DAH7PS synthase has been found which contains a regulatory chorismate mutase domain (CM) along with the catalytic DAH7PS domain [80]. Other unregulated DAH7PS which consists only a core barrel domain in their overall structure have also been reported in *Pyrococcus furiosus* [81].

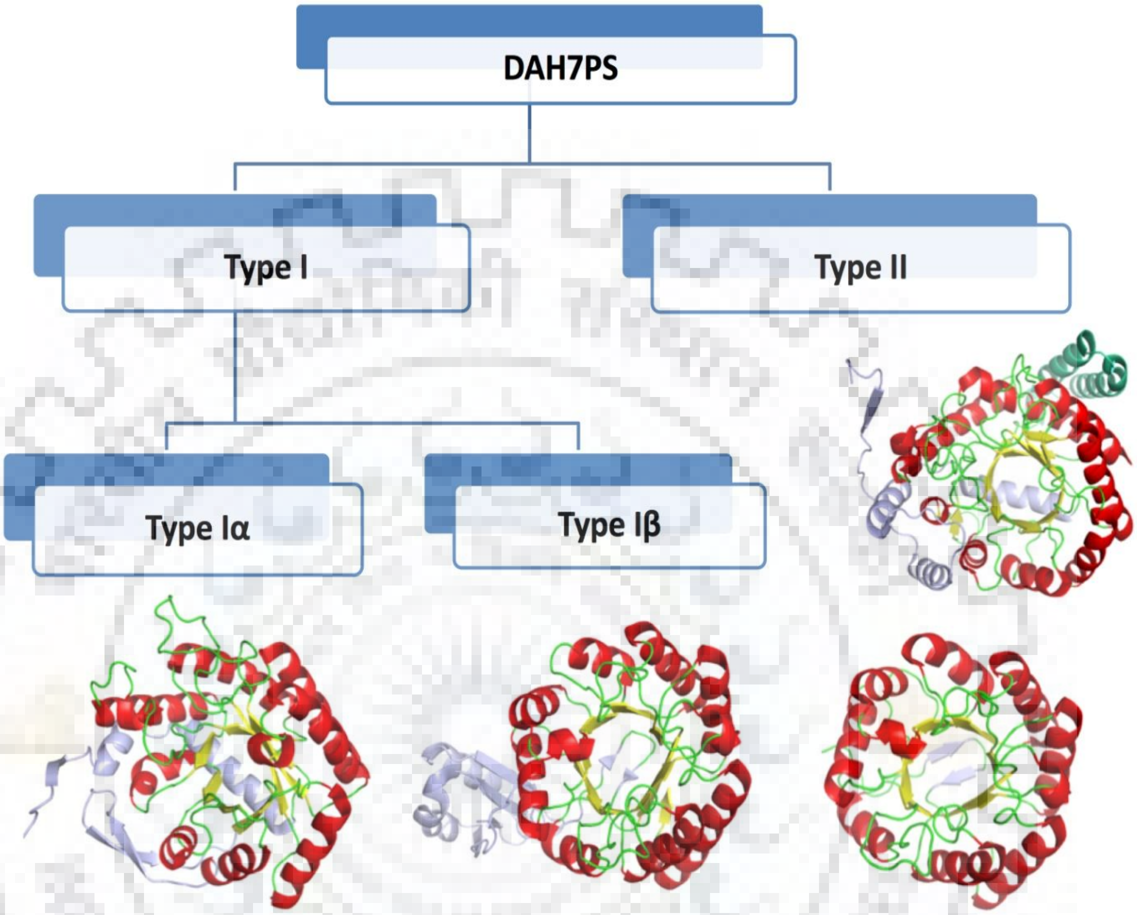

Figure 1.6: Classification of microbial DAH7PS. The different DAH7PS families showing the monomer $(\beta/\alpha)_8$ TIM barrel fold of the characterized DAH7PS. The secondary structures helices, sheets and loops of the core barrel have been shown in different colors red, yellow, and green respectively and other decorative internal and external extensions have shown in light blue color and sea green (present in Type II MtDAH7PS), respectively.

Moreover, Type I DAH7PS family has been further subdivided into the two subfamilies: Type Iα and Type Iβ (Figure 1.6). Type Iα contains solely the DAH7PS, while Type Iβ also contains KDO8PS enzymes along with the DAH7PS enzymes. Furthermore, Type Iβ enzymes have been also subdivided into the subfamilies Iβ$_D$ and Iβ$_K$, which contain DAH7PS and KDO8PS enzymes, respectively. Till now, the representative enzymes from all different subfamilies have been well-characterized biochemically and structurally. An outline of the DAH7PS enzymes is highlighted in the table 1.1.

Table 1.1 Outline of different biochemically and structurally characterized DAH7PS.

Classification	**Species**	**PDB Codes**	**References**
Type Iα	*Escherichia coli*	1QR7,1KFL,1GG1	[82]
	Saccharomyces cerevisiae	1OAB,1OFB,1OFO	[83]
	Neisseria meningitidis	5DCB,5DCD,5DCE	[84]
	Salmonella typhimurium		[85]
	Neurospora crassa		[86]
Type Iβ	*Thermotoga maritima*	1RZM,1VR6	[87-89]
	Pyrococcus furiosus	1ZCO	[88]
	Aeropyrum pernix	1VS1	[90]
	Listeria monocytogenes	3NVT	[91]
	Geobacillus sp.	5J6F	[80]
	Bacillus subtilis (CM domain)	5GMU, 5GO2	[92]
Type II	*Mycobacterium tuberculosis*	2B7O, 2YPQ	[78] [93]

Intrestingly, in some organisms, such as *Pseudomonas aeruginosa*, *Acanthamoeba*, *Xanthomonas campestris*, *Stigmatella aurantiaca*, *Amycolatopsis mediterranei*, and *Amycolatopsis methanolica*, both Type I and Type II DAH7PS have been recognized [94-97].

1.3.3 Metal activation of DAH7PS

Till now, all the characterized DAH7PS have been reported as the metal-dependent enzymes and they use divalent metal ions for the catalysis of reaction. In the presence of the ethylene diamine tetra acetic acid (EDTA), a chelating agent, these enzymes lost their activity but addition of the divalent cations resulted in the restoration of the activity of enzyme [76, 77, 80]. Sequence alignment and structural analysis of all the known DAH7PS enzymes have shown the presence of conserved (Cys, His, Glu and Asp) metal ions interacting residues [82, 98]. However, all the DAH7PS are metalloenzyme, but DAH7PS enzymes of different organisms and even the isoforms of a microbial species require different metal ions for their catalytic activity. All the three isoforms of EcDAH7PS have revealed a significant loss in their activity due to the treatment of EDTA. But their reactivation occured with a range of metal ions in the following order: $Mn^{2+} > Cd^{2+} > Fe^{2+} > Co^{2+} > Ni^{2+} > Cu^{2+} > Zn^{2+} > Ca^{2+}$. Mn^{2+} has shown the highest activity but can be easily displaced from the DAH7PS enzyme by any other divalent metal ions. Similarly, ScDAH7PS (Phe) has also demonstrated the highest enzymatic activity in the presence of Mn^{2+}, whereas other isoform of ScDAH7PS (Tyr) have shown Cd^{2+} as the most activating metal ion.

1.3.4 Metal catalyzed oxidation of EcDAH7PS (Phe)

Interestingly EcDAH7PS (Phe), in the absence of the substrate (PEP), was found to be vulnerable towards the metal-catalyzed oxidation [99]. In this case, the presence of the redox metals (Cu^{2+} and Fe^{2+}) was greatly affecting the oligomeric state and the activity of the EcDAH7PS (Phe). In the presence of Cu^{2+}, the functionally active tetrameric state of the EcDAH7PS (Phe) was dissociated and converted into the inactive monomeric form. EcDAH7PS (Phe) have also shown the spontaneous inactivation, which is associated with the loss of two thiols groups, but was completely restored on the addition of reducing agent (DTT). Mutation in two active-site cysteine residues (Cys61 and Cys328) resulted in the insensitiveness of DAH7PS enzyme towaards the metal ion attack and lack of oligomer subunit dissociation even on the Cu^{2+} treatment. Further, in the peptide mass mapping of the inactivated EcDAH7PS an extra unexpected mass of the peptide clearly depicted the presence of a disulfide linkage, formed between these two cysteine residues. The substrate (PEP) usually stabilizes the DAH7PS enzyme during purification and storage conditions; however, another substrate (E4P) demonstrates the opposite effect and increases the rate of spontaneous inactivation of the enzyme through a Schiff-base formation between the aldehyde group of the E4P and lysine residue of active site. Site-directed mutagenesis, chemical modification, spectroscopic, and structural analysis have shown that the invariant Cys61 and His268 residues of EcDAH7PS (Phe) are involved in metal binding and are also essential for enzyme catalysis [99].

1.4 Structural features of DAH7PS

1.4.1 Structural features of the microbial Type Iα DAH7PS

Type I DAH7PS have been well-studied enzyme in comparison to the Type II DAH7PS. The majority of the reported 3D structures of DAH7PS belongs to the Type I, and have been extensively studied from the *Escherichia coli* and eukaryotic organism *Saccharomyces cerevisiae* [82, 83]. The overall structure of DAH7PS enzymes from both the organisms comprise of a $(\beta/\alpha)_8$ TIM barrel fold, which is a characteristic feature of this family. TIM $(\beta/\alpha)_8$ barrel fold of both the enzymes are decorated with an extension at the N-terminal end (strand β0 followed by α00 and α0 helices), and an extra β6a/β6b sheet inserted before the β6 strand of the barrel (Figure 1.7). An α-helix present at the N-terminal end of DAH7PS hinders its barrel.

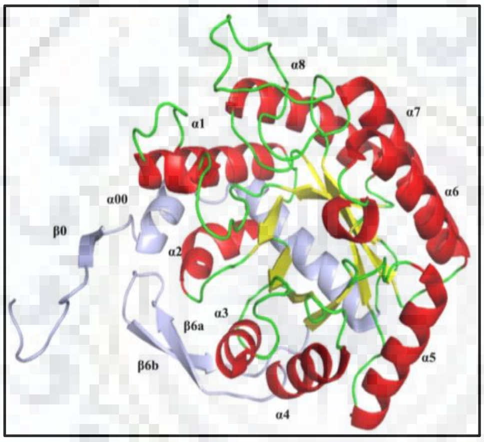

Figure 1.7: Monomeric structure of Type Iα DAH7PS. EcDAH7PS showing the core TIM $(\beta/\alpha)_8$ barrel, with the N-terminal extension and internal extension light blue in color (PDB ID 1KFL).

Although, both these DAH7PS have originated from the different organisms and possess different pattern of regulation, but their 3D structures were found very similar to each other. Both EcDAH7PS (Phe) and ScDAH7PS (Tyr) are reported as the tetramer structures, which consist of two tight dimers (Figure 1.8). The dimers of *E. coli* and *S. cerevisiae* DAH7PS can be superimposed to each other, but the association of the two dimers in a functional tetrameric unit was found significantly different [82, 83]. In ScDAH7PS, tetrameric association is purely based on the hydrophobic interactions. However, in EcDAH7PS, the residues of the helices α4 and α5 and loops β2–α2, β3–α3, β4–α4, α4–β5, β5–α5, and α5–β6A undergoes association via multiple contact factors like electrostatic, hydrogen bonding, and van der Waals interactions. Additionally in both the DAH7PS, the association of the dimeric unit is also significantly enhanced by the construction of a three-stranded antiparallel β-sheet, which involves the N-terminal β0 strand of one monomeric unit and the extended β6a–β6b strands of the other monomeric unit.

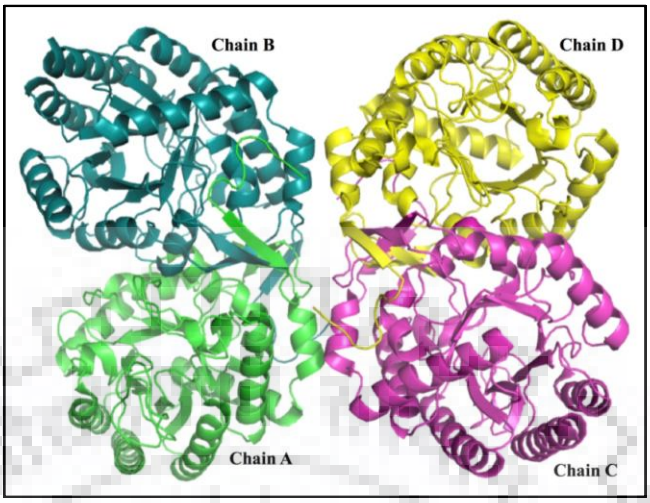

Figure 1.8: Quaternary structure of EcDAH7PS. The tetramer oligomer of the DAH7PS depicting the monomer chain with different color (PDB ID 1KFL).

The active site of DAH7PS is located at the C-terminal end of $(\beta/\alpha)_8$ TIM barrel and comprises of protein secondary structures; β-strands-β2, β5, β8 and β-α loops (the nomenclature and amino acids number have been assigned according to the EcDAH7PS). The active site majorly comprises of the positively charged amino acid residues including Arg92, Lys97, Arg165, Lys186, Arg234, which interact with the substrate (PEP) (Figure 1.9A).

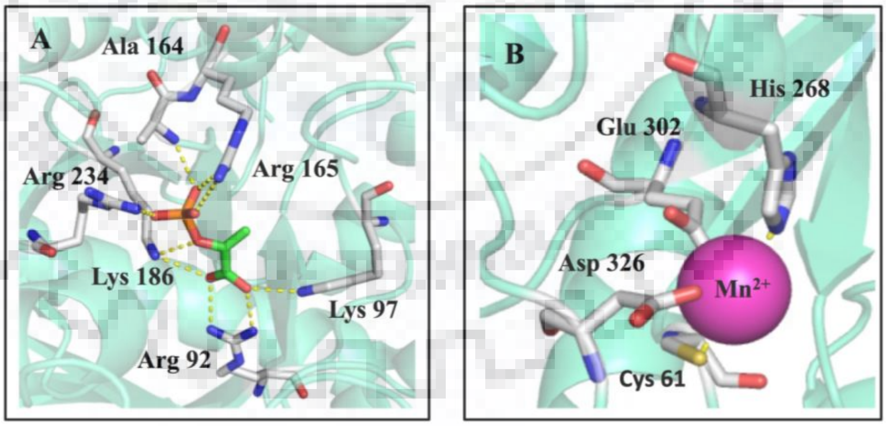

Figure 1.9: (A) The active site architecture of DAH7PS. The positively charged residues including Arg92, Lys97, Arg165, Lys186, Arg234 interacting with the substrate (PEP) comprise the active site at the C-terminal end of $(\beta/\alpha)_8$ TIM barrel. Green and grey color sticks are showing the bound substrate and its interacting residues, respectively. **(B) The metal ion binding site.** EcDAH7PS showing the metal ion (Mn^{2+}) in purple color and co-ordinating

residues (Cys61, His268, Glu302, and Asp326) are depicting in grey color sticks (PDB ID 1N8F).

The metal ion present at the active site of DAH7PS interacts with amino acid residues Cys61, His268, Glu302, and Asp326. Both the substrate and the metal ion (PEP and Pb^{2+}) are in close vicinity and co-ordinate to interact with each other (Figure 1.9B). The overall organization of the active sites of both EcDAH7PS (Phe) and ScDAH7PS (Tyr) are very similar in terms of the arrangement and conservation of amino acid residues involved in metal and substrate binding. The inhibitor binding site of the DAH7PS formed by nine residues Pro19, Asp146-Ala154, Gly178-Ser180, which are distinctly located in the primary sequence of the protein but cluster together in the 3D structure, is situated outside the core of barrel (Figure 1.10). Alterations in the protein's conformation or dynamics occur, on binding of the inhibitors, lead to the changes at the active site and prevent the further binding of the substrate with DAH7PS.

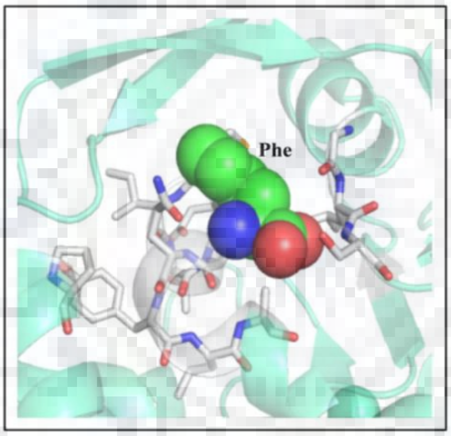

Figure 1.10: The allosteric inhibitor binding site. EcDAH7PS showing bound inhibitor (Phe) at the allosteric site as green color and interacting residues are depicting in grey color sticks (PDB ID 1N8F).

1.4.2 Structural features of Type Iβ DAH7PS

The crystal structures of Type Iβ DAH7PS enzyme from *Thermotoga maritima*, *Pyrococcus furiosus* and *Aeropyrum pernix* have been determined [80, 87-89]. As in case of Type Iα DAH7PS, TmDAH7PS and PfDAH7PS also depicted similar $(\beta/\alpha)_8$ TIM barrel structural fold and both of the enzymes crystallized in the tetrameric form. The tetrameric functional unit of TmDAH7PS is constructed via association of two dimers which include the contribution of α5-α8 helices and β5-α5, β6-α6, and β7-α7 loops. Each barrel of TmDAH7PS contains a two-stranded hairpin like structure and a ferredoxin-like (FL) domain at the N-terminal end (Figure

1.11). The ferredoxin-like (FL) domain containing distinctive βαββαβ fold connects with barrel via a flexible linker. It has been clearly shown that ferredoxin-like (FL) domain is involved in the feedback regulation of the DAH7PS (Figure 1.11). Ferredoxin-like (FL) domain is found remarkably similar to the ACT domain and fuses with other enzymes like aspartate kinase, chorismate mutase, and tyrA (prephenate dehydrogenase) involved in the amino acid biosynthesis.

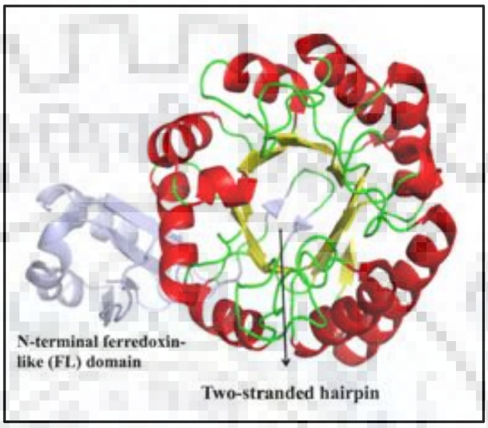

Figure 1.11: Monomeric structure of the Type Iβ DAH7PS. TmDAH7PS contains a two-stranded hairpin like structure and a ferredoxin-like (FL) domain at the N-terminal end depicting in the light blue color (PDB ID1RZM).

The PfDAH7PS is also tetrameric and contains two stranded hairpin structure but is devoid of the ferredoxin-like (FL) regulatory domain (Figure 1.12A). Similarly, ApDAH7PS also contains $(\beta/\alpha)_8$ TIM barrel fold in its overall 3D structure and exists as tetramer (Figure 1.12B). But it does not contain any internal or external decorative structural domain responsible for the regulation.

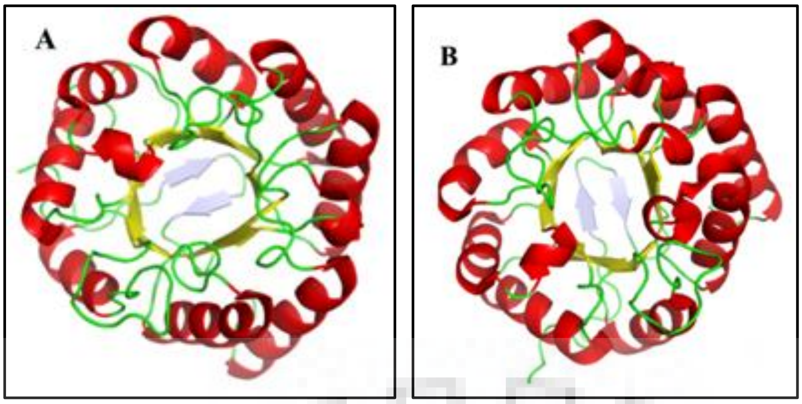

Figure 1.12: Monomeric structure of the Type Iβ. (A) PfDAH7PS **(B)** ApDAH7PS monomeric structures of both showing the core $(\beta/\alpha)_8$ barrel and a hairpin like structure is depicting in light blue color.

1.4.3 Structural features of Type II DAH7PS

3D structure of Type II DAH7PS has been characterized only from *Mycobacterium tuberculosis* [77]. Like Type I DAH7PS, the structure of Type II DAH7PS also depicted the presence of $(\beta/\alpha)_8$ TIM barrel fold (Figure 1.13). MtDAH7PS structure consists of two tight dimers, which interacts with each other to form a functional homotetramer. Moreover, MtDAH7PS contains two additional decorative extensions with the core barrel, which play a role in the allosteric regulation of the enzyme. The first extension containing a β-strand followed by three α helices α0a, α0b and α0c (residues 1-80) extends from the N-terminus end and makes theend of the barrel close off, while the second extension consists of two helices α2a and α2b (residues 190-241) extending from the α2-β3 connecting loop.

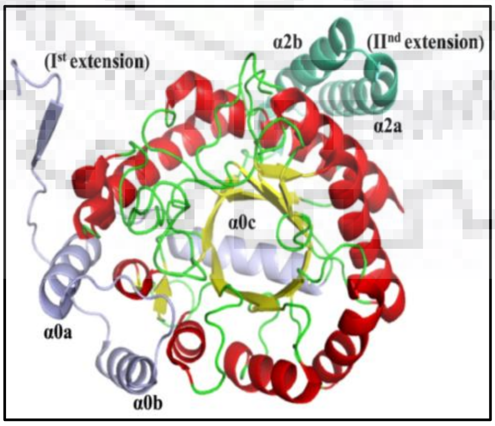

Figure 1.13: Monomeric structure of the Type II DAH7PS. MtDAH7PS monomeric structure showing the core $(\beta/\alpha)_8$ barrel and two additional decorative extensions depicting in the shown in light blue color and sea green, respectively.

Similar to Type I DAH7PS enzymes the active site of MtDAH7PS is also positioned at the C-terminal end of the barrel, and hosts substrate (PEP) and divalent metal ion, (Mn^{2+}). The β-strands and α-helices of the C-terminal end contain the residues which involve in the active site organization. The residues Glu283, Arg284, Lys306, Arg337 and two water molecules interact with the substrate (PEP) phosphate and carboxylate groups via network of H-bonding (Figure 1.14A). The carboxylate group of the substrate forms H-bond with Arg126, Lys306 residue and additional water molecule (Figure 1.14A).

The residues Cys87, His369, Glu411, and Asp441 form the metal binding site and interact with the divalent metal (Figure 1.14B). Additionally, one sulfate ion interacting with Arg135, Arg284, and Ser136 residues is also observed at the active site suggesting the possible position of the phosphate group of another substrate (E4P) on binding with the enzyme (Figure 1.14B).

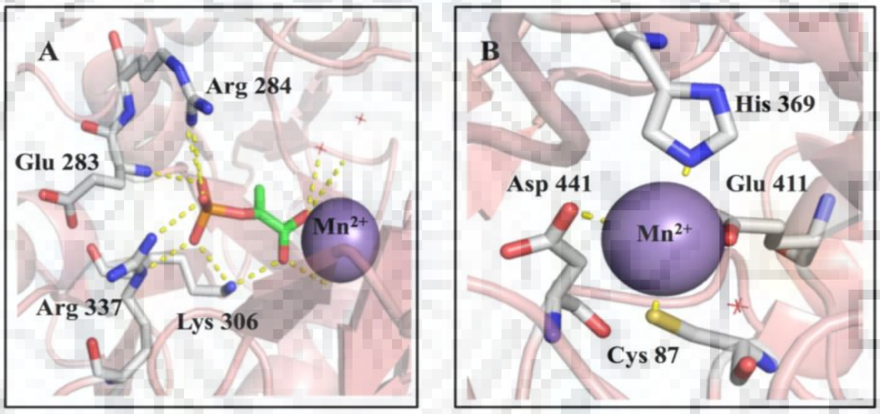

Figure 1.14: The active site architecture of MtDAH7PS. The positively charged residues including Glu283, Arg284, Lys306, Arg337 and two water molecules (pink color dots) involved in the network of H-bonding with the substrate (PEP) comprise the active site at the C-terminal end of $(\beta/\alpha)_8$ TIM barrel. Green and grey color sticks are showing the bound substrate and its interacting residues, respectively. The violet color sphere is depicting the catalytic metal ion at the active site.

1.4.4 Microbial DAH7PS regulation and inhibition

To prevent the wastage of resources, all organisms regulate and control the amount of biosynthesis of any product mediated through metabolic pathways. The main approach to control the cellular level of aromatic compounds, synthesized via the shikimate pathway, is to inhibit a reaction catalyzed by the committed enzyme (DAH7PS) of this pathway. Microbial DAH7PS generally show feedback regulation and inhibiton either by end product or intermediate of the pathway.

Different microbial species employ different ways for the regulation of DAH7PS and each type of DAH7PS has a unique method of allosteric regulation. Different microbial species contain one to three DAH7PS isoforms and show the regulation by feedback inhibition. These can be inhibited either by the end-products/intermediates of the pathway, or a combination of the two.

E. coli genome encodes three isoforms of DAH7PS, via genes aroF, aroG, and aroH, which are feedback regulated by one of the three aromatic amino acids (Phe, Tyr, and Trp) and these isoforms are named as DAH7PS (Phe), DAH7PS (Tyr), and DAH7PS (Trp) accordingly. Similarly, *Salmonella typhimurium* and *Nuerospora crassa* comprise of three isoforms of DAH7PS, whereas *S. cerevisiae* encodes only two isoforms of DAH7PS which are feedback regulated by the Phe and Tyr. Binding of an end/intermediate product of the pathway at a remote location (allosteric site) from the active site of DAH7PS introduces conformational changes and alters the active site. Finally it halts the performance and intended function of DAH7PS [84, 88].

The mechanisms of allosteric inhibition employed by DAH7PS for their regulation have been reported by various 3D structures of DAH7PS [88, 100]. All regulated DAH7PS of different microbes hold diverse types of decorative structures, attached to core $(\beta/\alpha)_8$ barrel, for their regulation. The structural comparison of native and inhibitor bound DAH7PS enzymes provides the insights about these additional decorative elements and also demonstrates the binding mode of the inhibitors at the allosteric site.

The crystal structures of Type Iα DAH7PS enzymes complexed with the Phe and Tyr, from the *E. coli* and *S.cerevisiae* respectively, have been reported. In both the structures, Phe and Tyr bound at the same site of the DAH7PS in a similar fashion [88]. The N-terminal extension along with an internal extension, positioned between α5 and β6 strands of the $(\beta/\alpha)_8$ barrel, construct a inhibitor (Phe and Tyr) binding allosteric site for regulation of enzyme via feedback inhibition (Figure 1.15). Moreover, the structural comparison of ligand/inhibitor bounded and native DAH7PS enzymes have also suggests the conformational changes in DAH7PS upon ligand/inhibitor binding. Crystal structures of other isoforms (DAH7PS (Tyr) and DAH7PS (Trp)) from *E. Coli* have not been determined yet and exact mechanism elucidation about the binding of Tyr and Trp with EcDAH7PS is also waiting for the structural data.

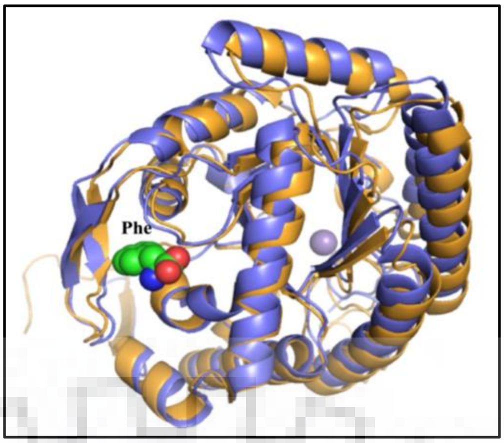

Figure 1.15: Feedback regulation of the Type Iα DAH7PS. The monomer structure of the native (no inhibitor bound) and inhibitor bound (Phe) with EcDAH7PS at its allosteric site are superimposed. The native structure is shown in blue color (PDB ID 1QR7) and inhibitor bound (PDB ID 1KFL) structure is shown in golden color. The bound ligand Phe has shown as sphere colored green with the metal ion shown as a grey sphere.

But truncation of seven amino acid residues from the N-terminal of EcDAH7PS (Tyr) constructed a Tyr-resistant EcDAH7PS enzyme evidently suggesting the central role of the N-terminal extension in the feedback inhibition of the DAH7PS. Mutagenesis studies have evidently shown that a single mutation at the conserved amino acid residue (Gly226 present in Tyr-regulated ScDAH7PS and Ser219 present in Phe-regulated ScDAH7PS) completely alters the regulatory pattern of the DAH7PS isoforms of the *S. cerevisiae.* The crystal structure of ScDAH7PS (Tyr) mutant (G226S) complexed with Phe was compared and analyzed with a wild-type ScDAH7PS (Tyr) complexed with Tyr. It revealed that mutation of Gly to Ser reduces the size of inhibitor binding cavity significantly which favored the binding of Phe rather than Tyr.

Some DAH7PS like PfDAH7PS and ApDAH7PS belonging to Type Iβ subfamily do not possess any extra structural elements, which drives the allosteric regulation [87]. Interestingly, none of the enzyme is inhibited by any end product/intermediate compounds of the shikimate pathway, which evidently proves that both are unregulated DAH7PS enzymes [101]. In contrast to this, TmDAH7PS which also belongs to the TypeIβ subfamily has shown strong inhibition with Tyr and Phe (to a lesser extent). TmDAH7PS has evolved the extension FL domain to $(\beta/\alpha)_8$ barrel which contributes to its regulation. 3D structure of TmDAH7PS complex with Tyr shows that a pair of the regulatory structures come together from diagonally opposite subunits of the enzyme to construct the binding site for inhibitor (Figure 1.16) [102]. Moreover, TmDAH7PS become catalytically more active on truncation of the N-terminal domain and was not inhibited by Tyr or Phe. Interestingly, fusion of the regulatory FL domain of TmDAH7PS with unregulated PfDAH7PS resulted in inhibition and regulation of PfDAH7PS by Tyr and Phe [103].

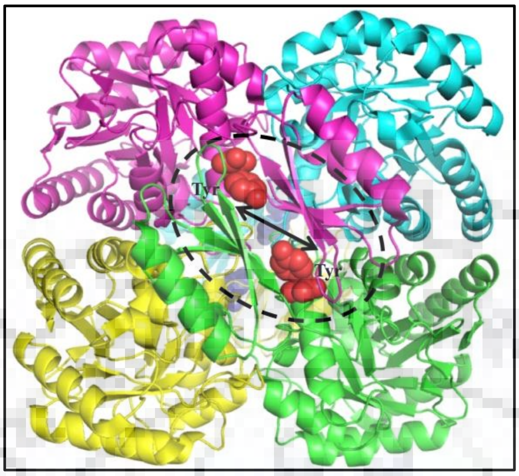

Figure 1.16: Feedback regulation of the Type Iβ DAH7PS. Tetramer of TmDAH7PS bound with Tyr on the allosteric site, formed by diagonally opposite subunits of the enzyme.

M. tuberculosis encodes a Type II DAH7PS enzyme, which possesses a complicated method of feedback regulation (Figure 1.17) [77, 100]. It demonstrated less sensitivity and inhibition in presence of any single aromatic amino acid. However, in the presence of combination of any two or more amino acids, MtDAH7PS depicted significantly more inhibition and thus MtDAH7PS has a synergistic nature of inhibition. The synergistic binding of Phe and Trp with decorative extension elements of the core $(\beta/\alpha)_8$ barrel caused significant inhibition, but the addition of Tyr led to entire loss in activity of the enzyme. MtDAH7PS contains three distinct allosteric sites for binding of each aromatic amino acid. Two allosteric sites are situated at the dimer and tetramer interfaces whereas third site is located near dimer interface on outside surface of the enzyme [100].

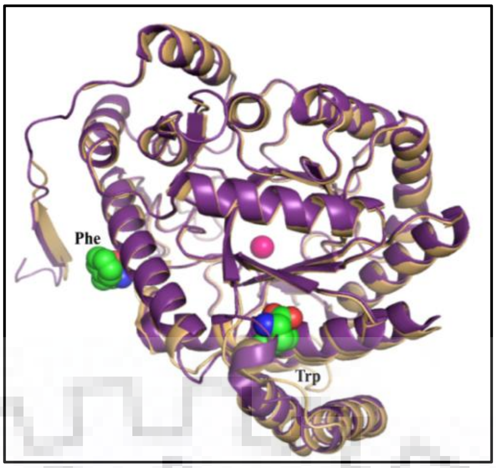

Figure 1.17: Feedback regulation of the Type II DAH7PS. The monomer structure of the native (no inhibitor bound) and inhibitor bound (Phe and Trp) MtDAH7PS at the two allosteric sites are superimposed. The native structure is shown in purple color (PDB ID 2B70) and inhibitors bound (PDB ID 3KGF) structure is shown in golden color with the N-terminal and internal barrel extensions with the metal ion shown as a hot pink sphere. The bound ligands Phe and Trp have shown as sphere in green color.

1.4.5 Chorismate mutase and DAH7PS fusion enzyme

In Type Iβ DAH7PS of *Bacillus subtilis* (BsDAH7PS), a slightly active and covalently fused chorismate mutase (CM) domain to its N-terminus end was identified. This fused CM domain is ~ 80 residues long and acts in the feedback regulation of the DAH7PS activity [80, 92]. The binding of any branch point intermediates compounds like chorismate and prephenate with the CM domain can alter DAH7PS domain of BsDAH7PS activity. Subsequently, in a number of other genera like *Porphyromonas gingivalis* (PgDAH7PS) and *Listeria monocytogenes* (LmDAH7PS) presence of CM domain has also been recognized [80, 90]. PgDAH7PS have also evidently shown the inhibition by prephenate and Chorismate.

Initially, it was considered that fused domain of DAH7PS in all these organisms have evolved for one and only purpose of the regulation rather than to afford bifunctionality [102]. The BsDAH7PS exhibited both DAH7PS domain activity and extremely low CM domain activity. However, *B. subtilis* also has another gene, which encodes a second intracellular CM domain (AroH) and is responsible for the biosynthesis of chorismate to prephenate [92].

To provide more insights on the evolution of fusion DAH7PS, truncation of both domains were performed in the several studies. The activity and inhibition of both the truncated domains were also checked [90, 91]. In case of BsDAH7PS analysis, CM truncated variant of BsDAH7PS only exhibited CM activity whereas DAH7PS truncated variant exhibited DAH7PS activity. In contrast to this, PgDAH7PS having a CM domain fused with C-terminal end of the catalytic barrel did not demonstrate either the DAH7PS or CM activity in its truncated variants.

Interestingly, both wild-type BsDAH7PS and PgDAH7PS were showing inhibition on the prephenate and chorismate binding. But, DAH7PS truncated variants of both the enzymes exhibited no signs of inhibition. The prephenate was showing more inhibitory effect in comparison to the chorismate. Thus, several findings and results have evidently shown that the organisms evolved these fusion domains to DAH7PS for the sole purpose of feedback regulation instead of bifunctionality.

Listeria monocytogenes and *Geobacillus sp* also depicted the presence of a fused CM domain at the N-terminus end of the core $(\beta/\alpha)_8$ barrel and this domain was attached to the barrel via a flexible linker region. Both of these enzymes crystallized as the tetramer containing two CM domains which emerge from the diagonally opposite sides of tetramer and interlock with each other to form a CM dimer (Figure 1.18A & 1.18B). CM dimer stabilizes the tetrameric form of DAH7PS in the same manner as the FL domain of TmDAH7PS and is thought to play a key role in the regulation of the enzyme. It has been depicted that these loosely associated CM dimers of DAH7PS tetramer binds with the prephenate or chorismate and introduce conformational changes. These conformational changes causes the interaction between catalytic DAH7PS domain and regulatory CM domain and further block the active site or induced conformational changes in the catalytic domain [90, 91].

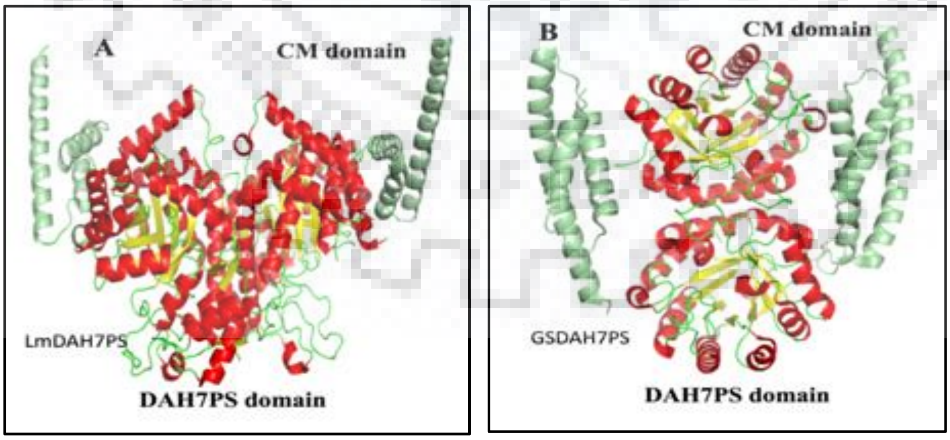

Figure 1.18: Chorismate mutase and DAH7PS fusion enzyme. LmDAH7PS (left) and GsDAH7PS (right) structures showing the presence of a fused regulatory CM domain (light green color) at the N-terminus of the core $(\beta/\alpha)_8$ barrel and this domain attached with the barrel

via a flexible linker region and shows the feedback regulation on the prephenate and chorismate binding.

1.5 Plant's DAH7PS and regulation

Plant's have Type II DAH7PS and show different regulation to that observed in the microbial DAH7PS. *Arabidopsis thaliana* has three isoforms of DAH7PS (DHS1, DHS2 and DHS3), which are encoded by three different loci (*At4g39980*, *At4g33510* and *At1g22410*) of the genome. Though, three isoforms generally expressed differentially in response to the various environmental conditions; physical or chemical wounding, site of expression, pathogen infiltration and redox state [104-106]. In plants, enzymes of the shikimate pathway essentially possess N-terminal signal sequence which is vital for the transportation of these proteins from cytosol to plastids [35, 106]. Plant's DAH7PS are found to be regulated at the transcriptional level rather than the feedback inhibition. In plants, DAH7PS are found functional in the reduced state and dependent on a reduced thioredoxin (TRX) [106]. Inside the plastids, DAH7PS is regulated by a Ferredoxin-Thioredoxin redox regulation system. Moreover, in the cytosol of several plants tissue, an additional Co^{2+} dependent enzyme showing DAH7PS activity has also been observed, but it is not further well-characterized till date [107-109]. Interestingly, in some plants DAH7PS like *Daucus carota* and *Solanum tuberosum,* aromatic amino acids which enhance the enzymatic activity were also detected such as Trp enhanced the activity of DAH7PS enzyme of carrot. Thus, the differences in the regulatory pattern between the plant and the bacterial DAH7PS reflect the fundamental role of these enzymes in the plants for the synthesis of aromatic secondary metabolites. Although, the crystal structure of any plant DAH7PS has not been solved yet and the exact mechanism of the plants DAH7PS still remains unclear.

1.6 Lipopolysaccharide (LPS) in Gram-negative bacteria

Gram-negative bacteria cells are covered with an extra cell envelop outside the cell wall [110]. This envelope comprises of two distinct membranes viz. an inner membrane (IM) and an outer (OM) membrane. Both the membranes are separated by a hydrophilic compartment i.e., a periplasmic space, which includes a layer of peptidoglycan (Figure 1.19) [111-115] .

IM is also known as the cytoplasmic or cell membrane which is comprised of a symmetrical bilayer of phospholipid, integral transmembrane proteins, and lipoproteins. The integral transmembrane proteins are embedded in the membrane with their α-helical transmembrane domains and lipoproteins facing toward the periplasm. Peripheral IM proteins occur either at the cytoplasmic side or the periplasmic side of IM [116, 117]. The periplasmic space includes membrane-derived oligosaccharides and a thin layer of peptidoglycan. This layer maintains the structural stability of cell, whereas membrane-derived oligosaccharide regulates the osmolarity of periplasm [114].

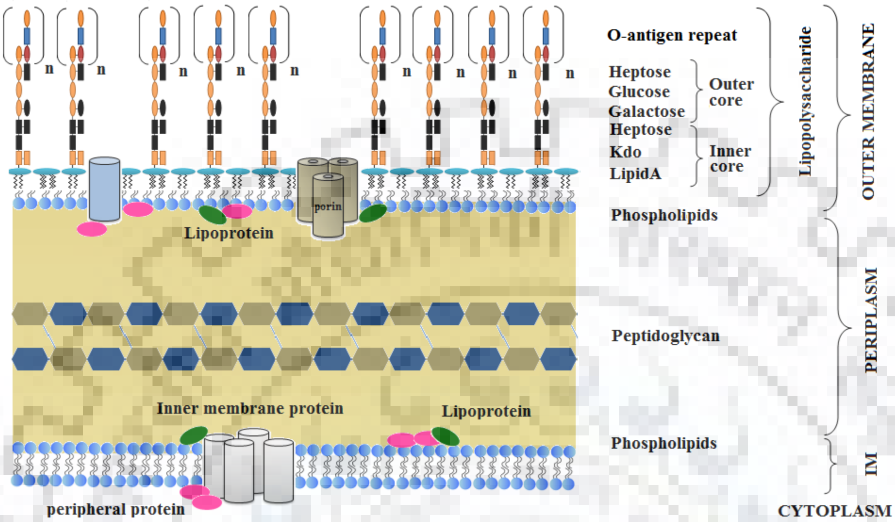

Figure 1.19: The cell envelope of Gram-negative bacteria. The envelope comprises via two distinct membranes called as an inner membrane (IM) depicted as the light blue color phospholipids symmetrical layer and an outer (OM) membrane depicted by two different blue color asymmetrical layers. Both membranes are separated by a hydrophilic compartment i.e., a periplasmic space, which includes a peptidoglycan layer (Figure adopted from Sperandeo et. al., 2009).

OM of the bacterial cell envelop is highly asymmetrical and consists of two leaflets (inner and outer). The inner leaflet of OM contains the similar phospholipids as in the IM, but enriched with phosphatidylethanolamine. The outer leaflet of the OM comprises of Lipopolysaccharides (LPS) [118]. Several proteins such as OM proteins (OMPs) and lipoproteins also exist in the OM lipid bilayer and function as the receptors, porins, channels, and other transport machinery [119]. These OMPs mediate the communication of cell with the external environment and also regulate the entry of diverse small molecules (Figure 1.19) [120].

In Gram-negative bacteria, LPS performs two main functions; firstly it provides a defense mechanism to the cell against various harsh environmental conditions. It is responsible and indispensable for the bacterial viability in the distinct types of ecosystems by providing a barrier against the surrounding stress factors such as antibiotics, detergents, bile salts, antimicrobial peptides and hostile environments encountered during host colonization or infection [115, 121, 122]. LPS also provides rigidity and tightness to the OM and mediates resistance in the bacterial cell against the external stress factors [123].

LPS is a well-conserved structure present in all Gram-negative bacteria and provides important pathogen associated molecular patterns (PAMPs). PAMPs are generally recognized by the cells of host innate immune system and subsequently provoke the clearance of bacterial infections. This important immunological reaction contributes to the manifestation of relatively conserved molecular structures in mammals for the recognition of PAMP [124]. Thus, strong activation of the host immune system in response to any infecting bacteria mainly occurs through the recognition and sensing of the LPS [125]. However, the initiated immune response has to be balanced. In some severe cases, the uncontrolled bacterial growth leads to the release of a large amount of non-membrane bound LPS within the host body. The exaggerated host immune responses results in septic shock condition with fatal consequences for the host [126, 127].

1.6.1 Structure of lipopolysaccharides

LPS, structurally is a complex glycolipid molecule and it is divided into three units: (i) lipid A, (ii) core oligosaccharide (iii) O-antigen (a long polysaccharide chain) (Figure 1.20) [128]. Lipid A is located in outer leaflet of the OM and represents the hydrophobic moiety of LPS. The core polysaccharides and O-antigen are located on the surface of the bacterial cells and both of these points towards the aqueous environment [118, 121]. LPS that contains all the three structural units is known as the smooth (S)-form type LPS whereas LPS lacking the O-antigen unit is named as the rough (R)-form type LPS or lipooligosaccharide (LOS) (Figure 1.20). The detailed structure of LPS shows variation among different bacterial species, and this variation also affects the virulence of a bacterium [129]. The unique permeable nature of the OM is due to the peculiar arrangement of the LPS structure in the outer leaflet.

LPS forms firmly packed layer due to the strong lateral interactions between LPS molecules and these interactions are mediated by the bridging action of divalent cations (Mg^{2+} and Ca^{2+}). Moreover, fully saturated fatty acyl chains of the LPS aliphatic domain is believed to create a gel-like lipid interior with a low fluidity that is responsible to low permeability of the hydrophobic solutes across the OM [115].

1.6.1.1 Lipid A

Lipid A, also known as Endotoxin, is primarily responsible for the toxic effects of Gram-negative bacteria [118, 130]. The lipid A backbone structure is formed by the 2-amino-2-

deoxyglucopyranose (GlcN) disaccharide molecules which are linked together via a β-(1→6)-linkage. It also consists of two negatively charged phosphate groups at the 1 and 4′ positions and an asymmetrical distribution of fatty acids. There is presence of four residues of (*R*)- 3-hydroxy-myristic acid with ester or amide-linkage at 2, 2′, 3 and 3′ positions. Generally, 2′ and 3′ positions also substituted by the lauric and myristic fatty acids, respectively, resulting in the formation of 3-acyloxyacyl structures [118, 131-134]. A hexa-acyl and negatively charged lipid A molecule has been found in *E. coli* and many other enterobacterial and nonenterobacterial genera including *Haemophilus* or *Neisseria.*

Additionally, in some other bacteria like *Aquifex pyrophilus*, [135] *Bordetella pertussis*, [136] and *Legionella pneumophila*, [137] the backbone structure of the lipid A comprises of a disaccharide backbone of two 2,3-diamino-2,3-dideoxy-D-glucopyranose (DAG) residues which are also linked through β-(1→6)-linkage. Moreover, *Campylobacter jejuni* shows the presence of a hybrid type lipid A disaccharide unit, which contains one GlcN and one DAG residue [138]. The *Rhizobium leguminosarum*, represents an exceptional backbone structure of lipid A, where one GlcN moiety is linked to a 2-amino-2-deoxy-gluconic acid residue which is a reducing sugar moiety [139].

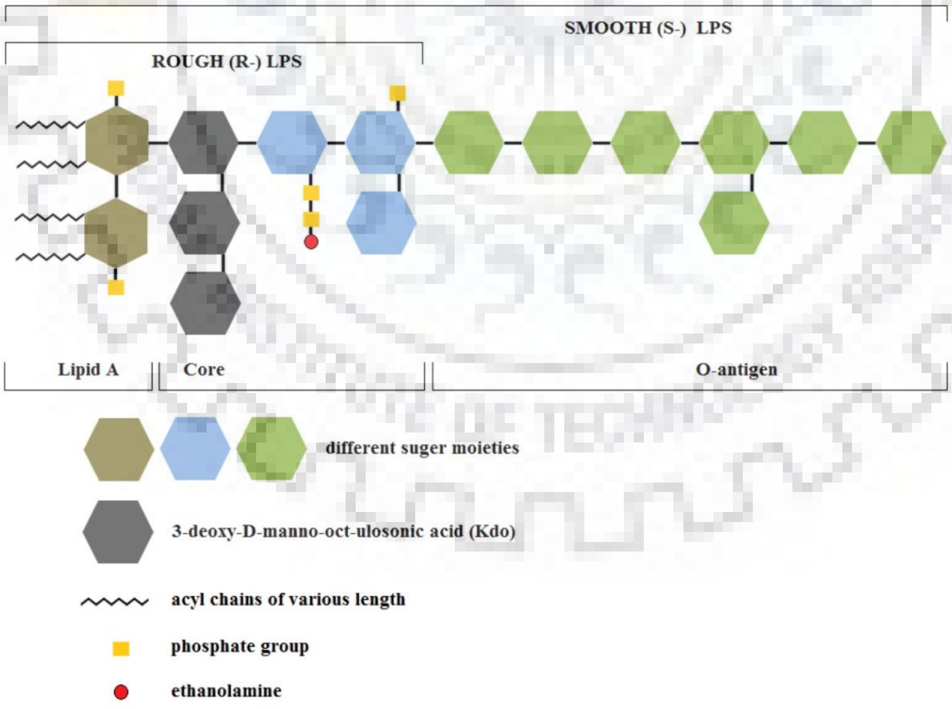

Figure 1.20: General structure of the LPS. Diagram is representing three subunits of the LPS; Lipid A, core region, and O-antigen (from left to right). The lipid A and core region constitute the rough (R)-type LPS and the association of the O-antigen together with these two from the smooth (S)-type LPS structure. The number and the chemical structure of the acyl

chain and the sugar moieties (represented as the hexagonal ring of different color) can vary. The associated phosphates and the ethanolamine groups have been indicated in yellow rectangles and the red circle, respectively (Figure modified from Steimle et. al., 2016).

1.6.1.2 The core oligosaccharide and O-antigen

The core oligosaccharide of LPS is further divided into a conserved inner core, proximal to the lipid A, and a variable outer core. The inner core is composed of Kdo (3-deoxy-D-manno-oct-2- ulosonic acid) and heptose (L-glycero-D-manno-heptose), whereas the structurally diverse outer core provides the attachment site for the O-antigen. The O-antigen is also named O-specific polysaccharide or simply “glycan” when it consists of repeating units of less than five sugar units. The polysaccharide chain can only found in smooth type (S)-form LPS and determines its antigenic properties [120].

1.6.2 Lipid A (Endotoxin) as an activator of innate immune system

The innate immune system of the higher organisms acts as the first line defense barrier and exhibits a rapid response to protect the host from bacterial infections (Figure 1.21) [118]. In Gram-negative bacteria the Lipid A (endotoxin), specifically, is a glucosamine-based phospholipid which acts as pathogen-associated molecular patterns (PAMP) [118]. The interaction of PAMP with the receptors of the innate immune system cells initiates the immune response against the invading pathogen. A receptor TLR4 (toll-like receptor), being present on the macrophages and other cells of the innate immune system has been identified and the lipid A molecules has also been detected in the picomolar levels in the infectious state.

The TLR4 (toll-like receptor 4) is a membrane-spanning protein, which is found distantly related to the IL1 receptor [140, 141]. In macrophage cells, lipid A interaction with TLR4 receptor, triggers the biosynthesis of various mediators causing inflammation such as TNF-α and IL1-β (Figure 1.21) [142, 143]. The ineraction of LPS with the host TLR4/myeloid differentiation-2 (TLR4/MD2) complex stimulates the expression of pro-inflammatory cytokines which further initiate the inflammatory responses [118, 124, 144-147]. In the mononuclear and endothelial cells, lipid A stimulates the production of tissue factors [148, 149]. It also activates the production of other co-stimulatory molecules that are further required for the adaptive immune response in the host [141]. These all events are desirable for the clearance of infection and work in a synergistic manner. Experiments with the synthetic lipid A have shown that it is responsible for inflammatory response and is sufficient to initiate immune response in the host [150, 151]. On the other hand, the overproduction of lipid A (i.e., high concentrations of LPS) usually leads to the septic shock, induces fever, increases heart rate, and further results in the death due to multi-organ failure (Figure 1.21) [118] .

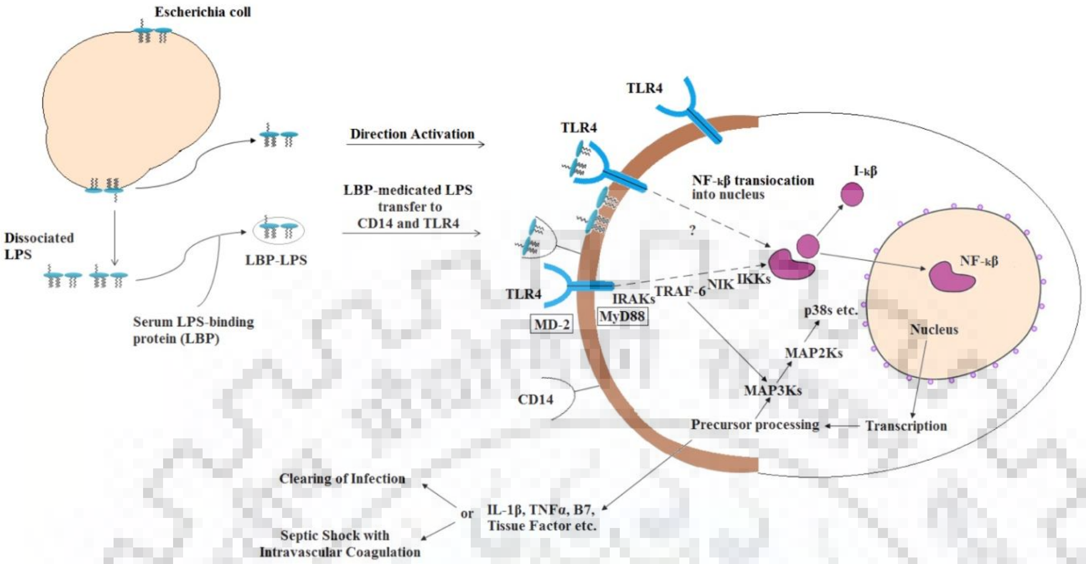

Figure 1.21: Schematic representation of the activation of the innate immune system of the host mediated via Lipid A (Endotoxin) (Figure modified from Raetz & Whitfield 2002).

1.6.2.1 TLR4 stimulation and signal transduction

After the entry of bacteria into the host cell, LPS dissociates from the bacterial membrane. The dissociated LPS stimulates the immune cells via serial interactions with several proteins viz. LBP (LPS binding protein), CD14, MD-2, and TLR4. Firstly, the LBP, a soluble serum protein, facilitates the transports of LPS to GPI linked protein CD14 (a glycosylphosphatidylinositol-anchored soluble protein) which is present on the surface of immune cells (macrophages, neutrophils, and dendritic cells). Then CD14 transfers and presents the bound LPS to the TLR4/MD-2 receptor complex. The binding of LPS to TLR4 leads to the oligomerization of TLR4 which results into the activation of an entire signal cascade reaction.

MD-2 is a soluble protein non-covalently associated with TLR4, and it can also form a complex directly with LPS even in the absence TLR4 [145, 152-155]. TLR4 signal transduction cascade further continue via either MyD88-dependent pathway (MDP) or MyD88-independent pathway (MIP)/TRIF-dependent pathway [147]. In MDP, the activation of TNF-receptor associated factor 6 (TRAF6) further progresses the activation of mitogen activated protein kinase cascade. Subsequently, it results in the activation of NFk-B which translocates to the nucleus (Figure 1.22). The MIP pathway involves the binding of intracellular domain of LPS-TLR4/MD2 to MyD88-adaptor-like (MAL), also known as Toll-interleukin 1 receptor adaptor protein (TIRAP) [124, 142]. Thus, LPS stimulation of TLR4 receptor process, involve the contribution and the recruitment of several adapter molecules like Trif, Tram, MyD88, and Mal within the cytoplasm and propagates a signal cascade as presented and outlined in the figure 1.22 [152, 155]. Finally, the amplification of the signal occurs, due to the activation of other protein kinases such as IRAK1, IRAK4, IKKi, and TBK1 within the cell, and further results in the induction or suppression of the genes which formulate the inflammatory responses [156, 157].

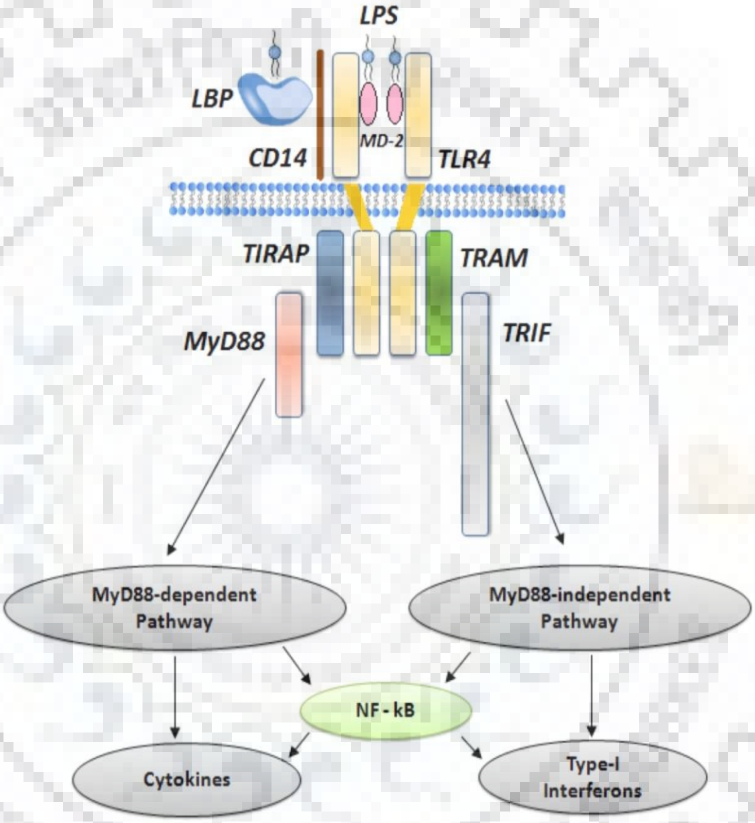

Figure 1.22: Schematic representation of the LPS/TLR4 signal transduction. The dissociated LPS recognition is facilitated by the LBP (LPS binding protein), a soluble serum protein, and CD14, further is mediated via TLR4/MD-2 receptor complex. TLR4 signal transduction cascade further continue either via MyD88-dependent pathway (MDP) or MyD88-independent pathway (MIP)/TRIF-dependent pathway and mediate the activation of various pro-inflammatory cytokine and Type I interferon production (Figure modified from Lu et. al., 2008).

Thus, LPS is a well-studied immunomodulatory component of the bacteria cell membrane and can induce the systemic inflammation, septic shock/acute sepsis and chronic inflammations on occurrence of excessive signals [118]. The mortality rate of septic shock is estimated to be 20-

80 %, and thus is a leading cause for the deaths of the patients in intensive care units. The incidents of sepsis are increasing at the alarming annual rate of ~ 9 %. Therefore, the assembly and the biosynthesis pathway of LPS is of great interest for the researchers. Any inhibitor of the LPS biosynthesis pathway might be useful in therapy against Gram-negative bacterial infections.

1.6.3 LPS biosynthesis and transport

The LPS biosynthesis mechanism has been studied extensively and these studies showed that all the constitutive enzymes involved in pathway are well conserved [112, 158]. In the biosynthesis of the Kdo2-lipid A, which is essentially required for the growth of bacteria, different steps are catalyzed by total nine enzymes (Figure 1.23) [112, 121]. Although, each enzymatic reaction of this pathway is found well conserved in all Gram-negative bacteria, but a few exceptions are also reported in the acylation state of the synthesis. This pathway is essential for the growth of all Gram-negative bacteria, but *Neisseria meningitidis* has shown the survival and the growth without *lpxa* gene [159].

The first step is catalyzed by an enzyme named as UDP-N-acetylglucosamine acyltransferase (LpxA) which performs acylation step of the UDP-N-acetylglucosamine (UDP-GlcNAc), a sugar nucleotide [160, 161]. During this step, LpxA transfers a R-3-hydroxymyristoyl group from the acyl carrier protein (ACP) to the 3-hydroxyl (3-OH) group of GlcNAc ring of UDP-N-acetyglucosamine and generates the end products viz. UDP-R-3-hydroxymyristoyl-GlcNAc and ACP [162]. LpxA of *E. coli* (EcLpxA) is highly selective for the β-hydroxymyristoyl acyl carrier protein molecule [163]. The active site of the EcLpxA functions as an accurate hydrocarbon ruler and incorporates a β-hydroxymyristoyl chain with two orders of magnitude faster than a β -hydroxylauroyl or a β- hydroxypalmitoyl chain [164]. Other LpxA are able to incorporate either a longer or shorter β-hydroxyacyl chain. The reaction catalyzed by LpxA is found thermodynamically unfavorable in the forward direction with an equilibrium constant of ~ 0.01(*Keq* -0.01) [164].

Furthermore, the committed step of this pathway is catalyzed by a zinc-dependent metalloenzyme named as UDP-3-O-acyl N-acetylglucosamine deacetylase (LpxC) [165, 166]. In this step, LpxC catalyzes the deacetylation (-CH_3CO) of UDP-3-*O*-acyl-N-acetylglucosamine at the 2-amino position of the GlcNAc ring [167]. LpxC is highly conserved in all the Gram-negative bacteria and it has no homology to any mammalian deacetylases or amidases. Therefore, LpxC has become an attractive drug target for the development of novel antibacterial compounds [168, 169].

After deacetylation, a second β-hydroxymyristoyl chain is also added at the 2-amino position of UDP-3-*O*-acyl-glucosamine by enzyme UDP-3-*O*-acyl-glucosamine *N*-acyltransferase (LpxD) and the generation of UDP-2,3-diacylglucosamine and ACP occur [170]. Both LpxA and LpxD enzymes utilize the acyl-acyl carrier protein (ACP) as the obligate acyl donor [170, 171]. LpxD is an acyltransferase and shares sequence and structural homology with other acyltransferase such as LpxA enzyme of the LPS pathway [172, 173]. LpxD has same novel protein fold having left-handed helix of short paralleled β-sheets.

The initial three steps catalyzing enzymes of this pathway are soluble cytoplasmic proteins, whereas the fourth and fifth step catalyzing enzymes are the peripheral membrane proteins. Next step catalyzes through UDP-2,3-diacylglucosamine pyrophosphatase (LpxH) enzyme, which perform the cleavage the pyrophosphate linkage of the UDP-2,3-diacylglucosamine (UDP-DAG) and generates the 2,3 diacyl glucosamine-1-phosphate (lipid X) and Uridine monophosphate (UMP) [174, 175]. In the next step, the condensation of UDP-2,3-diacylglucoasmine and one molecule of lipid X by the action of LpxB enzyme results in the formation of UDP and a characteristic β-1-6 glycosidic linkage containing a tetra-acylated disaccharide-1-phosphate (DSMP) molecule [176].

The further final steps of constitutive LPS pathway are catalyzed by four enzymes known as LpxK, KdtA (WaaA), LpxL(HtrB), and LpxM (MsbB) and all these enzymes are integral membrane proteins [121]. All these enzymes are associated with the membrane but catalyze their reaction on the cytoplasmic face of the IM. Since, all these reactions require some cytolosic factors so the active sites of these enzymes are apparent in the cytoplasm. Tetra-acyldisaccharide 4'-kinase (LpxK), an ATP dependent membrane bound kinase, which catalyzes the phosphorylation reaction at the 4'-position of DSMP molecule and also synthesizes a key lipid A intermediate, lipid IV_A molecule [177].

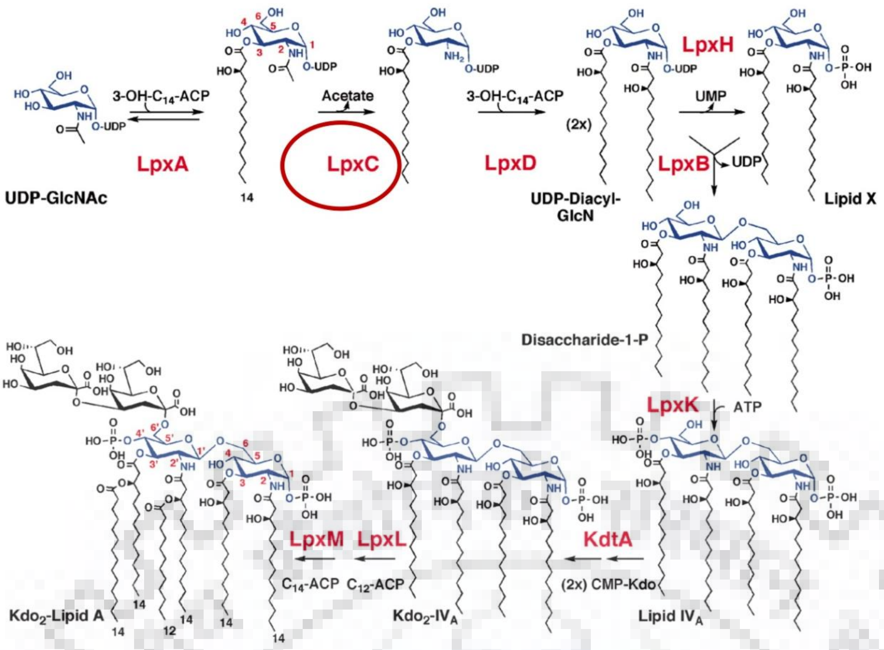

Figure 1.23: Lipid A Biosynthesis in *E. coli*. Lipid A is an essential component for Gram-negative bacteria to maintain their viability. Disruption of lipid A biosynthesis is lethal to most Gram-negative bacteria. Inhibition of any of the first six enzymes interrupts the growth of *E. coli cells* (Figure adapted from Raetz & Whitfield 2002).

The seventh enzyme of the LPS pathway is 3-deoxy-D-manno-octulosonic-acid transferase (KdtA) and it acts as a bifunctional enzyme in E.coli. KdtA catalyzes the transfer of two 3-Deoxy-D-manno-oct-2-ulosonic acid (Kdo) molecules at the 6' position of lipid IV_A and synthesizes Kdo2-lipid IVA molecule [178-180]. Kdo2-lipid IVA lauroyl-ACP acyltransferase (LpxL) and KDO2-lauroyl-lipid IVA myristoyl-ACP acyltransferase (LpxM) catalyzes the final step of lipid A biosynthesis. Both the enzymes are homologous and belong to acyltransferase family. These two enzymes catalyze the transfer of lauroyl (C12) and myristoyl (C14) secondary acyl chains to the 2' hydroxy and 3' hydroxy positions of Kdo2-lipid IVA, respectively and synthesize Kdo2-lipid A [179]. These enzymes do not share any sequence or structural homology with other two acyltransferases of this pathway i.e., LpxA and LpxD. The variations in length, placement, and number of these secondary acyl chains generally contribute to the diverse nature of LPS molecule structure as present in different bacteria [181].

This Kdo2-lipid A moiety created by nine sequential steps represents an essential and minimal necessary structure for robust growth of bacteria under the laboratory conditions. Although, bacteria require all units of the membrane, however, the final two steps are essential for their viability. Lacking of LPS core and O-antigen sugar structures result in the susceptibility of the cell toward various stress factors such as bile salts and antimicrobial peptides [121].

Thus, after the generation of Kdo2-lipid A molecule, various members of the Waa family of glycosyltransferases add sugars from nucleotide donors to the proximal Kdo, forming the rest of the inner and outer core of LPS [182].The identity of the core sugar moieties also varies among different bacterial species. This glycosylated lipid A is flipped into the periplasmic space by ABC transporter MsbA, which has been crystallized in multiple conformations (Figure 1.24) [121, 183]. Here, at the outer leaflet of the IM, the O-antigen repeat (anchored to the membrane through undecaprenyl diphosphate) are ligated to the outer core sugars by WaaL [118, 184]. However the exact mechanism is still under the investigation, multiple proteins of the Lpt family are thought to be responsible for transporting the LPS to the outer membrane and flipping it into the extracellular space, though no assay for the transport processes has yet been reported (Figure 1.24) [185, 186]. Currently, it is believed that LptB uses ATP hydrolysis along with LptC, LptF, and LptG to extract LPS from the inner membrane and flip it into the periplasmic space. LptA has been implicated in shuttling of LPS through the peptidoglycan to the outer membrane while a complex of LptD and LptE transport LPS to the outer leaflet of the OM [187].

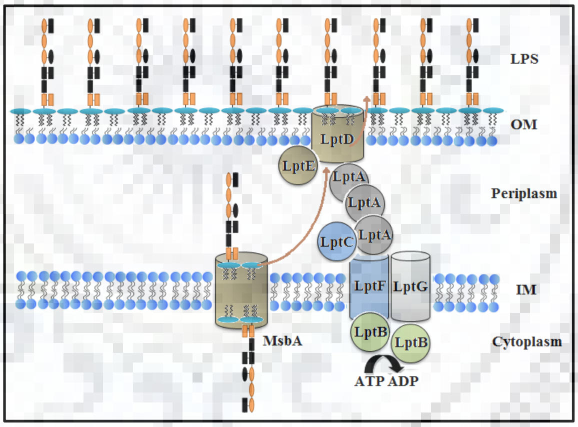

Figure 1.24: Schemetic representation of LPS transport to outer membrane (Figure modified from Sperandeo et. al., 2009).

1.6.4 LpxC as an unexploited antibiotic target

LPS plays a crucial role in the OM integrity and is essential for the viability and the virulence of most Gram-negative bacteria [121]. Disruption of lipid A biosynthesis deploys the lethal effects on most of the bacteria [171]. The inhibition of the first six enzymes of the lipid A biosynthesis can arrest the growth of *E. coli* [167]. Thus, all the enzymes involved in early steps of LPS biosynthesis are most validated potential targets and can provide a way to design and develop a plethora of antibiotics [188-191]. Currently, structures of all soluble cytosolic enzymes (LpxA, LpxC, and LpxD) and LpxH, the functional ortholog LpxI, and KdtA have been reported form the different bacterial species [163, 173, 192, 193]. But no structure of LpxB enzyme is determined yet. Moreover, the detailed structural (via X-ray and NMR) and functional aspects of most of the catalyzing enzymes can aid the discovery of novel compounds against pathogens [118]. Thus, characterizing the atomic structures of all enzymes of the LPS pathway would allocate a better understanding to design and develop the inhibitory molecules against each enzyme of this pathway. LpxC is a highly conserved and catalyzes the initial committed step of the LPS pathway in Gram-negative bacteria. Additionally, LpxC shows no structural and sequential homology to any human and mammalian protein. Thus, these unique features make it a promising target for the development of antibacterial agents [194, 195].

1.6.4.1 LpxC a zinc metalloamidases

The lpxC locus was identified for the first time from a hypersensitive *E. coli* (penicillin-sensitive strain) generated due to a mutation envA (named for envelope mutant A). This mutant strain showed the slow and filamentous growth with an interrupted cell division and susceptibility towards the various antibiotics [165, 196]. The discovery of the hydroxamate moiety containing inhibitors, which generally chelate the metal ions, preliminarily indicated that LpxC is a metalloenzyme [195]. Further, activity of LpxC was inhibited in the presence of EDTA and dipicolinic acid but the activity was restored by the substitution of metals such as zinc, cobalt, nickel or manganese [167]. Moreover, the plasma emission spectroscopic studies clearly demonstrated that the purified LpxC protein contains zinc metal. Excess of zinc inhibits the activity of LpxC as in case of other zinc amidases enzymes. The genetic analysis suggested that two zinc ligands His79 and His238 in EcLpxC and His74 and His226 in AaLpxC, and two possibilities for a third zinc ligand (His265 or Asp246; His253 or Asp234 of AaLpxC) [197]. Further, the extended X-ray absorption fine structure (EXAFS) studies reported that zinc of LpxC also coordinates with two oxygen and two nitrogen atoms [198]. The current facts about the LpxC mechanism and structure are primarily derived on the basis studies of LpxC from *E. coli* (EcLpxC) and *Aquifex aeolicus* (AaLpxC), *a* hyperthermophilic bacterium.

The structure of *Aa*LpxC was solved by NMR spectroscopy [199]. These studies have reported the presence of a unique structural fold and a novel zinc-binding motif of LpxC. These characteristic features distinguish the LpxC enzyme from the other zinc hydrolases [199]. LpxC contains two bound zinc ions at its active site. One of these is a catalytic zinc ion (ZnA), which acts as a cofactor to mediates the LpxC activity and coordinates with His79, His238, Asp242, and a water molecule (Figure 1.25A & 1.25B). While, the other zinc ion (ZnB) leads to inhibition of LpxC, due to excess amount of zinc, and coordinates with Glu78, His265, a fatty acid, and a bridging solvent molecule. Mutational studies of the active site residues (Glu78, Asp246, and His265 to Ala) have depicted a decrease in the catalytic activity of LpxC. On the basis of these studies, LpxC was suggested to function via metalloprotease-like mechanism [197, 200].

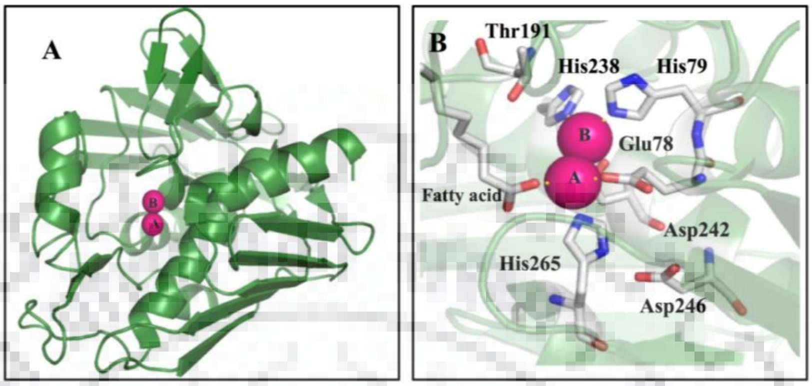

Figure 1.25: Structure of Zinc-inhibited LpxC. (A) The AaLpxC showing the binuclear zinc cluster of LpxC at the active site and depicted in the purple color sphere **(B)** One catalytic zinc ion (ZnA) coordinates with the His79, His238, Asp242, (grey sticks) and a water molecule and another inhibitory zinc ion (ZnB), coordinates with Glu78, His265, a fatty acid, and a bridging solvent molecule (PDB ID 1P42).

1.6.4.2 LpxC adopts unique structural fold

A large number of three-dimensional structures of LpxC from various bacteria have been reported in literature. The first structure of LpxC at a high atomic resolution was determined from a thermophilic bacterium *A. aeolicus* (AaLpxC) [199]. All the characterized LpxC structures revealed the presence of a novel "β-α-α-β sandwich" fold, where four internal α-helices sandwiched between two β-sheets (Figure 1.26) [200-205]. The overall structure of LpxC contains two domains (Domain I and II), which are comprised of αα/βββββ structural motif. Both the domains have similar fold and possess a layer of two α-helices and one five-stranded β-sheet with parallel and antiparallel orientations that support the internal α-helices. However, the β-sheets of the Domain I are severely distorted whereas the sheets of Domain II are comparatively flat. Additionally, both the domains have a unique sub-domain; insert I (antiparallel β-sheet) and insert II (β-α-β structure) in the Domain I and Domain II, respectively. Insert I covers one side of the active site of the LpxC and insert II forms a hydrophobic passage that accommodates the acyl chain of the substrate/hydrophobic moiety of various inhibitors. The complexed structures of LpxC bound with the substrate analog (TU-514) (PDB ID 2GO4) and an inhibitor (CHIR-090) (PDB ID 5U39), have clearly shown that the α-helix of hydrophobic passage accommodates the acyl chain of TU-514 and CHIR-090 (Figures 1.26) [192, 202, 205]. Furthermore, studies have shown that LpxC encompasses an unusual substrate recognition mechanism and depicted its greater affinity towards a natural substrate (UDP-3-*O*-(*R*-3-hydroxymyristoyl)-GlcNAc) (20,000-fold greater) in comparison to a substrate analog lacking long acyl chain (UDP-GlcNAc) [206]. Several biochemical and structural evidence have demonstrated the presence of well conserved HKΦΦD unique zinc-binding motif in most of the LpxC enzymes except in *Burkholderia* family. This motif is different from the zinc motif (HEXXH, HXXE or HXXEH) which reported in other metalloamidases. In AaLpxC, His226 and Asp230 (first and last residues of this motif) and His74 have shown their participation in catalytic zinc ion coordination. The conserved Lys residue has an important role in the UDP binding and the other two hydrophobic residues ("Φ") of this zinc-binding motif position the motif helix against core structural elements [207].

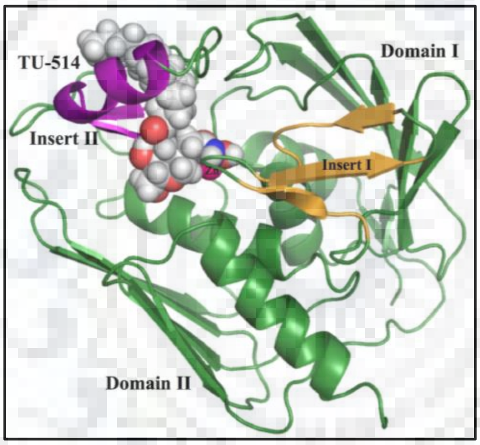

Figure 1.26: Three dimensional structure of the AaLpxC/TU514 complex. AaLpxC has shown in the ribbon diagram, which contains two domain I and II (depicted with the forest green color), and unique sub-domains; insert I (antiparallel β-sheet) and insert II (β-α-β structure) present in the both domains I and II and depicted in gold and violet color, respectively. The bound TU514 has shown as the grey space-filling model.

1.6.4.3. Sites of LpxC for inhibitors exploitation

The strcurural studies of LpxC-inhibitor complex have identified three different inhibitor binding sites which are nearby the active site of LpxC and these sites are described in the following section (Figure 1.27):

(i). **A hydrophobic passage:** It is formed by insert II structural elements of the LpxC and accommodates the hydrophobic acyl-chain of its natural substrate and the hydrophobic moieties of the different inhibitors. This hydrophobic passage is partially enclosed by the connecting loops (β1 and β2) of the domain I. This site principally determines the specificities of inhibitors binding [192, 205].

(ii). **A basic patch:** This site is nearly located at the active site and opposite to the hydrophobic passage. It contains basic and positively charged residues Arg137, Lys227, Arg250 and the ionized form of His253. These basic patch residues interact with the di-phosphate group of the UDP moieties of the LpxC substrate [201].

(iii). **A hydrophobic patch:** This site is located next to the two-stranded parallel β-sheets of Insert II of the Domain II. Phe155, Phe180 and Phe182 residues of the AaLpxC interacts with the hexose ring of the TU-514 inhibitor [192, 208].

Thus, the three potential binding sites are found notably important for the designing of novel inhibitors against LpxC and provide better understanding inhibitors specificities.

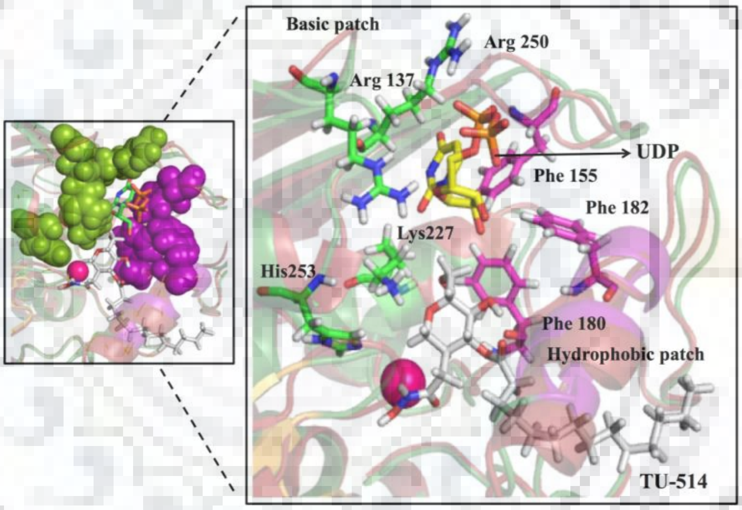

Figure 1.27: LpxC inhibitors binding sites. Different inhibitor binding sites (a hydrophobic passage, a basic patch, and a hydrophobic patch) has been identified nearby the active site of the LpxC. A basic patch interacts with the UDP moieties of the LpxC substrate (green sticks) and a hydrophobic patch has shown in the purple color spheres bound with the TU514 inhibitor (grey sticks). In the enlarge view, the associated residues of these sites have been shown as the sticks and metal as the hot pink sphere. These sites have been found notably important for the better understanding their specificities and the designing of novel inhibitors against LpxC.

1.6.5 LpxC inhibitors

The LpxC enzyme has become a prime target for discovery, designing and development of the novel potential antibacterial molecules. A large number of the inhibitors have been reported in literature, but none of them has reached the clinical trials to become effective antibiotic. Most of the reported inhibitors are competitive in nature with the substrate of LpxC. However, there is an open provocation to follow other new approaches, which allow in the future identification of an uncompetitive or noncompetitive type inhibitor against the LpxC. In this section, we have provided information about the most important and potent LpxC inhibitors (Figures 1.28).

1.6.5.1 Classical LpxC inhibitors

The first small molecule group of the LpxC inhibitors was discovered in the Merck Research Laboratories (in1980s) during the screening of 14C-galactose uptake inhibiting compounds for *E. coli* cells [167]. The effect of compound named L-573,656 was checked against all the enzymes of LPS pathway, but the compound showed the inhibitory activity specifically against LpxC enzyme. The core chemical structure of L-573,656 contained a hydroxamic acid group attached to the 2-phenyloxazaline ring (Figure 1.28). Furthermore, the generation of analog compound known as L-161,240 was performed after several optimization efforts and the compound inhibited ~ 99.9 % growth of *E. coli* within four hours (Figure 1.28). The effectiveness and potential of this compound was comparable to that of ampicillin, and its dissociation constant (*K*I) for EcLpxC was in the nanomolar range (~50 nM) [195].

Clements and coworkers also screened a metalloenzyme inhibitors library and they discovered a compound, known as the BB-78485, with a unique a sulfonamide hydroxamate-based scaffold which branches into two naphthalene rings. BB-78485 showed a minimal inhibitory concentration (MIC) value ~ 2 μg/mL and estimated ~ 20 nM of *K*I value for EcLpxC. Nevertheless, none of these inhibitors showed a broad-spectrum activity despite their excellent antibacterial activities against *E. coli*. These inhibitors were not able to control the growth of other clinically-important pathogenic bacteria including *P. aeruginosa* and *Serratia marcescens* [209].

Jackman and coworkers have also made efforts to develop a broad-spectrum inhibitor of LpxC and designed a substrate-based analog series of inhibitors [195, 210]. TU-514 inhibitor from this series showed inhibition against broadest range of LpxC orthologs, however, does not cross the membrane of bacteria very efficiently. It showed the *K*I value in the nanomolar range against the AaLpxC ~650 nM at both the acidic and basic pH. The *K*I value of TU-514 varied against the EcLpxC at the acidic pH (650 nM at pH 5.5) and basic pH (1 nM at pH 7.4) [169, 195]. The complexed structure of AaLpxC-TU-514 has provided important insights about the substrate binding at the active site of LpxC.

Andersen and coworkers made a significantly breakthrough research by disclosing a novel *N*-aroyl-L-threonine hydroxamate (CHIR-090) inhibitor of the LpxC. CHIR-090 has inhibited both *E. coli* and *P. aeruginosa* bacteria and showed an efficacy as good as to the ciprofloxacin and tobramycin in the disc diffusion assay [169, 211]. Unlike the other previously described inhibitors, which showed instantaneous inhibitor binding and dissociation, CHIR-090 is a slow, time-dependent and tight-binding inhibitor. However, even the CHIR-090 exhibited the limited inhibitory activities against certain bacteria and it is a less effective inhibitor for *Acinetobacter*, *Burkholderia*, and *Rhizobium* strains [169, 212].

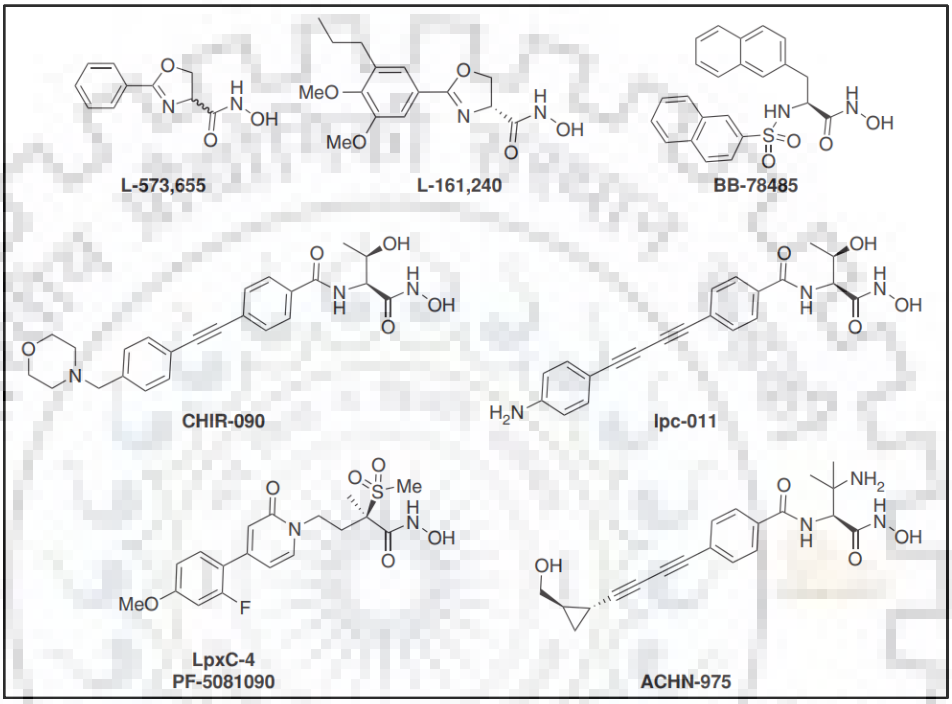

Figure1.28: Chemical structures of potent LpxC inhibitors block the committed step of LPS.

1.6.5.2 Recent LpxC inhibitors

Recently, Mansoor and coworkers have developed two series of novel inhibitors benzolactam and urea derivatives by modifying a parent compound CHR-12 [213]. This parent compound is almost similar to CHIR-090 inhibitor, but does not include the morpholine group. On the cycling of the amide NH of the threonyl moiety, a benzolactam series was generated and this modification also led to a noteworthy loss in the antibacterial potency of the compounds. This clearly suggests that hydrogen bonding occuring between amide proton and Thr179 residue is a critical interaction for the LpxC inhibition. However, the urea derivatives have displayed a relatively small decrement in antibacterial potency. The structure-activity relationship data suggested that the firmness and rigidity of the urea moieties, piperidine and piperazine rings maintained the inhibitory activities. Moreover, neither compound of this series exhibited an improved potency in comparison to their parent compound (CHR-12) or CHIR-090 [213].

Recently from 2011 to 2012, Pfizer laboratories have developed and reported a variety of the biphenyl methylsulfone based inhibitors in five patents. The parent “Compound 1a” of the series has distinct structural features which are distinct from CHIR-090 [214-217]. The inhibitors of this series have shown a nanomolar or even a sub-nanomolar range of the inhibitory activity against PaLpxC. In this series, the alkylation of methyl-sulfone with 1-bromo-4-(2-bromoethyl) benzene generated an ethyl linker, which tie the biphenyl group to methyl-sulfone head group. The amide-linker of the CHIR-090 inhibitor was replaced with this ethyl-linker in this series. However, this modification potentially abrogates the hydrogen bonds between amide group of CHIR-090 and LpxC residues. It provided a molecular flexibility and also reduced the potential steric hindrance, which may exist at the active site of LpxC. The sulfone moiety of this series functions like the threonyl group of CHIR-090 inhibitor and contributes to LpxC binding with inhibitors. The antibiotic potency and the effectiveness of CHIR-090 inhibitor are majorly contributed due to its threonyl group. Some favorable and conserved interactions were responsible for the binding of these methyl-sulfone derivatives with LpxC. In methyl-sulfone hydroxamate derivatives, van der Waal interactions occur between its methyl group and aromatic ring of Phe192, and a hydrogen bond forms between its hydroxyl groups and the side-chains of Lys239 of EcLpxC. The oxygen of this sulfone moiety forms a hydrogen bond with the conserved Lys238 (PaLpxC), and van der Waal interactions with Phe192 (PaLpxC) are maintained by the methyl group of the methyl-sulfone moiety.

Montgomery and coworkers, have further designed and synthesized a new series of the methyl-sulfone based derivatives. The central phenyl ring of the biphenyl moiety, which is proximal to the hydroxamate group, was substituted with a pyridine ring to get better *in vivo* efficacy and to improve pharmacokinetic properties, particularly for the plasma stability. This strategy led to the synthesis of an advanced and the most potent compound PF-5081090 (LpxC-4) which displayed the enhanced antibiotic activity against a wide range of Gram-negative bacteria including *P.aeruginosa*, *Burkholderia cepacia* and *Stenotrophomonas maltophilia.* No toxicology has been reported for PF-5081090 (Figure 1.28). Additionaly, Achaogen Inc. developed an inhibitor known as ACHN-975, which entered in the Phase I evaluation in humans but further clinical studies were halted due to inflammation at the injection site. And in late 2015, ACHN-975 is the only LpxC inhibitor that has entered clinical trials (Figure 1.28) [214-218].

CHAPTER 2

BIOPHYSICAL AND BIOCHEMICAL CHARACTERIZATION OF DAH7PS FROM *PROVINDENCIA ALCALIFACIENS* (PaDAH7PS)

2.1 Introduction

The biosynthesis of essential aromatic amino acids (Phe, Tyr, and Trp) and other important secondary metabolites is mediated by seven different enzyme-catalyzed reactions in shikimate pathway [34, 219]. The first enzyme of this pathway is 3-deoxy-D-arabino-heptulosonate-7-phosphate synthase (DAH7PS), a metalloenzyme, which catalyzes the stereospecific condensation of intermediate compounds phosphoenolpyruvate (PEP) and D-erythrose-4-phosphate (E4P) generated from the glycolytic pathway and the pentose phosphate pathway respectively, and forms 3-deoxy-D-arabino-heptulosonate-7-phosphate (DAHP) and inorganic phosphate (Pi). Since this pathway is employed only in plants, fungi, microbes, and apicomplexans, enzymes of this pathway are potential targets for the development of drug molecules and herbicides. The genetic modifications in the enzymes of this pathway via recombinant DNA technology show high yield of production of the essential amino acids during microbial fermentation at industrial level [39, 220-225]. The shikimate pathway is controlled by three regulatory enzymes: 3-deoxy-D-arabino heptulosonate 7-phosphate synthase (DAH7PS), chorismate mutase (CM) and prephenate dehydratase (PDT). As a committed enzyme, the regulation of DAH7PS is a key point for the metabolic flux of this pathway [226]. DAH7PS are categorized into two different families; Type I (microbial type) and Type II (plant type, including few microbial) based on their sequence similarity and molecular masses [227, 228]. Despite the very low sequence identity between two families of DAH7PS, they share similarities in the functional and the mechanistic features. All characterized DAH7PS possess a common core catalytic $(\beta/\alpha)_8$ TIM barrel fold and show conservation in the substrate and metal ion interacting key residues [88]. Although, DAH7PS from different sources show significant differences in their biologically active oligomeric states and additional regulatory extensions [229].

Oligomerization of the DAH7PS is essential for their catalytic activity as well as for the interaction of regulatory molecules at the allosteric site. Several studies have shown that microbial DAH7PS are feedback regulated enzymes through the diverse allosteric mechanism; inhibit either by the end products (Phe, Tyr, and Trp) or intermediate compounds formed in the pathway [229]. However, the plant's DAH7PS show redox regulatory mechanism [106]. The monofunctional isoenzyme of *Escherichia coli i.e.* DAH7PS, regulated by the end product (Phe), DAH7PS of *Thermotoga maritima* (Tyr/Phe) and bifunctional DAH7PS of *Listeria monocytogenes* and *Geobacillus sp*. are tetrameric proteins, whereas other two isoenzymes of *E. coli* (Tyr and Trp) and DAH7PS of *Saccharomyces cerevisiae* (Tyr) exist in the dimeric state [72, 87, 230-232]. The unregulated DAH7PS of *Pyrococcus furiosus* and *Aeropyrum pernix* show dimeric as well as tetrameric forms [81, 101, 233]. A Type II DAH7PS of *Mycobacterium tuberculosis* is also a tetrameric protein, which is regulated synergistically by all three aromatic amino acids [100].

In 1999, Park and Bauerle reported that phenylalanine regulated *E. coli* DAH7PS (EcDAH7PS) is a metal catalyzed oxidation enzyme system. The biologically active homotetrameric form of EcDAH7PS dissociates into an inactive monomeric form due to the formation of a disulfide linkage, catalyzed by redox metal ions in the absence of substrate (PEP), between the two cysteine residues (Cys61 and Cys328) of the active-site [99]. Recently, Sobota and coworkers have also shown that enzymatic activity of EcDAH7PS is poisoned by hydrogen peroxide and superoxide. Here, in the presence of peroxide an inactivated apoprotein with oxidized cysteine residues was generated due to the removal of prosthetic iron metal, whereas under superoxide stress active site metal was replaced by a non-activating zinc metal [234]. In *in-vivo* and *in-vitro* conditions, redox metal catalyzed oxidation, peroxidation, superoxidation, and other environmental oxidative stress conditions are common mechanisms of oxidative damages in the proteins [235, 236]. Consequently, amino acids in the proteins undergo a variety of chemical modifications such as isomerization, deamidation, peptide bond cleavage, and oxidation which leads to the aggregation and degradation process [237]. EcDAH7PS has shown multiple damage effects under different oxidative stress conditions; however, oxidative damages in DAH7PS of any other organism have not been studied and a clear molecular mechanism is undetermined.

In the present study, we cloned, expressed, and purified a homologous DAH7PS from a Gram-negative pathogenic bacterium *Providencia alcalifaciens* (PaDAH7PS) which belongs to the family Enterobacteriaceae and commonly causes traveler's diarrhea and urinary tract infections [238, 239]. Here, we determined the oligomeric state and enzymatic activity of purified

PaDAH7PS, under different environmental conditions. Furthermore, we investigated the influence of redox metal oxidative stress and its impact on the modification of amino acid residues of PaDAH7PS via FTIR and Mass spectrometry. Moreover, we also characterized the unfolding/partial folding and conformational changes in PaDAH7PS due to oxidative damage by circular dichroism and fluorescence spectroscopy.

2.2 Materials and methods

2.2.1 Materials

All restriction enzymes (BamHI and XhoI), DNA polymerase, and T4 DNA ligase were purchased from New England Biolabs. DNA isolation, plasmid isolation, purification, and gel extraction kits were purchased from Qiagen. *E. coli* BL21 (DE3), DH5α cells, and pET28c plasmid vector were taken from Novagen. The Ni-NTA resins, bis-tris propane buffer (BTP), phosphoenolpyruvic acid sodium salt (PEP), erythrose-4-phosphate (E4P) and Thioflavin T (ThT) were purchased from Sigma-Aldrich (St. Louis, MO, USA). All other chemicals such as TCA, periodic acid, sodium arsenite, 1, 4-dithio-D-threitol (DTT), BSA and $CuCl_2$ were purchased from HiMedia (India). Thiobarbituric acid was purchased from Loba Chemie (Mumbai, India). Trypsin from Promega, Amicon ultra concentrator, and Millex syringe filters (γ-irradiated, pore size 0.45 μm, filter diam. 33 mm) from Millipore Corporation, Billerica, MA. Dialysis membrane of 3500 Da cutoffs was taken from Pierce, Rockford, USA.

2.2.2 Methods

2.2.2.1 Molecular cloning and overexpression of recombinant PaDAH7PS

The genomic DNA of *Providencia alcalifaciens* (MTCC No. 4430) was isolated by DNA extraction Kit and the gene of 1054 bp (EKT65704.1) was amplified with the forward (BamHI) 5’GATTCT**GGATCC**CAATGAACTATCAGAACGATGACGTC-3’ and reverse (XhoI) 5’GATTCT**CTCGAG**TTATTTATTTCGACGAGCAATGACTG-3’ designed primers and further cloned into the pET28c-His-Tev vector. For expression of soluble PaDAH7PS, the cloned and screened recombinant plasmid (pET28c + DAH7PS gene) from DH5α was isolated. Furthermore, transformed into the *E. coli* BL21 (DE3) competent cells formed by the $CaCl_2$ method and plated on the LB agar plates containing 50 μg/ml kanamycin. A single colony was inoculated into the LB broth with 50 μg/ml kanamycin for seed culture preparation. Next day, 1000 ml LB broth was inoculated with 1 % of seed culture and allowed to grow at 37 °C with 200 rpm until OD 600 reached up to 0.6-0.7. Subsequently, the culture was induced with 0.4

mM isopropyl β-D-thiogalactosidase (IPTG) and incubated at 18 °C at 200 rpm for the next 16 h. Next day, bacterial cells were harvested by centrifugation at 5,000 rpm for 15 min, the supernatant was decanted and pellets were stored at -80 °C [240, 241].

2.2.2.2 Purification and cleavage of His-Tag of PaDAH7PS

Bacterial cell pellets were resuspended in 30 ml lysis buffer containing substrate (PEP) and reducing agent DTT (20 mM BTP pH 7.5, 100 mM NaCl, 25 mM Imidazole, 0.1 mM $MnCl_2$, 1 mM DTT, and 400 µM PEP) and lysed using constant cell disrupter system. The lysate was centrifuged at 12,000 rpm for 60 min at 4 °C. The supernatant was collected and loaded onto the pre-equilibrated Ni-NTA affinity chromatography column and incubated for 30 min. The unbound impurities were removed by two washings with increasing step-wise gradient containing 25 mM and 50 mM imidazole, respectively. Furthermore, PaDAH7PS was eluted with a higher gradient (100 mM to 250 mM) of imidazole. The molecular mass and purity of eluted fractions of protein were determined on the 12 % SDS-PAGE with standard molecular weight protein marker (Bio-Rad). Subsequently, PaDAH7PS was incubated with purified Tev-protease at 20 °C for 12 h to remove N-terminal His-tag from the protein. Moreover, PaDAH7PS was buffer exchanged (buffer without imidazole) to remove high concentration of imidazole and to separate out the residual His-tagged protein, PaDAH7PS was again loaded onto the pre-equilibrated column for reverse Ni-NTA affinity chromatography. The non-tagged PaDAH7PS was obtained in the flow through. The cleaved protein was collected and concentrated up to a final volume of 1 ml using a 3 kDa cutoff concentrator (Amicon Ultra-15) and further subjected to size exclusion chromatography. We also followed the same procedure during purification of PaDAH7PS in the oxidizing environment. In oxidized condition, neither the reducing agent (DTT) nor the substrate (PEP) was added in the lysis buffer.

2.2.2.3 Size exclusion chromatography

To determine the oligomeric state of purified PaDAH7PS in different environmental conditions (reduced and oxidized) size exclusion chromatography was performed. The concentrated protein sample (~10 mg/ml) was centrifuged at high speed at 4 °C for 15 min and subsequently loaded onto the prepacked Hi-Load16/60 Superdex 200 (Prep Grade) column from GE Healthcare. The column was pre-equilibrated with different buffer compositions, as mentioned in the previous section, in accordance with the purification environmental conditions. Pure fractions of PaDAH7PS (3 ml) were collected in tubes by AKTA purifier system with a flow rate 0.5 ml/min and absorbance was recorded at 280 nm. The gel filtration column was calibrated for construction of the standard curve and the molecular mass of PaDAH7PS was estimated by using Gel Filtration HMW Calibration Kit containing ferritin (440 kDa), aldolase (158 kDa), Conalbumin (75 kDa) and ovalbumin (44 kDa) (GE Healthcare).

2.2.2.4 Glutaraldehyde cross-linking and Native-PAGE

Additionally, the oligomeric state of PaDAH7PS was also analyzed by performing cross-linking of protein with glutaraldehyde and the experiment was set up by following the procedure as described by Fadouloglou et al.[242]. The oligomerization of PaDAH7PS was also analyzed by native-page electrophoresis. Electrophoresis was performed by using Tris-glycine buffer (pH 8.3) as an electrode buffer at a constant current of 25 mA at 4 °C for 8 h. Subsequently, the gel was stained by using Coomassie Brilliant Blue R-250.

2.2.2.5 Metal-catalyzed oxidation effect on the oligomeric state of PaDAH7PS

The purified non-tagged PaDAH7PS fractions in all previously described conditions were pooled separately. These were subsequently incubated in the presence of 75 µM $CuCl_2$ for 22 h at 20 °C to investigate the effect of redox metal treatment on the oligomeric state stability of the protein. The PaDAH7PS, incubated with redox metal, was concentrated and further loaded onto the gel filtration column with buffer according to the purification conditions in the presence of $CuCl_2$.

2.2.2.6 FTIR spectroscopy

FTIR spectrum of oxidized protein (PaDAH7PS-Tetox) was recorded by using Thermo Nicolet Nexus (FTIR) spectrophotometer with a spectral resolution of 2.0 cm^{-1} in the range 400-4000 cm^{-1}. The spectrum measurement was carried out in KBr pellets and protein sample was concentrated up to ~10 mg/ml. The vibrational peaks present in the fingerprint region of 900-1100 cm^{-1} range were analyzed.

2.2.2.7 Mass spectrometric analysis

The oligomerization of both His tagged-PaDAH7PS and non-tagged PaDAH7PS and detection of the removal of extra N-terminal His-tag were also analyzed by using sinapinic acid (matrix) through MALDI/TOF mass spectrometer (Bruker Daltonics, Germany).

Additionally, for the identification of methionine modification in PaDAH7PS the peak fractions from each chromatogram were loaded onto the 12 % SDS-PAGE and bands were digested with the trypsin as described earlier [243]. Briefly, excised gel pieces were de-stained by adding the ammonium bicarbonate/acetonitrile (1:1, V/V) and acetonitrile (100 %), alternating incubation for 30 min, following trypsin digestion for 16 h at 37 °C. After digestion, the reaction was stopped through formic acid and digested peptides were recollected in extraction buffer (1:2 (V/V) 5% formic acid/acetonitrile) at room temperature. The collected peptides were dried in SpeedyVac and stored at -20 °C. The samples were spotted on the MALDI ground steel plate with HCCA (α-cyano-4-hydroxy-cinnamic acid) matrix. Mass spectrometric analysis was carried out on Ultraflextreme MALDI-TOF/TOF mass spectrometer (Bruker Daltonics) equipped with a 60-Hz nitrogen laser. Mass spectra were acquired in the reverse positive mode. The acquisition of spectra was controlled by flexControl 3.4, spectral data were processed using flexAnalysis 3.4 (both software by Bruker Daltonics). The instrument was calibrated externally using Peptide Calibration Standard (Bruker Daltonics) and to cover masses in the m/z range of 500 - 3500. Spectra were accumulated from 1200 laser shots. The searches were done using Mascot Server 2.4 (Matrix Science, UK) and employed mass tolerances for precursors and fragment ions of ±200 ppm and ±0.7 Da, respectively. Trypsin was set as a protease with 1 missed cleavage allowed; carbamidomethylation of cysteine was set as a fixed modification and methionine oxidation as a variable modification. Peptide mass fingerprinting (MS), for protein identification and tandem mass spectrometry (MS/MS), for sequencing was done using the Mascot search engine (Matrix Science) and BioTools complemented with NCBI database. The theoretical *m*/*z* values for trypsin-digested peptides of *Pa*DAH7PS were assessed using the online Expasy tool [244].

2.2.2.8 Enzymatic activity of PaDAH7PS

The enzymatic activity of different oligomeric state of PaDAH7PS was estimated by discontinuous Aminoff periodate thiobarbituric acid assay method [245]. The activity of the enzyme was calculated by measuring the amount of product formed by the condensation reaction of phosphoenolpyruvate (PEP) and erythrose-4-Phosphate (E4P) at 37 °C catalyzed by PaDAH7PS. A reaction mixture of total 100 µl with the purified enzyme in 100 mM BTP buffer with PEP in the presence of the $MnCl_2$ was set up at the room temperature and the final enzymatic reaction was started by adding another substrate, i.e. E4P, and the reaction mixture was kept at 37 °C for 5 min. Measurements were carried out at 549 nm with Cary UV-visible spectrophotometer using quartz cuvette. The kinetic parameters (Km, Vmax, Kcat) for the both PEP and E4P (250 µM to 2000 µM were determined by varying the substrate concentration (50 µM to 400 µM). All reactions were performed in triplicates. The obtained data were fitted using non-linear regression analysis by graph pad prism software [246].

2.2.2.9 Atomic force microscopic imaging of PaDAH7PS

The morphological features of different oligomeric states of PaDAH7PS were detected by Atomic force microscopy. AFM images of protein were collected in semi-contact imaging mode with SPM NT-MDT Netgra system, a facility provided at the Institute Instrumentation Centre, IIT Roorkee, India. 10 µl of freshly prepared protein samples in each condition were used for imaging. A silicon nitride coating cantilever of 100 µM and force contact 5.5-22.5 N/m at a frequency of 1.01Hz with pyramidal geometry was used to generate the images. At least three regions of the sample surface were investigated to confirm homogeneity. All images were processed by using Nova software (1.026.1424 version) provided with the instrument.

2.2.2.10 Circular dichroism spectroscopy

The secondary structure assessment of different states of PaDAH7PS was performed by using Jasco 1500 spectropolarimeter equipped with the Peltier system. The purified PaDAH7PS under different conditions (5.0 µm concentration) in 25 mM sodium phosphate buffer (pH 7.5) was filtered through 0.45 µm Millex syringe filter and a baseline with reference buffer was set up before spectrum acquisition. The spectrum of each sample was recorded in the far-UV region (190-240 nm) at 25 °C with a scanning speed of 50 nm min^{-1} by using 0.1 mm quartz cell with a bandwidth of 1 nm. The final CD spectra of the different oligomeric states of PaDAH7PS were then averaged and smoothed values of three independent acquisitions. The data were analyzed to estimate the percentages of secondary structure using the Dichroweb server and spectrum of every sample is represented from 190-240 nm in CD mDeg [247-249].

2.2.2.11 Fluorescence spectroscopy

To examine the conformational and structural perturbation in PaDAH7PS due to oxidation intrinsic and extrinsic fluorescence studies was performed using the spectrofluorometer Fluorolog®-3 (Jobin Yvon Inc.USA) with 5 nm emission slits and cuvette of 1-cm path length at room temperature. All protein samples were diluted up to 5.0 µM in 25 mM sodium phosphate buffer (pH 7.5) and intrinsic fluorescence was measured by exciting specifically Trp residue (λexc = 295 nm) recording the emission spectra between 300-500 nm. The extrinsic fluorescence was measured by ANS binding with protein and excitation was performed at λexc = 380 nm and emission spectra were collected from 400-600 nm.

2.2.2.12 ThT binding assay

Furthermore, to rule out the possibility of amyloid fibrils formation during aggregation ThT binding was also performed with different oligomeric states of PaDAH7PS. A stock solution of ThT (Thioflavin T) was prepared in distilled water and final 10 µM was added in each oligomeric state of PaDAH7PS and incubated the mixture for 30 min in the dark. The ThT excitation was performed at λexc = 440 nm and emission spectra were recorded from 450-600 nm by using spectrofluorometer.

2.3 Results

2.3.1 Cloning, expression, purification, and oligomeric state determination of PaDAH7PS

The open reading frame of 1054 bp PaDAH7PS gene from *P. alcalifaciens* was cloned and overexpressed with high solubility in *E. coli* BL21 (DE3) cells. The PaDAH7PS protein was purified by affinity chromatography and single band of the expected molecular weight ~41 kDa with N-terminal His-tag was observed on 12% SDS-PAGE profile. Purified PaDAH7PS with His-tag was loaded onto the gel filtration column with the substrate and a prominent peak at ~62 ml elution volume with two partially resolved small peaks (~ 49 ml and ~ 54 ml) were observed on the chromatogram, which corresponds to the hexameric form of PaDAH7PS (Figure 2.1A). In contrast, earlier studies have shown that all Type I DAH7PS exhibit either a tetramer or a dimeric state [88, 231]. Several reports have revealed that His-tag in the recombinant proteins alters the binding, kinetics, structural as well as oligomerization properties of a recombinant protein when compared to the wild-type protein [250-252]. Therefore, His-tag of PaDAH7PS was cleaved and non-tagged protein was again loaded onto the gel-filtration column. Non-tagged PaDAH7PS unexpectedly showed two peaks on the chromatogram (Figure 2.1B). A prominent peak at ~62 ml (i.e. the hexameric form) similar to the tagged protein and a second peak at ~68 ml elution volume corresponding to the tetrameric form of PaDAH7PS (Table 2.1). Moreover, the homogeneity and purity of both peak fractions were checked on the 12 % SDS-PAGE (Figure 2.1C). The first peak fractions showed single bands of purified PaDAH7PS, while elution fractions of the second peak showed two closely stacked bands (indicated by underline), one migrating at a little slower rate (Figure 2.1D). The presence of a slowly migrating upper band on SDS-PAGE profile indicated the increment in molecular weight of PaDAH7PS.

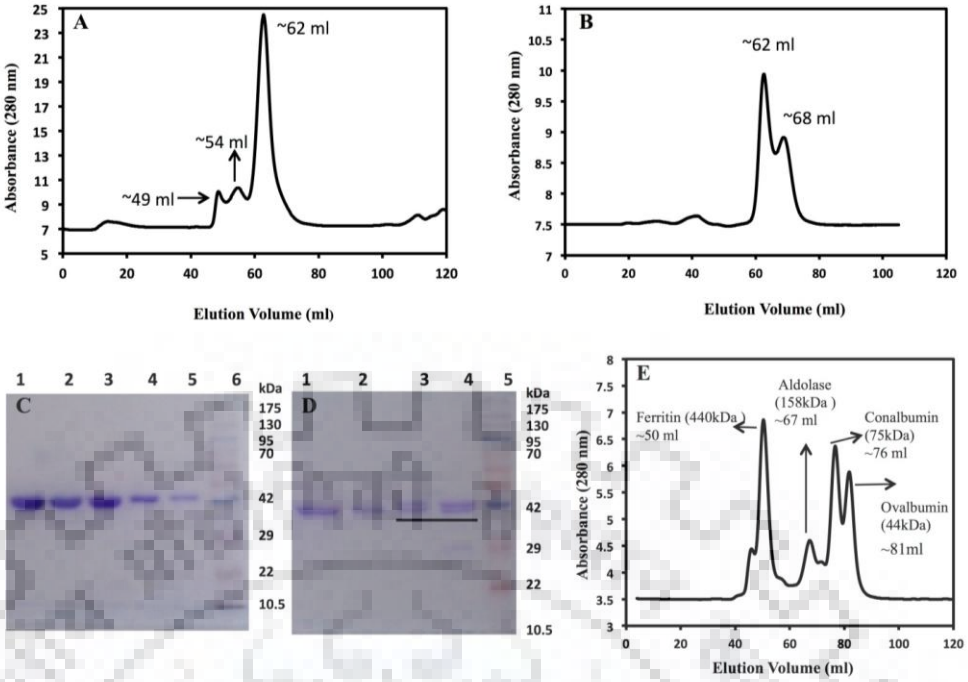

Figure 2.1: Purification profile and oligomeric state characterization of PaDAH7PS. (A) Gel-filtration chromatogram of PaDAH7PS with His-tag. **(B)** Gel-filtration chromatogram of PaDAH7PS after His-tag cleavage. **(C)** 12% SDS-PAGE profile of elution fractions from ~62 ml peak, Lane 1-5 Single bands of the expected mass of ~41 kDa of purified PaDAH7PS, Lane 6 Molecular weight marker (kDa). **(D)** 12% SDS-PAGE profile of both peak fractions, Lane 1 & 2 Single bands from non-oxidized hexameric state peak (62 ml), Lane 3 & 4 Two closely stacked bands with different migration rate from tetrameric state peak (68 ml) fractions which are indicated the oxidation of PaDAH7PS on SDS-PAGE, Lane 5 Molecular weight marker (kDa). **(E)** Gel-filtration chromatogram profile of the high molecular weight standard markers on the Superdex 200 column.

Table 2.1 Different purification conditions and their effects on the oligomeric state of PaDAH7PS.

Purifications Conditions			Effects		
Sr. No.	**Substrate**	**Reducing Agent**	**Elution Volume**	**Oligomeric State**	**Oxidized/ Non Oxidized**
1.	+ PEP	+ DTT	~62 ml	Hexamer (PaDAH7PS-Hexnox)	Non Oxidized
			~68 ml	Tetramer (PaDAH7PS-Tetox)	Oxidized
2.	-	-	~76 ml	Dimer (PaDAH7PS-Diox)	Oxidized

Furthermore, to rule out the possibility of the influence of His-tag on the oligomerization of PaDAH7PS and to verify the proper cleavage of His-tag from PaDAH7PS, we confirmed the molecular masses and the oligomeric states of both tagged and non-tagged PaDAH7PS using MALDI-TOF-MS. His-Tagged PaDAH7PS showed two major peaks with high intensity at ~42097.129 Da (B1) and ~83539.558 Da (B2) with a few traces of higher oligomeric states (B3), while after removal of His-tag two major peaks of ~38611.796 Da (A1) and ~77576.5668 Da (A2) were observed in the mass spectrum, consistent with the complete removal of N-terminal His-tag, which correspond to the monomeric and dimeric states of PaDAH7PS respectively (Figure 2.2A). All reported DAH7PS exist as non-covalently assembled loose oligomers, consisting two monomeric units in a ‘tight-dimer’. The sinapinic acid matrix used in MALDI-TOF analysis cannot detect the non-covalently attached oligomeric form of a protein [253]. Therefore, the hexameric form of PaDAH7PS was not detected in the mass spectrum as represented by size exclusion chromatogram. Moreover, the presence of oligomeric state was also confirmed through the native-PAGE and glutaraldehyde cross-linking profile of PaDAH7PS as shown in the figure 2.2B & 2.2C, respectively.

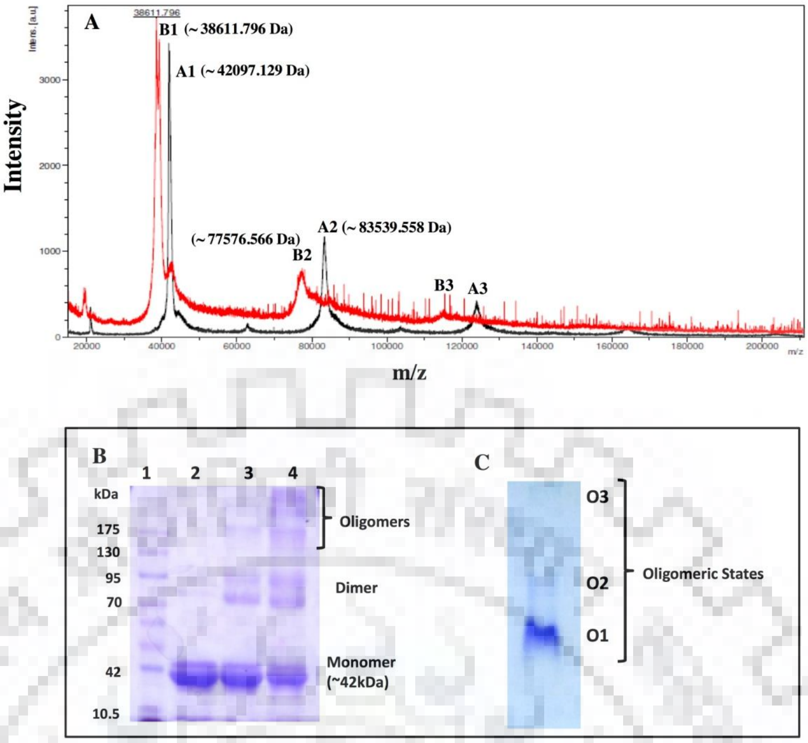

Figure 2.2: (A) MALDI-TOF MS spectrum of His-tagged PaDAH7PS (black color) showing two peaks corresponding to ~42097.129 Da (A1) and ~83539.558 Da (A2). MALDI-TOF MS spectrum of PaDAH7PS without His-tag (red color) showing two intense peaks at ~38611.796 Da (B1) and ~77576.566 Da (B2) corresponding to monomer and dimer and both spectra depicting few traces (A3 and B3) of higher oligomeric states of PaDAH7PS. **(B)** PaDAH7PS profile after glutaraldehyde cross-linking, Lane 1 Molecular weight marker, Lane 2 Purified protein nottreated with glutaraldehyde (Control), Lane 3 & 4 Protein treated with 0.05% and 0.1% glutaraldehyde respectively showing monomer and cross-linked oligomers of PaDAH7PS. **(C)** The native-PAGE profile of protein purified in reduced condition with substrate, where band O1 indicating the hexameric oligomeric form and bands O2 and O3 the other higher forms (i.e. aggeregated form) of PaDAH7PS.

Unexpectedly, PaDAH7PS depicted a non-oxidized hexameric (PaDAH7PS-Hexnox) and an oxidized tetrameric (PaDAH7PS-Tetox) oligomeric state, even in the presence of substrate (PEP) and reducing agent (DTT) during purification. Generally, metalloproteins are targeted by the redox metal ions at a specific site in the oxidative process. The redox metals might have introduced during the purification with contaminated reagents, formulation of buffer solutions, and leaching of metallic containers. Therefore, the effects of different environmental conditions and redox metal oxidation on the oligomeric state and stability of PaDAH7PS were further analyzed.

2.3.2 Influence of oxidative condition and redox metal treatment on the PaDAH7PS

PaDAH7PS was purified in the absence of both reducing agent and substrate to study the effect of oxidized condition. The oligomeric state of purified PaDAH7PS was analyzed by the size exclusion chromatography and homogeneity was checked on 12% SDS-PAGE. The purified PaDAH7PS in oxidative condition showed a peak at ~76 ml elution volume, which corresponds to the dimeric state of PaDAH7PS (Figure 2.3A). It also exhibited two closely stacked bands on SDS-PAGE, which clearly indicated the oxidation of PaDAH7PS.

Furthermore, the effect of redox metal treatment on the DAH7PS was critical to evaluate the stability of the quaternary structure. Therefore, PaDAH7PS was purified and cleaved in both the previously mentioned conditions and subsequently was loaded onto the Superdex (200) gel filtration column after treating with it $CuCl_2$. The chromatograms in both the conditions showed one prominent peak at ~47 ml and another small peak at ~76 ml elution volume, which correspond to the higher oligomeric and the dimeric state of PaDAH7PS, respectively (Figure 2.3B).

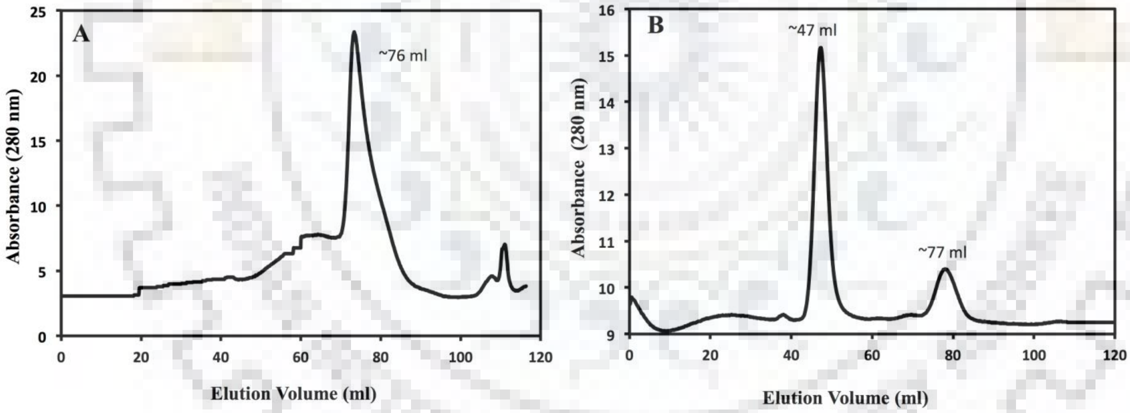

Figure 2.3: Effect of oxidized purification condition and redox metal treatment on the oligomeric state of PaDAH7PS. (A) Gel-filtration chromatogram showing the elution profile of PaDAH7PS purified without both substrate and reducing agent (i.e. oxidized condition). **(B)** Gel filtration chromatogram showing the elution profile of protein on the redox metal (Copper) treatment.

Thus, PaDAH7PS, when treated with redox metal, dissociated into a small population of the oxidized dimeric state (PaDAH7PS-Dimox*), whereas, the majority of the protein population transformed into the higher oligomeric state (PaDAH7PS-Homox*) (Table 2.2).

Table 2.2 Effect of redox metal treatment on the oligomeric state of PaDAH7PS in different purification conditions.

Redox metal treatment of PaDAH7PS						
Conditions			**Redox Metal Treatment**	**Effects**		
Sr. No.	**Substrate**	**Reducing Agent**		**Elution Volume**	**Oligomeric State**	**Oxidized/ Non Oxidized**
1.	+ PEP	+ DTT	+ $CuCl_2$	~47 ml	Higher oligomer (PaDAH7PS-HOmox*)	Oxidized
				~76 ml	Dimer (PaDAH7PS-Dimox*)	Oxidized
2.	-	-	+ $CuCl_2$	~47 ml	Higher oligomer (PaDAH7PS-HOmox*)	Oxidized
				~76 ml	Dimer (PaDAH7PS-Dimox*)	Oxidized

This higher oligomeric state could be an aggregated state of PaDAH7PS, which might have occurred due to the oxidative damage. Therefore, we further studied the modifications in PaDAH7PS to gain insight on the effect of oxidation.

2.3.3 FTIR spectroscopy analysis

The effect of oxidation on PaDAH7PS was identified by investigating the fingerprint region (900-1200 cm^{-1}) in the FTIR spectrum of PaDAH7PS-Tetox. Methionine and cysteine residues in the protein are the most vulnerable amino acids for oxidation by any agents [254]. In the FTIR spectrum of PaDAH7PS-Tetox, three small peaks in the range of ~1040, 1088, 1124 cm^{-1}, were observed, indicating the modification of methionine residues to methionine sulfoxide (MetSO) in the oxidized state of PaDAH7PS (Figure 2.4).

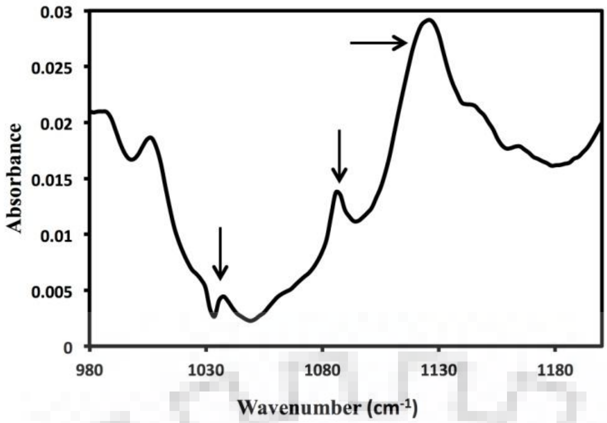

Figure 2.4: FTIR absorption spectrum of PaDAH7PS-Tetox in the fingerprint region (900–1200 cm^{-1}) and the presence of three small peaks (depicted by the arrow) indicated that methionine residues were oxidized into methionine sulfoxide.

2.3.4 Identification of the oxidative modification in PaDAH7PS

Additionally, the oxidized methionine residues in PaDAH7PS were also confirmed through the peptide mass fingerprinting (PMF) analysis by mass spectrometry. As depicted in the theoretical trypsin digestion profile of PaDAH7PS contains total seven methionine residues Met1, Met91, Met113, Met157, Met263, Met279, and Met300 which should be depicted the peptides of expected masses 1154.489, 962.497, 2180.018, 4047.089, 2414.238, 1864.870 and 3000.498 Da, respectively, resulting after the trypsin digestion. Here, the PMF of PaDAH7PS-Hexnox showed all released peptide peaks of the expected masses and only peptides peaks of 1023.5788, 962.549, 2180.253 Da were depicted with no modification in any methionine residue (Figure 2.5 & Table 2.3).

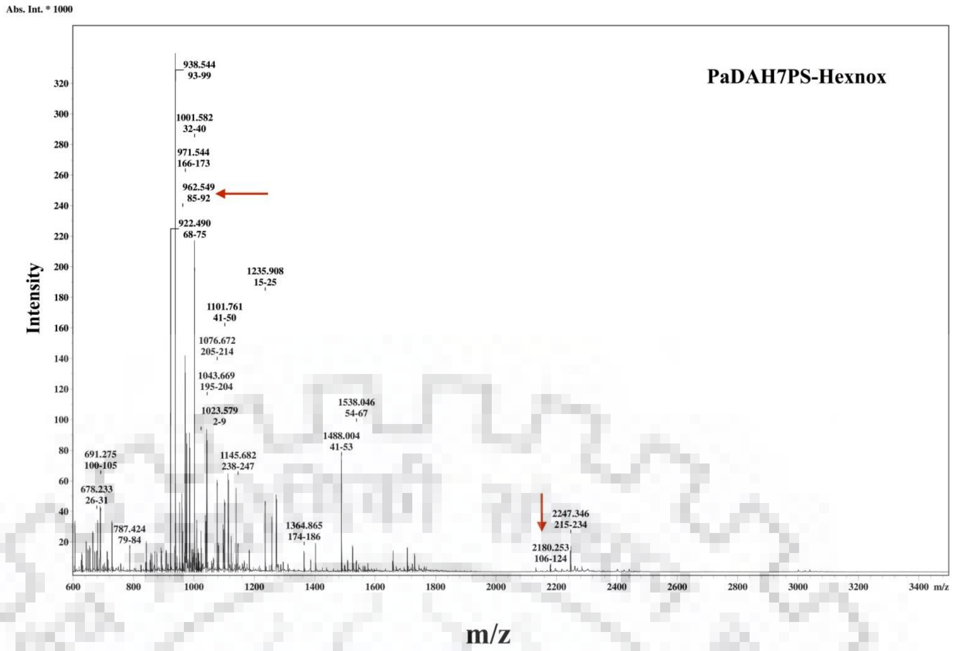

Figure 2.5: Mass spectrometric analysis of PaDAH7PS-Hexnox. Here, all released peptides obtained after trypsin digestion of expected masses and peptides containing methionine residue (non-oxidized) are indicated by the red color arrows.

In contrast, on the PMF of PaDAH7PS-Tetox, two additional peptide peaks of ~2195.933 Da and ~3016.454 Da were detected (Figure 2.6A & Table 2.3). Thus, the extra generated peptides i.e. ~2195.933 Da and ~3016.454 Da with an increment of 16 Da in their masses on the PMF of PaDAH7PS-Tetox correspond to the peptide masses of 2180.0189 Da and 3000.4982 Da, which contain Met113 and Met300 residues respectively. In addition, PMF of PaDAH7PS-Diox showed three more oxidized residues: Met91, Met263, and Met279 along with Met113 and Met300 in Mascot search engine which clearly indicated the occurrence of higher oxidation in the absence of substrate and reducing agent (Figure 2.6B & Table 2.3). Evidently, the oxidation of methionine residue to methionine sulfoxide (MetSO) is confirmed by peptide mass fingerprinting, which indicated the addition of oxygen and also supported the FTIR spectroscopy.

Table 2.3 Methionine residues containing peptides generated by trypsin digestion from different oligomeric states of PaDAH7PS.

Sequential position	**Mass observed**	**Mass expected**	**Methionine containing peptides fragments of PaDAH7PS after trypsin digestion**
PaDAH7PS-Hexnox			
85-92	962.5491	961.5418	85-DSLEIVMR-92
106-124	2180.2528	2179.2456	106-GLINDPHMDHSFDINEGLR-124
PaDAH7PS-Tetox			
85-92	962.4656	961.4583	85-DSLEIVMR-92
106-124	2179.9079	2178.9006	#106-GLINDPHMDHSFDINEGLR-124#
	2195.9326	2194.9253	#106-GLINDPH**M***DHSFDINEGLR-124#
295-322	3000.4255	2999.4183	#295-SITGVMIESHLVEGNQNLESGEPLVYGK-322#
	3016.4536	3015.4463	#295-SITGV**M***IESHLVEGNQNLESGEPLVYGK-322#
PaDAH7PS-Diox			
85-92	962.4788	961.4715	85-DSLEIVMR-92
	978.4775	977.4682	85-DSLEIV**M***R-92

106-124	2179.9869	2178.9796	106-GLINDPHMDHSFDINEGLR-124
	2195.9868	2194.9795	106-GLINDPH**M***DHSFDINEGLR-124
251-273	2402.1860	2401.1788	251-EGLINAGLIPSIMIDFSHANSSK-273
	2418.1803	2417.1731	251-EGLINAGLIPSI**M***IDFSHANSSK-273
278-294	1820.7990	1819.7918	278-QMEVATDVSTQLSQGDR-294
	1836.7998	1835.7925	278-Q**M***EVATDVSTQLSQGDR-294
295-322	3000.5833	2999.5760	295-SITGVMIESHLVEGNQNLESGEPLVYGK-322
	3016.5833	3015.5769	295-SITGV**M***IESHLVEGNQNLESGEPLVYGK-322

M*- Modified methionine residue into methionine sulfoxide, **#** - Peptide sequences were identified further from MS/MS spectrum of selected peptides.

Furthermore, we also located the modified methionine residues in peptides by tandem mass spectrometry where the amino acid sequences of the released peptides were analyzed through the generated y and b type ions series. The MS/MS spectrum (MS^2) of non-oxidized peptide of 2179.908 Da depicted b8 (m/z 878.419) and y12 (m/z 1433.586) whereas spectrum of oxidized peptide of 2195.933 Da depicted the b8 (m/z 894.176) and y12 (m/z 1449.576) ions series. The ion series of non-oxidized peptide 2179.908 Da indicated that no methionine residue was oxidized (Figure 2.7A). Whereas the presence of b8 (m/z 894.176) and y12 (m/z 1449.576) ion series in ~21965.933 Da peptide with an increment of 16 Da ions conspicuously indicated the oxidation of Met113 in "106-GLINDPH**M***DHSFDINEGLR-124" peptide sequence (Figure 2.7B). Similarly, the MS^2 spectrum of ~3000 Da non-oxidized peptide and ~3016 Da oxidized peptide represented, b6 (m/z 589.146) and y23 (m/z 2543.237) ion series and b6 (m/z 605.296) and y23 (m/z 2559.532) ion series, respectively (Figure 2.8A & 2.8B). The ion series of 3016

Da also confirmed the oxidation of Met300 in "295-SITGV**M***IESHLVEGNQNLESGEPLVYGK-322" peptide sequence. In addition, the neutral loss of 64 Da from precursor ion due to the elimination of methane sulfonate (CH_3SOH) from the side chain of methionine (Figure 2.7B & 2.8B) and detection of immonium ion (120) were identified in the Mascot search engine inspection. In the MS^2 spectrum, loss of CH_3SOH (-64 Da) and detection of immonium ion (120) are unique characteristics which confirm the presence of methionine sulfoxide (MetSO) [255]. Additionally, in redox metal treated PaDAH7PS-Homox*****, the peptide mass fingerprinting analysis not showed any methionine containing peptides. This might be attributed to the limited proteolytic cleavage of higher oligomeric state. In contrast, the peptide map and level of oxidation of PaDAH7PS-Dimox***** were similar to the PaDAH7PS-Diox (Table 2.3). Thus, the mass spectra of all PaDAH7PS states have evidently shown a varied degree of oxidation under different purification conditions.

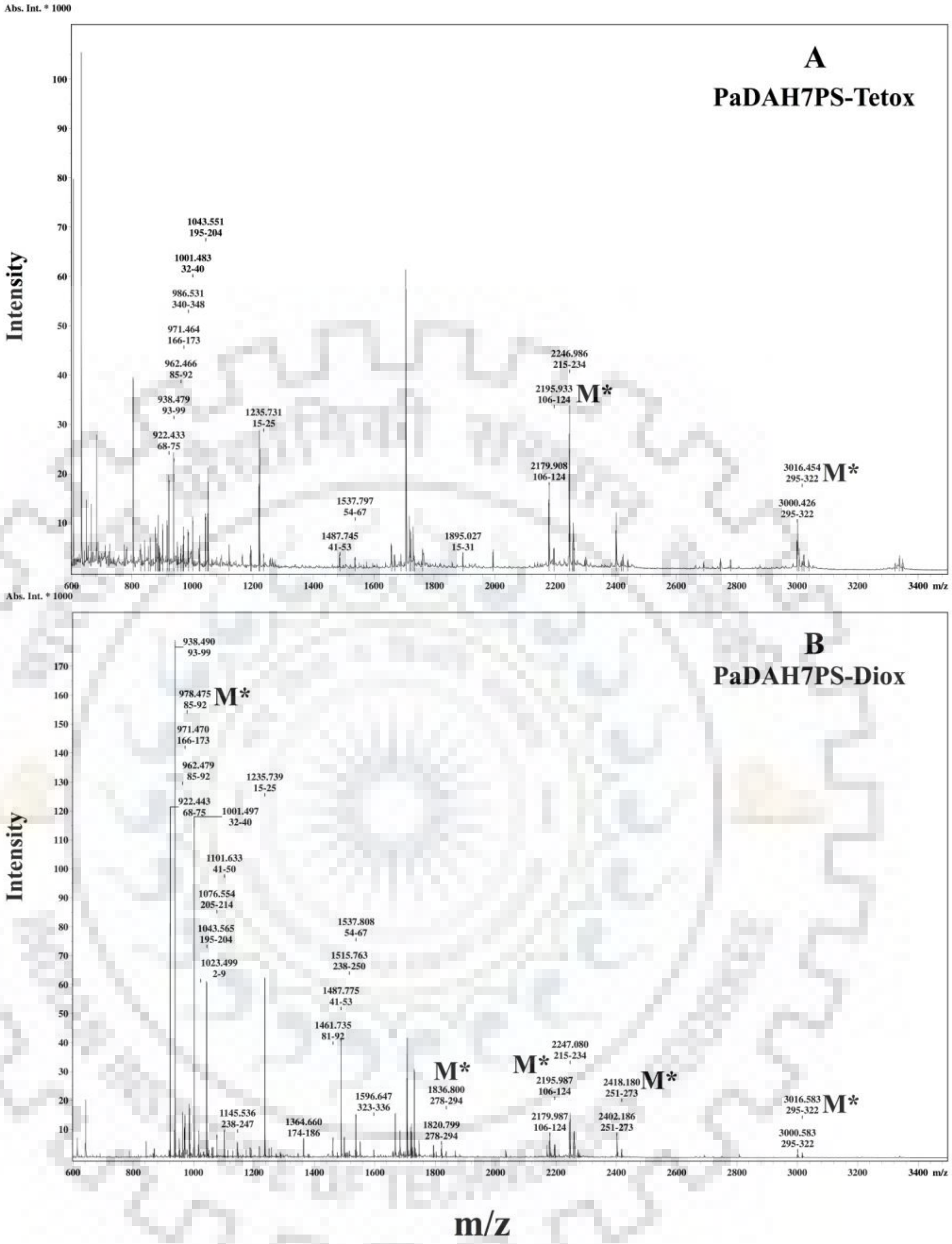

Figure 2.6: Mass spectrometric analysis of PaDAH7PS. (A) PMF of PaDAH7PS-Tetox obtained by tryptic digestion. **(B)** PMF of PaDAH7PS-Diox obtained by tryptic digestion; The increment of 16 Da indicated the oxidation of these peptides.

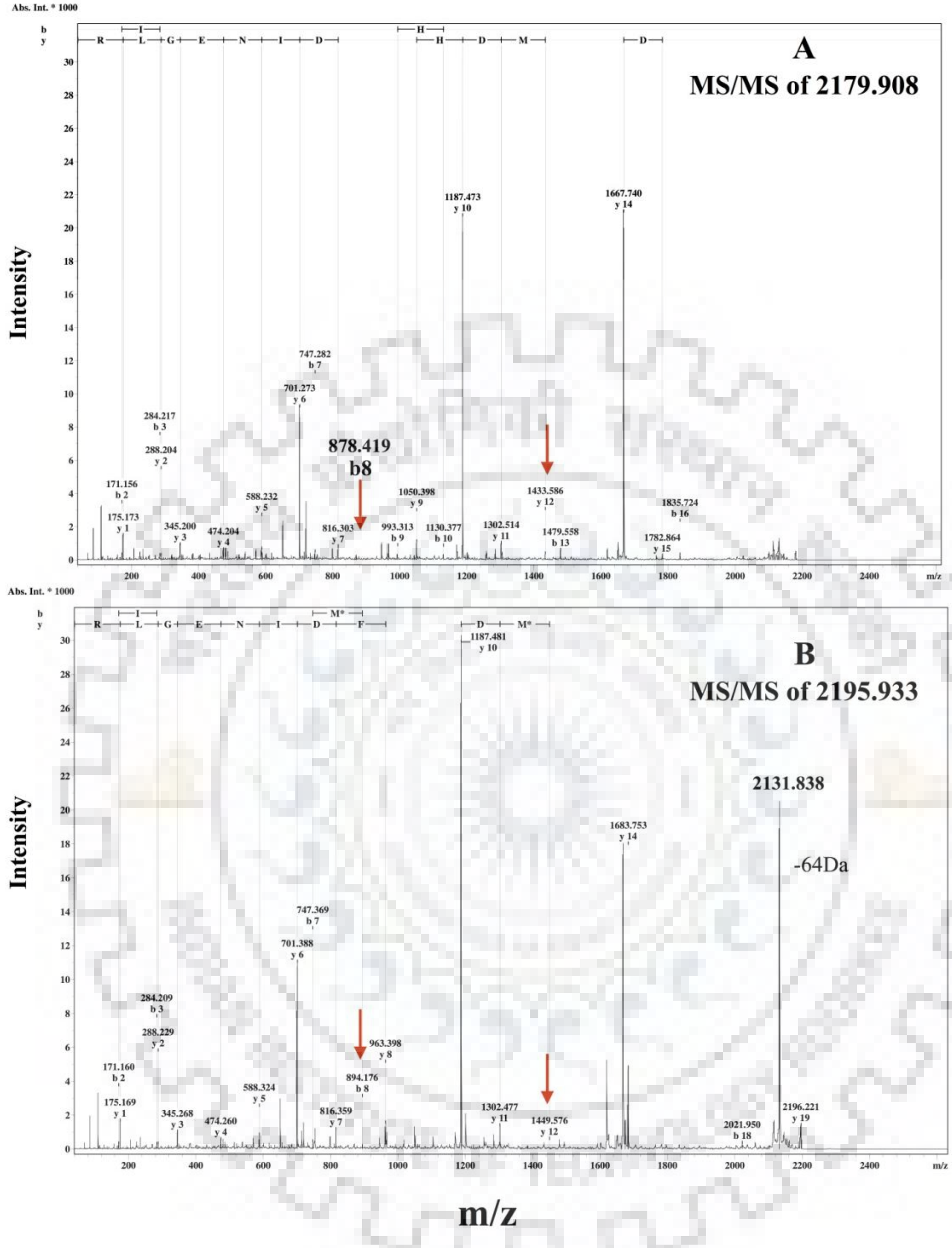

Figure 2.7: (A) MS/MS spectrum of 2179.908 Da peptide. **(B)** MS/MS spectrum of 2195.933 Da peptide; The neutral loss of 64 Da in the spectrum is a valuable fingerprint and detection of immonium ion (120) in Mascot search is also the unique characteristic of methionine oxidation.

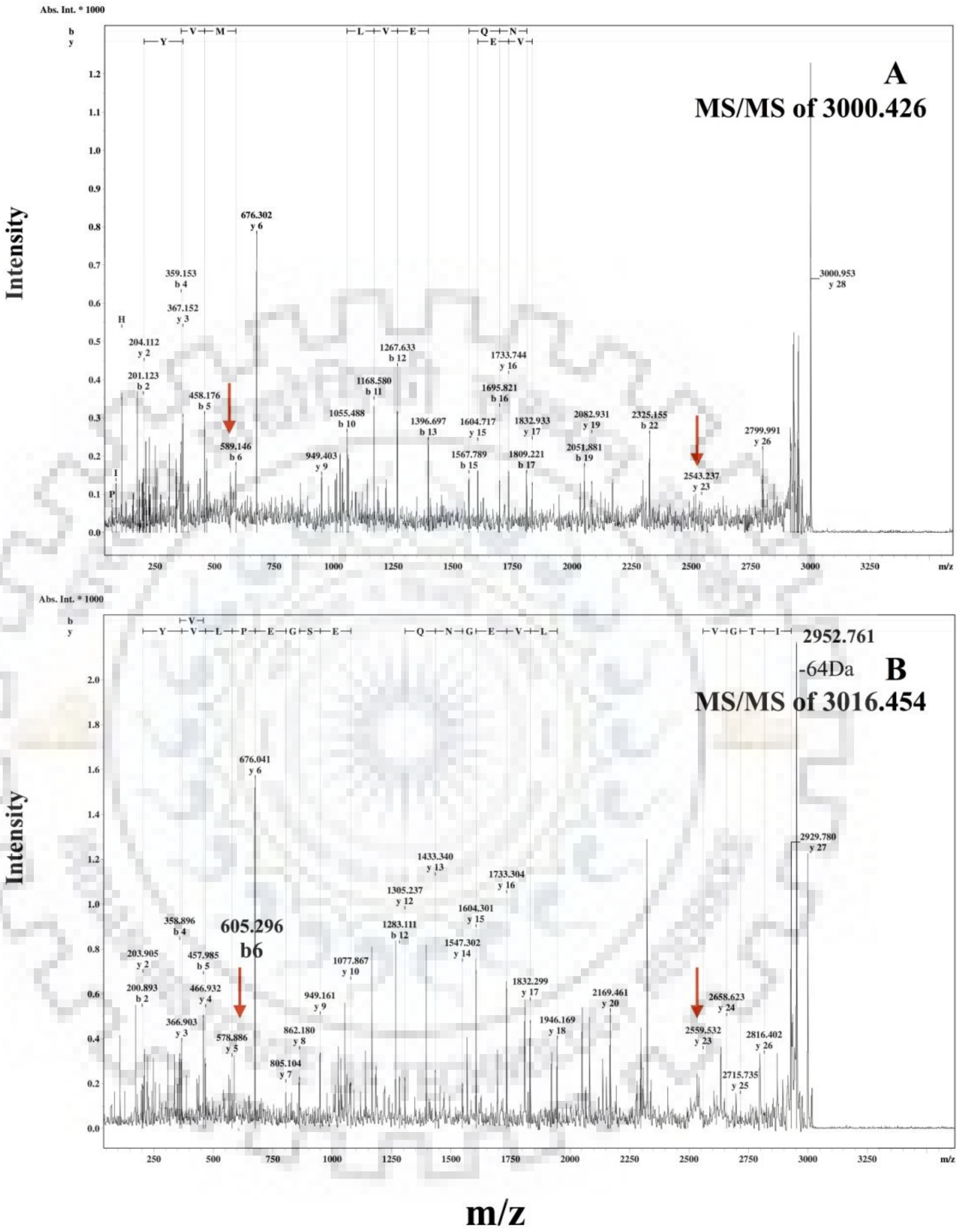

Figure 2.8: (A) MS/MS spectrum of 3000.426 Da peptide. **(B)** MS/MS spectrum of 3016.454 Da peptide.

2.3.5 Enzymatic activity of different oligomeric states of PaDAH7PS

Oligomerization of enzymes is an essential feature, which enables the core biological activity and also facilitates the scaffolds for allosteric regulation of a few proteins, including DAH7PS [256, 257]. As the oxidative modification of a protein can alter its specific function, we checked the enzymatic activity of all oligomeric states of PaDAH7PS. The PaDAH7PS-Hexnox had the highest activity, whereas the PaDAH7PS-Tetox showed ~ 20% relative enzymatic activity. Contrastingly, PaDAH7PS-Diox and redox metal catalyzed oxidized oligomeric forms possessed negligible activity (Figure 2.9A). Furthermore, the kinetics parameters for PEP and E4P (K_m, K_{cat}, V_{max}, k_{cat}/K_m) of the most active state of PaDAH7PS were also determined and compared with other Type I DAH7PS (Figure 2.9B & 2.9C). The kinetic parameters of PaDAH7PS-Hexnox are represented in the (Table 2.4).

Table 2.4 Comparison of kinetic parameters of PaDAH7PS-Hexnox oligomeric state with its homologs.

DAH7PS from Organisms	**K_m^{PEP} (μM)**	**K_m^{E4P} (μM)**	**k_{cat} (s^{-1})**	**k_{cat}/K_m^{PEP} ($s^{-1}\mu M^{-1}$)**	**k_{cat}/K_m^{E4P} ($s^{-1}\ \mu M^{-1}$)**
PaDAH7PS	48.49 ± 3.12	256.8 ± 18.15	7.81± 0.89	0.161	0.030
EcDAH7PS	80	900	ND	ND	ND
NmDAH7PS	11 ± 1	43 ± 4	25.5 ± 0.5	2.3	0.59

ND- Not Determined, NmDAH7PS-*Neisseria meningitidis* DAH7PS

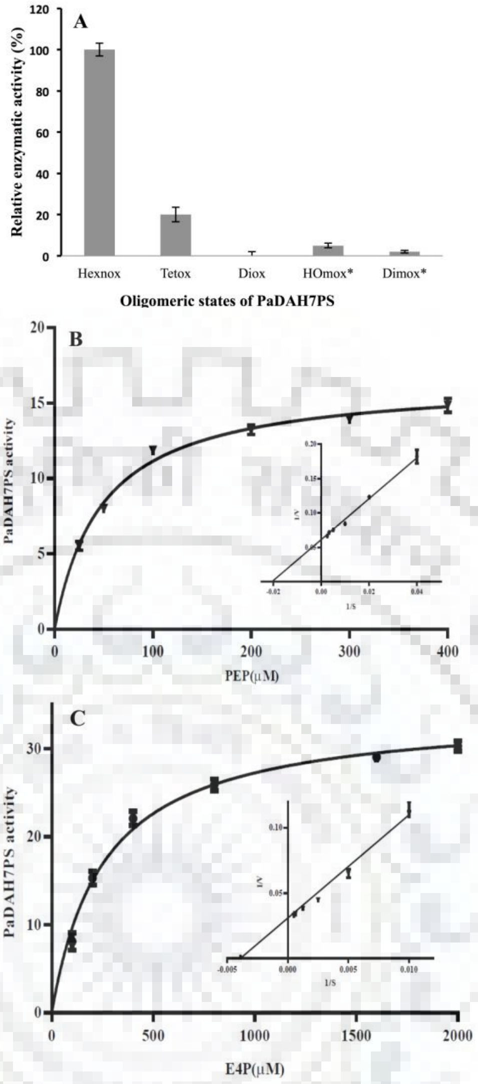

Figure 2.9: (A) Enzyme activity in different oligomeric forms of PaDAH7PS. **(B & C)** Michaelis-Menten kinetic parameters calculated for the both substrates, PEP and E4P, respectively. Each of these values is average of three independent measurements. Insets show the double reciprocal plot for respective substrates.

2.3.6 Morphological studies of different oligomeric forms of PaDAH7PS

Atomic force microscopy is a well-suited technique to detect the topographical features, oligomeric nature, and various types of intermediate structure formation during protein folding/unfolding, aggregation and fibrillation [258-260]. The morphologies of the PaDAH7PS oligomeric species were visualized using AFM to get the detailed information. The PaDAH7PS-Hexnox showed the spherical/globular shape particles and the PaDAH7PS-Tetox contained the heterogeneous particles with varied length, height, and shapes (Figure 2.10A & 2.10B). The magnified 3D images of the nephroid, trefoil, and quardifoil shapes have been shown in figure 2.10C, 2.10D, & 2.10E, respectively. Interestingly, PaDAH7PS-HOmox***** clearly exhibited amorphous aggregate type structures, which might be an outcome of the association of the destabilized/dissociated-oxidized species (Figure 11A & 11B).

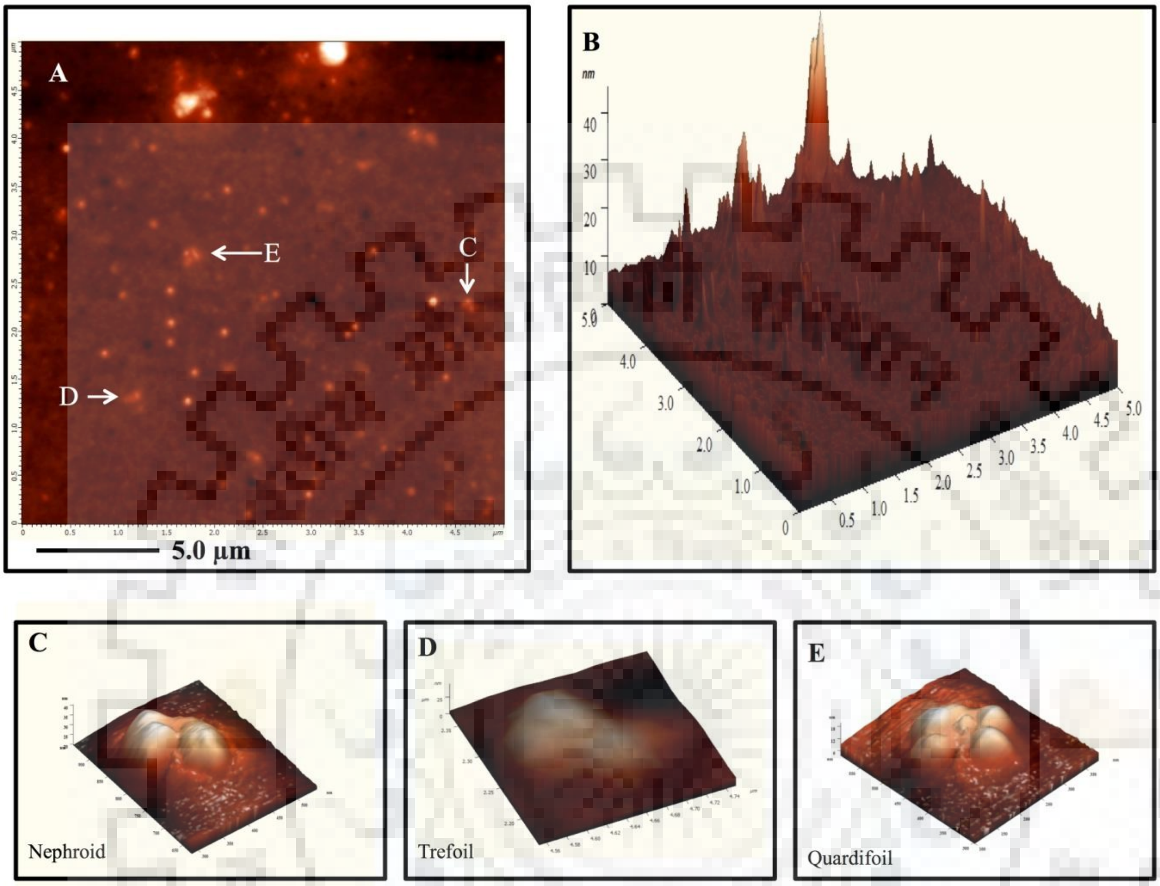

Figure 2.10: (A) AFM 2D image of PaDAH7PS-Tetox form of protein; different shape like neproid, trefoil, and quardifoil which are indicated by the white arrows and presence of these different forms suggest that protein aggregates on oxidation. **(B)** 3D image profile of the PaDAH7PS-Tetox form. **(C, D, & E)** Panels showing the 3D profile of the nephroid, trefoil, and quardifoil, respectively. The scale bar has shown at the bottom of image.

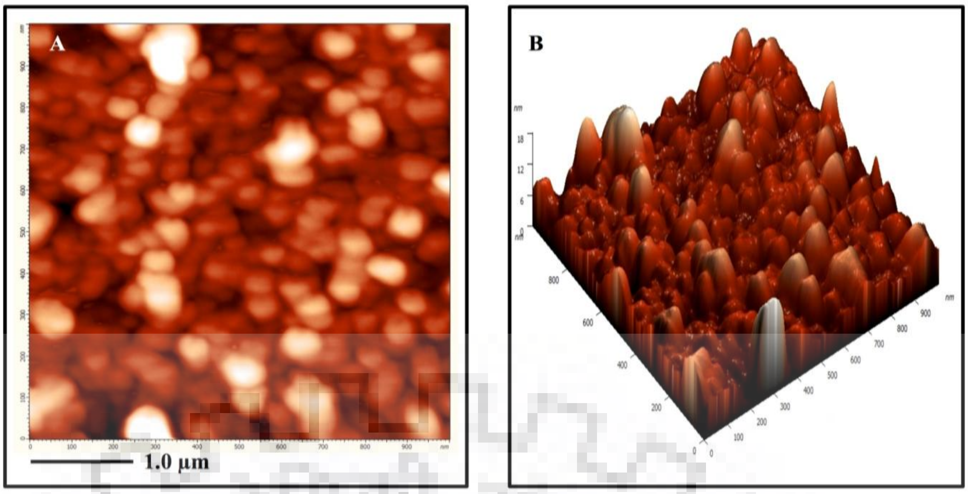

Figure 2.11: (A) AFM 2D image of PaDAH7PS-HOmox* form of protein showing the amorphous aggregates. **(B)** Showing 3D profile of the amorphous aggregates. The scale bar is shown at the bottom of image.

2.3.7 Monitoring the changes in secondary structures of different oligomeric forms of PaDAH7PS

The changes in secondary structure of different oligomeric states of PaDAH7PS were elucidated by comparing their far-UV CD spectra as presented in the figure 2.12A. The most active PaDAH7PS-Hexnox state, exhibited two minima at 208 nm and 222 nm and a single maxima at 195 nm which indicated the α/β secondary structure, as expected, which is consistent with the other characterized DAH7PS [88, 98]. As the PaDAH7PS-Tetox showed the similar CD spectrum so the ratio of ellipticity $[(\theta)_{208}/(\theta)_{222}]$, which basically depends on the secondary structural elements packing of a protein, was also determined. Remarkably, the values acquired by PaDAH7PS-Hexnox and PaDAH7PS-Tetox were 0.9 and 1.09 respectively. The value 1.09 being closer to the range (1.1-1.4), illustrates a feature unique to the partially folded state of PaDAH7PS. In contrast, the CD spectrum of PaDAH7PS-HOmox***** depicted a peak at ~203 nm and a significant reduction (~55%) in ellipticity at 222 nm (Figure 2.12B). This suggests the presence of the random coil conformation and loss in the helical content of protein [248, 261].

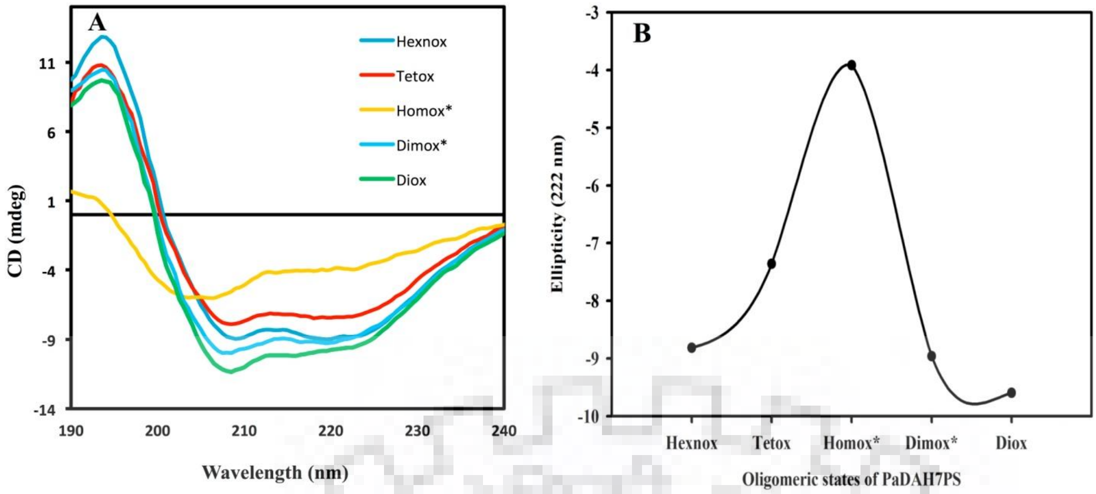

Figure 2.12: (A) Far-UV CD spectra comparison of different oligomeric states of PaDAH7PS. **(B)** Changes observed in ellipticity at 222 nm in different oligomeric states; A significant loss in ellipticity was noticed in PaDAH7PS-HOmox * form which suggests that enzyme has lost its helical structure content.

The ratios of ellipticity [$(\theta)_{215}/(\theta)_{222}$] and [$(\theta)_{205}/(\theta)_{222}$] of all states of PaDAH7PS were also measured to validate the emergence of β-content and enhancement in disorderness, respectively (Table 2.5). When PaDAH7PS-HOmox* was compared to PaDAH7PS-Hexnox, a noteworthy increment in both the values of the ratios of ellipticity was observed (Table 2.5). Thus, the increment in the β-structure and random coil conformation content on methionine oxidation is probably associated with the aggregation of PaDAH7PS as also reported in earlier studies on aggregation of proteins [258, 262, 263].

Table 2.5 Secondary structure content of different oligomeric states of PaDAH7PS.

Oligomeric State of PaDAH7PS	**Helical content (%)**	**β-content (%)**	**Random Coil (%)**	**[$(\theta)_{215}/(\theta)_{222}$]**	**[$(\theta)_{205}/(\theta)_{222}$]**
Hexnox	~21	~27	~52	0.9472	0.7411
Tetox	~17	~31	~52	0.9766	0.8214
Diox	~19	~27	~54	1.0440	1.5160
HOmox*	~9	~42	~49	0.9998	0.9210
Dimox*	~17	~30	~53	1.0584	0.9724

2.3.8 Fluorescence spectroscopic characterization of different oligomeric states of PaDAH7PS

Furthermore, the fluorescence spectroscopy was also performed to analyze the tertiary structural perturbation in all oligomeric states of PaDAH7PS. The intrinsic emission spectra of Trp (λexc=295 nm) residues in all PaDAH7PS oligomeric states were analyzed. The comparative modeling of the PaDAH7PS monomeric structure revealed the existence of total four Trp104, Trp331, Trp159, and Trp215 residues. Between these Trp104 and Trp331 were surface exposed while Trp159 was located inside the barrel of PaDAH7PS (data not shown). The intrinsic fluorescence spectra of PaDAH7PS-Hexnox, PaDAH7PS-Tetox, and PaDAH7PS-Diox depicted maximum emission at λmax=346.5 nm, which suggests that the Trp residues are exposed to the hydrophilic environment [264]. Notably, PaDAH7PS-Homox* and PaDAH7PS-Dimox* exhibited a red shift of 6.5 nm and 1 nm, respectively, and a concomitant loss was detected in fluorescence intensity of PaDAH7PS-HOmox*(Figure 2.13A). The aforesaid red shift indicated that more exposure and interaction of Trp residues occurred with the solvent on oxidation. Thus the occurrence of conformational changes in PaDAH7PS, as denoted by the above analysis, resulted in the alteration of the hydrophobic core of the protein. Moreover, we also probed the nature of partially folded and unfolded states of PaDAH7PS using Anilino-naphthalene-sulfonic acid (ANS) binding dye (λexc=380 nm) (Figure 2.13B). A few plausible hydrophobic sites are present in PaDAH7PS structure, which can accommodate the extrinsic ANS dye owing to which, PaDAH7PS-Hexnox (folded form) contributed noticeably to the fluorescence intensity with ANS. The PaDAH7PS-Tetox exhibited highest intensity of all oligomeric states due to the strong binding of ANS, suggesting the generation of a partially folded state with a destabilized hydrophobic core. In contrast, the PaDAH7PS-Homox* and the PaDAH7PS-Dimox* showed negligible fluorescence intensity, as expected, due to less binding of ANS in more unfolded state of a protein (Figure 2.13B).

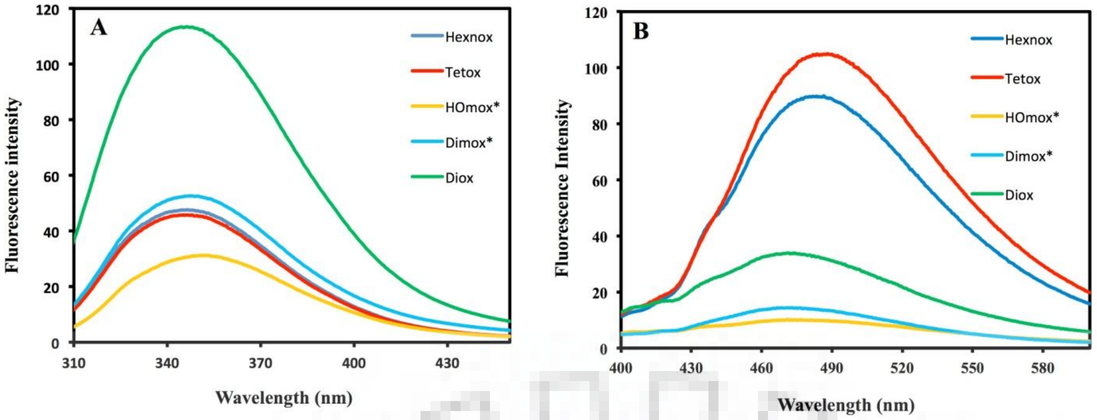

Figure 2.13: (A) Intrinsic Fluorescence spectra of different oligomeric states of PaDAH7PS; change in Trp fluorescence intensity was measuered at (exc = 295 nm). **(B)** Extrinsic fluorescence spectra of different oligomeric states of PaDAH7PS and change in ANS fluorescence intensity of at (exc = 380 nm) was measured.

2.3.9 ThT binding study of different oligomeric states of PaDAH7PS

The ThT binding study of all forms of PaDAH7PS was analyzed to clarify the presence of the amyloid fibrils. In figure 2.14A, the PaDAH7PS-Hexnox, showed almost negligible increment in the fluorescence intensity of ThT. Intrestingly, PaDAH7PS-Tetox, PaDAH7PS-Diox and PaDAH7PS-Dimox***** states depicted more ThT binding intensity as compare to the PaDAH7PS-Hexnox. This may be occurred due to the presence of exposed hydrophobic surface with high β-content in these intermediates partial folded/unfolded states of PaDAH7PS. The PaDAH7PS-HOmox***** exhibited the lowest binding with the ThT. ThT dye, basically interacts with a core cross β-sheet ordered structures present like in the amyloid fibrils. But in PaDAH7PS the partially folded and unfolded intermediates states might be rapidly interacted between their hydrophobic surfaces and self- associated with intermolecular β ladders, which have no long range order like amyloid fibrils and thus enhanced the process of amorphous aggregation rather than fibrillation.

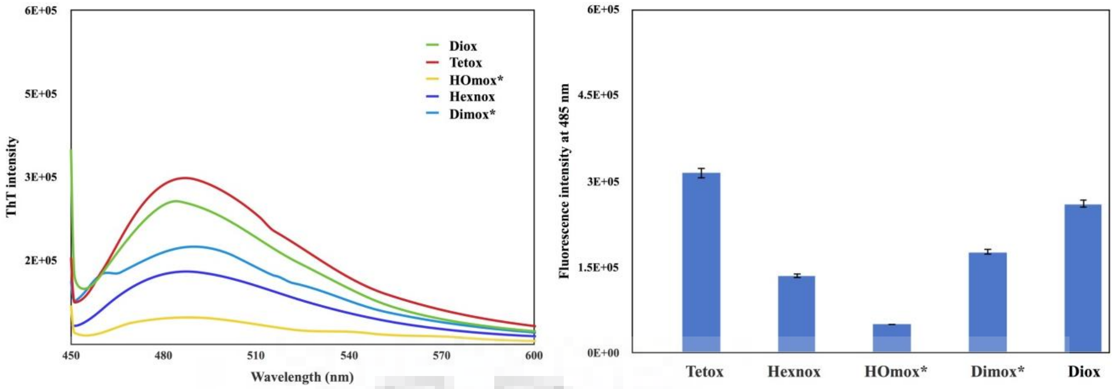

Figure 2.14: (A) ThT binding assay; ThT fluorescence spectra of all oligomeric states of PaDAH7PS. **(B)** Fluorescence intensity of ThT at 485 nm with all oligomeric states is represented in bar diagram.

2.4 Discussion

The DAH7PS, a well-characterized enzyme from different sources, has shown more diverse quaternary structures and allosteric control. The evolution of quaternary structures of DAH7PS is fundamentally connected with their uniquely controlled allosteric mechanism [229]. The evolutionary link between different types of DAH7PS enzymes has been determined on the basis of various properties such as metal requirement, substrate specificity, and allosteric regulation [80]. In the present study, PaDAH7PS, sequentially homologous (~79% identity) to homotetrameric EcDAH7PS, contains conserved active site and divalent metal binding site residues [88]. The purified PaDAH7PS exhibits a functional hexameric state rather than the tetrameric state, as in EcDAH7PS, which is shown by size exclusion chromatography, native-page, glutaraldehyde cross-linking [265].

In vitro, instability of EcDAH7PS due to redox metal oxidation is prevented by binding of substrate (PEP) at the active site of DAH7PS and the restoration of thiol (-SH) content is achieved by reducing agent (DTT) [99]. Surprisingly, even in the presence of both the protecting agents (PEP & DTT), the quaternary structure of PaDAH7PS destabilizes into a tetrameric oxidized state (PaDAH7PS-Tetox) with less enzymatic activity. But when both the protecting agents are absent, the protein oxidizes and transforms into an inactive dimeric state (PaDAH7PS-Diox). Moreover, during redox metal treatment, PaDAH7PS does not dissociates completely into a monomeric state, as found in EcDAH7PS, but converts into an unexpected higher oligomeric form (PaDAH7PS-HOmox*) and an oxidized dimeric form (PaDAH7PS-Dimox*).

Proteins are the more susceptible targets for oxidation in biological systems due to their low redox potential [266, 267]. Methionine, cysteine, and histidine are the most vulnerable amino acid residues to get oxidized in the presence of oxidative stress [254, 268]. In PaDAH7PS, the oxidation of methionine residues to methionine sulfoxide is seen through FTIR spectroscopy where the absorption bands are seen in the fingerprinting region due to the stretching vibration of the sulfoxide (S=O) group. Similarly methionine oxidation in human serum albumin, RNase, and other therapeutic proteins has been detected by FTIR spectroscopy [269-271].

The susceptibility of methionine residues for oxidation depends on their location in the three-dimensional structure of a protein and their solvent accessibility i.e., the more surface exposed residues are more labile for oxidation [254]. In mass spectrometry analysis PaDAH7PS-Tetox, Met113, located on the surface of the protein, as well as Met300, located inside the barrel closer to the active site of the protein, are oxidized. Whereas, in PaDAH7PS-Diox and PaDAH7PS-Dimox* five methionine residues (Met91, Met113, Met263, Met279, and Met300) that get oxidized. Thus, the degree of susceptibility of methionine residues for oxidation increases due to redox metal treatment. The generation of the unexpected higher oligomeric state as well as the oxidation of methionine residues occurs in PaDAH7PS, which is in contrast with the feature of EcDAH7PS, where an inactivated monomeric state with oxidized cysteine residues was depicted. Thus, the unpredicted oxidation of methionine residues with increment in the degree of oxidation and the generation of high oligomeric state encouraged us to further insight the effects on the morphological features, as well as secondary and tertiary structural changes in PaDAH7PS during stress conditions.

Oxidative modifications in proteins usually affect their conformational stability, which can further induce the aggregation and fibrillation process [267, 272, 273]. Additionally, the atomic force microscopic analysis of all forms of PaDAH7PS reveals the presence of amorphous aggregates formation under oxidative stress conditions. Similarly, the oxidation of methionine residues in the light chain of immunoglobulin and other therapeutic proteins also provoked amorphous aggregation [274, 275]. Methionine oxidation also promotes the process of fibrillation in apolipoprotein A-I [276] and k-Casein [277]. In Parkinson and Alzheimer diseases, the metal-triggered oxidation of methionine residue resulted in the formation of fibril and amyloid β-plaques, respectively [278-281]. Methionine oxidation is also considered as the triggering agent for the cascade of principal events occurs during PrP misfolding and formation of various toxic β-sheet rich species in the several prion associated diseases [282, 283]. In contrast, the fibrillation of α-synuclein, transthyretin, and apolipoprotein C-II was inhibited due to the methionine oxidation [284-286]. Therefore, it suggests that methionine oxidation affects the behavior of different proteins in multiple ways.

The protein aggregation is a critical aspect which is affected by several intrinsic and extrinsic factors [287-290]. The partially folded, unfolded, and misfolded states of a protein can lead to the process of aggregation [291-293]. Generally, protein tends to show the higher beta structure which is responsible for the nucleation process of aggregation [237, 294]. Similarly, in the far-UV CD spectra analysis, ratio of ellipticity $[(\theta)_{208}/(\theta)_{222}]$ acquired value1.09 and high binding affinity for ANS of PaDAH7PS-Tetox which clearly indicates that it possesses a unique feature of the partially folded state, which might have caused the oxidation of unexposed methionine residue i.e. Met300, located inside the hydrophobic core of the protein [295-297]. PaDAH7PS-HOmox*, PaDAH7PS-Dimox*, and PaDAH7PS-Diox unveil the clear emergence of β-content in CD spectra [298, 299]. Remarkably, the lack of tertiary structure and reduced binding affinity with ANS in the above three oligomeric states indicate the more unfolding of PaDAH7PS, which increase the degree of its oxidation and aggregation propensity. The ThT binding assay results also supported that the partially folded and unfolded intermediates states might be rapidly interacted between their hydrophobic surfaces and self-associated enhanced the process of amorphous aggregation [298]. Thus, PaDAH7PS significantly shows the methionine modifications, conformational changes, perturbation of hydrophobic core, and enhancement in the propensity to aggregate in oxidative stress conditions.

2.5 Conclusion and future perspectives

In this study, we have shown that PaDAH7PS is functional in its hexameric state, which is susceptible to metal-catalyzed oxidation. Here, for the first time, we have identified that methionine residues are vulnerable to oxidation during stress conditions rather than active site cysteine residues in PaDAH7PS. The quaternary structure of PaDAH7PS destabilizes and attains a partially folded and unfolded state with high β-content. These presumably act as the critical precursors, which enable specific intermolecular interactions responsible for the aggregation. To elucidate the molecular mechanism and kinetics of the aggregation process of PaDAH7PS, further studies are required.

CHAPTER 3

STRUCTURAL CHARACTERIZATION OF DAH7PS FROM *PROVINDENCIA ALCALIFACIENS* (PaDAH7PS)

3.1 Introduction

DAH7PS enzyme of the shikimate pathway is considered as a potential drug target. The structure determination of DAH7PS from different organisms will be helpful for the development and designing of antibacterial agents [219]. *Providencia alcalifaciens,* a Gram-negative bacterium belongs to the family Enterobacteriaceae [238]. Similar to *Escherichia coli, P*. *alcalifaciens* genome also encodes three isoforms of the DAH7PS enzyme, which can be feedback regulated by end products (Phe, Tyr, and Trp) of the pathway.

Our main goal of the project on DAH7PS enzyme from the *Providencia alcalifaciens* was to crystallize and determine the 3D structure of PaDAH7PS. Initially, despite of our several attempts have been taken to crystallize PaDAH7PS, we were not able to get its crystalized. But after some experimental studies carried out on PaDAH7PS protein as mentioned in the previous chapter [300]. We found that purified PaDAH7PS is not a stable and homogenous protein in *in-vitro* conditions. PaDAH7PS was showing oxidation of methionine residues which further leaded to the amorphous aggregation of protein.

The biochemical activity assay and gel-filtration chromatography results have shown that PaDAH7PS is most active and functional in its hexameric state. PaDAH7PS is also found susceptible to metal-catalyzed oxidation as mentioned in the previous chapter. We found that PaDAH7PS-Hexnox (non-oxidized hexameric state) was the most active and homogeneous form of the protein purified with the substrate (+ PEP) and reducing agent (+ DTT) [300]. Therefore, to crystallize and determine the structure of the PaDAH7PS, we decided to purify it in the same conditions and also tried to prevent and reduced the oxidation process for maintaining the homogeneity and stability of protein during the process of crystallization.

In the current chapter, we have crystallized the PaDAH7PS in the native form after trying and optimizing several crystallization conditions. Further, we have investigated the structural features of native PaDAH7PS using the X-ray crystallography. Moreover, we have compared the native structure of PaDAH7PS with the earlier reported native DAH7PS and complexed DAH7PS structures with the metal, substrate, and allosteric inhibitor.

3.2 Materials and methods

3.2.1 General procedure for crystallization

The most stable and homogenous oligomeric state of PaDAH7PS protein (PaDAH7PS-Hexnox) obtained after the size exclusion chromatography step was used for its crystallization. Additionally, concentration of substrate (PEP) and reducing agent (DTT) was also properly maintained in the size exclusion chromatography running buffer to prevent the oxidation of PaDAH7PS. PaDAH7PS was concentrated by centrifugation (Amicon concentrators) up to the 10 mg/mL. All the initial crystallization trials were performed at 20 °C and all crystal trays were checked periodically under the microscope.

3.2.2 Initial crystallization trials and optimization of crystal conditions

Initially, all crystallization trials of PaDAH7PS were performed manually using the sitting drop method at 20 °C. A total of 576 crystallization conditions from pre-formulated crystal screens Crystal I & II, PEG_{ion}/PEG_{RX}, $Salt_{RX}$ I & II, Index I & II, JCSG I & II, Morpheus I & II provided by the Hampton Research, (USA) were used in the initial crystallization trials of PaDAH7PS. We have taken 100 µl of each solution and filled it into the reservoir wells of 96-well protein crystallization plates (Corning® Crystal*EX* 96 Well Crystallization plates) from the Hampton Research (USA). After this, concentrated protein sample and solution from the reservoir well in the 1:1 ratio were filled and mixed into the small upper wells of the 96-well plates. The trays were then sealed with an optically clear and UV compatible 3 inches tape (Crystal Clear Sealing Tape, Hampton research) and kept in a shock-proof chamber with maintained temperature at the 20 °C.

Moreover, crystallization trials for PaDAH7PS were also performed using the hanging drop method in the 24-well trays (VDX Plate without sealant, Hampton Research, USA). The top of all wells was lined with (Dow Corning® 7 Release Compound Grease) grease (Hampton Research USA) and 500 µl of precipitant solution was added into all wells. A small volume of the purified PaDAH7PS (2 µl) was added on a siliconized glass coverslip and 2 µl of mother liquor solution was also added and mixed properly. After this, all siliconized glass coverslips were inverted and gently pressed on top of the pre-greased wells. Trays were kept in the shock-proof chamber at the 20 °C. The promising crystallization conditions obtained from the initial trials were identified and optimized by altering the concentration and pH of different constituents used as the precipitant and buffer solutions.

3.2.3 Preparation of PaDAH7PS crystals for the data collection

The obtained crystals of PaDAH7PS were then transferred to a 5 μl drop of mother liquor solution containing 20 % v/v glycerol as a cryoprotectant agent using cryo-loops (Hampton Research, USA). PaDAH7PS crystals were incubated with this solution for ~30-40 sec and immersed into liquid nitrogen (-196 °C) and further transferred and packed into a crystals carrying dewar (-196 °C).

3.2.4 X-Ray diffraction data collection and processing

The diffraction data of PaDAH7PS were collected at the European Synchrotron Radiation Facility (ESRF) using BM14 beamline (Grenoble France). The data were indexed and scaled using the program, XDS, HKL 2000 and CCP4 [301, 302]. Output was examined and re-scaled to optimize Rmerge, I/σi, values, and data completeness.

3.2.5 Overview of structure modeling and refinement

For the structure solution, all reflections were indexed, integrated, and scaled using the HKL2000 program suite [302-304]. The PaDAH7PS crystal belongs to space group $P2_1$, the corresponding refinement statistics are shown in table 3.1. The initial phases for PaDAH7PS were obtained by molecular replacement with MOLREP of the CCP4 suite [305] by using a monomer of EcDAH7PS structure (PDB ID 1N8F, Chain A) as the search model [306]. The reflections within the resolution range 82.7-3.3 Å were selected for refinement. The rigid body refinement was followed by iterative cycles of restrained atomic parameter refinement including TLS refinement with REFMAC5 [307, 308] and PHENIX [309]. The repetitive cycles of model rebuilding based on σA-weighted 2Fo-Fc and Fo-Fc maps were performed by employing COOT [310, 311].

The water molecules were added in the peaks contoured at 3σ in the Fo-Fc difference Fourier map which simultaneously satisfying density contoured at 1σ in the 2Fo-2Fc map. Several rounds of refinements and model rebuilding were used until an acceptable R_{cryst} and R_{free} were achieved. The stereochemical attributes of refined model were validated by using the program PROCHECK [312] and refinement statistics are also presented in table 3.1. The statistics of the Ramachandran plot distribution shows 97.0 % residues in the most favored regions with 0.085

% outliers. The structure-model figures of this chapter are prepared with PyMOL [313].

3.2.6 Structure determination of PaDAH7PS

3.2.6.1 Matthew’s coefficient

The MATTHEWS_COEF program available within the CCP4 suit was used to determine the number of monomeric subunits in the asymmetric unit [314]. The number of the subunits in an asymmetric unit was selected on the basis of the solvent content.

3.2.6.2 Molecular replacement

Molecular replacement method (MR) for the structure determination can be used when a structure of a homologous protein is already available and deposited in the Protein Data Bank. A homologous structure has >25-30 % usually considered as a suitable model for the molecular replacement. The initial phases for PaDAH7PS were obtained by performing the molecular replacement with MOLREP of the CCP4 suite [315] and 3D structure from *E. coli* (PDB ID 1N8F Chain A) was used as the model [306].

3.2.6.3 Model building and refinement

The PaDAH7PS was modeled using PHASER within CCP4 [316] and automated building was performed using the PHENIX AutoBuild wizard [317]. The manual model building was performed within COOT [310]. The model was built into 2Fo-Fc and Fo-Fc maps contoured to 1σ and 3σ, respectively. The initial model is far from the final structure and it undergoes further various refinements to improve the phases and to maximize the agreement between model and observed X-ray data. Various parameters like atomic coordinates, atomic displacement parameters (ADPs), and scale factors were optimized until a best fit model was achieved between observed diffraction patterns and calculated one.

The model refinement of protein is commonly done by the most frequently used Refmac 5.0 (maximum likelihood refinement) within CCP4 suit [307] and the Phenix.refine (maximum likelihood refinement and simulated annealing) [309, 318, 319]. In both methods, restraints like bond angles, distances, torsions, and temperature (B-factors) were considered.

In maximum likelihood method, the phases are adjusted in order to minimize the R_{factor} values. In the simulated annealing, structure is heated virtually (i.e., temperature increment) to add randomness and slowly cooled and refined. The randomness reduced the probability of going into the wrong local minimum and it achieves a more optimal solution by allowing motion against the gradient. For cross-validation, the diffraction data is divided into two sets. (i) In a set 90 % data includes and comprises the large working set: (ii) 10 % remaining data comprises a small complementary test set. The data of the large working set is basically used for the refinement process. The cross-validation of structural refinement is monitored by the Rfree value which is calculated (in the same way as of the R_{factor} for remaining 5-10 % complementary test set. If the model is correct and errors are statistical R_{free} is expected to be close to the R_{factor} [320].

3.2.6.3.1 Refinement process with REFMAC5

REFMAC is a program to perform the rigid body refinement, TLS (translation libration and screw rotation) refinement, restrained refinement of the X-ray data. During the rigid body refinement, atoms kept fixed and whole structure is moved as the rigid body unit. And during the restrained refinement, all the bond lengths and bond angles should remain within a specified range of the value. REFMAC is a program within the CCP4 suite [321] and it refines the atomic model by adjusting models parameters like co-ordinates, B-factors, TLS etc in order to obtain a best fit in the experimental data. MTZ file containing a set of the observed structure factors and an initial atomic model obtained from the molecular replacement is needed as an input file for the refinement. Initially, a rigid body refinement was done and followed by the restrained refinement. The difference between the R_{factor} and R_{free} should not be greater than 5 % [311].

3.2.6.3.2 Refinement process with Phenix.refine

Phenix.refine is a refinement module within the PHENIX suite [309, 322]. Likely to the Refmac5, Phenix.refine also requires a structure factor file (i.e., input .mtz) and a PDB file of the initial model obtained after the molecular replacement. Refinement strategy includes XYZ coordinates, real-space, rigid body, TLS refinements. It also includes individual or group B-factors in refine strategy. A number of restraints like model restraints, secondary structures, and Ramachandran restraints can be imposed. If any ligand present in structure due to the complex formation, a crystallographic information file (CIF) of ligand is required for the input. It can be available in the ligand library of the PHENIX/CCP4, and ligands also can be generated through the eBlOW module of the PHENIX suite [309].

3.2.6.3.3 Model building with Crystallographic Object-Oriented Toolkit (COOT)

The PDB file containing the coordinates and the structure factor file (with Phase information) can be visualized in the Crystallographic Object-Oriented Toolkit (COOT) [302, 310]. In the COOT, we can visualize the Fourier map ($2F_O$-F_C) which appears in blue color. Difference map (F_O-F_C) consists of two types of the maps, one is positive contour map in which the structure fragments that are absent from the current model and needed to be built are shown in the green color by default. The other is negative contour map which indicates incorrectly placed atoms and display in the red color by default. Fourier map ($2F_O$-F_C) is contoured to 1σ to visualize the map in order to avoid while difference map is countered at the 2.5σ, where σ refers to the root mean square deviation (rmsd) in the mean density (electrons/3Å) in the maps. The water molecules were added in the peaks contoured at 3σ in the Fo-Fc difference Fourier map which simultaneously satisfying density contoured at 1σ in the 2Fo-2Fc map. After each cycle of the refinement, model was scrutinized and manual rebuilding was done by inspection of the Fourier map ($2F_O$-F_C) and difference map (F_O-F_C) electron density maps by using the model building software COOT [310, 311, 323].

3.2.7 Structural analysis and validation

The stereo-chemical attributes of refined PaDAH7PS model were further validated by using the PROCHECK program [312] and its refinement statistics are also presented in table 3.1. The statistics of the Ramachandran plot distribution showed the residues in the most favored regions with the outliers regions. The structure-model figures represented in the present chapter were prepared using PyMOL [313].

3.3 Results and discussion

3.3.1 Crystallization and structure solution of PaDAH7PS

After maintaining buffer conditions during the purification to prevent oxidation of PaDAH7PS and on variations in precipitant, salts, additives and different buffers with a wide range of pH (4.0-10.0) was scereened during crystallization. We obtained extremely tiny and quasi-crystals of PaDAH7PS in initial screening at acidic pH (4.5) citrate buffer, with PEG 3350, 1 mM substrate (PEP), 10 mM DTT as a reducing agent (Figure 3.1A). But, crystals obtained at acidic pH neither diffracted-well (at the low-resolution 12-7Å) nor the data were properly indexed during data processing step. So we were not able to collect the data of crystals obtained at the acidic pH. Subsequently, after several more attempts on crystal optimization, we got some crystals at basic pH (7.8) with ~10 mg/ml concentration of PaDAH7PS. This time also we obtained small plate-like crystals of PaDAH7PS instead of good quality 3D crystals. Furthermore optimization around these hit providing conditions and using TCEP as the reducing agent is resulted in the growth of some large plate-like but mountable crystals of PaDAH7PS (Figure 3.1B). These crystals were allowed to grow in full size over the course of four-five weeks and sent to the ESRF at BM14 beamline (Grenoble) for the data collection.

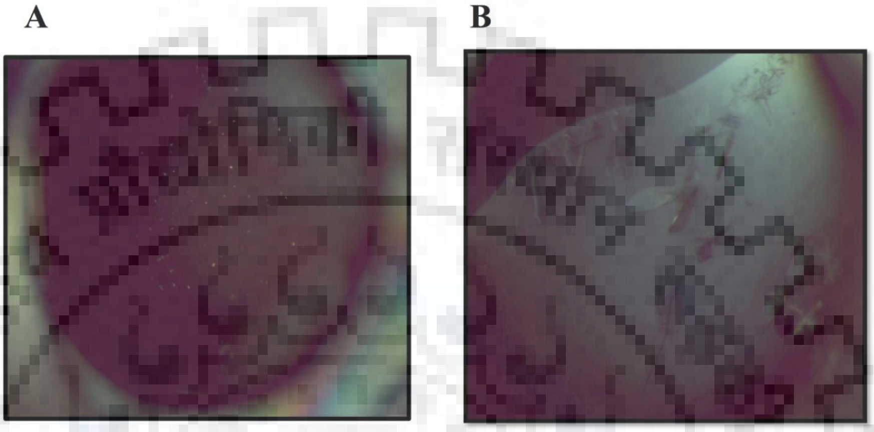

Figure 3.1: Crystals of PaDAH7PS obtained by the vapor-diffusion method. (A) Small crystal obtained at the acidic pH. **(B)** Plate-like crystals were obtained using Bis-Tris propane buffer pH (7.8) and 14 % w/v Polyethylene glycol 3500 as precipitants at 20 °C.

A plate-like crystal of PaDAH7PS was diffracted upto 3.3 Å resolution. The data were processed and scaled using autoproc program and a data set with 98.10 % completeness was collected. The crystal belongs to *P*1211 space group with unit cell parameters *a, b, c* = 54.55, 165.46, 77.08 and *α, β, γ* = 90, 106.5, 90. The calculated Matthew's coefficient assuming four molecules per asymmetric unit was 2.19 with a solvent content of 43.98 %. The data collection statistics of PaDAH7PS has shown in the table 3.1.

The initial phases were calculated by molecular replacement method using MolRep of the CCP4 suite [315] utilizing a monomer (Chain A) of the EcDAH7PS (Phe) (PDB ID 1N8F) structure as a search template [306]. The molecular replacement results showed wRFac 0.464, score 0.606, and contrast 9.08 and suggested one possible rotation and translation solution. This was also showing consistency with Matthew's coefficient calculation and predicted four molecules per asymmetric unit.

For the initial refinement, Refmac5 program of CCP4 was used and these solutions were subjected to rigid body refinement considering PaDAH7PS monomer as rigid body [307]. The resulting model from Refmac was used for subsequent refinement steps of simulated annealing, B-factor refinement, and minimization using Phenix Refine program of Phenix crystallography suite [309]. For the initial refinement starting temperature was set to 2500 K for simulated annealing whereas B-factor refinement and energy minimization were carried out on the default settings. The program was also used to calculate sigma-A weighted Fo-Fc and 2Fo- Fc difference maps. The 2Fo-Fc maps matched very nicely with the refined PaDAH7PS model which reflected its accuracy and high quality. The water molecules were added to the final model using Phenix solvent picking protocol that chooses peaks greater than 3σ in the Fo- Fc electron density maps. To verify the errors, all water molecules were inspected manually. The statistics of the Ramachandran plot distribution showed 95.6 % residues in the most favoured regions with 0.08 % outliers in the final model.

Table 3.1 Data collection and refinement statistic of PaDAH7PS.

Wavelength (Å)	0.87313
Resolution range (Å)	82.7 – 3.3 (3.4 – 3.3)
Space group	*P*1 21 1
Unit cell *a, b, c* (Å) *α, β, γ*	54.55, 165.46, 77.08 = 90, 106.5, 90
Unique reflections	18991 (1904)
Completeness (%)	99.33 (99.63)
Mean I/sigma(I)	11.43
Wilson B-factor	86.98
R-work	0.2102
R-free	0.2556
Number of protein residues	1195
Number of water molecules	18
RMS(bonds)	0.003
RMS(angles)	0.65
Ramachandran Favored (%) Allowed (%)	 95.6 4.2
Ramachandran outliers (%)	0.08
Average B-factor	75.2

3.3.2 Sequence characteristics of PaDAH7PS

The multiple sequence alignment of DAH7PS protein from *Providencia alcalifaciens was* performed with the *Escherichia coli, Neisseria meningitidis, Saccharomyces cerevesaeaie, Francisella tularensis* was performed (Figure 3.2). PaDAH7PS protein showed 79 % identity with DAH7PS from *Escherichia coli* and 65 % *Neisseria meningitides* and followed by the 54 % and 51 % identity with DAH7PS protein of *Saccharomyces cerevesaeaie, Francisella tularensis*, respectively.

The typical conserved motif of Type Iα family DAH7PS RxxxxxxKPRT, xGxR and DxxHxN motifs are highlighted in the boxes. Identical conserved amino acid residues are highlighted in red background and similar amino acid residues are highlighted in the yellow background. The positively charged residues Arg92, Lys97, Arg165, Lys186, Arg234, and His268 are also found conserved in PaDAH7PS, which are key residue for the catalytic function and substrate binding of enzyme. Moreover, conserved Cys61, His268, Glu302, and Asp326, have identified in all sequences and these are metal coordinating site residues located at the C-terminal end of barrel. The residues Glu24, Lys25, Arg124, His219 are also found conserved and mainly associated with the oligomerization of DAH7PS enzymes [82].

The residues Pro19, Asp146-Ala154, Gly178-Ser180 are also found conserved and associated in the formation of an allosteric binding site and which is responsible for the feedback inhibition of DAH7PS enzyme on inhibitor (Phe) binding. The rest of the conserved amino acids either located near at the predicted interface of tetramer or in positions participating in the secondary structure stabilization.

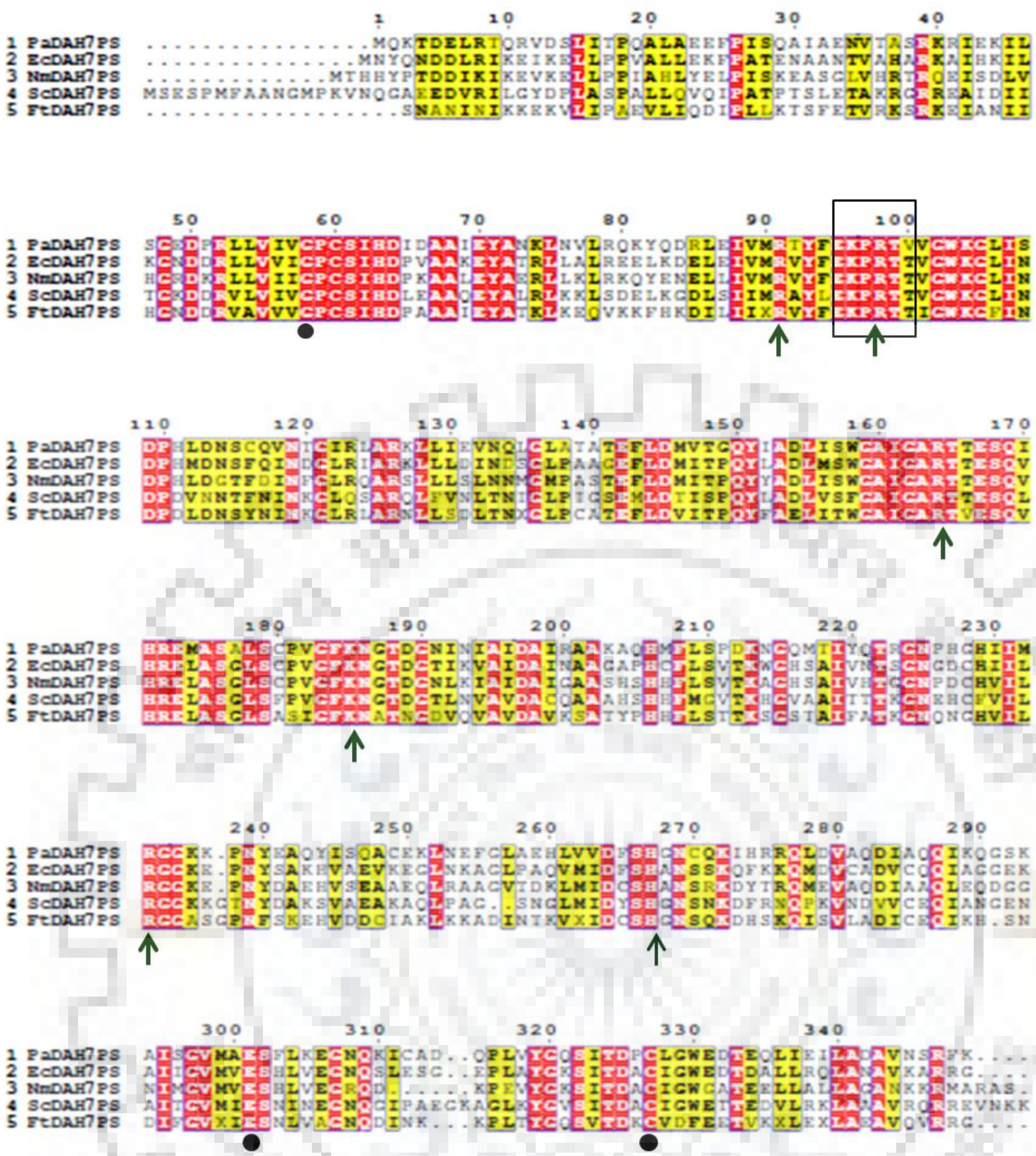

Figure 3.2: Primary sequence analysis of PaDAH7PS with structurally related DAH7PS. Multiple sequence alignment of deduced amino acid sequence of *P. alcalifaciens* DAH7PS with DAH7PS of *Escherichia coli, Neisseria meningitidis, Saccharomyces cerevesaeaie, Francisella tularensis*. Identical and similar amino acids are highlighted in red and yellow color, respectively. The presence of RxxxxxxKPRT(S/T) conserved phosphate binding motif of the Type I DAH7PS enclosed in the black box. The conserved amino acid residues at active site have been indicated by arrows and metal interacting residues have been shown by filled black circles. The post script image of alignment was prepared by ESPript 3.0 program.

3.3.3 Overall structure of PaDAH7PS

PaDAH7PS molecule adopted a typical well conserved $(\beta/\alpha)_8$ TIM-barrel fold, where eight parallel β-strands forms core of the barrel, which is surrounded by the eight α-helices (Figure

3.3 & table 3.2) and connecting loops of varying length. The PaDAH7PS is also found a tetramer as earlier reported structures of other DAH7PS from different microbial sources. But in the PaDAH7PS structure, four chains of tetramer have shown a different packing arrangement in the crystal. In crystal structure of PaDAH7PS, there is no electron density of the substrate (PEP) and divalent metal ion, although PaDAH7PS was purified with substrate and $MnCl_2$ and both were also added in the crystallization step. Therefore, obtained structure of PaDAH7PS will be referred to as an apo structure (Figure 3.3).

Type Iα DAH7PS show the presence of several extra decorative structural elements, β0 strand followed by α00 and α0 helical region and an antiparallel β sheet (β6a/β6b) along with their basic $(\beta/\alpha)_8$ barrel, which are essential for oligomerization and regulation of DAH7PS [300]. PaDAH7PS, a member of the Type Iα, contains 53 residues long N-terminal region and electron density of first seven residues of this region was not detected. In PaDAH7PS monomeric structure, β0 strand at the N-terminal extension region was not formed and only a loop was detected at this region. Although, other extra structural elements, α00 and α0 helical extensions were observed at the N-terminal of apo PaDAH7PS structure. A two-stranded, antiparallel β sheet β6a/β6b, is incorporated between α5 and α6 and situated outside of the barrel (Figure 3.3 & 3.4).

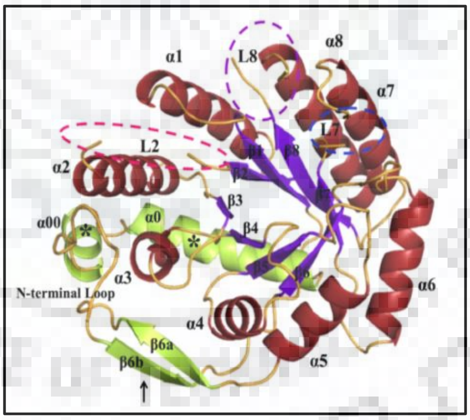

Figure 3.3: Structure of apo PaDAH7PS, Type Iα DAH7PS enzyme from the *Providencia alcalifaciens*. Representation of overall structural TIM $(\beta/\alpha)_8$ barrel fold of apo PaDAH7PS. Helices are shown in fire brick red color and β-strand of the core barrel and connecting loops are shown in blue and orange color, respectively. External N-terminal loop (orange color) and internal decorative extensions α00 and α0 helices (labeled with a star symbol) and β6a/β6b anti-parallel sheets are (labeled with upward arrow) are shown in lime green color. The disordered loops L2 and L8 are encircled in pink and violet color, respectively. The missing region (missing Asn270) observed in L7 loop is encircled with blue color.

The disordered loops regions observed in apo PaDAH7PS structure (Figure 3.4) and these regions have also shown high B-factor near chain breaks (Figure 3.5).

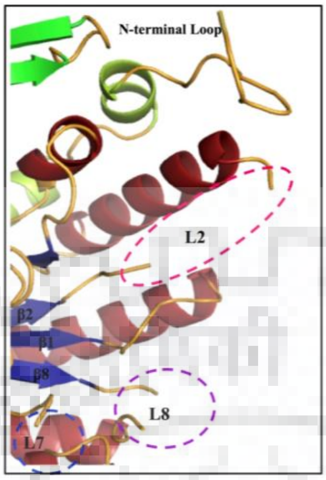

Figure 3.4: Enlarge view of the disordered regions observed in apo PaDAH7PS structure.

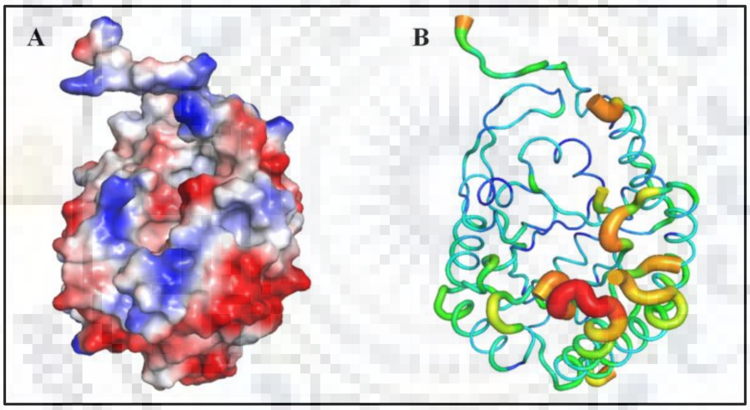

Figure 3.5: Overall structure of PaDAH7PS in apo form. **(A)** Electrostatic surfaces **(B)** Temperature factor. The disordered loop regions are showing high B-factor near chain breaks.

~ 20 % of residues of PaDAH7PS belong to β strands (Table 3.2) and ~ 42.0 % belong to α-helices. A longest helix (α8) of PaDAH7PS is present at the C-terminal of protein (Figure 3.6 & Table 3.3). A detailed description and distinct arrangement of the secondary structures of PaDAH7PS have shown in the figure 3.7.

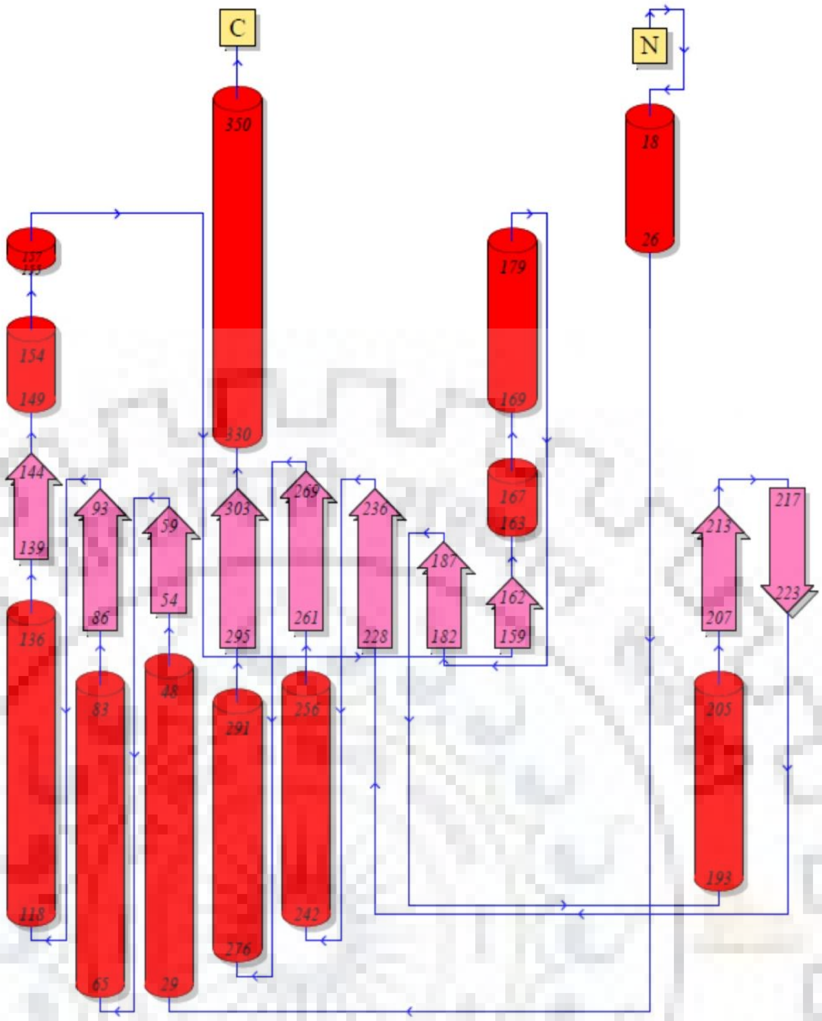

Figure 3.6: Topology diagram of PaDAH7PS monomer. The diagram illustrates how the β-strands, represented by the block arrows, join up, side-by-side, to form the protein fold. The diagram also shows the relative locations of α-helices, here represented by cylinders. The small arrow indicates directionality of the protein chain, from N-terminus to C-terminus. The numbers within the secondary structural elements correspond to the residue numbering given in the PDB file.

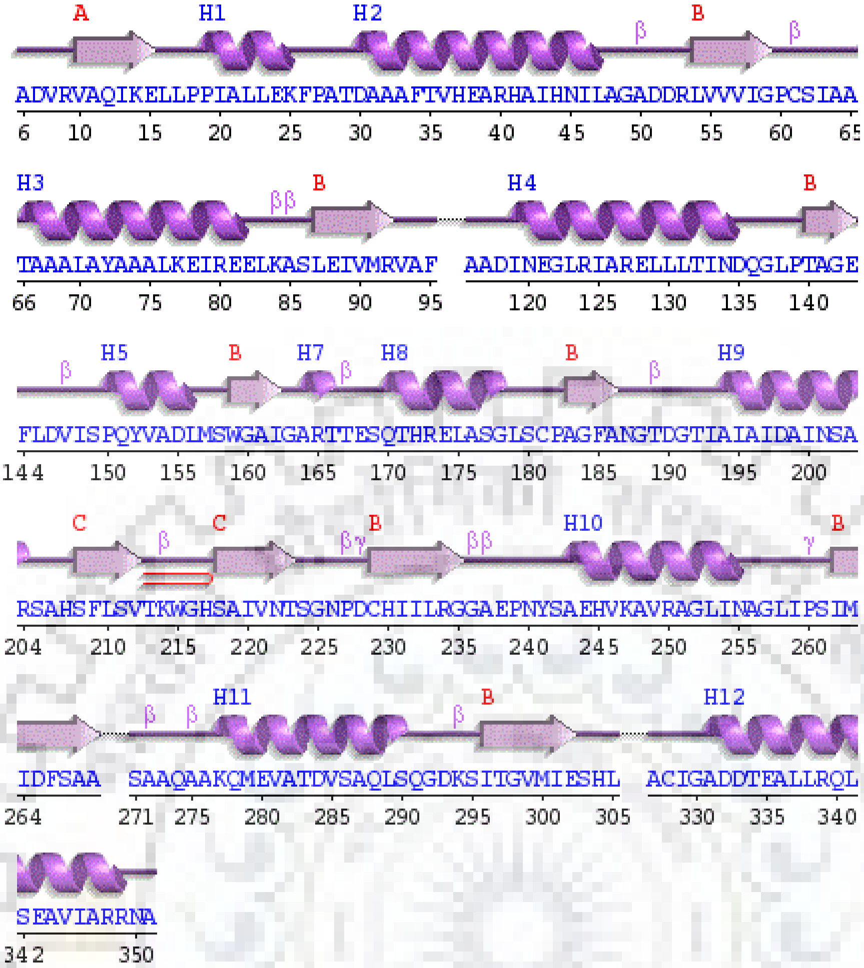

Figure 3.7: Overview of the secondary structures of PaDAH7PS represented as wiring diagram prepared by PDBSum server.

Table 3.2 Statistics of β-strands in PaDAH7PS structure. For each beta strand in the PaDAH7PS chain, the table gives the strand number (assigned sequentially from the N-terminus of the protein), the start and end residues, the number of residues in the strand and its amino acid sequence.

Strand	Start	End	No. of Residues	Sequence
β0	Val10	Glu15	6	VAQIKE
β1	Leu54	Gly59	6	LVVVIG
β2	Leu87	Arg92	6	LEIVMR
β3	Thr140	Glu143	4	TAGE

β4	Trp159	Ile162	4	WGAI
β5	Ala183	Ala186	4	AGFA
β6a	Ser208	Val212	5	SFLSV
β6b	Ser218	Thr223	6	SAIVNT
β6	Cys229	Gly235	7	CHIILRG
β7	Ile261	Ala269	8	IMIDFSAA
β8	Ile296	Glu302	7	ITGVMIE

Table 3.3 Statistics of α-helices in PaDAH7PS structure. The data displayed in the table for each helix includes helix number (assigned sequentially starting with 1 at the N-terminus of the protein), the residue numbers corresponding to start and end of helices. This is followed by the number of residues in the helix and the final column in the table gives the helix's amino acid sequence.

Helix	**Start**	**End**	**No. of Residues**	**Sequence**
α0	Pro19	Lys25	7	PIALLEK
α00	Asp30	Leu47	18	DAAAFTVHEARHAIHNIL
α1	Thr66	Glu82	17	TAAALAYAAALKEIREE
α2	Ile119	Asp135	17	INEGLRIARELLLTIND
α*	Pro150	Val153	4	PQYV
α *	Ala154	Leu156	3	ADL
α*	Ala 164	Thr166	3	ART

α4	Gln170	Gly178	9	QTHRELASG
α5	Ala194	Arg204	11	AIAIDAINSAR
α6	Ala243	Asn255	13	AEHVKAVRAGLIN
α7	Lys277	Ser290	14	KQMEVATDVSAQLS
α8	Ala331	Arg349	19	ADDTEALLRQLSEAVIARR

3.3.4 Quaternary structure of PaDAH7PS

The oligomerization of DAH7PS enzymes is essential for their functionality and regulation. Similar to earlier reported structure DAH7PS, apo PaDAH7PS has also shown a tetramer in crystal. But overall arrangement and orientation of all subunits in the tetrameric assembly of apo PaDAH7PS is found significantly different from DAH7PS tetramer of *E.coli* (complexed with the substrate and catlytic metal ions) as well as from apo DAH7PS of *Saccharomyces cerevesaeaie* [83, 306] (Figure 3.8). The subunits A and C of PaDAH7PS are arranged in a plane as a dimer and B subunit is also located adjacent to the C subunit in the similar plane. But subunit D is arranged in a perpendicular plane (90° angle) in the tetramer of PaDAH7PS (Figure 3.9A). PaDAH7PS showed a pairing between A and C subunits and monomers in the dimer form via multiple hydrogen-bonds, electrostatic, and Van der Waals interactions (Figure 3.9B & 3.10A) as shown in table 3.4. Additionally, external N-terminal loop extension of one unit interacted with the anti-parallel β sheet, β6a/β6b, internal extension of another subunit and formed a dimer as exhibited in EcDAH7PS tetramer. But other two subunits B and D of PaDAH7PS were oriented in a completely different manner (Figure 3.9B & 3.10C). The N-terminal regions of these units were positioned in the totally opposite directions to each other and no interactions occur between their N-terminal and internal (anti-parallel β sheet, β6a/β6b) extension structural elements (Figure 3.8A)

Table 3.4 Statistics for all the interfaces interactions in PaDAH7PS tetramer.

Chains	**No. of interface residues**	**Interface area (Å^2)**	**No. of hydrogen bonds**	**No. of Salt bridges**	**No. of non-bonded contacts**
A }{ B	3:4	346:339	1	1	6
A }{ C	45:42	2257:2248	22	2	256
B }{ D	2:3	150:135	1	1	11

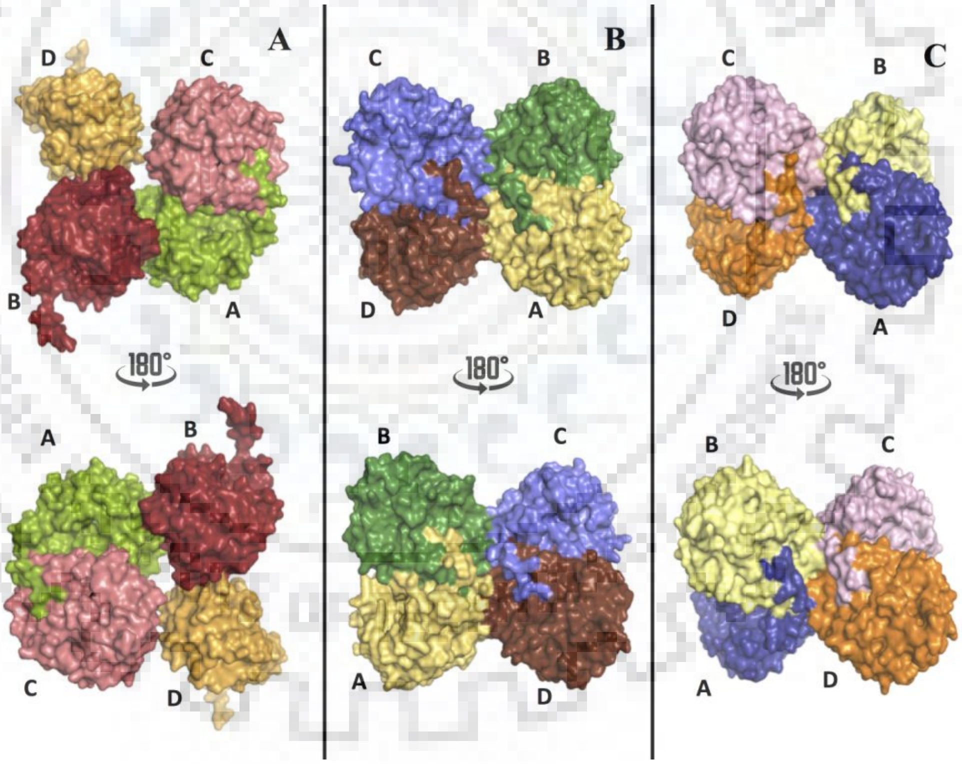

Figure 3.8: Comparison of oligomeric states of apo PaDAH7PS. (A) The assembly of Apo PaDAH7PS tetramer has shown in a surface representation. Each monomer is colored separately and named as A, B, C and D subunits. The subunit A and C forming the dimer and N-terminal loops of both units are interacting with the β6a/β6b anti-parallel sheets containing region to their partner unit. The subunit D is oriented in a different plane and the N-terminal loops of both units are arranged in the opposite directions. **(B)** The surface representation of the

EcDAH7PS (complexed with PEP and metal) tetramer contains two tight dimers. **(C)** The surface representation of apo ScDAH7PS tetramer also contains two tight dimers, similar to the complexed EcDAH7PS.

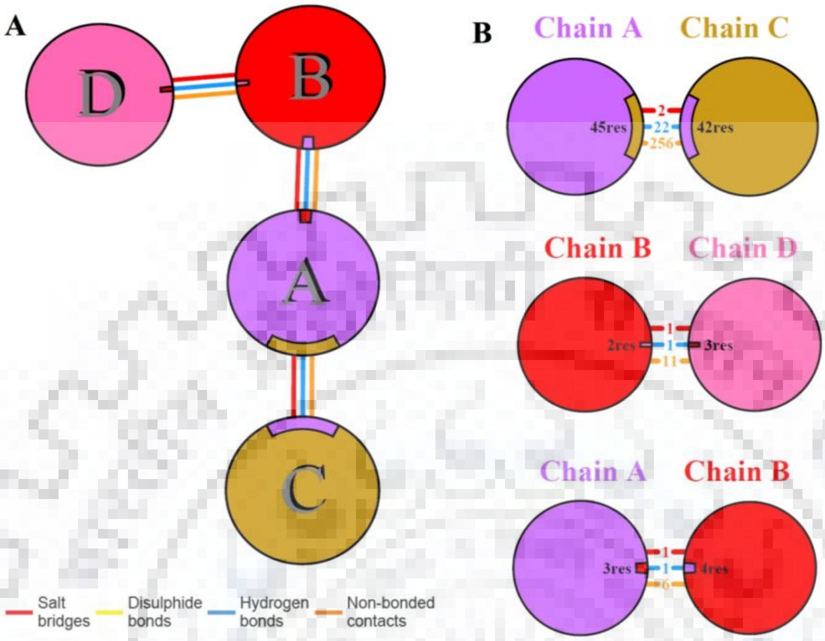

Figure 3.9: Schematic diagram of interactions between protein chains. Interacting chains are joined by coloured lines; yellow colour line represents non-bonded interaction and blue colored line indicates hydrogen bond interaction. The area of each circle is proportional to the surface area of the corresponding protein chain. The extent of the interface region on each chain is represented by a colored wedge whose color corresponds to the color of the other chain and whose size signifies the interface surface area.

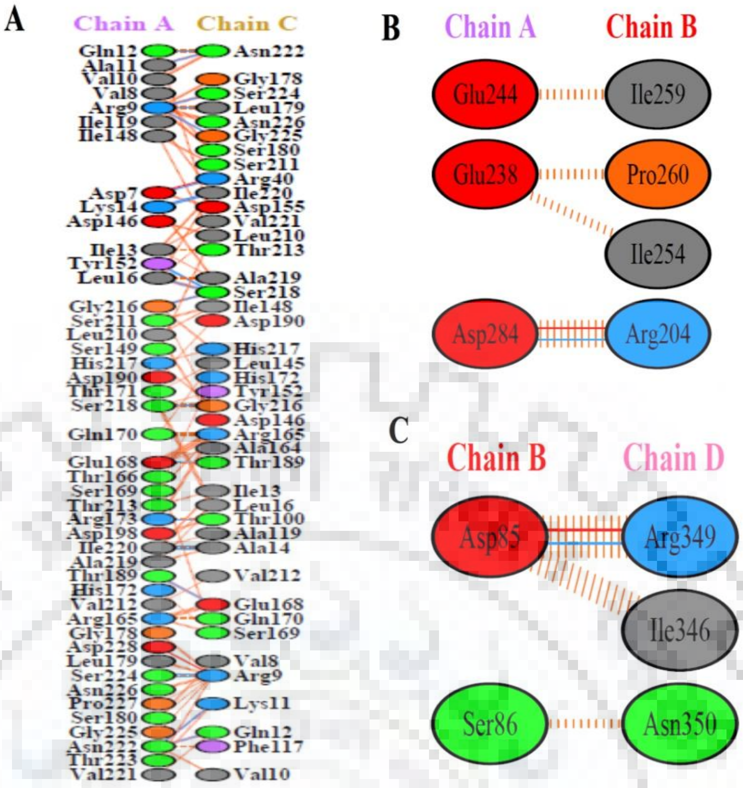

Figure 3.10: Schematic representation of interacting residues at the interfaces. The number of H-bond lines between any two residues indicates the number of potential hydrogen bonds between them. For non-bonded contacts, which are plentiful, the width of the striped line is proportional to the number of atomic contacts. **Residue colors:** Positive (H,K,R); negative (D,E); S,T,N,Q = neutral; A,V,L,I,M = aliphatic; F,Y,W = aromatic and P,G = Pro & Gly.

3.3.5 Comparison of PaDAH7PS structure

As we have obtained an apo form of PaDAH7PS, instead of complex structure with the substrate (PEP) and catalytic metal ion. So, we have compared the structure of PaDAH7PS with a complexed DAH7PS (PEP and metal) and apo DAH7PS structure characterized from *E. coli* (PDB ID 1N8F) [306] and *Saccahromyces cerevesaeaie* (PDB ID 1OFP), respectively [83]. The overall structural fold of PaDAH7PS was found very similar to the complexed and apo DAH7PS enzymes and but the differences also occur in some regions which have been described in the next sections (Figure 3.11).

Figure 3.11: The superimposition of apo PaDAH7PS with the complexed EcDAH7PS and apo ScDAH7PS. The substrate and metal bound in the complexed structure have shown as the stick (green color) and sphere (purple color), respectively.

3.3.5.1 Comparison of PaDAH7PS with complexed EcDAH7PS

The overall structural fold of apo PaDAH7PS and complexed EcDAH7PS (Figure 3.12) is found very similar with a RMSD of 0.362 Å. In PaDAH7PS structure, residues 96-116 (corresponding to the connecting loop (L2) of β2-α2 region) and residues 306-326 (corresponding to the connecting loop (L8) of β8-α8 region) from all chains were missing, which clearly indicates the structural flexibility of these loop regions, in absence of the substrate and catalyti metal (Figure 3.13).

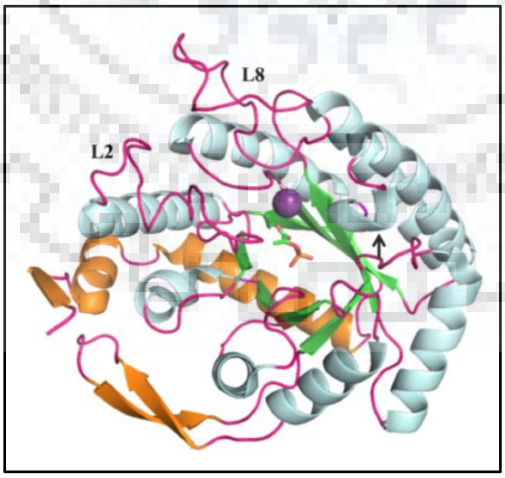

Figure 3.12: Structure of complexed EcDAH7PS. Representation of the overall fold of complexed EcDAH7PS. N-terminal β0 strand and other internal extensions (α00 and α0 helices and β6a/β6b antiparallel) are showed in the orange color. The connecting loops have shown in hot pink color and L2 and L8 loops also labeled in complexed EcDAH7PS and short helix is

highlighted in the black color arrow. The bound substrate (PEP) and metal have shown as the stick (green) and sphere (violet), respectively. A short helical segment formed with 267-271 residues has indicated by the black color arrow.

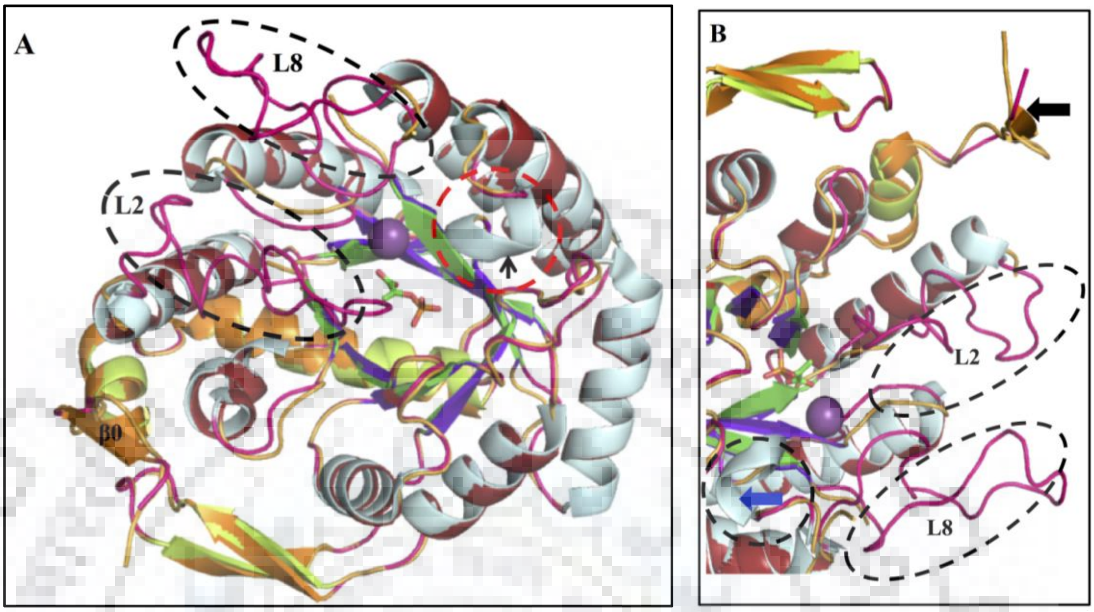

Figure 3.13: Comparison of PaDAH7PS with complexed EcDAH7PS. Superimposition of apo PaDAH7PS (Fire brick red color) with EcDAH7PS structure (Sky blue color), which showed the 0.362 Å rmsd. The disordered loop regions in apo PaDAH7PS structure are highlighted in the black dash circles. A region 267-271 forming a short helical segment is encircled by dash red color. **(B)** An enlarge view is depicting the differences in complexed EcDAH7PS and apo PaDAH7PS structure.

In complexed EcDAH7PS, all connecting loops are completely present and loops L2, L4, L6, L7 and L8 of EcDAH7PS contain the residues, which are involved in binding of the substrate at the C-terminal active site of DAH7PS (Figure 3.12) [82, 306]. Similarly, loops L1, L7 and L8 contain residues mainly responsible for the interaction of catalytic metal ion at the active site (Figure 3.13). Moreover, in complxed EcDAH7PS structure residues 267-271 formed a short helical segment that contains His268 an important residue, which interacts with catalytic metal and substrate at the active site of the protein (Figure 3.12). But in apo PaDAH7PS structure, a loop is observed at this site and the electron density of a residue Gln270 is also missing from this region and orientation of the side chain of His268 was also found different (Figure 3.13).

3.3.5.2 Comparison of PaDAH7PS with apo ScDAH7PS

The apo PaDAH7PS was also compared with an apo structure of DAH7PS from *Saccahromyces cerevesaeaie* (ScDAH7PS). The overall folds of both apo DAH7PS were showing similar structures and 0.593 Å rmsd. Previous studies have shown the presence of the N-terminal β0 strand and a similar type assembly of tetramer in apo ScDAH7PS, as it was arranged and depicted in complexed ScDAH7PS and other Type Iα DAH7PS proteins [83] (Figure 3.14).

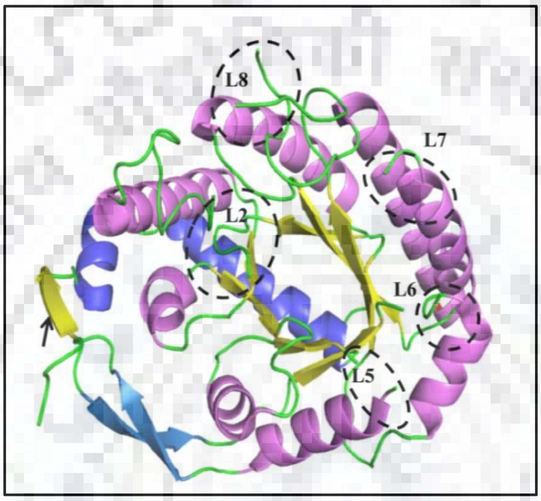

Figure 3.14: Monomer structure of the apo ScDAH7PS. Representation of the overall fold of apo ScDAH7PS. N-terminal β0 strand is indicated by the arrow and other internal extensions (α00 and α0 helices and β6a/β6b anti-parallel) are showed in the blue color. The disordered loops in apo structure are highlighted in the black dashed circle.

In contrast, apo PaDAH7PS is neither contained the N-terminal β0 strand and nor exhibited the similar tetrameric assembly. On the superimposition of monomers of both structures, we observed that PaDAH7PS has little shorter α-helices and β-strands in comparison to the apo ScDAH7PS. ScDAH7PS structure also showed the breaks in the L2 (282-288) and L8 (327-334) residues were missing loops similarly to the PaDAH7PS (Figure 3.14). Additionally, in ScDAH7PS structure few residues from several loops; L5 (203-206), L6 (251-254), and L7 (282-288) were also missing in the absence of the substrate and metal ions [83]. Moreover, PaDAH7PS structure has also shown a change in length of the sixth helix (α6) and it is found little longer in comparison to the helix (α6) of ScDAH7PS structure (Figure 3.15). In ScDAH7PS, the substrate and metal interacting essential His282 (corresponding to His268 of PaDAH7PS) containing loop (L7) 282-288 region (corresponding to 267-271 residues of PaDAH7PS) was also missing.

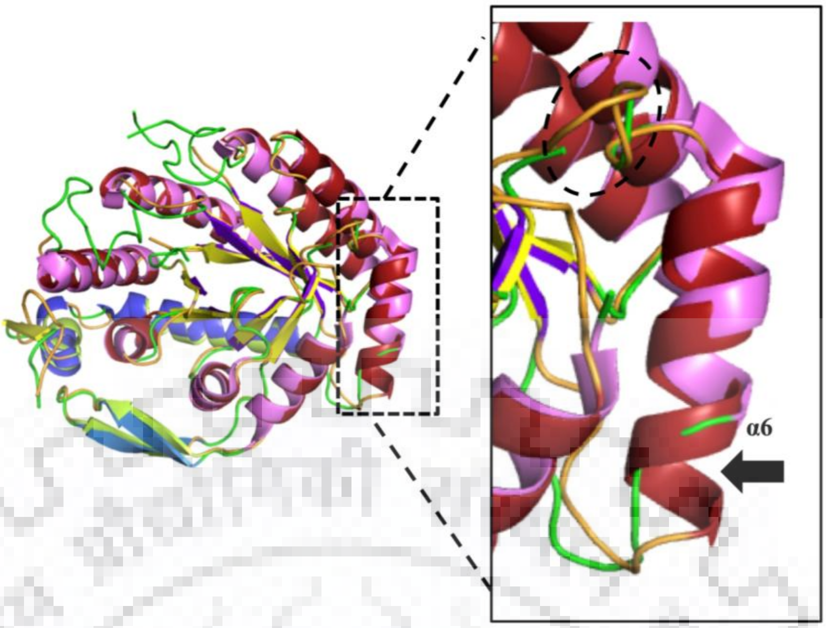

Figure 3.15: Comparison of PaDAH7PS with apo ScDAH7PS. Superimposition of apo PaDAH7PS (Fire brick red color) with apo ScDAH7PS structure (Light pink color), which showed the 0.593 Å rmsd. The enlarge view showing a change in the length of sixth helix (α6) and PaDAH7PS showed a little longer in comparison to the helix (α6) of the ScDAH7PS structure and indicated by the black filled arrow. The ScDAH7PS is showing the absence of the loop (L7), which is clearly depicted in PaDAH7PS structure and highlighted in the black dashed circle.

3.3.5.3 Comparison of the active site

Although, we added both the substrate (PEP) and a metal ion ($MnCl^{2+}$) during the purification step and crystallization conditions of PaDAH7PS, the solved crystal structure of PaDAH7PS did not show any interpretable electron density for PEP and metal ion. The absence of substrate and metal may have resulted in more flexibility in loops (L2 and L8) for the substrate and metal binding region. Therefore, these loop regions were found disordered in apo PaDAH7PS structure. Some of the residues located on these loops along with other amino acids contribute in the formation of an active site.

The active site residues of both EcDAH7PS and PaDAH7PS proteins contain positively charged residues Arg92, Lys97, Arg165, Lys186, Arg234, and His268 for the PEP interaction and Cys61, His268, Glu302, and Asp326 for the metal interaction (Figure 3.16) [82, 306]. The equivalent amino acids forming a similar site in ScDAH7PS were Arg107, Lys112, Arg180, Lys200, Arg249, and His282 for PEP interaction and Cys76, His282, Glu316, and Asp342 for the metal interaction [83].

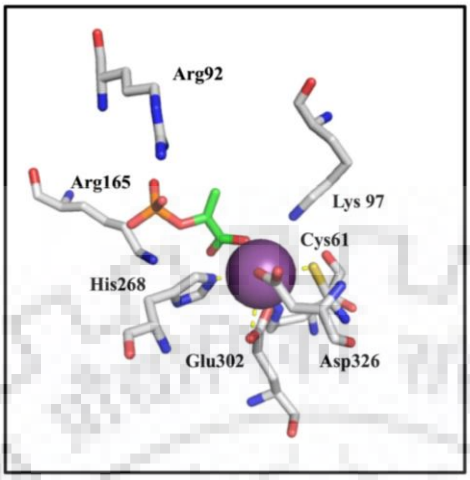

Figure 3.16: Representing the active site architecture of EcDAH7PS. The interacting residues with the substrate and metal ion have shown as the sticks (grey color). The catalytic metal has shown as the violet color sphere and substrate as green color sticks.

Superimposition of PaDAH7PS with PEP and metal bound EcDAH7PS and apo ScDAH7PS revealed some differences in the orientations of the interacting residues as shown in figure 3.17A. The residues Arg92, Arg165 and His268 interact with the PEP are identified with the different orientations in the apo DAH7PS (Figure 3.17A). The residue Lys186 has attained almost similar orientation as in EcDAH7PS and apo ScDAH7PS structures. The metal interacting Glu302 is similarly arranged and Asp326 is missing in PaDAH7PS but similarly located in EcDAH7PS and ScDAH7PS structures. The location of Cys61 is found very similar in EcDAH7PS and ScDAH7PS, but it is tilted outward due to the loop shifting in PaDAH7PS structure (Figure 3.17B). Moreover, we have also compared the allosteric binding site of apo PaDAH7PS comprise by the Pro19, Asp146-Ala154, Gly178-Ser180 with the complexed structure of EcDAH7PS (PDB ID 1KFL) with inhibitor (Phe) [324]. Both the allosteric sites of both the proteins are comprised of the similar residues and exhibited the same orientation as shown in the (Figure 3.18).

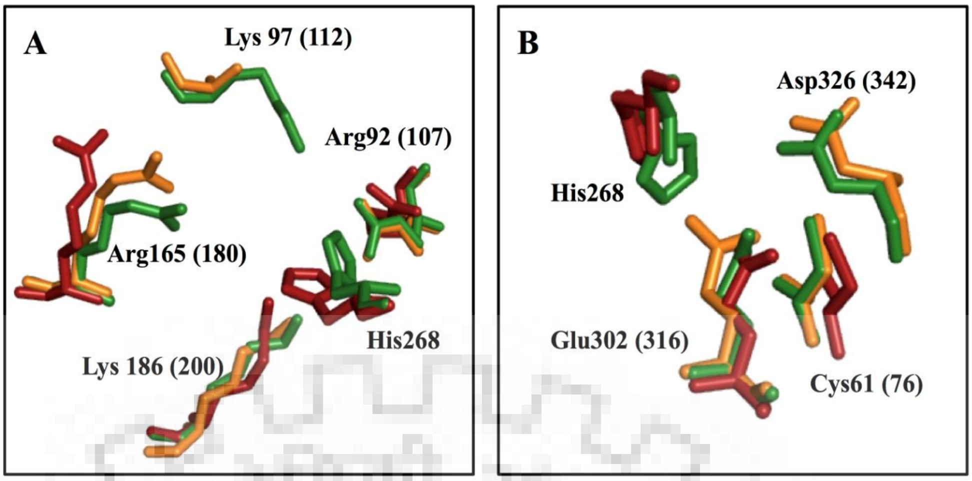

Figure 3.17: The active site comparison of PaDAH7PS. (A) Superimposition of the substrate (PEP) binding residues PaDAH7PS (Fire brick red) with the complexed EcDAH7PS (Green) and apo ScDAH7PS (Golden) has shown in sticks. His268 and Arg165 residues are showing the different orientations in the PaDAH7PS. In the complexed structure of EcDAH7PS these residues are located toward the binding site of PEP and metal, but in apo PaDAH7PS and ScDAH7PS structures these move toward outside. **(B)** Superimposition of the metal binding residues PaDAH7PS (Fire brick red) with the complexed EcDAH7PS (Green) and apo ScDAH7PS (Golden) has shown in sticks. Residues mentioned in the parentheses belong to the ScDAH7PS.

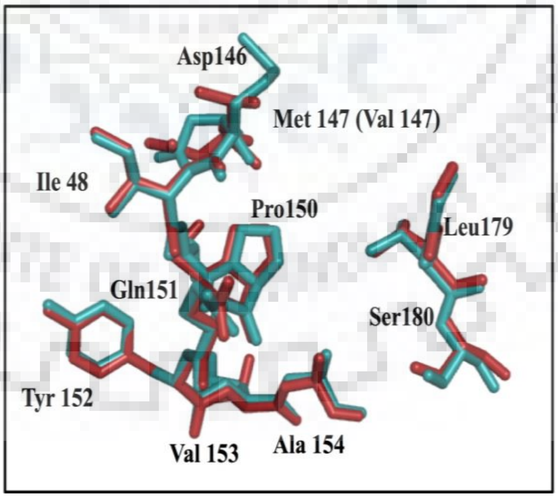

Figure 3.18: The allosteric site comparison of PaDAH7PS. Superimposition of the allosteric site forming residues PaDAH7PS (Fire brick red) with the complexed EcDAH7PS (Teal blue) has shown in sticks. All the residues are found located at the similar positions as observed in the complexed EcDAH7PS structure contains bound Phe at the allosteric site.

3.4 Conclusion and future perspectives

In present chapter, the crystal structure of apo PaDAH7PS was obtained at 3.3 Å and solved using molecular replacement method. The structural fold of PaDAH7PS protein is highly similar to other Type Iα DAH7PS enzymes and exhibited a different oligomeric assembly. PaDAH7PS does not contain an extension element β0 strand at the N-terminal region as found in all other Type Iα DAH7PS enzymes. Apart from this, no electron density was observed of the substrate interacting flexible loops (L2 and L8). The conserved His268, Arg92, active site residues are identified in the different orientations. However, furthermore high-resolution apo PaDAH7PS structure and complexed structures with the PEP, metal and the inhibitor will be helpful to get more insight on the structural and oligomeric state differences of PaDAH7PS.

CHAPTER 4

BIOCHEMICAL, BIOPHYSICAL AND STRUCTURAL CHARACTERIZATION OF BIFUNCTIONAL DAH7PS FROM *BACILLUS SUBTILIS* (BsDAH7PS)

4.1 Introduction

In bacteria, fungi, apicomplexan parasites, and plants, the synthesis of the diverse set of the important and essential aromatic compounds are employed by a series of the seven enzymatic reactions of the shikimate pathway [34, 39]. Since this pathway is not employed in the other higher organisms, including mammals and also essential for the survival of the above-mentioned organisms. Thus the enzymes of this pathway are evidence for the potential targets for the development of the antibiotics, herbicides, and pesticides [42, 219, 300]. The first committed step of the pathway is catalyzed by an enzyme 3-deoxy-D-arabino-heptulosonate 7-phosphate synthase (DAH7PS); the condensation reaction of the PEP and the E4P molecule, which results in the formation of the DAHP. The generated DAHP acts a substrate for the further enzymatic reaction and finally leads to the formation of the "chorismate". Chorismate is a precursor molecule and positioned at the biosynthetic branch point of the pathway [34, 39, 52, 325]. It can further direct toward the different paths and allow forming the aromatic metabolites by the performance of the different enzymes like (i) Chorismate mutase (generate prephenate and Phe, Tyr), (ii) anthranilate synthase (Trp), (iii) chorismate lyase (ubiquinones), and (iv) aminodeoxychorismate synthase (folate) [34, 39, 52, 325].

The regulation of the catalytic activity of DAH7PS is a key step to control the pathway flux and maintain the metabolic demand of the aromatic amino acids at the cellular level [87, 100, 232, 326]. The regulation of the DAH7PS in different microbes is often regulated by the feedback mechanism through the variety of allosteric strategies and machinery [230]. Till now all the functionally and structurally characterized DAH7PS enzymes (including Type Iα, Type Iβ and Type II) from the diverse organisms share the same core catalytic $(\beta/\alpha)_8$ barrel and a similar active site. But all these enzymes exhibit strikingly different type appended extensions with the core barrel for the purpose of allosteric control on the binding of the intermediate and end products of the pathway [229]. The cellular level of the chorismate, prephenate, and aromatic amino acids are the important checkpoints for feedback inhibition of the DAH7PS function [87, 100, 232, 326].

Type Iα DAH7PS enzymes from *Escherichia coli, Neisseria meningitidis,* and *Saccharomyces cerevesaeaie* comprise N-terminal and loop extensions to facilitate the construction of a single ligand binding allosteric site for one of the aromatic amino acids (Phe, Tyr, Trp). The Type II DAH7PS enzyme from *Mycobacterium tuberculosis* has multiple extensions with the barrel, which facilitate the construction of three allosteric sites for ligands binding. These three sites function in a synergistic manner to provide an allosteric response on the binding of the Phe or Tyr and Trp and Tyr. Furthermore, *M. tuberculosis* has shown a non-covalent complex formation on the interaction of chorismate mutase (CM) with DAH7PS and control the allosteric regulation of both the enzymes[327].

Moreover, the other Type Iβ DAH7PS enzymes have shown more variations in the regulation and allosteric mechanisms. These DAH7PS display, discrete domains either ACT-like domain or a Chorismate mutase (AroQ) domain, which are appended to the N or C terminus of the core catalytic barrel. The DAH7PS enzymes from the *Pyrococcus furiosus and Aeropyrum pernix* are consist of solely TIM barrel $(\beta/\alpha)_8$ fold and do not contain any extra N-terminal or C-terminal extensions for allosteric regulation i.e., these are unregulated enzymes [89, 101]. The regulated Type Iβ DAH7PS from *Thermotoga maritima* contains a discrete N-terminal ferredoxin-like (FL) domain (ACT-like domain) and in the presence of the aromatic amino acids (Phe or Tyr) regulatory domains of the opposite chains dimerize and form the allosteric binding site for these ligands,which causes the conformational change and block the accessibility of the substrate to the active site [87, 102].

Interestingly, the DAH7PS enzyme from *Listeria monocytogenes,* contain N-terminal fused CM domain, which on binding with chorismate or prephenate inhibited the enzymatic activity of the DAH7PS domain [229]. Similarly, the DAH7PS of *Bacillus subtilis* and *Geobacillus sp*. also have fused CM domains at their N-terminal which function as a binding site for the chorismate (CM substrate) or prephenate and primarily responsible for the regulation and inhibition of the DAH7PS activity. Both of these CM domains were also showing the little catalytic activity [91, 328].

Nazmi *et al*., 2016, have reported the crystal structure of the *Geobacillus sp*. bound with the prephenate. The structural analysis and small angle X-ray scattering results suggested that binding of the prephenate, with the fused regulatory CM domain, introduced some conformational changes and bring both DAH7PS (catalytic domain) and CM (regulatory domain) closer and also adopt a more compact conformation. Thus, structural rearrangements and inter-domain conformational changes in the *Geobacillus sp*. DAH7PS inhibited the catalytic activity of the DAH7PS domain by limiting the accessibility of the substrate to the active site [91, 329].

Recently in 2017, Pratap et al., our group members have also reported the crystal structure of the truncated N-terminal regulatory CM domain of a bifunctional DAH7PS of the *B. subtilis* complexed with the chlorogenic acid. The structural and biochemical data have evidently shown that chlorogenic acid (a structural analog of chorismic acid) acts as an inhibitor of the truncated truncated N-terminal regulatory CM domain (chorismate mutase) of the *B. subtilis*. We have also hypothesized that binding of the substrate, product or their analogs at the active site of N-terminal regulatory CM domain form a domain-domain interface with the DAH7PS catalytic domain and induce conformational changes and inhibit the catalytic activity [92].

Keeping this in view, in the present study, we have cloned, expressed and purified a full length bi-functional DAH7PS enzyme (N-terminal regulatory CM domain along with the DAH7PS catalytic domain) from the *B. subtilis* (BsDAH7PS). Furthermore, we have investigated the binding features of full length BsDAH7PS with the chlorogenic acid and also other synthesized compounds from the Shikimate pathway (Prephenate, Ferulic acid, and Shikimate) using circular dichroism and fluorescence spectroscopy. Subsequently, we have used Isothermal titration calorimetry (ITC) to determine the thermodynamic parameters of the binding of these compounds. The molecular modeling of the full length BsDAH7PS and docking studies have been performed to analyze the molecular interactions and selective binding mode of the all these compounds. Furthermore, we have performed growth inhibition assays and evaluated the minimum inhibitory concentration (MIC) values of all compounds against the *B. subtilis*. The current study will be significant for the further designing and optimization of analogs of these compounds in the expectation of progress towards the development of multi-targeted and broad-spectrum antimicrobial agents.

4.2 Materials and methods

4.2.1 Materials

Bacillus subtilis strain 3256 (MTCC No.1427) was obtained from the Microbial Type Culture Collection (Chandigarh India) and subcultured and revived in our laboratory. *Escherichia coli* DH5α cells and BL21 (DE3) host cells were obtained from the Novagene. Primers used for the amplification of gene were procured from the Eurofins. All kits used during the cloning procedure were purchased from Qiagen and all enzymes were collected from the New England Biolabs. All other chemicals, buffer, and inhibitors were analytical grade (Sigma) and used without further purification. All media used for the bacterial growth were procured from HiMedia (India).

4.2.2 Molecular cloning and expression of BsDAH7PS

The genomic DNA of *Bacillus subtilis* (MTCC No. 1427) was isolated by DNA extraction Kit. A BsDAH7PS synthase (AAC00298.1) ~1074 bp long fragment encoding a full length 358 amino acid residues was amplified by the PCR with the forward (NheI) 5′GATTCT**GCTAGC**CAATGAACTATCAGAACGATGACGTC-3′ and reverse (XhoI) 5′GATTCT**CTCGAG**TTATTTATTTCGACGAGCAATGACTG-3′ designed primers. The amplified product was purified and digested with the high fidelity restriction enzymes. The digested product was purified by the gel extraction kit. The purified product was further ligated using T4 DNA ligase enzyme with the pET28c digested vector with similar enzymes. The ligated product was transformed into the *E. coli* DH5α cells. After then, a positive clone was transformed into in the host *E. coli* BL21 (DE3) cells by $CaCl_2$ Method. The transformed *E. coli* cells were cultured in 10 ml Luria-Bertani medium for the small-scale expression of BsDAH7PS protein and optimized for obtaining the soluble protein by inducing with the addition of five different concentration of (0.1 mM to 0.5 mM) IPTG and three different temperatures at (18 °C, 25 °C and 37 °C).

4.2.3 BsDAH7PS purification by IMAC

The cell pellets were resuspended in the lysis buffer (25 mM Tris-HCl pH 7.5, 200 mM NaCl, 5 mM imidazole, 0.1 mM DTT). Further, the disruption of the cells was carried out by using the high-pressure French press system. The solubilized cell lysate was clarified by the centrifugation at 12000 rpm for 1 h at 4 °C and the clear supernatant was separated from the cell debris by decanted into a fresh container. The obtained supernatant was applied to the Ni-

NTA affinity pre-equilibrated column. To remove the impurities, the column was washed with the two wash buffers containing 25 mM and 50 mM imidazole, respectively. The desired BsDAH7PS protein was eluted with a linear step gradient of 100-250 mM imidazole containing buffer. The purity of the elution fractions was analyzed by 12% SDS -PAGE gel electrophoresis with Tris-glycine buffer (pH 8.3) at 80 V for 3 h. The fractions of the purified BsDAH7PS were pooled and dialyzed overnight at 4 °C against 25 mM Tris buffer (pH 7.5) and concentrated up to ~ 5 mg/ml using a 10 kDa cutoff Amicon Ultra-15 concentrator and protein was used for the further studies.

4.2.4 Enzymatic activity assay

The enzymatic activity of the BsDAH7PS (i.e., DAH7PS catalytic C-terminal domain) was estimated by continuous assay method. The standard assay was performed in the (50 mM Tris-HCl, pH 7.5) in the presence of $MnCl_2$ at the 25 °C with a final reaction volume of 100 μl. All measurements were carried out at 232 nm with Cary UV-vis spectrophotometer by using quartz cuvette. The kinetic parameters (*Km*, *Vmax*, *kcat*) for both substrates were calculated by varying the concentrations. All reactions were carried out in triplicates. The obtained data were fitted using non-linear regression analysis by graph pad prism software.

4.2.5 Inhibition studies

The natural phenolic compounds chlorogenic acid (CHL), ferulate (FER), shikimate (SKA), and prephenate (PRE) were tested against the BsDAH7PS. The chemical structures of all these compounds have shown in the figure 4.1. IC_{50} values of each compound were calculated by keeping the PEP (substrate) concentration constant (100 μM). Kinetic inhibition constant (*Ki*) was calculated by varying the inhibitor (10-150 μM) and substrate concentration (10-200 μM). BsDAH7PS was incubated with the inhibitors for 1 h at 4 °C after then the enzymatic reaction was initiated by adding another substrate (E4P). Subsequently, a decrease in the absorbance of PEP at 232 nm was measured spectrophotometrically.

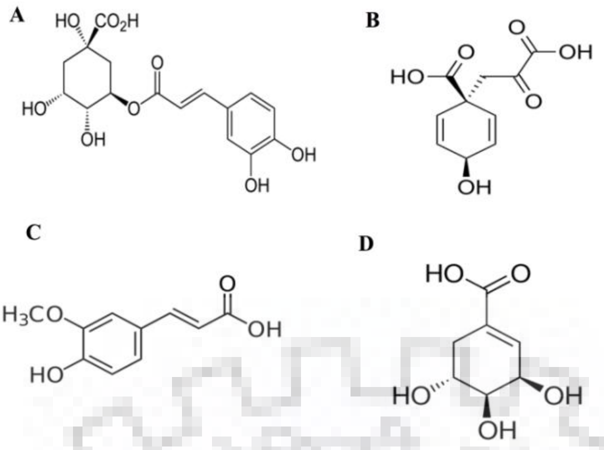

Figure 4.1: Chemical structures of the inhibitors. (A) Chlorogenic acid (CHL), **(B)** Prephenate (PRE), **(C)** Ferulate (FER) and **(D)** Shikimate (SKA) structure.

4.2.6 Circular dichroism measurements

The circular dichroism experiments were performed by using Jasco spectropolarimeter (1500) equipped with the peilter system. All CD spectra were measured at 25 °C using a quartz cuvette of 0.1 cm path length. BsDAH7PS was taken up to the concentration of ~5 μM and CD spectra of BsDAH7PS were recorded both in the absence and presence of all compounds (CHL, FER, PRE, and SKA) in the far-UV region. Finally, CD data were converted into mean residue ellipticity (MRE) in deg. $cm^2 \cdot dmol^{-1}$ in the by using the following equation (1)

$$MRE = \frac{\text{Observed CD (mdeg)}}{10 * C_p n l} \qquad (1)$$

Here C_p is the molar concentration of BsDAH7PS, *n* is the number of amino acid residues and *l* is the path length in centimeters [330].

4.2.7 Fluorescence measurements

All fluorescence measurements were carried out with the spectrofluorometer Fluorolog®-3 (Jobin Yvon Inc.USA) with 5 nm emission slits and cuvette of 1.0 cm path length at 25 °C with a Xenon lamp (150W). The intrinsic fluorescence was measured by exciting specifically Trp residue (λexc = 295 nm) and recorded the emission spectra between 300-500 nm. The protein samples were kept in a thermostatic cuvette holder sample cell. The interaction between the inhibitors and BsDAH7PS was carried out by titrated the protein in the cuvette with increasing amount of the inhibitors.

4.2.8 Isothermal titration calorimetry

All calorimetric measurements were performed using Microcal ITC200 (GE Healthcare) which is characterized by 280 µl of the sample cell volume with a 40 µl dosing syringe capacity. The reference cell was filled with the degassed water and system was equilibrated at 25 °C and reference cell power was set to 8 µW. The protein sample was dialyzed against (20 mM Tris buffer pH 7.8, 100 mM NaCl, 5 % glycerol, 500 µM TCEP) buffer and all ligands stock solutions also diluted in the same buffer. A total of 30 injections (CHL and PRE) and 16 injections (FER and SKA) and separated by 180 s and with duration of 4 s each of 1 µl of titrant were injected into the sample at 25 °C. The obtained ITC data were analyzed by using Origin 7.0 software package and fitted to the "sequential binding site model" and all thermodynamic parameters were calculated by the following the equation (2)

$$\Delta G = \Delta H - T\Delta S \ldots\ldots\ldots\ldots\ldots\ldots (2)$$

Here, ΔG is the Gibbs free energy change, ΔH is the enthalpy change, ΔS is the entropy change and T is the temperature (298 K).

4.2.9 Molecular modeling

The 3D structural model of the full length BsDAH7PS (with both N-terminal regulatory CM domain and C-terminal catalytic DAH7PS domain) was generated through the homology modeling. The template for the model generation was selected from the Protein Data Bank (PDB) by using NCBI BLAST search tool with BLOSUM62 as a scoring matrix on the basis of sequence identity. The obtained best template hit (PDB ID 5J6F) was used was used for the 3D model generation by using the Swiss model [331] and MODELLER 9.17 program [332]. The sequence alignment was performed by using the ClustalW program [333]. Furthermore, the quality of the generated 3D structural model was assessed by using the PROCHECK [312], Verify 3D [334], Ramachandran plot [335], ERRAT plot [336] and ProSA analysis [337].

4.2.10 Molecular docking

All the molecular docking analysis and visualization were performed by using AutoDock 4.2 and AutoDockTools 4.2 [338]. The ligands were converted into the .pdbqt file format by using the open babel program. The best-generated 3D model structure of BsDAH7PS was used to determine the binding mode of all tested inhibitors at the N-terminal regulatory domain of full length protein. All the water molecules removed and non-polar hydrogen and kollman charges were added to the protein by using AutoDock Tools and also saved in .pdbqt file format. The

BsDAH7PS was enclosed in a 30 Å × 30 Å × 30 Å box with the number of grid points in xyz directions, and a grid spacing of 0.375 Å and all other parameters were used as default settings. Lamarckian genetic algorithms and other default parameters with total 50 runs were used for the docking [339]. The binding modes of all the ligands with protein were analyzed and conformations with the minimum binding energy was selected and also visualized by using the Pymol [340].

4.2.11 Antibacterial susceptibility assay

Minimal inhibition concentration (MIC) values were determined for all the tested inhibitors against the *Bacillus subtilis* by following the standard assay method of the National Committee for Clinical Laboratory Standards [341]. Briefly, an inoculum of the 5 x 10^5 cfu/ml was prepared from the dilution of fresh bacterial culture. The concentration gradient (0.5 µg/ml - 256 µg/ml) of all the inhibitors was added in the 96 well microtiter plates by broth microdilution method. The evaluation of the bacterial growth was measured after 16 h by the microplate reader at 600 nm and lowest concentration of inhibitors, which inhibit the growth of the bacteria, was considered as the MIC value of each inhibitor. All experiments were performed in the triplicates.

4.3. Results

4.3.1 Molecular cloning, expression and purification of the BsDAH7PS

B. subtilis genome encoded the full length BsDAH7PS (with regulatory CM domain and DAH7PS catalytic domain) was successfully amplified and cloned. The construction of the recombinant plasmid pET-BsDAH7PS was validated by the restriction digestion, colony PCR. The analysis of PCR product on 1 % agarose gel electrophoresis confirmed the presence of a single amplification band of ~ 1000 bp size, corresponding to the BsDAH7PS gene size ~ 1074 bp (Figure 4.2A) Furthermore, DNA sequencing results also confirmed that full length DAH7PS gene from the *B. subtilis* (GeneBank. AAC00289.1) was properly inserted into the recombinant pET28c-BsDAH7PS. The optimum expression and solubility of the BsDAH7PS were observed with 0.4 mM IPTG concentration at 18 °C temperature (Figure 4.2B). The BsDAH7PS was purified via the immobilized metal-affinity chromatography (IMAC) method. The purified His-tagged BsDAH7PS exhibited the single band of ~ 42 kDa size on the 12 % SDS-PAGE profile (Figure 4.2C). The fractions containing BsDAH7PS were pooled and concentration of the purified protein was measured by the UV spectroscopy using a molar extinction coefficient of 12950 M^{-1} cm^{-1}. The purification process resulted in the yield of approximately 10 mg/ml of purified BsDAH7PS (> 90 % purity) from 5 g of the cells pellet.

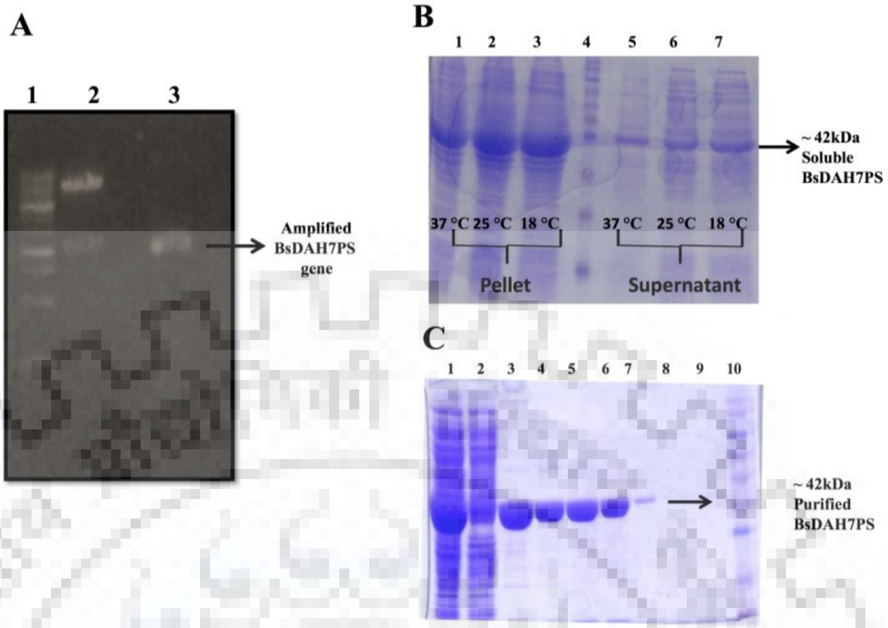

Figure 4.2: Cloning, expression and purification profile of BsDAH7PS. (A) 1% agarose gel electrophoresis profile; Lane 1 showing the and the molecular ladder, Lane 2 showing the restriction digestion profile of BsDAH7PS gene depicted by lower band and upper band showing the digested plasmid, Lane 3 showing the amplified gene of the BsDAH7PS. **(B)** Expression profile of the BsDAH7PS; Lane 1-3 showing the over-expressed BsDAH7PS protein in cell pellet at the different temperature (37, 25, and 18 °C), Lane 4 representing the molecular weight marker (kDa) and Lane 5-7 showing the over-expressed BsDAH7PS protein in supernatant at the different temperature (37, 25, and 18 °C). **(C)** Purification profile of the BsDAH7PS protein; Lane 1 showing the supernatant fraction and Lane 2 showing the Flow through, Lane 3-6 single bands of the purified His-tagged BsDAH7PS protein (~ 42 kDa) Lane 8, Molecular marker (kDa).

4.3.2 Enzymatic activity

The enzymatic activity of full length BsDAH7PS was determined using a continuous assay. A decrease in the absorbance of PEP was monitored at 232 nm (molar extinction coefficient of 2840 $M^{-1}\cdot cm^{-1}$) and the kinetic parameters (K_m, k_{cat}, and k_{cat}/K_m) of both substrates (PEP and E4P) were calculated. The data were fitted into the Michaelis-Menten equation and observed parameters for PEP and E4P also compared with the other homologs DAH7PS as shown in the table 4.1.

Table 4.1 Comparison of the kinetic parameters of full length BsDAH7PS with other homologs DAH7PS (Type Iβ).

DAH7PS (TypeIβ)	**K_m^{PEP} (μM)**	**K_m^{E4P} (μM)**	**k_{cat} (s^{-1})**	**k_{cat}/K_m^{PEP} ($s^{-1}μM^{-1}$)**	**k_{cat}/K_m^{E4P} (s^{-1} $μM^{-1}$)**	**References**
BsDAH7PS	178 ± 31.86	441.2 ± 52.72	0.52 ± 0.034 (PEP) 0.68 ± 0.032 (E4P)	0.002	0.001	Present study
BsDAH7PS Marburg (ATCC 6051)	139 ± 11.4	1760 ± 110	4.6 ± 0.1	.033	0.0026	[328]
TmDAH7PS	9.5	350	7.6	0.8	0.021	[98]
GsDAH7PS	87 ± 9	95 ± 8	45 ± 4.0	0.52	0.47	[91]

Michaelis-Menten plots of the BsDAH7PS have shown in figure 4.3A & 4.3B.

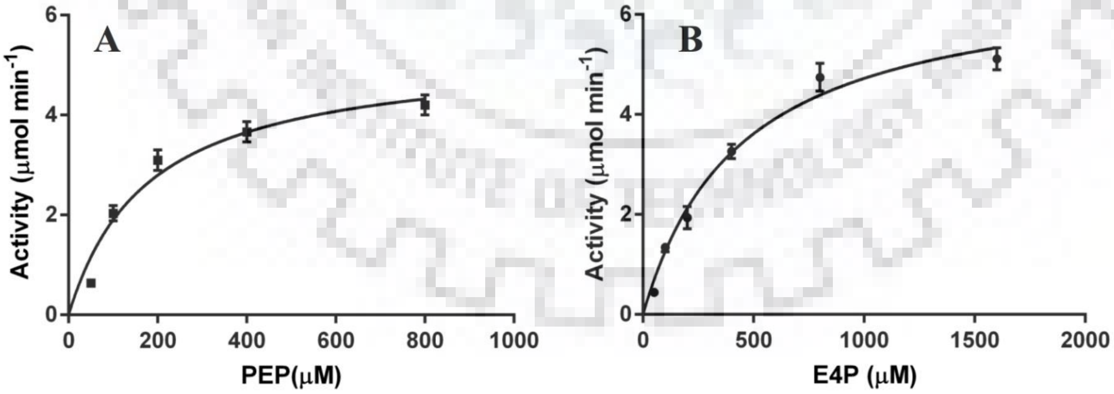

Figure 4.3: Biochemical characterization of BsDAH7PS. (A) & **(B)** Michaelis-Menten kinetics parameters were calculated for the both substrates PEP and E4P, respectively.

Moreover, the inhibitory effect of all the compounds (CHL, FER, PRE, and SKA) was checked against the BsDAH7PS also determined and IC_{50} values of all compounds have been calculated at a constant substrate (PEP) concentration (100 μM) by using the non-linear regression analysis. Table 4.2 is showing the K_i and IC_{50} values of all these compounds. Here, CHL and PRE have lower K_i and IC_{50} values than FER and SKA. Further, the mechanism of inhibition of these inhibitors were analyzed via plotting the double reciprocal curves (Figure no.) Based on the analysis of these plots, CHL, PRE and SKA were found to be non-competitive inhibitors of BsDAH7PS (Figure 4.4A, 4.4B, & 4.4D). The lines were not intersecting at 1/V axis clearly indicated the non-competitive type of inhibition mechanism. Whereas, the plot of FER inhibition is depicting the parallel lines, which indicated the un-competitive type mode of inhibition of FER as shown in figure 4.4C.

Table 4.2 Inhibitory activities of chlorogenic acid, prephenate, ferulate, and shikimate against the full length BsDAH7PS.

Ligand	**K_i (μM)**	**IC_{50} (μM)**
PRE	38.30 ± 5.9	102.3 ± 6.2
CHL	21.58 ± 5.4	60.49 ± 2.9
FER	74.2 ± 5.6	121 ± 11.2
SKA	67.2 ± 3.4	117 ± 9.10

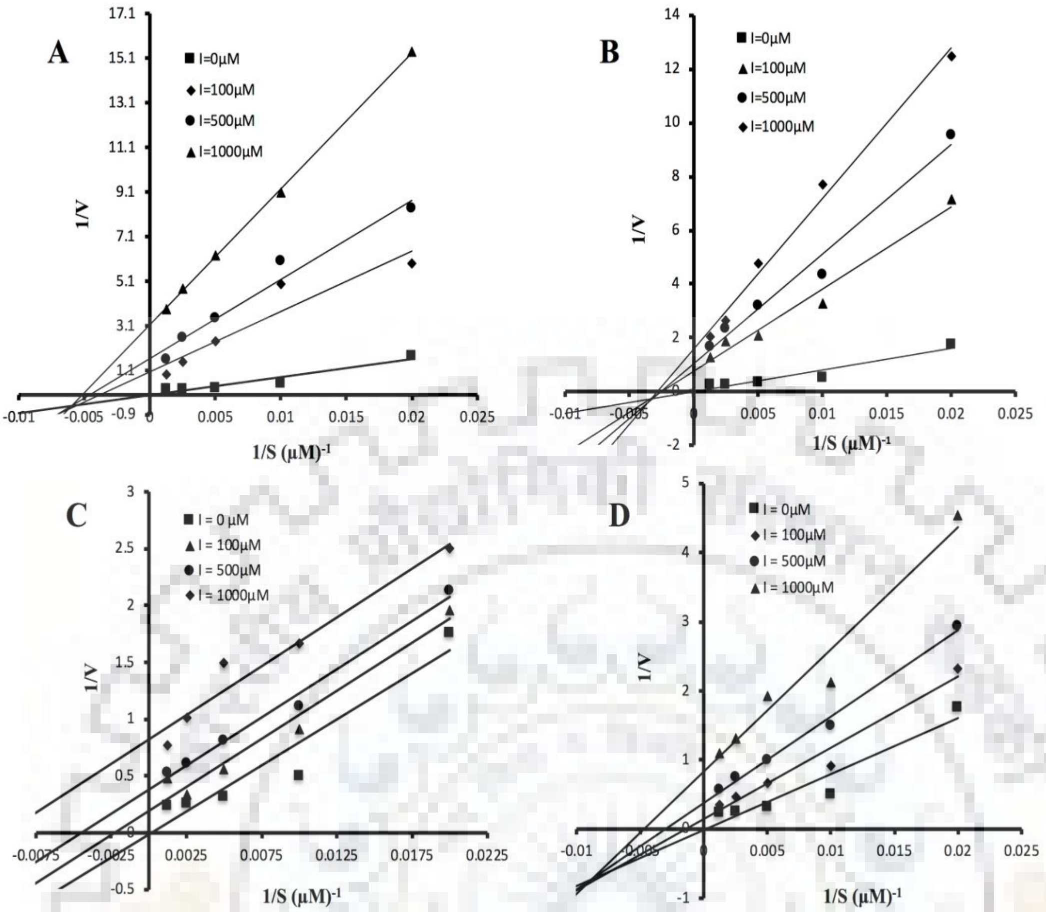

Figure 4.4: Kinetic analysis of inhibition mechanism. **(A)** & **(B)** representing the Double reciprocal plots (1/V vs 1/S) of CHL and PRE, respectively at different inhibitor concentrations. **(C)** & **(D)** showing the plots of the FER and SKA, respectively. The lines were not intersecting at 1/V axis which clearly indicated the non-competitive type of inhibition mechanism as shown by the CHL, PRE, and SKA. Whereas, the plot of FER inhibition is depicting the parallel lines, which indicated the un-competitive type mode of inhibition of FER as shown in the panel C. All the reactions were performed in the triplicates and mean of the data have plotted here.

4.3.3 CD spectroscopic studies

There are several biophysical techniques have been applied to characterized the structural and conformational changes occur in the protein under the different environmental conditions like alteration in pH and temperature and any ligand binding like substrate, co-factor, and inhibitor of the protein. The circular dichroism is a very sensitive, easy to handle, and a valuable technique to investigate the molecular basis of proteins secondary and tertiary structure changes, protein folding and stability studies. In general, the far UV (180- 240 nm) and the near UV (260-320 nm) spectra provide the information regarding the secondary (helix, sheet, turn and coil) and tertiary structure of a protein, respectively [342-344].

In the far-UV CD spectrum, native BsDAH7PS exhibited the two negative minima at 208 nm and 220 nm, and a maxima at the 194 nm, which clearly notified the α-helical and β-sheet contents of the BsDAH7PS (Figure 4.5A). In the CD spectrum of α-helix, 208 nm and 222 nm bands occur due to the π-π* and n-π* transitions of peptide bonds, respectively. In β-sheets and random coils, the occurrence of a minimum at 215 nm and a maxima at 192-198 nm are due to the n-π* and π-π* transitions of the peptide bonds, respectively [261, 344, 345]. Moreover, the secondary structure content of the BsDAH7PS was also calculated using CONTINLL method program of the dichroweb server [346] and shown in the figure 4.6A. The native BsDAH7PS depicted ~ 40.6 % helical, ~ 9.3 % sheets, ~ 51.6 % disordered structures (Figure 4.6A).

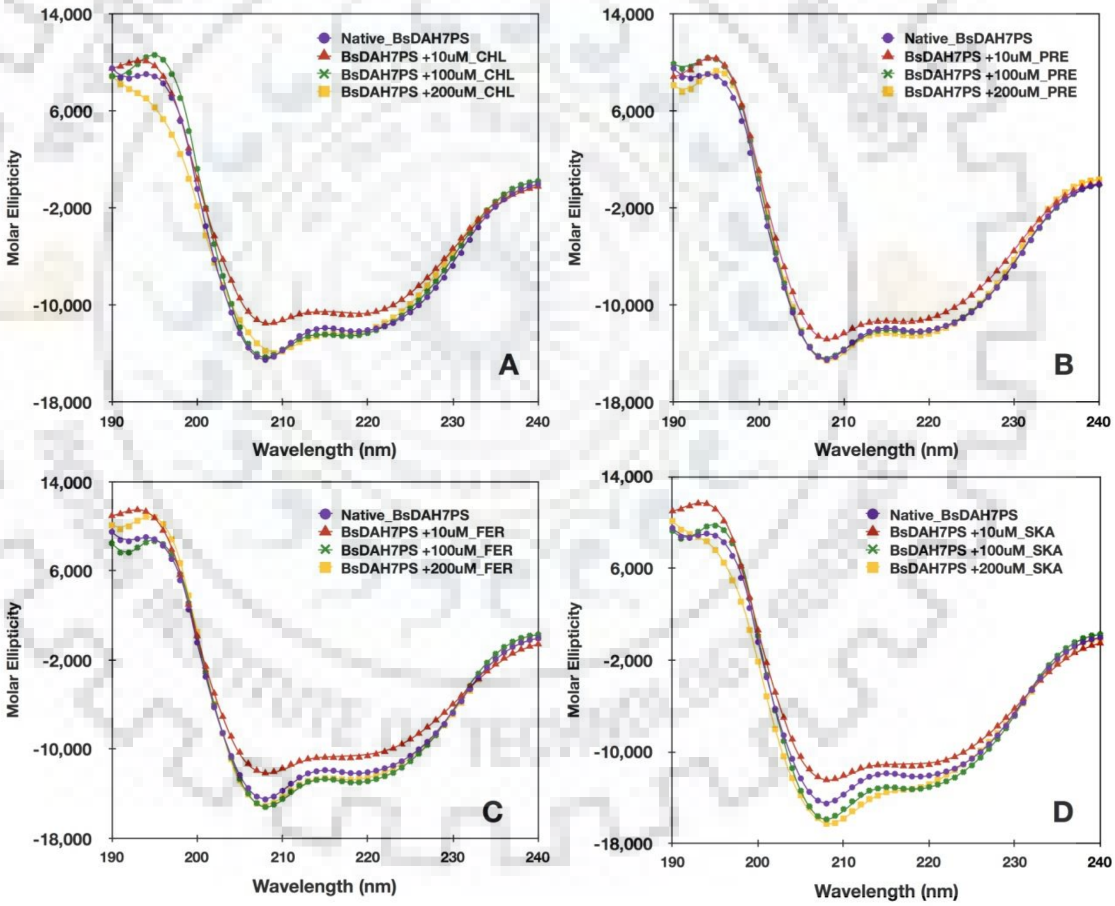

Figure 4.5: Circular dichroism spectroscopic studies of BsDAH7PS. (A) & **(B)** Far-UV spectra in the presence of varying amount of the CHL and PRE, respectively. **(C)** & **(D)** Far-UV spectra in the presence of varying amount of the FER and SKA, respectively.

4.3.3.1 Effects of the ligand binding

Furthermore, we compared the far-UV CD spectra of BSDAH7PS in the presence of varying concentrations of all compounds (CHL, PRE, SKA, FER) and also calculated the structure contents by Dichroweb server [346]. Initially, we found on the lower concentration of these compounds, BsDAH7PS depicted a small decrease in the ellipticity and loss in the helical content. But on the increasing concentration of these compounds, we noticed an increase in the ellipticity in all the far-UV spectra of BsDAH7PS as shown in the figure 4.6A & 4.6B. CHL and PRE showed the increment in the helical content of BsDAH7PS from 40 % to ~ 42 % and ~ 45 %, respectively. Similarly, the binding of FER and SKA depicted ~ 44 % and ~ 47 % helical content in the secondary structure (Figure 4.6C & 4.6D). This clearly suggests that on the binding of the compounds binding full length BsDAH7PS showed a gradual increment in the α-helical content.

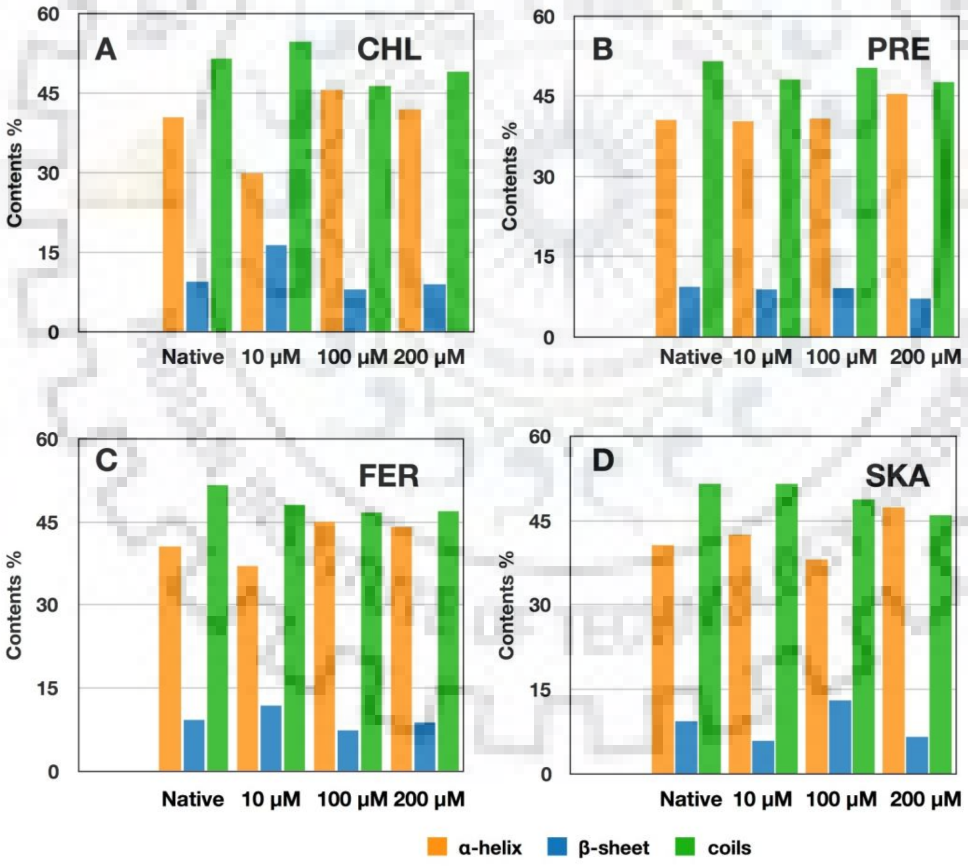

Figure 4.6: Effect of different ligands binding on BsDAH7PS. (A) & **(B)** The secondary structure content of the BsDAH7PS on the binding of various concentrations of CHL and PRE, respectively. **(C)** & **(D)** The secondary structure content of the BsDAH7PS on the binding of various concentrations of FER and SKA, respectively.

4.3.4. Fluorescence analysis

Fluorescence-based studies have been widely used to examine the interaction of a protein with different ligands (drugs, inhibitors etc). The aromatic amino acids (Trp, Phe, and Tyr) residues in the proteins contribute to the intrinsic fluorescence. The fluorescence measurements generally provide basic information about the conformational changes and environment around the fluorophore [347, 348].

Herein, the occurrence of the conformational changes and molecular basis of the full length BsDAH7PS binding with all ligands (CHL, PRE, FER, and SKA) were investigated by measuring the tryptophan specific intrinsic fluorescence and quenching mechanism. The full-length BsDAH7PS contains a surface exposed Trp346 residue in the DAH7PS domain. The native BsDAH7PS depicted an emission maximum at ~ 340 nm when excited at 295 nm specifically to Trp residue. This is clearly suggesting that Trp346 residue in the native BsDAH7PS is exposed towards the surface and hydrophilic environment (Figure 4.7A) [347, 348].

Further, the interaction of the all these ligands with BsDAH7PS has exhibited a decrease in Trp fluorescence intensity and a concomitant red shift in the emission maximum. The binding of the CHL and FER with the BsDAH7PS resulted into the red shift of ~ 10 nm and 6 nm, respectively, (Figure 4.7A & 4.7C) while the binding of the SKA and PRE depicted 4 nm and 2 nm red shift respectively (Figure 4.7B & 4.7D). The extent of red shift was more observed in CHL and FER binding in comparison to the other ligands. Thus these results have shown that binding of ligands with the full length BsDAH7PS have introduced the hydrophilic environment surrounding the Trp residue.

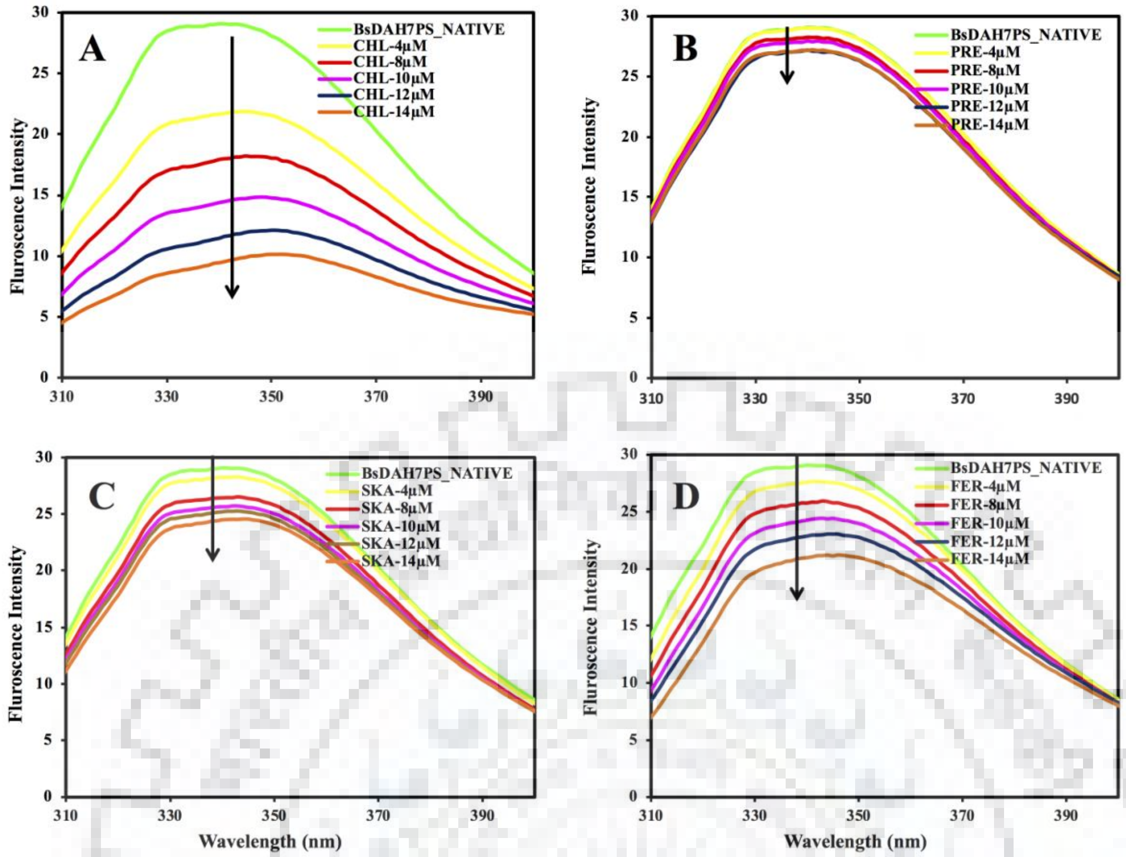

Figure 4.7: Fluorescence based quenching studies of BsDAH7PS. The intrinsic fluorescence emission spectra of native BsDAH7PS and quenching effect of the ligands on its fluorescence intensity at 25 °C (λex = 295 nm); **(A)** BsDAH7PS-CHL, **(B)** BsDAH7PS-PRE, **(C)** BsDAH7PS-FER **(D)** BsDAH7PS- SKA systems.

4.3.4.1 Quenching mechanism determination

The quenching is generally defined as the decrease in the fluorescent intensity of a protein on the ligand binding, which can occur due to the different molecular mechanisms like molecular rearrangements, excited-state reactions, ground-state complex formation, energy transfer, and collisional quenching. Quenching mechanism can be classified into the dynamic or a static process or by mixed type pattern and can be distinguished by varying temperature and viscosity. In dynamic quenching, a rise in the temperature causes the faster diffusion resulting in the increment of quenching constant. While in the static process, an increment in the temperature leads to decreases in the quenching constant.

Moreover, to validate the mode of possible quenching mechanism exhibited by the full length BsDAH7PS on the binding of ligands we have used the Stern-Volmer equation (SV) and analyzed the fluorescence data of all titrations experiments by the following equation.

$$F_o/F = 1 + K_{SV}[Q] = 1 + k_q \tau o\ [Q]$$

Where F_o and F denote the fluorescence intensity in the absence and the presence of quencher (ligands) respectively, [Q] is the concentration of quencher (ligand) and K_{SV} is the Stern-Volmer constant. To calculate the value of the k_q, the value of the protein fluorescence lifetime (τo) in the absence of the quencher (ligand) was taken 10^{-8} s [349]. Here, on the fitting of the data in the SV equation, linear plots on all ligands binding with the BsDAH7PS were obtained as shown in the figure 4.8A, 4.8B & 4.8C. Generally, a linear plot defines whether a quenching process is static or dynamic, whereas a nonlinear plot defines a mixed type quenching mechanism [349, 350].

Furthermore, we have determined the quenching mechanism by calculating K_q value ($K_q = K_{sv}/\tau_o$). For dynamic quenching process K_q found to be less than 10^{10}, whereas for static quenching K_q value found to be higher than 10^{10} value. Herein, K_q values for all ligand-BsDAH7PS interaction were found to $>10^{10}$, which show that possible mechanism of quenching is static and indicated the formation of the ground state protein-ligand complexes [350-352]. Table 4.3 is showing the values of K_{sv}, K_q, and R^2 (goodness of fit).

Table 4.3 Quenching constants (K_q) and Stern-Volmer constants (K_{SV}) derived from SV equation on the ligands binding with BsDAH7PS.

Ligand	**K_{sv} (M^{-1})**	**K_q ($M^{-1}S^{-1}$)**	**R^2**
CHL	1.73×10^5	1.73×10^{13}	0.94
PRT	1×10^4	1×10^{12}	0.95
FER	1.52×10^4	1.52×10^{12}	0.99
SKA	4.0×10^4	4.0×10^{12}	0.99

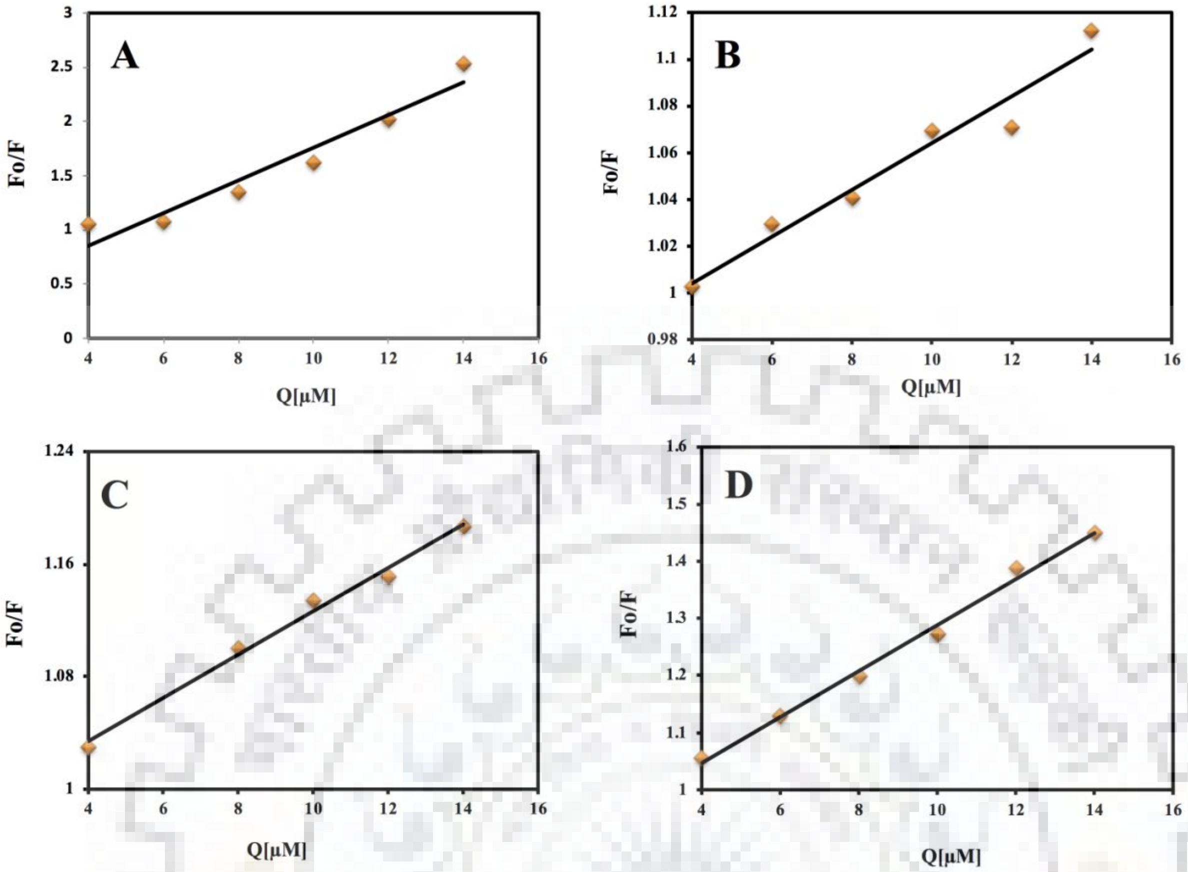

Figure 4.8: Stern-Volmer plots analysis of BsDAH7PS. **(A)** & **(B)** Stern-Volmer plots of BsDAH7PS with CHL and PRE, respectively. **(C)** & **(D)** Stern-Volmer plots of BsDAH7PS with FER and SKA, respectively.

4.3.5. Isothermal titration calorimetry

The detailed thermodynamic parameters (ΔG, ΔH, ΔS) of the molecular interactions of these ligands with the BsDAH7PS were explored using the ITC. Here, we have measured the binding affinities of all these ligands and their representative isotherms are shown in the figure 4.9A, 4.9B, 4.9C & 4.9D, respectively. The downward trends as observed in CHL, PRE, FER, and SKA interactions depict the exothermic nature of reactions. All the data were fitted in a sequential binding site model keeping 4 binding sites to evaluate the binding affinities. Subsequently, BsDAH7PS affinities for all ligands were also calculated by measuring the K_D ($1/K_a$) (Table 4.4). All of these reactions are spontaneous in nature as evident from the negative value of free energy change ($\Delta G<0$) as depicted in the table 4.4[353].

Table 4.4 Thermodynamic binding parameters of BsDAH7PS with inhibitors.

Ligand	**K_D (µM)**	**ΔH (cal/mol)**	**ΔS (cal/mol/deg)**	**ΔG (cal/mol)**
CHL	K_{D1} = 13.85	$\Delta H1 = -1.773\times10^4$	ΔS1= -37.2	ΔG1= -6644
	K_{D2} = 9.17	$\Delta H2 = 3.150\times10^4$	ΔS2= 129	ΔG2 = -6942
	K_{D3} = 8.54	$\Delta H3 = -8.395\times10^4$	ΔS3= -258	ΔG3= -7066
	K_{D4}= 8.4	$\Delta H4 = -6.509\times10^4$	ΔS4= 241	ΔG4= -6728
FER	K_{D1} = 12.2	$\Delta H1 = -1.090\times10^4$	ΔS1 = -14.1	ΔG1 = -6699
	K_{D2} =31.4	ΔH2= 9299	ΔS2= 51.8	ΔG2 = -6137
	K_{D3} =29.4	ΔH3= -5798	ΔS3= 1.28	ΔG3= -6179
	K_{D4} =3.25	ΔH4= -5831	ΔS4= 5.55	ΔG4= -7484
PRE	K_{D1} = 105.1	ΔH1= -4360	ΔS1= 3.58	ΔG1= -5426
	K_{D2} = 47.84	ΔH2= 3899	ΔS2= 32.8	ΔG2 = -5875
	K_{D3} = 55.55	ΔH3= -2889	ΔS3= 9.78	ΔG3= -5803
	K_{D4}= 61.72	ΔH4= -129.2	ΔS4= 18.8	ΔG4= -5731
SKA	K_{D1} = 26.52	ΔH1= -6277	ΔS1=- 0.115	ΔG1= 6311
	K_{D2} =7.04	$\Delta H2 = 1.255\times10^4$	ΔS2= 65.6	ΔG2 = -7018
	K_{D3} = 9.43	$\Delta H3 = -1.968\times10^4$	ΔS3= -43.0	ΔG3= -6866
	K_{D4}= 9.80	$\Delta H4 = 1.393\times10^4$	ΔS4= 69.6	ΔG4= -6810

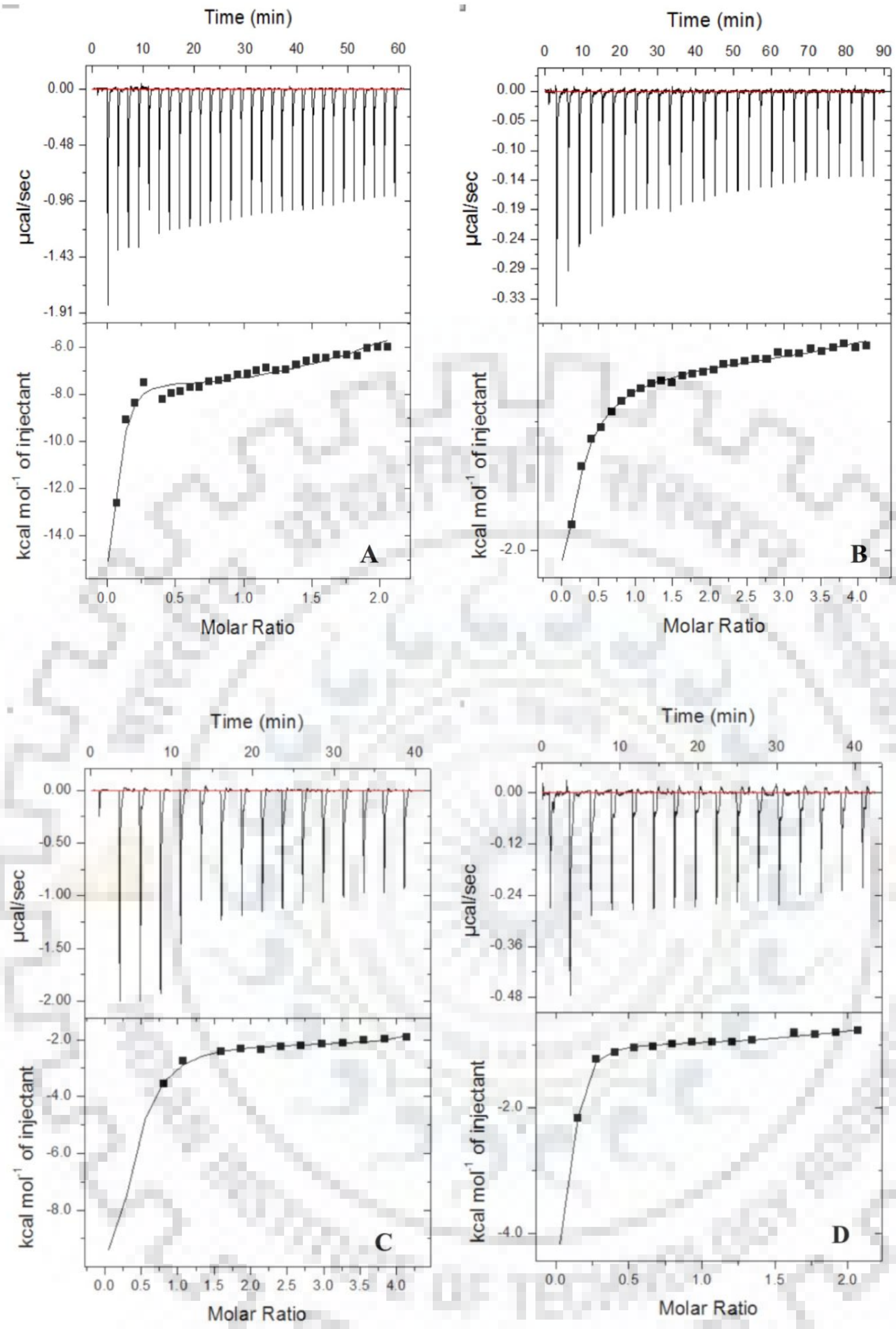

Figure 4.9: ITC profiles of BsDAH7PS describing the binding of ligands. (A) BsDAH7PS-CHL, **(B)** BsDAH7PS-PRE, **(C)** BsDAH7PS-FER **(D)** BsDAH7PS- SKA systems. The upper panel is showing the thermogram (thermal power Vs time) after baseline correction, and lower panel is showing the binding isotherm (normalized heat vs molar ratio of reactants). Binding of all the compounds with BsDAH7PS are exothermic reactions.

4.3.6 Sequence analysis and molecular modeling

Multiple sequence alignment (MSA) of full length BsDAH7PS with other homologs and the *E.coli* CM domain (EcCM) was performed using ClustalW server. BsDAH7PS exhibited the highest (81 %) identity with the GsDAH7PS and 76 % identity with the LmDAH7PS and showed the 56 % identity with the unregulated PfDAH7PS. Further sequence analysis has revealed that despite the very low sequence identity between the CM domain of BsDAH7PS and EcCM both of these proteins contain conserved catalytic polar residues (Arg10, Arg27, Lys38, Glu51, and Gln86) at their active sites. But exhibit the presence of the different type of hydrophobic residues; EcCM contain Ala32, Val35, Ile81, and Val85 and CM domain of BsDAH7PS contain Val31, Ile34, Phe79, Leu83. Additionally, an important residue Ser84 of EcCM replaced with the Gly84 in BsDAH7PS (Figure 4.10). Moreover, BsDAH7PS exhibit the presence of $_{150}$RGGAFKPRTS$_{160}$ sequence, and which contains the RxxxxxxKPRT(S/T) phosphate binding motif as also present in the other reported Type I DAH7PS. Figure 4.11 is showing the MSA profile of BsDAH7PS with other homologs which is generated using Espript [354].

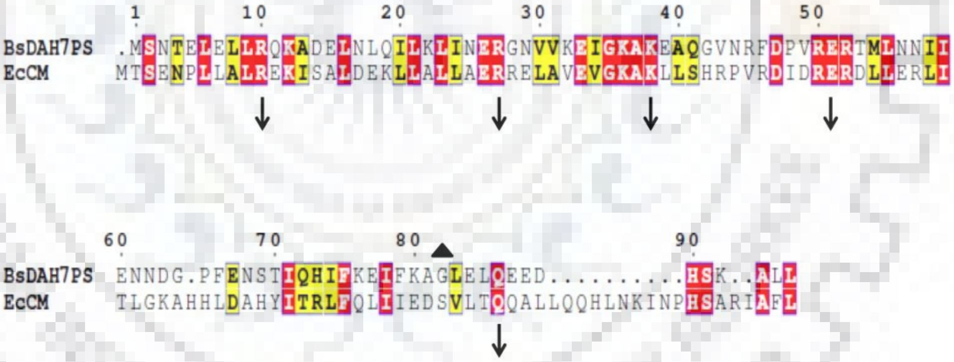

Figure 4.10: Pairwise sequence alignment. The sequence region encoding the regulatory CM domain of the BsDAH7PS protein was aligned with the EcCM protein sequence. The downward black arrows under the sequence indicate the conserved catalytic polar residues (Arg10, Arg27, Lys38, Glu51, and Gln86) at their active sites. Additionally, an important residue Ser84 of EcCM replaced with the Gly84 in BsDAH7PS and indicated as triangle.

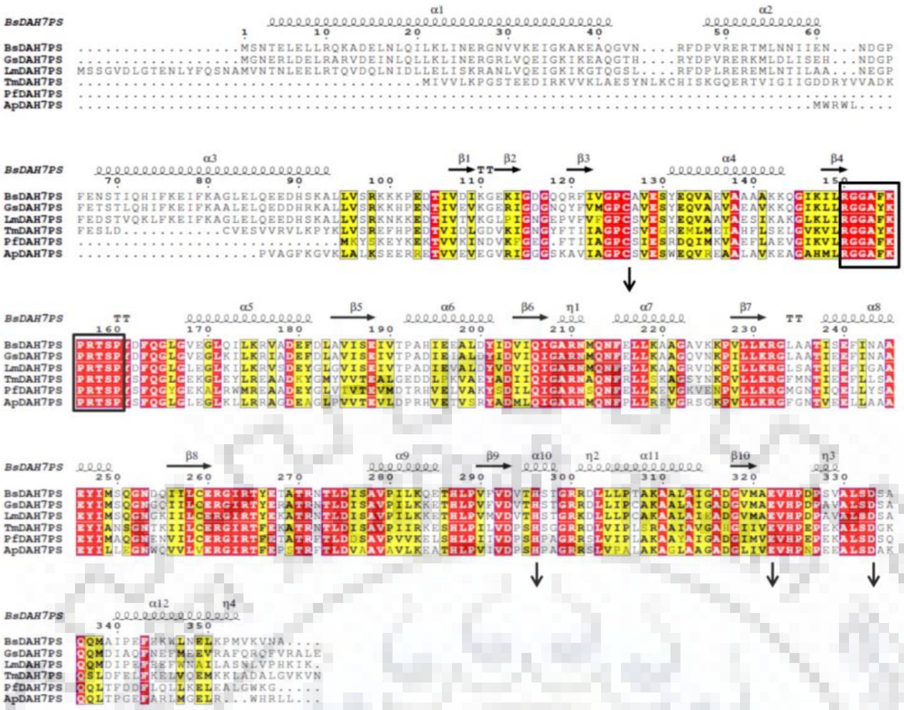

Figure 4.11: The multiple sequence alignment. BsDAH7PS sequence was aligned with the other TypeIβ DAH7PS protein sequences, GsDAH7PS, LmDAH7PS, TmDAH7PS, PfDAH7PS, and ApDAH7PS. The identical and similar residues are shown in red and yellow color, respectively. The presence of $_{150}$RGGAFKPRTS$_{160}$ sequence, which contains the RxxxxxxKPRT(S/T) conserved phosphate binding motif of the Type I DAH7PS enclosed in the black color box. The downward black arrows under the sequence indicate the conserved metal binding residues at the active site. The alignment figure was prepared using ESPript3.

As the 3D structure of the full length BsDAH7PS is currently not available, we performed the homology modeling to predict the 3D structure. For this purpose firstly, we followed a similarity search with BsDAH7PS against PDB database by using NCBI-BLAST and search revealed best suitable template (PDB ID 56JF) sequence identity 81.0 % and 98.0 % query coverage. The best-generated 3D model was selected and its quality was assessed by using PROCHECK, Verify3D package of the SAVES server. The Ramachandran plot analysis was performed to validate the backbone dihedral angles of the generated model. In the refined BsDAH7PS model, 94.2 % of the residues were in the favored region, 5.8 % in the allowed region (Figure 4.12A). This clearly indicated that the backbone dihedral angles Φ and Ψ in the BsDAH7PS model were reasonably accurate. In the PROCHECK result, the generated model was correctly passed and Verify 3D [65] result revealed that 92.31 % of the residues have an averaged 3D1D score > =0.2. These results demonstrated that the folding energy patterns of the predicted BsDAH7PS model is in complete agreement and also supported the correctness of the predicted model. Furthermore, ProSA server gives the Z score value - 9.22, which lies within the range of scores generally found for the protein native 3D structures, determined by NMR and X-ray crystallography (Figure 4.12B). In the ERRAT plot analysis, the overall quality factor value of the BsDAH7PS model was found 97.0 % which indicated the good quality of the predicted model, where good resolution structures always show value ~ 95 % or a higher value (Figure 4.12C). The ProQ server was revealed the LG score (3.698) and MaxSub score (0.250) of the predicted model also indicated very good quality.

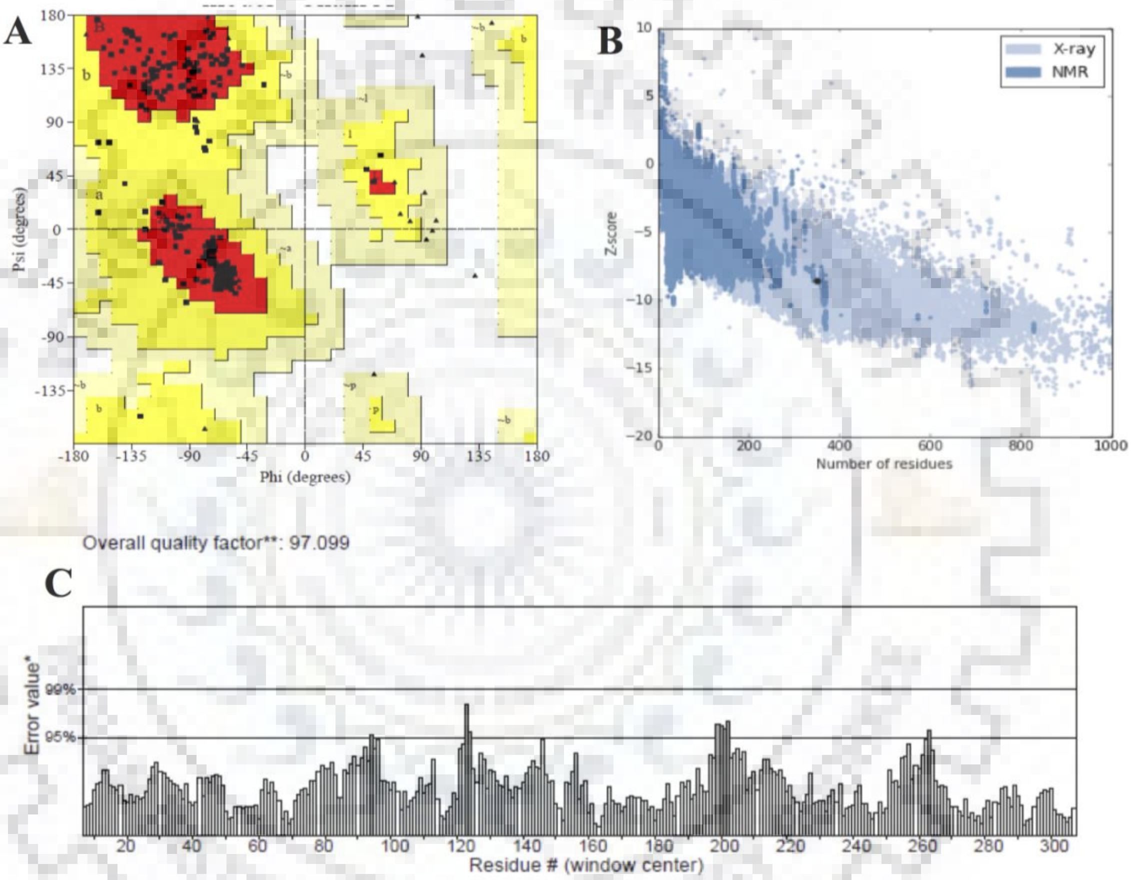

Figure 4.12: Structure validation of the predicted BsDAH7PS model. (A) Ramachandran plot of the predicted 3D model of the BsDAH7PS. **(B)** ProSA-web Z-scores of the predicted 3D model of BsDAH7PS (black dot) in relation to all proteins deposited in Protein Data Bank determined by X-ray crystallography (light blue) or NMR (dark blue) with respect to their length, the plot showing only chains with less than 1,000 residues and a Z-score >10. **(C)** ERRAT plot of the BsDAH7PS showing the overall quality factor or ERRAT score of the model.

The overall structure of the BsDAH7PS is composed by a core catalytic TIM $(\beta/\alpha)_8$ barrel (106-362 residues) as commonly reported in the all characterized DAH7PS and a regulatory

CM domain (1-86 residues) which connected with the catalytic domain via a short linker region (86-105 residues) (Figure 4.13). The active site of CM domain and DAH7PS catalytic domain were also found conserved as reported in the GsDAH7PS structure. Moreover, the conserved metal coordinating residues Cys126, His296, Glu322, and Asp333 are also identified at the C-terminal end of the barrel. Thus, the predicted 3D model of the BsDAH7PS was satisfactorily accurate and used further molecular docking studies.

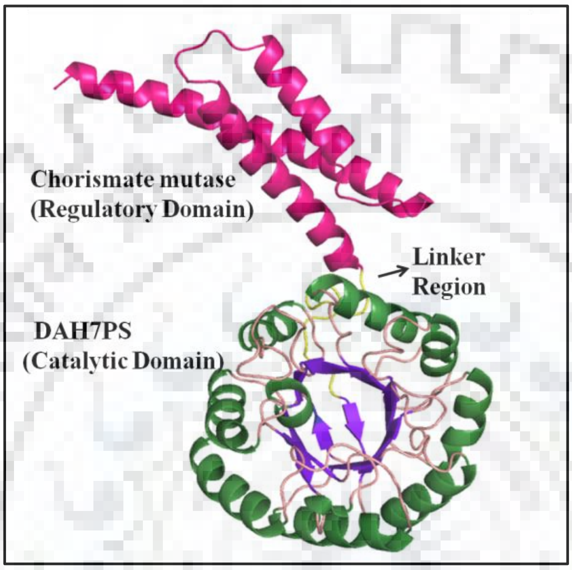

Figure 4.13: Molecular modeling of full length BsDAH7PS. Cartoon diagram showing the best 3D generated model of BsDAH7PS. The secondary structure elements of the two domains belong to the regulatory CM domain and the catalytic DAH7PS domain are depicted in the different colors. α-helices of CM regulatory domain (hot pink color), linker region has shown in yellow color and β- sheets (purple color) of TIM barrel catalytic DAH7PS domain and α-helices (green color) and loops (light pink).

4.3.7 Molecular docking

The molecular docking studies are routinely used for the better understanding of drug-protein interaction in the modern drug designing and development process [355, 356]. Therefore, in order to get further insights of the binding modes and affinities of the CHL, PRE, SKA and FER compounds. The molecular docking of ligands with the dimer regulatory CM domain of the full length BsDAH7PS was performed using AutoDock4. The program is utilized to predict the binding affinities (i.e., how strongly any ligand binds to a receptor) and the CHL exhibited the maximum binding affinity -8.0 kcal mol^{-1} and followed by the PRE -7.3 kcalmol^{-1} and SKA and FER exhibited -7.0 kcalmol^{-1} and -6.0 kcalmol^{-1} binding affinities, respectively (Table 4.5). All ligands were found to be interacted in a similar fashion with the CM domain's residues of the BsDAH7PS as found in the reported crystal structures (PDB ID 5UMG & 56JF). The binding modes of all ligands have been shown in the figure 4.14.

Table 4.5 Selective binding interactions of McLpxC with inhibitors.

Compound	**Hydrogen bonded residues**	**Other interacted residues**	**Binding energy (kcalmol^{-1})**
PRE	Arg27, Arg50, Glu51, and Arg10*	Phe79, Met54, Lys38 and Asp47	-7.3
CHL	Arg27, Arg50, Glu51 Lys38, Asp47, Gln86 and Arg10*	Gly82, Leu83, Val36, Val31, Asp47, Ile34 and Ala13*	-8.0
SKA	Arg27, Glu51, Arg50, and Arg10*	Phe79, Asp47, Lys38, and Met54	-7.0
FER	Asp47	Gln86, Leu83, Arg50, Glu51, Lys83, Met54, Ile34, Ala13*and Arg10*	-6.0

CHL interacted with protein via polar Arg27, Arg50, Glu51, Lys38, Asp47, Gln86 (Chain A) and Arg10*(Chain B) of dimeric CM domain of BsDAH7PS found involved in the H-bonding and Gly82, Leu83, Val36, Val31, Asp47, Ile34 (Chain A) and Ala13* (Chain B) residues involved in the hydrophobic and other interactions (Figure 4.14A).

Similarly, PRE and SKA also interacted via the polar interactions and Arg27, Arg50, Glu51 (Chain A) and Arg10*(Chain B) polar residues of the CM domain are found involved in the hydrogen bonding (Figure 4.14B & 4.14D). The other residues Phe79, Met54, Lys38, and Asp47 (Chain A) of the active site are implicated in the hydrophobic and Van der-Waals interactions. Whereas, FER is formed H-bonding with Asp47 only and Gln86, Leu83, Arg50, Glu51, Lys83, Met54, Ile34, (Chain A) and Ala13*and Arg10*(Chain B) majorly contributed to the other hydrophobic and non-polar interactions (Figure 4.14C).

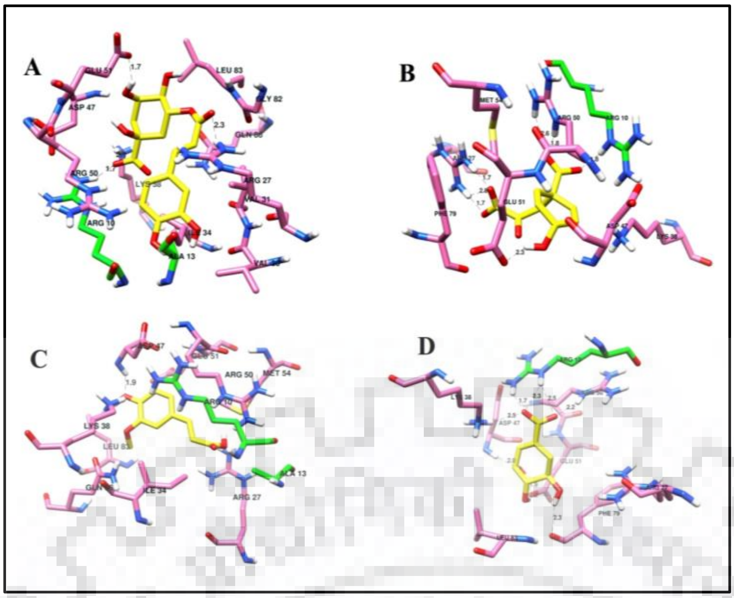

Figure 4.14: Molecular docking studies. (A) & **(B)** Docking poses of the BsDAH7PS with CHL and PRE, respectively. **(C)** & **(D)** Docking poses of the BsDAH7PS with FER and SKA, respectively. Interacting residues with the ligands belong to chain A of the dimeric BsDAH7PS are shown as the pink color sticks and residues of the chain B are shown as green color sticks. Hydrogen bonds are shown as black color dash lines. Docked ligands are shown as yellow color sticks.

4.3.8 Growth inhibition assays

Further, *in vivo* inhibition efficacies of the CHL, PRE, SKA, and FER were assessed by the whole cell growth inhibition assays and Minimum inhibitory concentration (MIC) values of all compounds were measured against *B. subtilis* using the broth microdilution method. CHL has shown the maximum inhibition of the bacterial growth with a MIC value of 30-40 µg/ml and followed by the FER (60-80 µg/ml). While the MIC values of SKA and PRE were found very higher range (~ 2.5 mg/ml) in comparison to the CHL and FER.

4.4 Discussion

The emergence of drug resistance and weakening of the efficacy of currently available antimicrobial agents against microbes are pressing the need to explore the potential drug targets and the development of novel broad-spectrum and multi-targeted antibacterial agents [4, 357] [358]. Natural compounds from the various sources have been explored and studied, which may offer a wide range of the chemical scaffolds for the development and designing of new antimicrobial molecules [359, 360]. Chlorogenic acid (CHL) is the ester of caffeic acid and quinic acid, one of the most abundant polyphenols in the human diet and has exhibited the antibacterial and the anti-cancerous activities [361, 362]. However, the exact molecular mechanism of these activities is still elusive. Recently, our group members have crystallized a truncated CM domain of the bifunctional DAH7PS (Type Iβ) with the CHL and also explored it's the antibacterial effect in the whole cell-based inhibition assays. In the present study, we have explored the detailed binding and inhibition of the full length BsDAH7PS with CHL and compared with the other compounds like PRE, SKA, and FER which also synthesized in the Shikimate pathway.

In the far-UV CD results, an increase in the negative ellipticity at 208 nm and 220 nm on these ligands binding clearly reveal a characteristic gain of α-helical content and loss in the β-sheets content. Similarly, the recently reported ligands bound crystal structures of the truncated CM domain with CHL from the *B. subtilis* (PDB ID 5UMG) [92] and a full length GsDAH7PS with the PRE ((PDB ID 5J6F) [91] have revealed the shortening of the loop (L1) and extension of the helix (H1) and adoption of a more compact form upon ligand binding at their CM domain active site. In the closed and more compact form, domain-domain interface formation occurs between CM domain and DAH7PS catalytic domain of the protein which limits the accessibility of the substrate to the catalytic (DAH7PS) domain site and inhibits its enzymatic activity.

Furthermore, the binding of these ligands with the full length BsDAH7PS was resulted into the decrease in the fluorescence intensity and formation of the ground state ligand-protein complex. Additionally, a red shift in the emission maximum of the BsDAH7PS depicts the increment in the hydrophilic environment surrounding the aromatic amino acids and evident the conformational changes in the DAH7PS catalytic domain. Thus, Trp346 might have moved toward the outer surface and due to conformational changes on ligands binding.

The plausible interacted residues involved in the binding of these ligands to BsDAH7PS were also investigated by the molecular docking studies. The binding pose of these ligands were compared with the crystal structure bound with CHL (PDB ID 5UMG) bound and PRE PDB ID 5J6F) and the interacting residues were determined. The binding locations of CHL, PRE, SKA, and FER were found at CM domain of BsDAH7PS and similar to the co-crystallized CHL and PRE structures. CHL, PRE, and SKA were interacting with the Arg27, Arg50, Glu51 and Arg10* via H-bonding. The binding of FER with BsDAH7PS did not show any H-bonding interaction with the Arg27 and Arg10*residues and it was showing lesser binding affinity (-6.0 kcalmol^{-1}) than other three ligands. It showed only the van der Waals and hydrophobic interactions forces are involved in the binding. Moreover, if we see the chemical structures of these polyphenols as shown in figure 4.1 and observe the differences in their hydroxyl and methoxy group patterns in the ring, which may be responsible for the variation in the binding energies and dissociation constant values. FER (2E)-3-(4-hydroxy-3-methoxyphenyl)-2-propenoic acid) has a hydrophobic methyl group in the ring and its presence made it more hydrophobic in comparison to the other CHL, SKA, and FER.

Further, as we have observed the binding features of these compounds from the ITC data, during the course of the binding of all ligands the K_D values were decreasing, which indicate the increment in their binding affinity. If we compare the final K_D values of all these ligands, CHL and SKA showed the same ~10 μM range but FER has a lower (~ 3.5 μM) K_D value i.e., high binding affinity. But in the docking studies, FER exhibited the lower binding in comparison to the other. FER has also shown the different inhibition mechanism (un-competitive) in the biochemical kinetic inhibition study. Thus, we can presume that the binding of FER with BsDAH7PS may have occurred in the different manner as followed by the other ligands.

4.5 Conclusion and future perspectives

In the current study, we have described the binding and inhibitory aspects of the polyphenols compounds (CHL, PRE, FER, and SKA) with bifunctional DAH7PS from *B. subtilis* using biochemical, biophysical, and *in silico* methods. The CD and fluorescence spectroscopic results have suggested that binding of the polyphenols at the CM domain active site of the full length BsDAH7PS enhanced the helical content and reduced the flexibility of the protein. Our results also determine that the fluorescence quenching mechanism of BsDAH7PS is a static process. Among these polyphenolic compounds chlorogenic acid and prephenate have shown the stronger binding affinity and growth inhibition with BsDAH7PS in comparison to the other compounds. Further, crystal structure of the full length BsDAH7PS complexed with the studied compounds (CHL, PRE, FER, and SKA) will provide the insights on the regulation and inhibition mechanism of the BsDAH7PS. Moreover, in future designing and optimization of more promising analog compounds on the basis of these scaffold will be helpful to obtained multi-targeted antibacterial agents.

CHAPTER 5

BIOCHEMICAL, BIOPHYSICAL AND STRUCTURAL CHARACTERIZATION OF LPXC FROM *MORAXELLA CATARRHALIS* (McLpxC)

5.1 Introduction

Moraxella catarrhalis, an aerobic Gram-negative drug resistant bacterium, infects both upper and lower respiratory systems, and causes otitis media, pneumonia, sinusitis, acute bronchitis, endocarditis, septicemia and meningitis like other clinical isolates such as *Streptococcus pneumonia* and *Hemophilus influenza* [363]. The prevalence, varying patterns of the resistance and the ability of *M. catarrhalis* to produce different β-lactamases emphasize the attention towards this species and the necessity to explore the potential drug targets to develop novel antimicrobial agents [364, 365].

Gram-negative bacteria contain an outer membrane (OM), which surrounds the cell wall and protects them from many antimicrobial agents [366]. This OM is composed of lipopolysaccharide molecule (LPS), which contains three components: O-antigen, a core polysaccharide, and lipid A [112, 367, 368]. Lipid A is synthesized via the nine enzymes of the LPS biosynthesis pathway. The committed step of this pathway is catalyzed by a zinc metalloenzyme UDP-3-O-(R-3-Hydroxymyristoyl)-N-acetylglucosamine deacetylase (LpxC). It hydrolyzes the *N*-acetylglucosamine molecule into glucosamine and acetate. LpxC is conserved and shows no homology to any human and mammalian enzyme making it suitable target for the development of new antibacterial agents [369-371].

In the last few decades, several LpxC inhibitors exhibiting potent activity against diverse bacteria have been reported in the literature [372]. Mostly, all characterized inhibitors share common structural features contain a hydroximic acid-based head group, which chelates catalytic Zn^{2+}, and a lipophilic side chain that accommodates in the hydrophobic tunnel of the LpxC. Initially, phenyloxazoline-based (L-573, 655, L-161, 240) and a sulfonamide based (BB-78485) compounds were characterized and these showed inhibition only against *Escherichia* *coli* [209, 373]. Subsequently, *N*-aroyl-L-threonine derivative (CHIR-090), a potent inhibitor was developed, which demonstrated the effectiveness against various Gram-negative bacteria including *Pseudomonas aeruginosa* [169]. Till now, an inhibitor developed by Achaogen (ACHN-975), that targets the wide range of LpxC from several bacterial species and exhibits the IC_{50} in nanomolar range against *P. aeruginosa* has only entered the clinical trials on human [218, 374].

Recently, methylsulfone hydroxamate-based inhibitors showing impressive activity and spectrum against a variety of Gram-negative bacteria have been developed. LpxC-4, a pyridone-substituted molecule of this series (LpxC-4) has shown the potent antibacterial activity against *E. coli, Enterobacter spp., P. aeruginosa, Klebsiella pneumonia, Burkholderia cepacia, Burkholderia pseudomallei, Stenotrophomonas maltophilia and Acinetobacter baumannii* [375-377]. However, the effectiveness and differential susceptibility of this series are yet to be systematically investigated against other more bacterial species.

Several reports have shown that LpxC exhibits large conformational variations and diverse morphologies of the active site and hydrophobic passage upon different inhibitors binding. The occurrence of the conformational changes is primarily responsible for the variation in the susceptibility of different inhibitors of the LpxC [204, 212]. Therefore, the identification of structural differences and conformational changes in LpxC on the binding of various inhibitors is essentially required to be explored for the development of the board spectrum inhibitory molecules.

Here, we have cloned, expressed, and purified LpxC enzyme from *M. catarrhalis* (McLpxC). Furthermore, we have investigated the binding features of McLpxC with the most LpxC-4 inhibitor and also compared it with LpxC-2 inhibitor using circular dichroism and fluorescence spectroscopy. Subsequently, we have used Isothermal titration calorimetric (ITC) to determine the thermodynamic parameters of binding of these inhibitors. The modeling and docking studies have been performed to analyze the molecular interactions and selective binding mode of the inhibitors. Furthermore, we have performed growth inhibition assays and evaluated the minimum inhibitory concentration (MIC) values of both inhibitors against the *M. catarrhalis.* The current study may be significant in the expectation of methylsulfone hydroxamate-based inhibitors for progress towards the clinical trials and development of broad spectrum antibiotics.

5.2 Materials and methods

5.2.1 Reagents and chemicals

All restriction enzymes, DNA polymerase and T4 DNA ligase were purchased from New England Bio Labs. All kits for plasmid isolation, purification and gel extraction were taken from Quiagen. All media components were purchased from HiMedia (India). All other chemicals and inhibitors were purchased from Sigma.

5.2.2 Cloning and expression of the McLpxC

The genomic DNA of *M. catarrhalis* (MTCC No.445) was extracted and McLpxC gene was amplified using the forward (5'-GGAC**CATATG**ACAAAACTCTACCAAAGAACGGTAGCC-3') and reverse primers (5'-GACC**CTCGAG**CTAAACAGCAGCTACATAATTAATTGGACAAGA-3'), which were designed by introducing NdeI and XhoI restriction sites, respectively. The amplified product was extracted and purified by kit methods. Both the pET28c His-Tev vector and amplified gene purified product were digested with the same restriction enzymes and ligated by using T4 DNA ligase for the construction of the pET-McLpxC recombinant plasmid. The ligated product was transformed into the *E. coli* (DH5α) cells. The sequence of the pET-McLpxC plasmid was subsequently validated by DNA sequencing. The recombinant pET-McLpxC plasmid was transformed into the Rosetta *E. coli* cells for the expression of the soluble McLpxC protein. The McLpxC was over expressed by inducing the culture (0.8 O.D) with the addition of 0.4 mM isopropyl-β-D-thiogalactopyranoside (IPTG) and 100 µM $ZnSO_4$, and further grown at the 25 °C and 200 rpm for next the 6 h. Bacterial cells were harvested by centrifugation at 6000 rpm for 15 min at 4 °C and pellets were stored at - 80 °C.

5.2.3 Purification of McLpxC by affinity chromatography

The pellets were resuspended in the lysis buffer (25 mM Tris-HCl pH 7.8, 200 mM NaCl, 5 % glycerol, 5 mM imidazole 200 µM $MgCl_2$, 0.1 mM DTT) and disrupted using the high-pressure French press system. The solubilized cell lysate was clarified by centrifugation at 12000 rpm for 1 h at 4 °C and the clear supernatant was separated from the cell debris. Then the supernatant was applied onto the pre-equilibrated Ni-NTA affinity column. To remove the impurities, the column was washed with the ~ 10-bed volumes of washing buffer I (15 mM imidazole) and buffer II (30 mM imidazole). The target protein was eluted in the wash buffer III (100 mM imidazole) and elution buffer (150 mM imidazole) fractions. The purity of the elution fractions was analyzed by 12 % SDS -PAGE gel electrophoresis with Tris-glycine buffer (pH 8.3) at 80 V for 3 h. The McLpxC pure fractions were pooled and concentrated upto the desired concentration using the Amicon Ultra-15 concentrators (10 kDa cutoff).

5.2.4 Fluorescence-based enzymatic activity assay of McLpxC

The enzymatic activity of the McLpxC was determined using a fluorescence-based assay with slight modifications [206]. In brief, UDP-GlcNAc, a commercially available substrate analog of the LpxC natural substrate was used due to unavailability of natural substrate. The deacetylation of the UDP-GlcNAc was measured by the detection of the free amine generated by the catalysis of McLpxC. The reaction mixture containing 50 mM Bis-Tris buffer, 100 mM NaCl, and 1 mM TCEP (pH 7.5) and 1.0 mM UDP-GlcNAc was pre-equilibrated at 25 °C and deacetylation reaction was initiated by the addition of enzyme (2 μM) and proceeded for the 30 min. The sample containing free amine was diluted fourfold with the 0.5 M Borate buffer (pH-9.0) and generated free amine was reacted with the fluorescamine dye, which was dissolved in the dimethylformamide (DMF), and resulted into the fluorescence signal. The fluorescence was measured by excitation at 395 nm and emission at 485 nm by using the FLUOstar OPTIMA plate reader. The activity of the McLpxC was also measured at different concentrations of the substrate i.e., UDP-GlcNAc (100-3000 µM), for the determination of the steady-state parameters, k_{cat}, K_m, and k_{cat}/K_m. and all the reactions were performed in triplicates. The obtained data were fitted by using the nonlinear regression analysis of graph pad prism software [246].

5.2.5 Kinetic inhibition of McLpxC

The inhibitors (LpxC-4 and LpxC-2) tested against the McLpxC were dissolved in the DMSO. The chemical structures of both the inhibitors used in this study have shown in the figure 5.1. Dose dependent IC_{50} values of both inhibitors were calculated at the constant substrate concentration (100 μM). McLpxC protein was incubated with the inhibitors for 30 min at 4 °C and deacetylation reaction was initiated by adding substrate. The detection of the generated free amine was done by following the fluorescence-based assay as described in the previous section.

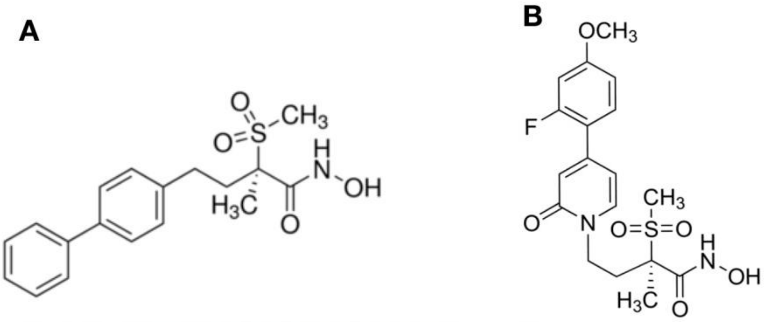

Figure 5.1: Chemical structures of the inhibitors. (A) LpxC-2 structure. **(B)** LpxC-4 structure.

5.2.6 Antibacterial susceptibility assay

To determine the minimum inhibitory concentration (MIC) of both inhibitors against the *M. catarrhalis* we performed the whole-cell antimicrobial activity assay by using the approved method described by Clinical and Laboratory Standards Institute [92, 341]. The culture of *M. catarrhalis* was grown overnight and adjusted upto 5×10^5 CFU/mL in the by diluting with the broth. Inhibitors were prepared in DMSO and added in 2-fold serial dilutions manner (0.1 µg/ml - 64 µg/ml) to all wells of 96-well microtiter plate except growth control and sterility control wells. Diluted culture, 50 µl was then added to all wells except sterility control and plates were further incubated at 37 °C for 16 h. Finally, MIC values were determined at the lowest concentration of inhibitors that completely inhibited visual bacterial growth.

5.2.7 Circular dichroism spectroscopy

The CD spectral studies of McLpxC were performed with the Jasco 1500 spectropolarimeter equipped with the thermostat Peltier system. The purified McLpxC was diluted to a final concentration of 0.2 mg/ml. A baseline with the buffer was acquired and corrected before the acquisition of the protein spectra. All the spectra were collected by using a quartz cuvette (0.1 mm) of 1 nm bandwidths with a 100 nm/min scanning speed at the room temperature. Three scans of each sample were collected and then averaged and smoothed. All spectra were finalized by subtracting the spectral contribution of each ligand. Finally, the data were analyzed and percentages of the secondary structure elements were predicted by using the DichroWeb online server with the CONTILL analysis algorithm [346]. All the results were expressed in molar ellipticity ($\Delta\varepsilon$) in deg. $cm^2.dmol^{-1}$, which is defined as per the following equation:

$$\Delta\varepsilon = \frac{\theta\,(\mathrm{mdeg}) \times 0.1 \times \mathrm{MRW}}{P \times \mathrm{C} \times 3298}$$

Where MRW is mean residue weight (Molecular weight of protein / no. of residues -1), P is the path length in cm, C is molar concentration of McLpxC protein and 3298 is the constant.

5.2.8 Fluorescence spectroscopy

The fluorescence studies of McLpxC were performed by using the spectrofluorometer Fluorolog®- 3 (Jobin Yvon Inc.USA) equipped with the Xe lamp. A quartz cuvette of the 1.0 cm was used during all the experiments. The McLpxC was diluted to the 5 µM and the excitation wavelength was kept at 295 nm to excite the Trp residues of the protein specifically. The intrinsic emission spectra of the protein were recorded from 300 to 500 nm. The fluorescence quenching of McLpxC protein with the inhibitors was also measured by increasing the amounts of the inhibitors (LpxC-4 and LpxC-2) from the range 1- 20 µM in the cuvette.

5.2.9 Isothermal titration calorimetry assays

The binding of both inhibitors with McLpxC was performed by using Microcal ITC200 (GE healthcare) at 25 °C. The purified McLpxC protein was extensively dialyzed against buffer (25 mM Tris-Buffer, pH 7.8, 100 mM NaCl, 2% glycerol and 0.5 mM TCEP) and inhibitors were dissolved in the DMSO. In order to prevent the buffer-buffer mismatch during the titration reaction, an amount of DMSO (~1%) was also added to the protein. Further, all the solutions were degassed under vacuum for 10 min on the MicroCal's thermovac unit to prevent the air bubbles formation inside the calorimeter cell. Briefly, the calorimeter syringe was filled with inhibitors (0.25 - 1.0 mM each) and the sample cell was filled with the McLpxC protein (50-100 µM). The stirring speed was kept constant at 800 rpm and 15-20 successive injections of inhibitor (2.0 µl each) with 180 seconds gap were allowed with the initial delay of 60 seconds. The change in the heat during titration reaction was monitored. The resulting data were fitted to the suitable model using MicroCal Origin software and the Gibbs free energy change is determined by the following equation:

$$\Delta G = \Delta H - T\Delta S$$

Here, ΔG represents the Gibbs free energy change (ΔG), ΔH is the enthalpy change, and ΔS is entropy change and T is the absolute temperature.

5.2.10 Sequence analysis and molecular modeling

The multiple sequence alignment of the McLpxC with other homolog sequences was done by using the ClustalW program with default parameters [333]. The template selection was done to the generation of the 3D model of the McLpxC from the Protein Data Bank using the BLASTp. The model building was performed by using the best-suited template with the Swiss-Model server [331] and Modeller program [332]. The stereo chemical quality and validation of the generated models were done by PROCHECK, ERRAT, PROVE, Verify3D [312], ProSA and ProQ analysis [337, 378].

5.2.11 Molecular docking studies

AutoDock 4 and MGLTools 1.5.4 were used to perform all the docking studies between the McLpxC and its inhibitors. Subsequently, the ligands were converted into pdbqt files using OpenBabel software and used as an input to AutoDock4 [339]. The McLpxC was enclosed in a 40 Å × 40 Å × 40 Å box with the number of grid points in xyz directions, and a grid spacing of 0.375 Å and all other parameters were used as default settings. The docking simulations were performed by using the Lamarckian genetic algorithm. The McLpxC-inhibitor complex structure having the lowest energy docked conformation was taken for the further analysis using Chimera [379].

5.3 Results

5.3.1 Molecular cloning, expression and purification of the McLpxC

M. catarrhalis genome encoded the McLpxC gene was successfully amplified and cloned (Figure 5.2A). The construction of the recombinant plasmid pET-McLpxC was validated by the restriction digestion and DNA sequencing results. Furthermore, the positive clone was successfully transformed into the host *E. coli* (Rosetta cells) and McLpxC protein was over-expressed by inducing it with 0.4 mM IPTG at 25 °C. The McLpxC was purified via immobilized metal-affinity chromatography (IMAC). The purified His-tagged McLpxC exhibited a single band of ~ 33 kDa size on the 12 % SDS-PAGE (Figure 5.2B). The fractions containing pure McLpxC were pooled and concentrated up to the desired concentration and used for the further studies.

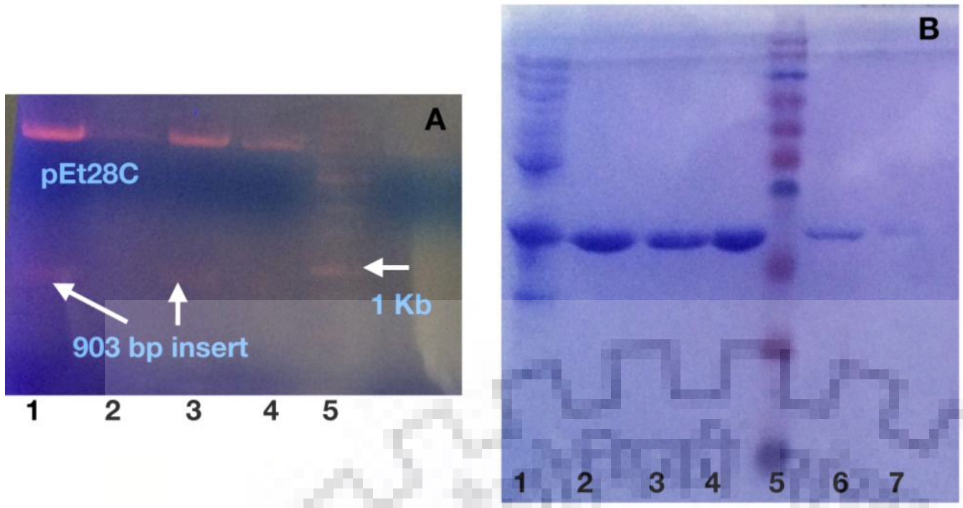

Figure 5.2: Molecular cloning and purification profile of McLpxC. (A) 1 % agarose gel electrophoresis profile on restriction digestion; Lane 1-3 showing ~ 903 bp insert of McLpxC gene, Lane 2 & 4 plasmid only, Lane 5 Molecular ladder **(C)** Purification profile of the McLpxC protein; Lane 1-4 showing the bands of the His-tagged McLpxC protein (~33kDa) on the 12% SDS-PAGE gel, Lane 5 Molecular weight marker (kDa), Lane 6-7 Purified McLpxC.

5.3.2 Enzymatic activity and inhibition assays

A fluorescence-based assay was performed to determine the deacetylation activity of the McLpxC with a commercially available surrogate substrate (UDP-GlcNAc). The deacetylation of UDP-GlcNAc by McLpxC was carried out and the detection of a fluorescent signal with fluorescamine dye clearly suggested that the primary amine was generated during the deacetylation reaction catalyzed by the McLpxC. The steady-state parameters K_m, k_{cat}, and k_{cat}/K_m were calculated by fitting the data into the Michaelis–Menten equation and we observed $K_m = 302.7 \pm 27.90$ (µM), $k_{cat} = 0.855 \pm .02\ S^{-1}$, $k_{cat}/K_m = 2.82 \times 10^3\ M^{-1}S^{-1}$ and $V_{max} = 8.55 \pm 0.193$ µmol min^{-1} for UDP-GlcNAc (Figure 5.3A & 5.3B). Herein, we observed that K_m value of this surrogate substrate is much larger than (150-fold) the K_m value (2.1 µM) of the natural substrate (*R*-3-hydroxymyristoyl group) of other LpxC orthologs. Moreover, the inhibitory effect of the LpxC-4 and LpxC-2 was also determined and IC_{50} values of both the inhibitors have been calculated at the constant substrate concentration (100 µM) by using the non-linear regression analysis. LpxC-4 has shown more inhibitory activity against McLpxC with IC_{50} value 26.0 ± 1.2 µM in comparison to LpxC-2, which has IC_{50} value 39.0 ± 2.45 µM (Figure 5.3C & 5.3D). Subsequently, to determine the antimicrobial susceptibility of both the inhibitors against the *M. catarrhalis*, whole-cell antimicrobial activity assays were performed using the broth micro-dilution in the 96-wells microtitre plate and the MIC values of the LpxC-4 and LpxC-2 were 16 ± 5 µg/ml and 32 ± 7 µg/ml, respectively.

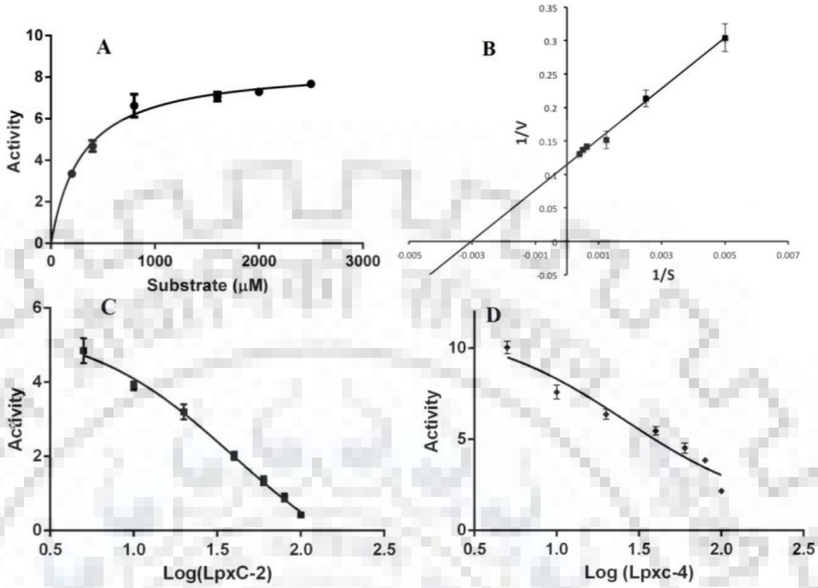

Figure 5.3: Biochemical characterization of McLpxC. (A) Kinetic analysis of McLpxC with the substrate analog and the enzymatic activity is expressed here in µM min^{-1}. Initial velocities were determined with increasing concentration of substrate (UDP-GlcNAc). **(B)** Double reciprocal plot. Data were analyzed using non-linear regression analysis. **(C)** & **(D)** Dose response curves (IC$_{50}$) of the McLpxC with LpxC-2 and LpxC-4 inhibitor, respectively.

5.3.3 CD spectroscopic studies

5.3.3.1 CD measurements of the McLpxC

In the far-UV CD spectrum, native McLpxC exhibited the two negative minima at 208 nm and 220 nm, and maxima at the 194 nm and single broad minima at 210-220 nm. These characteristic bands clearly notified the α-helical and β-sheet contents of the McLpxC (Figure 5.4A) [261, 300] . In the CD spectrum of α-helix, 208 nm and 222 nm bands occur due to the π-π* and n-π* transitions of peptide bonds respectively. In β-sheets and random coils, the occurrence of a minimum at 215 nm and a maxima at 192-198 nm are due to the n-π* and π-π* transitions of the peptide bonds respectively [344, 380]. Moreover, the secondary structure content of the McLpxC was also calculated using CONTINLL method program of the dichroweb server. The native McLpxC depicted the ~22.0 % helical, ~ 23.0 % sheets, ~ 27.1 % turns, and ~ 27.6 % disordered structures (Figure 5.4A). Additionally, in the near UV spectrum, the native McLpxC showed a few remarkable fine bands at the 300-310 nm, 270-280 nm and 260-270 nm contributed by Trp, Tyr and Phe residues, respectively (Figure 5.4B). The near-UV spectrum of the protein is due to the presence of the aromatic amino acids residues.

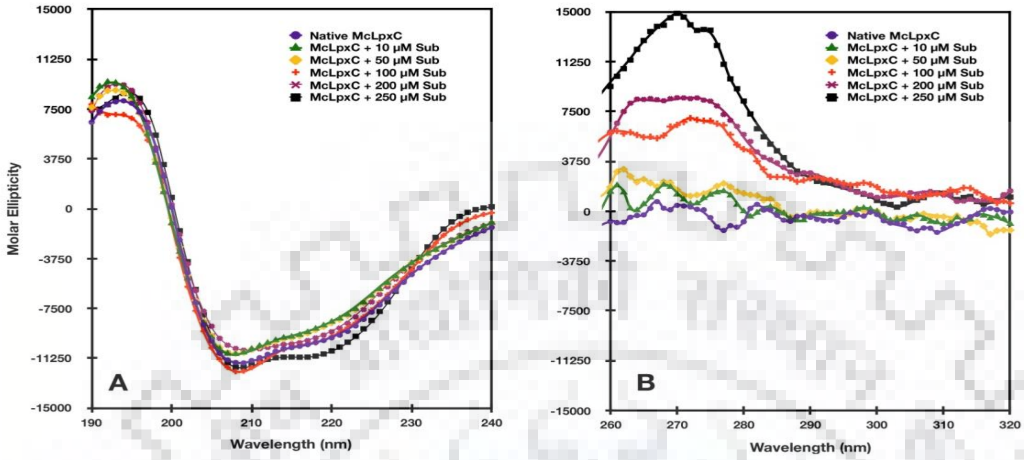

Figure 5.4: Circular dichroism measurements. (A) & (B) The far-UV and near-UV CD spectra of the McLpxC under the native condition and as well as with the varying concentration of the substrate (UDP-GlcNAc).

5.3.3.2 Effect of the substrate binding

Furthermore, initially on substrate binding at the lower concentration (10-50 μM), McLpxC showed a slight increase in the helical content and estimated ~ 25-27 % in comparison to the native McLpxC (~ 22 %). Similarly, on the higher concentration (200-250 μM) of the substrate, two clearly separated negative peaks at 208 nm and 220 nm were depicted and indicated an increase in the helical content and it reached upto 30 %. Whereas, the β-sheets content of the McLpxC was decreased and reached upto 17 % on the high concentration of substrate binding. Thus, on the substrate binding, changes in the McLpxC secondary structures were observed. Moreover, in the near-UV spectral profile of McLpxC, we observed that the region from 260 nm to 280 nm, contributed by the Phe residues, considerably shift toward the positive ellipticity with the increasing concentration of the substrate. Simultaneously, a few changes in the region from 280 nm to 305 nm, due to the Tyr and Trp residues respectively, on high substrate concentration (Figure 5.4B).

5.3.3.3 Effect of the Inhibitors binding

Additionally, we compared the far-UV and near-UV CD spectra profile of McLpxC in the presence of varying concentrations of both the inhibitors. Interestingly, we observed a remarkable difference in the far-UV spectra of McLpxC in the presence both the inhibitors as shown in the figure 5.5A & 5.5B. Here, McLpxC has shown a drastic loss in ellipticity at the 208 nm and 220 nm and a considerable shift of the peak at 226 nm that suggesting a loss in helical content and generation of the β-sheets on high concentration of the LpxC-4 inhibitor (Figure 5.5A). Similarly, on the LpxC-2 binding, McLpxC also showed a gradual decrease in the α-helical content an increment in the β-sheets with increasing concentration of the inhibitor (Figure 5.5B). Subsequently, in the near-UV spectral profile, we observed a remarkable increment in the negative value of ellipticity in the region from 250 to 270 nm at the higher concentration of the LpxC-4, which determines the increment in the flexibility of phenylalanine residues (Figure 5.5C). On the other hand, McLpxC showed the increment in ellipticity values toward the positive direction in all the three 255-270 nm, 275-305 nm and 285-305 nm region in the presence of the LpxC-2 (Figure 5.5D).

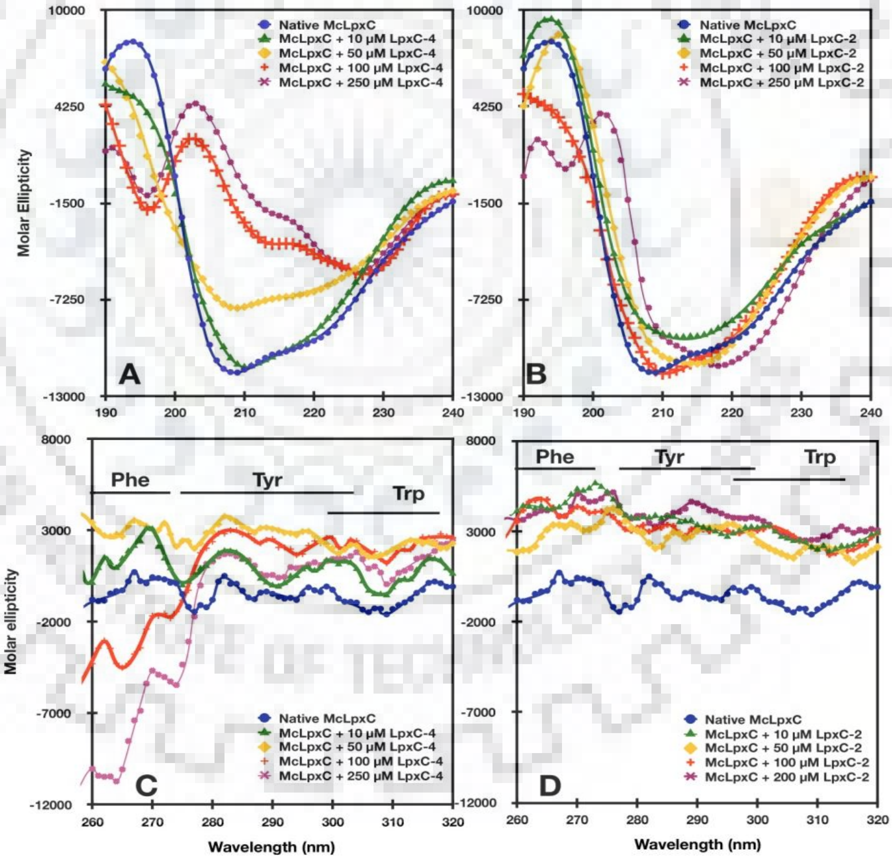

Figure 5.5: Effect of the inhibitors on the McLpxC. (A) & **(B)** The far-UV spectra in the varying concentration of the LpxC-4 and LpxC-2 inhibitor respectively. **(C)** & **(D)** Near-UV CD spectra of the McLpxC in the varying amount of the LpxC-4 and LpxC-2 inhibitor, respectively.

The overall changes in the secondary structure content of McLpxC with varying concentrations of substrate and inhibitors were calculated by online Dichroweb server and have been shown in the figure 5.6A, 5.6B & 5.6C. These findings suggest that changes in the secondary and tertiary structure of McLpxC occurred on binding of both the inhibitors.

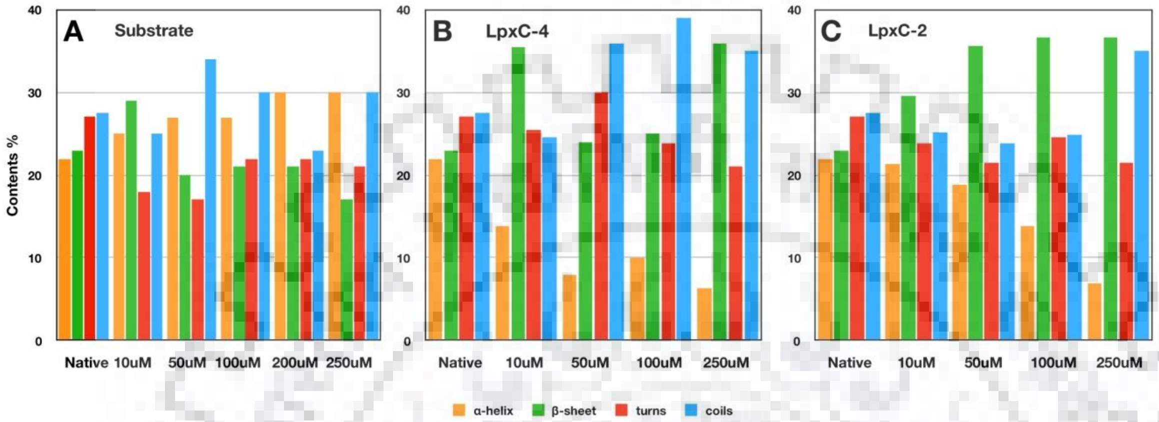

Figure 5.6: Secondary structure content of McLpxC. (A) The percentages of the secondary structure content upon the substrate binding. **(B)** & **(C)** The percentages of the secondary structure content on the LpxC-4 and LpxC-2 inhibitor, respectively.

5.3.4 Fluorescence quenching mechanism

The occurrence of the conformational changes and the molecular basis of the McLpxC binding with the inhibitors and the substrate were investigated by measuring the tryptophan specific intrinsic fluorescence and quenching mechanism. The McLpxC has shown the presence of surface exposed Trp residue. The intrinsic fluorescence spectral profile of the McLpxC depicted an emission maximum at the ~ 348 nm, when excited at the 295 nm specifically to the Trp, clearly suggesting that the Trp143 residue in the native McLpxC is located towards the surface and interacts with the solvent. In addition, the interaction of the substrate with McLpxC has exhibited a decrease in the Trp fluorescence intensity and a concomitant blue shift in the emission maximum (Figure 5.7A). The emission of the Trp residues in a protein provides the details about its surrounding environment and polarity of solvent. A characterstic blue shift in the emission maximum of proteins generally depicts a decrement in the polarity (i.e., invrement in hydrophobicity) of environment surrounding the Trp residue [347]. Thus, Trp143 in McLpxC might also have moved toward hydrophobic environment due to the conformational changes occur in structure of McLpxC on the binding of substrate.

Furthermore, the interactions of the inhibitors with the McLpxC were also studied by evaluating the fluorescence quenching. The quenching is generally defined as the decrease in the fluorescent intensity of a protein on the ligand binding, which can occur due to the different molecular mechanisms like molecular rearrangements, excited-state reactions, ground-state complex formation, energy transfer, and collisional quenching [347]. Herein, we have measured the changes in the intensity of the McLpxC in the fluorescence spectra profile by adding the substrate and both the inhibitors in varying concentrations. The LpxC-2 binding with McLpxC is exhibited ~ 20 % loss in the fluorescence intensity and a blue shift in emission spectrum (Figure 5.7B). The binding of LpxC-4 with McLpxC, has shown ~ 30 % loss in the fluorescence intensity with a concomitant red shift (~ 12-14 nm) in the emission maxima (Figure 5.7C). Thus, LpxC-4 causes more quenching and places the fluorophore of McLpxC towards the more hydrophilic environment, which might have occurred due to the large conformational changes in the structure of McLpxC, in comparison to the LpxC-2.

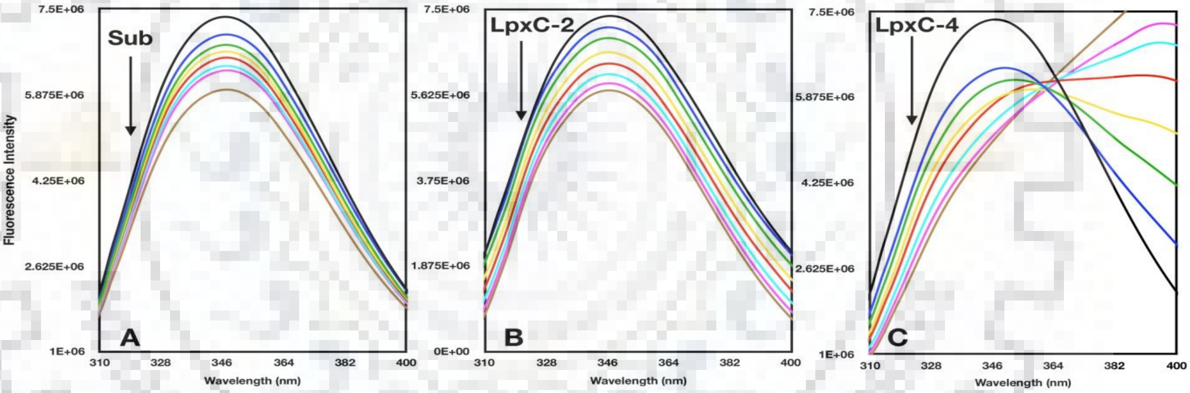

Figure 5.7: Fluorescence based quenching studies. The intrinsic fluorescence emission spectra of native McLpxC and the quenching effect of ligands on its fluorescence intensity at 25 °C (λex = 295 nm); **(A)** McLpxC-substrate analog, **(B)** McLpxC-LpxC-2, **(C)** McLpxC-LpxC-4 system.

5.3.4.1 Quenching mechanism determination

Quenching of the protein fluorescence is either a dynamic or a static process depending on the temperature and the viscosity. The dynamic quenching (collisional) occurs due to the interaction of the quencher with an excited fluorophore and rise in the temperature causes the faster diffusion resulting in the increment of quenching constants. Contrastingly, in the static quenching process, occurring due to the interaction of fluorophore and quencher in ground-state, the increment in the temperature leads to the dissociation of bound complexes, which decreases the quenching constant [347, 348].

Moreover, to validate the mode of possible quenching mechanism exhibited by the McLpxC on the binding of inhibitors we have used the Stern–Volmer equation (SV) and analyzed the fluorescence data of all titrations experiments by the following equation.

$$F_o/F = 1+ K_{SV}[Q]= 1+k_q \tau o \,[Q]$$

Where F_o and F denotes the fluorescence intensity in the absence and the presence of quencher (inhibitor) respectively, [Q] is the quencher (inhibitor) concentration and K_{SV} is the Stern-Volmer constant. To calculate the value of the k_q, the value of the McLpxC fluorescence lifetime (τo) in the absence of the quencher (inhibitor) was taken 10^{-8} s [349].

Here, on the fitting of the data in the SV equation, linear plots on both the inhibitors and substarte binding with the McLpxC were obtained as shown in the figure 5.8A, 5.8B & 5.8C. Generally, a linear plot defines whether a quenching process is static or dynamic whereas a nonlinear plot defines a mixed type quenching mechanism.

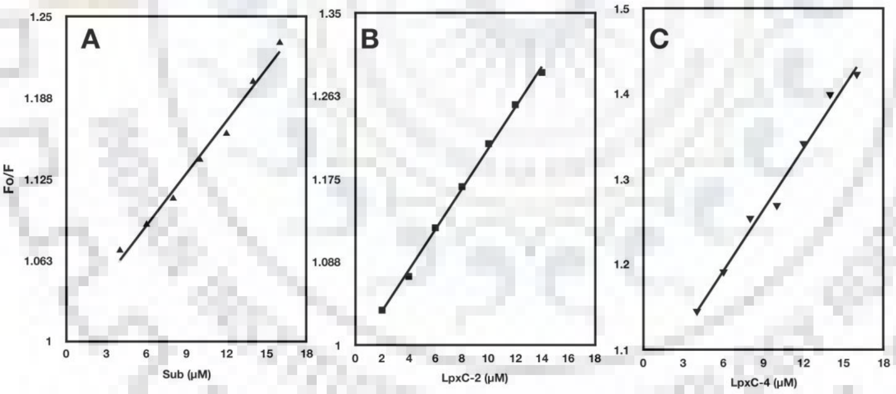

Figure 5.8: Quenching mechanism studies of the McLpxC. (A) Stern-Volmer plots of the McLpxC with substrate. **(B & C)** Stern-Volmer plots of the McLpxC with LpxC-2 and LpxC-4, respectively.

Further, the bimolecular quenching constant (kq values) and the Stern-Volmer constant (K_{SV} values) were also calculated and shown in the Table 1 and quenching mechanism was determined. The value of k_q constant can differentiate between the static and dynamic quenching process, the value of the k_q constant higher than the 10^{10} $M^{-1}S^{-1}$ clearly indicates the static quenching mechanism (ground-state complex formation) whereas a value lower than ~ 10^{10} $M^{-1}S^{-1}$ indicates the dynamic quenching mechanism [351] [352]. Thus, the values are shown in the Table 1 suggest that the binding of the inhibitors with McLpxC caused static quenching mechanism and a ground state complex was formed between McLpxC and the inhibitors.

Table 5.1 Quenching constants (K_q) and Stern Volmer constants (K_{SV}) derived from SV equation on the inhibitors binding with McLpxC

Inhibitor	**K*sv* (M^{-1})**	**K_q ($M^{-1}S^{-1}$)**	**R^2**
LpxC-4	2.38×10^4	2.38×10^{12}	0.98
LpxC-2	2.9×10^3	2.9×10^{11}	0.90
Substrate	9.2×10^3	9.2×10^{11}	0.96

5.3.5 Thermodynamics of inhibitors binding to McLpxC

ITC is one of the fastest emerging biophysical and label-free techniques, which determines the various biological interactions and provides the detailed thermodynamic profile (ΔG, ΔH, ΔS) and measures the heat absorbed or released during any molecular interaction process [381, 382]. Here, we have determined the binding affinity of LpxC-4 and LpxC-2 for McLpxC by using ITC at 25 °C and their representative isotherms are shown in the figure 5.9A & 5.9B, respectively. The titration curves exhibited the negative peaks in the plots, which suggest that the interaction between McLpxC and the inhibitors is exothermic. All the data were fitted in a sequential binding site model keeping 3 binding sites to evaluate the binding affinities. Here, the binding reactions of both LpxC-4 and LpxC-2 were enthalpy driven and exothermic nature as depicted from the negative values of the enthalpies ($\Delta H < 0$). This suggested that the polar interactions were the major contributing forces in the LpxC-4 binding, whereas the positive values of the entropy ($\Delta S > 0$) in LpxC-2 denoted some contributions of the hydrophobic interaction along with the polar forces.

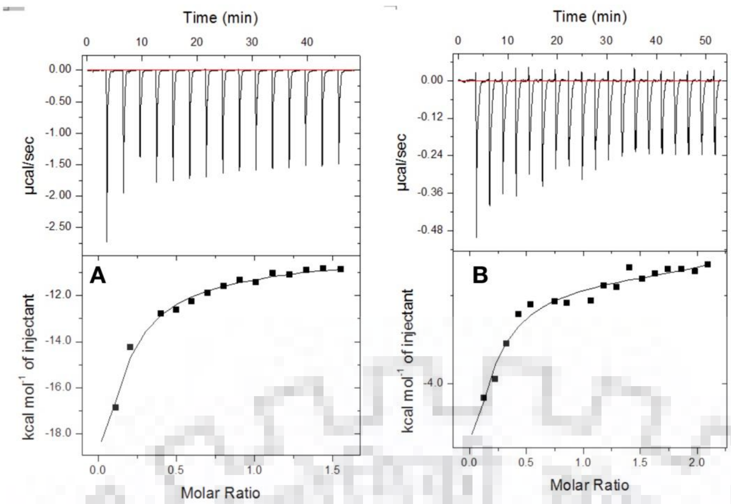

Figure 5.9: ITC studies of McLpxC describing the thermodynamics parameters. (A) McLpxC-LpxC-4, **(B)** McLpxC-LpxC-2 systems. The upper panel is showing the thermogram (thermal power Vs time) after baseline correction, and lower panel is showing the binding isotherm (normalized heat vs molar ratio of reactants). Binding of both inhibitors to McLpxC are showing exothermic reactions.

Both of these reactions were spontaneous in nature as evident from the negative value of free energy change (ΔG<0). Subsequently, McLpxC affinities for both inhibitors were also calculated by measuring the K_D ($1/K_a$). Here, it should be noted that LpxC-4 and LpxC-2 have the comparable binding affinity with McLpxC as shown in the table 5.2.

Table 5.2 Thermodynamic parameters of McLpxC.

Inhibitor	**K_D (µM)**	**ΔH (cal/mol)**	**ΔS (cal/mol/deg)**	**ΔG (cal/mol)**
LpxC-4	K_{D1} = 10.79 K_{D2} = 8.92 K_{D3} = 9.8	ΔH1= -2.07×10^4 ΔH2=2821 ΔH3= -2.331×10^4	ΔS1= -46.8 ΔS2= 32.6 ΔS3= -55.2	ΔG1= -6753.6 ΔG2 = -6893 ΔG3= -6860
LpxC-2	K_{D1} = 10.55 K_{D2} =10.85 K_{D3} =11.64	ΔH1= -5156 ΔH2= 100.8 ΔH3= -5408	ΔS1 = 5.47 ΔS2= 23.1 ΔS3= 4.45	ΔG1 = -6786 ΔG2 = -6783 ΔG3= -6734

5.3.6 Sequence analysis and molecular modeling of McLpxC

The LpxC of the *P. aeruginosa* (PaLpxC) (PDB ID: 2VES) was selected as the best-suited template for the McLpxC, which showed highest 53 % sequence identity and the 98 % query coverage. The sequence alignment showed that residues secondary structural elements were found conserved among target (McLpxC) and template (PaLpxC) (Figure 5.10). Further, in McLpxC, the essential Zn^{2+} binding motif (HKXXD) is conserved from 238 to 243 residues (HKMLD), which is similar to the Zn^{2+} binding motif of the EcLpxC and AaLpxC and dissimilar to the Zn^{2+}binding motif (HKILD) of the PaLpxC. As the earlier reported LpxC, McLpxC also depicted the presence of the conserved Phe 161, Phe 192, and Phe 194 residues, which forms a hydrophobic patch at the active site of LpxC (Figure5.11). Furthermore, the PROCHECK and Verify 3D (an averaged 3D1D score > =0.2 of 92.23% residues) results supported the correctness of the generated 3D model. Subsequently, the Ramachandran plot analysis clearly indicated that the backbone dihedral angles Φ and Ψ in the McLpxC model were reasonably accurate.

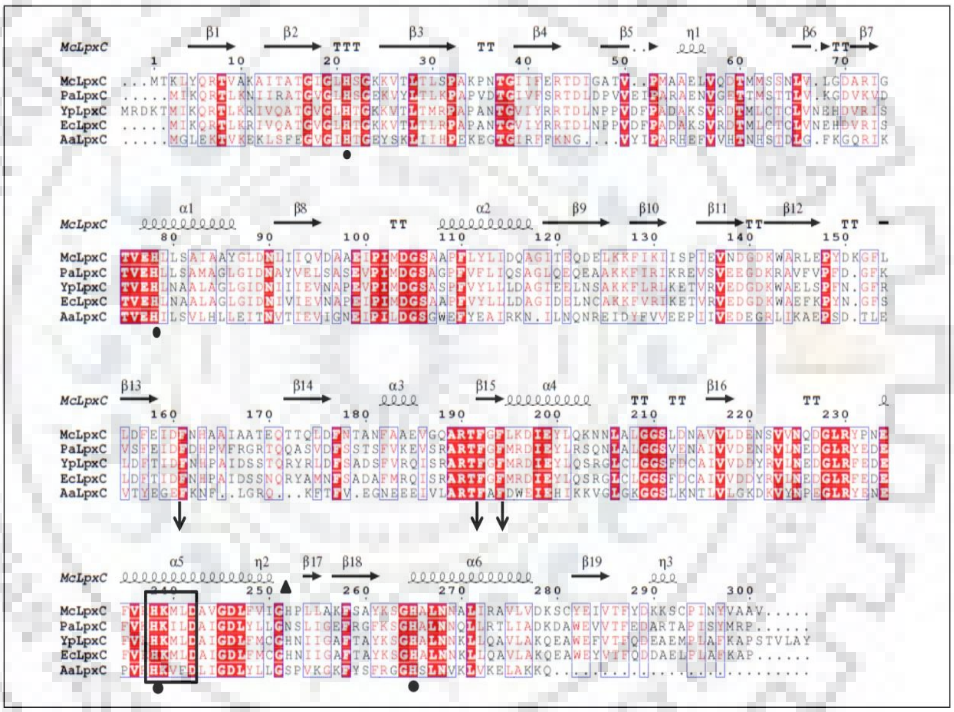

Figure 5.10: Multiple sequence alignment of McLpxC. The McLpxC sequence was aligned with *P. aeruginosa* (PaLpxC), *Yersinia pestis* (YpLpxC), *E. coli* (EcLpxC), *Aquifex aeolicus* (AaLpxC). Conserved identical residues are shown in red color background and the zinc binding motif (HKXXD residues) enclosed in a black box. The downward black arrows under the residues indicate the conserved hydrophobic residues (Phe) from hydrophobic patch at the active site. Black filled circles indicate the four conserved His residues, whereas triangle indicates the His252 in the McLpxC likely to the EcLpxC. The alignment figure was prepared using ESPript3.

The overall structure of the McLpxC contains two domains; domain I and domain II and connected via a 16-residue long linker. Each domain consists of two major α-helices and a five-stranded β-sheets which cover the helices from each end as shown in the figure 5.11A. Each domain of the McLpxC depicted an identical topology of secondary structure despite a significant difference in the amino acid sequence. Additionally, both domains contain a unique insert region (Insert I of Domain I and Insert II of Domain II) that adopts a distinct structure. Insert I form a small three-stranded β-sheet that partially defines the boundary of the active site located at the interface of these two domains, whereas Insert II adopts a β-α-β structure that forms a topologically closed hydrophobic tunnel which occupies the fatty acyl chain of the substrate during the catalytic activity of the protein as well as inhibitors (Figure5.11A). The active site of the McLpxC is surrounded by Met61, Met62, Ser63, Asn225, Leu212, Ala207, and Gln202 residues (Figure 5.11B) and the active site of the PaLpxC contained the Thr61, Met62, Ser63, Asn224, Val211, Ala206, and Arg201 residues (Figure 5.11B). Thus, the comparison of the active site analysis revealed that the active site of the McLpxC is slightly different from the active site of the PaLpxC. The generated 3D model of the McLpxC was further used for the molecular docking analysis.

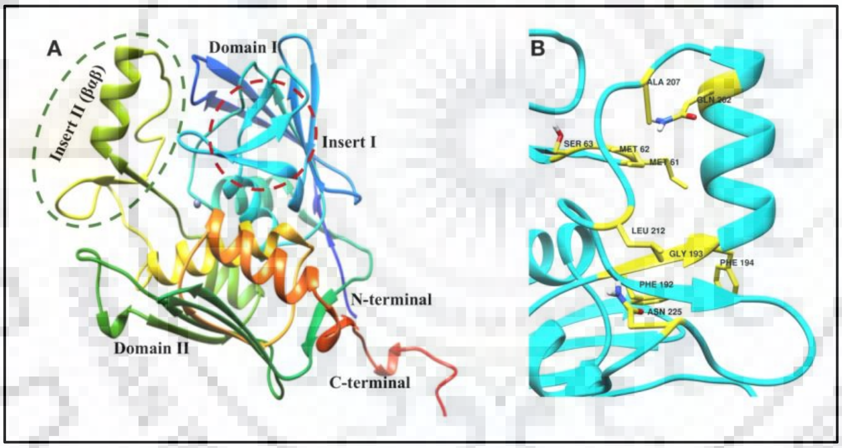

Figure 5.11: Molecular modeling of McLpxC. (A) Ribbon diagram showing the best 3D generated monomeric model of the McLpxC. The secondary structure elements of the two domains that belong to the β–α–α–β unique fold are colored in blue, sky blue, orange, and green, respectively. The insert I and the insert II (β-α-β) regions highlighted in the red and parrot green color circle. **(B)** The active site architecture; key residues of the McLpxC active site have shown as stick representation in yellow color.

5.3.7 Molecular docking

The molecular docking studies were performed to analyze the comparative binding mode of both the inhibitors using AutoDock4. This program is also utilized to predict the binding affinities (kcal mol^{-1}), i.e., how strongly inhibitors bind to the protein, here, LpxC-4 and LpxC-

2 depicted the -10.0 and -9.6 kcal mol^{-1} binding affinities, respectively. Both the inhibitors were well accommodated at the active site pocket of the McLpxC as shown in the figure 5.12A & 5.12B.

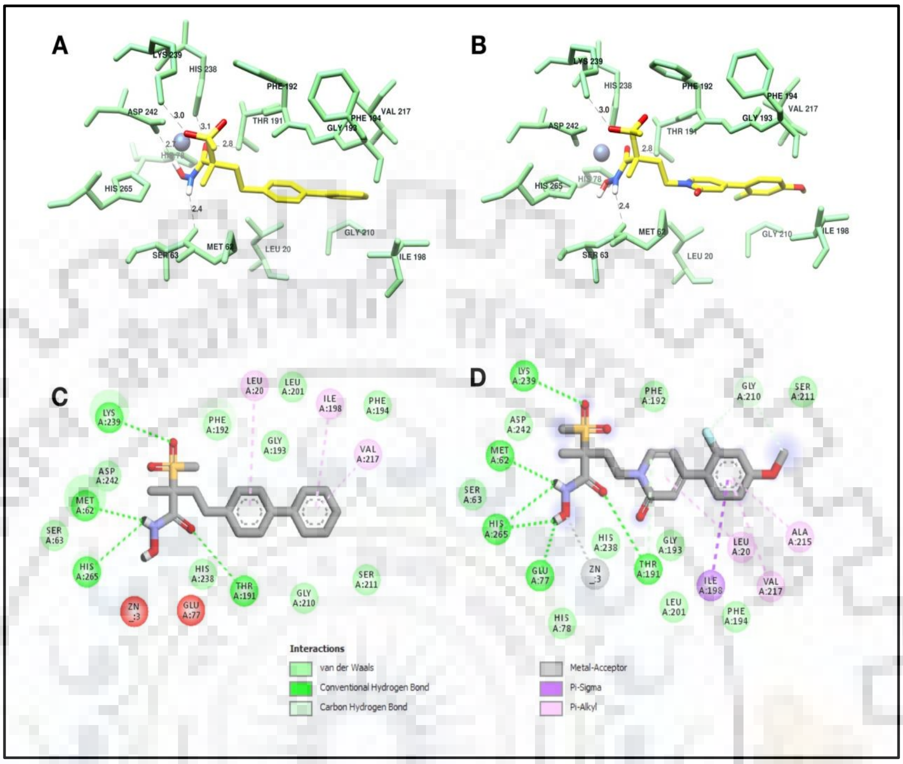

Figure 5.12: Molecular docking studies. (A) & **(B)** Predicted docking poses of the McLpxC with LpxC-2 and LpxC-4 inhibitors, respectively. Interacting residues of the McLpxC with the inhibitors have shown as sticks and colored as light green. Zinc ion has shown in grey color. Hydrogen bonds are shown as black color dash lines. Docked inhibitors are shown in yellow color. **(C)** & **(D)** 2D interaction diagram representing the binding mode of the LpxC-2 and LpxC-4, respectively.

Residues within a 4 Å distance of the inhibitors were selected as the actively participating in the binding of inhibitors (Table 5.3). The following amino acid residues of McLpxC played an active role in the interaction with inhibitors: Met62, Ser63, Lys239, Thr191, Phe192, Gly193, Phe194, His238, His265, Glu77, Gly193, Leu201, GLy210, Leu20, Val217, and Ile198 (Figure 5.12C & 5.12D). The hydroxamate moiety of the inhibitory molecule accommodated towards the Zn^{2+} and phenyl pyridone chain arranged in hydrophobic tunnel of the McLpxC (Figure 5.12A & 5.12B).

Table 5.3 Selective binding interactions of McLpxC with inhibitors.

Inhibitor	**Hydrogen bonded residues**	**Other interacted residues**	**Binding energy (kcalmol^{-1})**
LpxC-4	Lys239, Thr191 Met62, His265, Glu 77	Ser63, Gly193, Gly210, Leu 201, His238, Leu20, Ala 215, Val217,Asp242,His78, Phe192, Ile198	-10.0
LpxC-2	Lys239, Thr191, Met62, His265	Ser63, Gly193, Gly210, Leu 201, Leu20, Val217, Ile198, His265, Ser211	-9.6

The sulfone oxygen atom of the inhibitors made H-bond with the ω-amino group of Lys239, and the carbonyl oxygen of the hydroxamate moiety also formed H-bond with the β-hydroxyl of Thr191of the McLpxC (Figure 5.12C & 5.12D). Moreover, the Ile198 residue of the McLpxC formed π-σ interaction with the pyridone ring, while the Phe192 residue showed π-alkyl mixed hydrophobic interaction with the methyl group of LpxC-4 inhibitor. Another π-σ and π-alkyl mixed hydrophobic interactions in both the inhibitors were depicted between phenyl pyridine of the inhibitors and the aliphatic residues (Leu20, Ala215, and Val217) of the McLpxC as represented in the 2D diagram in figure 5.12C & 5.12D.

5.4 Discussion

Till now, a variety of LpxC inhibitors with different chemical scaffolds have been characterized, but none of them has reached to the clinical trials [218]. Recently, a methyl-sulfone hydroxamate scaffold based series have been developed, which has shown great solubility, favorable physicochemical properties and increased free fraction [216, 375]. Keeping this in view, we have evaluated the inhibitory and binding effect of this series against the McLpxC using the biochemical, biophysical and *in silico* investigations.

In the enzymatic activity assay, the purified McLpxC has shown activity with the substrate analog (UDPGlcNAc), but the K_m value (~302.7±27.90) was higher than the natural substrate (UDP–3-*O*-(*R*-3-hydroxymyristoyl) - *N*-acetylglucosamine) as reported in the other LpxC. It has been clarified in earlier reports that the length of the acyl chain on the 3-*O*-position of the glucosamine unit exhibits a crucial role in determining the binding affinity of the substrate with the LpxC enzyme. The substrate with a long acyl chain shows low K_m value with high binding affinity and catalytic efficiency, whereas a medium length acyl chain has moderate K_m value with sufficient catalytic efficiency [206]. Thus, in this case, the high K_m value of the McLpxC might be due to the variation of the substrate preferences. In the inhibition assays, LpxC-4 exhibits the better inhibitory activity and effectiveness against the *M. catarrhalis* in comparison LpxC-2. Similarly, *In vitro* microbiological assessment of these inhibitors against a wider spectrum of Gram-negative bacteria including *P. aeruginosa and A. baumannii* have been performed and the inhibitors of this series have shown the superior activities compared to the CHIR-90 and meropenem (Table 5.4) [375].

Table 5.4 MIC and IC_{50} the values of the inhibitors with the Gram-negative bacteria

Clinical Isolates	**LpxC-4**		**LpxC-2**		**References**
	MIC_{90} (µg/ml)	**IC_{50} (nM)**	**MIC_{90} (µg/ml)**	**IC_{50} (nM)**	
P.aeruginosa	1	1.1	4	1.4	[375]
E. coli	0.25	0.693	2	ND	
K. pneumonia	1	2.1	16	1.0	
S. maltophilia	2	ND	ND	ND	
B. cepacia	0.5	ND	ND	ND	
A. baumannii	> 64	183	> 32	> 41	

In case of LpxC, several previous studies have suggested that the catalytic domain and the hydrophobic tunnel of LpxC show a few minor, but potential structural differences and conformational changes on the binding with different inhibitors [204, 212, 383]. In the far-UV CD results, a remarkable loss in negative ellipticity at 208 nm and 220 nm and a concomitant shift in the peak at 226 nm clearly reveal the loss of helical content and the generation of the sheets content, concurrently, in the near-UV spectra analysis, an increment in the negative value of the ellipticity (MRE) in the 260-270 nm region depicts the increased flexibility of the Phe residues in McLpxC with the increasing amount of the LpxC-4 inhibitor. Contrastingly, on binding with the LpxC-2 and substrate, McLpxC demonstrated different effects such as, an increment in the positive ellipticity (MRE) values in 260-270 nm region. These features indicate the stabilization and the reduction in the flexibility of the Phe residues in McLpxC on binding with the LpxC-2 inhibitor and the substrate.

According to these findings, we can assume that a few structural rearrangements in the insert II region of domain II, which contains a "β-α-β substructure" might have occurred on inhibitors/substrate binding. The α-helix of this region involves directly in the inhibitors/substrate intercation. Thus, it may be implicit that the inhibitors interaction might be accompanied with the uncoiling/disordering of this α-helix and reduced the flexibility and enhanced the stability of the β-sheets of the "β-α-β substructure". Herein, based on these findings of CD spectroscopic results, we can say that the McLpxC depicts secondary, tertiary structural changes along with substantial conformational changes on binding with different ligands. Similarly, the LpxC of various other bacteria also represented the various conformational changes on binding with different inhibitors [204, 212, 383].

Furthermore, the fluorescence quenching results have shown the formation of a complex between the McLpxC and the ligands (inhibitors and substrate) and also support the similar behavior of structure alternations in the McLpxC on the binding. In intrinsic fluorescence spectra, McLpxC has also shown a distinctive red shift (~12-14 nm), which characterizes the exposure of the Trp143 residue towards the more hydrophilic environment and its interaction with the solvent in the presence of LpxC-4. On the other hand, on the substrate and the LpxC-2 binding, the McLpxC has depicted a blue shift, which defines the increase in the hydrophobicity of the protein [384]. These changes in the microenvironment of the aromatic amino acid residue also evidently show that the LpxC-4 has introduced large conformational changes in the McLpxC in comparison to the LpxC-2 and the substrate. Thus, the overall CD, and fluorescence spectroscopic studies revealed that the binding of the inhibitors with McLpxC lead to the conformational changes in its structure and a ground state complex formation occur on the interaction with the inhibitors/substrate.

Herein, the thermodynamic binding properties of these inhibitors with McLpxC are determined by ITC and the negative values of enthalpy (ΔH) and Gibbs free energy (ΔG) of both the inhibitors suggest the reactions are enthalpy driven and spontaneous in nature. Although, the calculated K_D values determine the comparative binding affinities of both the inhibitors and the enthalpy ($\Delta H<0$) indicates that polar interactions are the major contributing factors. But in case of the LpxC-2, the positive value of entropy (ΔS) also favored the interaction and notify the importance of the hydrophobic interactions are also contributing factor.

In the docking study, the conformation with the most negative energy value and the maximum number of hydrogen bonds represents the strongest and most favorable binding between the protein and drug molecules. The binding mode of the both docked inhibitors has been compared and the overall binding mode is similar and also consistent with the co-crystallized inhibitor. The LpxC-2 forms two H-bond with the Lys239, Thr191 residues, but in the LpxC-4 structure, an electronegative fluorine atom is present, which may form an extra with the residue of the "β-α-β substructure" along with the H-bond formed with Lys239, Thr191 H-bond which are believed to contribute towards the stability of the docked conformations. However, the interaction between McLpxC and its inhibitors cannot be presumed to be exclusively polar in nature; as the hydrophobic tail of the inhibitors well accommodates in the hydrophobic tunnel by forming hydrophobic interacting with the participating residues Phe192, Gly193, and Phe194 of the "β-α-β substructure. Hence, it can be concluded that inhibitors bind to a hydrophobic tunnel located at the active site involving both hydrogen bonding and hydrophobic interactions. The overall study suggests that on the interaction of both inhibitors, the structural behavior of the McLpxC varies and conformational changes occur in a different manner. Hence, the determination and the characterization of such structural and conformational alterations in LpxC, which occur on the binding of inhibitors, might assist the design of more potent inhibitory molecules with a broad-spectrum antibacterial activity.

5.5 Conclusion and future perspectives

The present study, describing the binding aspects of the most potent methyl-sulfone hydroxamate based inhibitors of the LpxC, using biochemical, biophysical, and in silico methods. The biochemical and inhibition studies have shown that both inhibitors can target the LpxC of the drug-resistant *Moraxella catarrhalis*. All the CD, UV, fluorescence spectroscopic results have revealed that pyridone substituted hydroxamate inhibitor introduced more substantial conformational changes in McLpxC structure in comparison to the biphenyl methyl sulfone hydroxamate inhibitor. Further, in-depth analysis of the crystal structures of McLPxC complex with these inhibitors will be helpful to confirm and validate whether the observed structural conformational plasticity variations reflected in McLpxC is only due to the inhibitors binding or an inherent species-specific feature or a combination of both.

References

[1] R.W. Pinner, S.M. Teutsch, L. Simonsen, L.A. Klug, J.M. Graber, M.J. Clarke, R.L. Berkelman, Trends in infectious diseases mortality in the United States, Jama 275(3) (1996) 189-193.

[2] B. Spellberg, J.H. Powers, E.P. Brass, L.G. Miller, J.E. Edwards Jr, Trends in antimicrobial drug development: implications for the future, Clinical Infectious Diseases 38(9) (2004) 1279-1286.

[3] W.H. Organization, The world health report 2002: reducing risks, promoting healthy life, World Health Organization2002.

[4] M.A. Fischbach, C.T. Walsh, Antibiotics for emerging pathogens, Science 325(5944) (2009) 1089-1093.

[5] P.S. Loomba, J. Taneja, B. Mishra, Methicillin and vancomycin resistant S. aureus in hospitalized patients, Journal of global infectious diseases 2(3) (2010) 275.

[6] M.N. Alekshun, S.B. Levy, Molecular mechanisms of antibacterial multidrug resistance, Cell 128(6) (2007) 1037-1050.

[7] W.H. Organization, Antimicrobial resistance: global report on surveillance, World Health Organization2014.

[8] R.J. Fair, Y. Tor, Antibiotics and bacterial resistance in the 21st century, Perspectives in medicinal chemistry 6 (2014) PMC. S14459.

[9] R.P. Wenzel, M.B. Edmond, Managing antibiotic resistance, Mass Medical Soc, 2000.

[10] J. Powers, Antimicrobial drug development–the past, the present, and the future, Clinical Microbiology and Infection 10(s4) (2004) 23-31.

[11] V. Economou, P. Gousia, Agriculture and food animals as a source of antimicrobial-resistant bacteria, Infection and drug resistance 8 (2015) 49.

[12] T.M. Barbosa, S.B. Levy, The impact of antibiotic use on resistance development and persistence, Drug resistance updates 3(5) (2000) 303-311.

[13] Z. Baharoglu, G. Garriss, D. Mazel, Multiple pathways of genome plasticity leading to development of antibiotic resistance, Antibiotics 2(2) (2013) 288-315.

[14] J.M. Munita, C.A. Arias, Mechanisms of antibiotic resistance, Microbiology spectrum 4(2) (2016).

[15] C.M. Thomas, K.M. Nielsen, Mechanisms of, and Barriers to, Horizontal Gene Transfer between Bacteria, Nature Reviews Microbiology 3 (2005) 711.

[16] C. Johnston, B. Martin, G. Fichant, P. Polard, J.-P. Claverys, Bacterial transformation: distribution, shared mechanisms and divergent control, Nature Reviews Microbiology 12(3) (2014) 181.

[17] J. Silva, Mechanisms of antibiotic resistance, Current therapeutic research 57(13) (1996) 30-35.

[18] T.S. Crofts, A.J. Gasparrini, G. Dantas, Next-generation approaches to understand and combat the antibiotic resistome, Nature Reviews Microbiology 15(7) (2017) 422.

[19] S. Kumar, M.F. Varela, Molecular mechanisms of bacterial resistance to antimicrobial agents, chemotherapy 14 (2013) 18.

[20] M.A. Kohanski, D.J. Dwyer, J.J. Collins, How antibiotics kill bacteria: from targets to networks, Nature Reviews Microbiology 8 (2010) 423.

[21] S.B. Levy, Active efflux mechanisms for antimicrobial resistance, Antimicrobial agents and chemotherapy 36(4) (1992) 695.

[22] C.T. Walsh, S.L. Fisher, I.-S. Park, M. Prahalad, Z. Wu, Bacterial resistance to vancomycin: five genes and one missing hydrogen bond tell the story, Chemistry & biology 3(1) (1996) 21-28.

[23] J. Davies, D. Davies, Origins and evolution of antibiotic resistance, Microbiology and molecular biology reviews 74(3) (2010) 417-433.

[24] C.J. Suárez, K. Lolans, M.V. Villegas, J.P. Quinn, Mechanisms of resistance to β-lactams in some common Gram-negative bacteria causing nosocomial infections, Expert review of anti-infective therapy 3(6) (2005) 915-922.

[25] K.F. Barker, Antibiotic resistance: a current perspective, British journal of clinical pharmacology 48(2) (1999) 109-124.

[26] D. Livermore, Beta-lactamase-mediated resistance and opportunities for its control, The Journal of antimicrobial chemotherapy 41(suppl_4) (1998) 25-41.

[27] C. Walsh, Molecular mechanisms that confer antibacterial drug resistance, Nature 406(6797) (2000) 775.

[28] V.T. Andriole, The quinolones: past, present, and future, Clinical infectious diseases 41(Supplement_2) (2005) S113-S119.

[29] I. Chopra, Glycylcyclines: third-generation tetracycline antibiotics, Current opinion in pharmacology 1(5) (2001) 464-469.

[30] S.Y. Essack, The development of β-lactam antibiotics in response to the evolution of β-lactamases, Pharmaceutical research 18(10) (2001) 1391-1399.

[31] D. McDevitt, M. Rosenberg, Exploiting genomics to discover new antibiotics, TRENDS in Microbiology 9(12) (2001) 611-617.

[32] T. Black, R. Hare, Will genomics revolutionize antimicrobial drug discovery?, Current opinion in microbiology 3(5) (2000) 522-527.

[33] D.J. Payne, M.N. Gwynn, D.J. Holmes, M. Rosenberg, Genomic approaches to antibacterial discovery, Genomics, Proteomics, and Clinical Bacteriology, Springer2004, pp. 231-259.

[34] R. Bentley, E. Haslam, The shikimate pathway—a metabolic tree with many branche, Critical reviews in biochemistry and molecular biology 25(5) (1990) 307-384.

[35] K.M. Herrmann, L.M. Weaver, The shikimate pathway, Annual review of plant biology 50(1) (1999) 473-503.

[36] D. Nasser, E. Nester, Aromatic amino acid biosynthesis: gene-enzyme relationships in Bacillus subtilis, Journal of bacteriology 94(5) (1967) 1706-1714.

[37] E. Haslam, Shikimic acid: metabolism and metabolites, John Wiley & Sons Inc1993.

[38] J. Coggins, C. Abell, L. Evans, M. Frederickson, D. Robinson, A. Roszak, A. Lapthorn, Experiences with the shikimate-pathway enzymes as targets for rational drug design, Portland Press Limited, 2003.

[39] H. Maeda, N. Dudareva, The shikimate pathway and aromatic amino acid biosynthesis in plants, Annual review of plant biology 63 (2012) 73-105.

[40] S. Ghosh, Y. Chisti, U.C. Banerjee, Production of shikimic acid, Biotechnology advances 30(6) (2012) 1425-1431.

[41] S. Hattori, S. Yoshida, M. Hasegawa, Occurrence of shikimic acid in the leaves of gymnosperms, Physiologia Plantarum 7(2) (1954) 283-289.

[42] R. Ducati, L.A. Basso, D.S. Santos, Mycobacterial shikimate pathway enzymes as targets for drug design, Current drug targets 8(3) (2007) 423-435.

[43] F. Roberts, C.W. Roberts, J.J. Johnson, D.E. Kyle, T. Krell, J.R. Coggins, G.H. Coombs, W.K. Milhous, S. Tzipori, D.J. Ferguson, Evidence for the shikimate pathway in apicomplexan parasites, Nature 393(6687) (1998) 801.

[44] C.W. Roberts, F. Roberts, R.E. Lyons, M.J. Kirisits, E.J. Mui, J. Finnerty, J.J. Johnson, D.J. Ferguson, J.R. Coggins, T. Krell, The shikimate pathway and its branches in apicomplexan parasites, The Journal of infectious diseases 185(Supplement_1) (2002) S25-S36.

[45] G.A. McConkey, J.W. Pinney, D.R. Westhead, K. Plueckhahn, T.B. Fitzpatrick, P. Macheroux, B. Kappes, Annotating the Plasmodium genome and the enigma of the shikimate pathway, TRENDS in Parasitology 20(2) (2004) 60-65.

[46] M.J. Gardner, N. Hall, E. Fung, O. White, M. Berriman, R.W. Hyman, J.M. Carlton, A. Pain, K.E. Nelson, S. Bowman, Genome sequence of the human malaria parasite Plasmodium falciparum, Nature 419(6906) (2002) 498.

[47] S. Campbell, T. Richards, E. Mui, B. Samuel, J. Coggins, R. McLeod, C. Roberts, A complete shikimate pathway in Toxoplasma gondii: an ancient eukaryotic innovation, International journal for parasitology 34(1) (2004) 5-13.

[48] G.I. McFadden, D.S. Roos, Apicomplexan plastids as drug targets, Trends in microbiology 7(8) (1999) 328-333.

[49] K. Mdluli, M. Spigelman, Novel targets for tuberculosis drug discovery, Current opinion in pharmacology 6(5) (2006) 459-467.

[50] B. Dias, V. Marcio, F. Ely, M.S. Palma, W.F. de Azevedo, L.A. Basso, D.S. Santos, Chorismate synthase: an attractive target for drug development against orphan diseases, Current drug targets 8(3) (2007) 437-444.

[51] K.M. Herrmann, The shikimate pathway: early steps in the biosynthesis of aromatic compounds, The Plant Cell 7(7) (1995) 907.

[52] K.M. Herrmann, The shikimate pathway as an entry to aromatic secondary metabolism, Plant Physiology 107(1) (1995) 7.

[53] W.E. Dyer, J.M. Henstrand, A.K. Handa, K.M. Herrmann, Wounding induces the first enzyme of the shikimate pathway in Solanaceae, Proceedings of the National Academy of Sciences 86(19) (1989) 7370-7373.

[54] T. Ogino, C. Garner, J.L. Markley, K.M. Herrmann, Biosynthesis of aromatic compounds: 13C NMR spectroscopy of whole Escherichia coli cells, Proceedings of the National Academy of Sciences 79(19) (1982) 5828-5832.

[55] P. Srinivasan, J. Rothschild, D. Sprinson, The enzymic conversion of 3-deoxy-D-arabino-heptulosonic acid 7-phosphate to 5-dehydroquinate, Journal of Biological Chemistry 238(10) (1963) 3176-3182.

[56] S.L. Bender, S. Mehdi, J.R. Knowles, Dehydroquinate synthase: the role of divalent metal cations and of nicotinamide adenine dinucleotide in catalysis, Biochemistry 28(19) (1989) 7555-7560.

[57] M. Daugherty, V. Vonstein, R. Overbeek, A. Osterman, Archaeal shikimate kinase, a new member of the GHMP-kinase family, Journal of bacteriology 183(1) (2001) 292-300.

[58] B. Ely, J. Pittard, Aromatic amino acid biosynthesis: regulation of shikimate kinase in Escherichia coli K-12, Journal of bacteriology 138(3) (1979) 933-943.

[59] Q.K. Huynh, Reaction of 5-enol-pyruvoylshikimate-3-phosphate synthase with diethyl pyrocarbonate: evidence for an essential histidine residue, Archives of biochemistry and biophysics 258(1) (1987) 233-239.

[60] S. Bornemann, M.K. Ramjee, S. Balasubramanian, C. Abell, J.R. Coggins, D.J. Lowe, R.N. Thorneley, Escherichia coli Chorismate Synthase Catalyzes the Conversion of (6S)-6-

Fluoro-5-enolpyruvylshikimate-3-phosphate to 6-Fluorochorismate implications for the enzyme mechanism and the antimicrobial action of (6s)-6-fluoroshikimate, Journal of Biological Chemistry 270(39) (1995) 22811-22815.

[61] E. Schönbrunn, S. Eschenburg, W.A. Shuttleworth, J.V. Schloss, N. Amrhein, J.N. Evans, W. Kabsch, Interaction of the herbicide glyphosate with its target enzyme 5-enolpyruvylshikimate 3-phosphate synthase in atomic detail, Proceedings of the National Academy of Sciences 98(4) (2001) 1376-1380.

[62] H.A. Arcuri, G.F. Zafalon, E.A. Marucci, C.E. Bonalumi, N.J. da Silveira, J.M. Machado, W.F. de Azevedo, M.S. Palma, SKPDB: a structural database of shikimate pathway enzymes, BMC bioinformatics 11(1) (2010) 12.

[63] J.M. Lambert, M.R. Boocock, J.R. Coggins, The 3-dehydroquinate synthase activity of the pentafunctional arom enzyme complex of Neurospora crassa is Zn2+-dependent, Biochemical journal 226(3) (1985) 817.

[64] G. Hrazdina, R.A. Jensen, Spatial organization of enzymes in plant metabolic pathways, Annual review of plant biology 43(1) (1992) 241-267.

[65] D.M. Mousdale, J.R. Coggins, Subcellular localization of the common shikimate-pathway enzymes in Pisum sativum L, Planta 163(2) (1985) 241-249.

[66] J. Schmid, N. Amrhein, Molecular organization of the shikimate pathway in higher plants, Phytochemistry 39(4) (1995) 737-749.

[67] A.R. Hawkins, H.K. Lamb, J.D. Moore, I.G. Charles, C.F. Roberts, The pre-chorismate (shikimate) and quinate pathways in filamentous fungi: theoretical and practical aspects, Microbiology 139(12) (1993) 2891-2899.

[68] V. Tzin, G. Galili, New insights into the shikimate and aromatic amino acids biosynthesis pathways in plants, Molecular plant 3(6) (2010) 956-972.

[69] A. DeLeo, D. Sprinson, Mechanism of 3-deoxy-D-arabino-heptulosonate 7-phosphate (DAHP) synthetase, Biochemical and biophysical research communications 32(5) (1968) 873-877.

[70] D. Onderka, H. Floss, Steric course of the chorismate synthetase reaction and the 3-deoxy-D-arabino-heptulosonate 7-phosphate (DAHP) synthetase reaction, Journal of the American Chemical Society 91(21) (1969) 5894-5896.

[71] D. Onderka, H. Floss, Stereospecificity of the 3-deoxy-D-arabino-heptulosonate 7-phosphate synthetase reaction, Biochemical and biophysical research communications 35(6) (1969) 801-804.

[72] J. Ray, R. Bauerle, Purification and properties of tryptophan-sensitive 3-deoxy-D-arabino-heptulosonate-7-phosphate synthase from Escherichia coli, Journal of bacteriology 173(6) (1991) 1894-1901.

[73] M. Staub, G. Dénes, A kinetic study of the mechanism of action of 3-deoxy-D-arabino-heptulosonate 7-phosphate synthase in Escherichia coli K 12, Biochimica et Biophysica Acta (BBA)-Enzymology 132(2) (1967) 528-530.

[74] M. Takahashi, W.W.-C. Chan, Separation and properties of isozymes of 3-deoxy-D-arabino-heptulosonate-7-phosphate synthetase from Saccharomyces cerevisiae, Canadian journal of biochemistry 49(9) (1971) 1015-1025.

[75] R.A. Jensen, D.S. Nasser, Comparative regulation of isoenzymic 3-deoxy-D-arabino-heptulosonate 7-phosphate synthetases in microorganisms, Journal of bacteriology 95(1) (1968) 188-196.

[76] C.M. Stephens, R. Bauerle, Analysis of the metal requirement of 3-deoxy-D-arabino-heptulosonate-7-phosphate synthase from Escherichia coli, Journal of Biological Chemistry 266(31) (1991) 20810-20817.

[77] C.J. Webby, H.M. Baker, J.S. Lott, E.N. Baker, E.J. Parker, The structure of 3-deoxy-D-arabino-heptulosonate 7-phosphate synthase from Mycobacterium tuberculosis reveals a common catalytic scaffold and ancestry for type I and type II enzymes, Journal of molecular biology 354(4) (2005) 927-939.

[78] C.J. Webby, M.L. Patchett, E.J. Parker, Characterization of a recombinant type II 3-deoxy-D-arabino-heptulosonate-7-phosphate synthase from Helicobacter pylori, Biochemical Journal 390(1) (2005) 223-230.

[79] R. Mir, S. Jallu, T. Singh, The shikimate pathway: Review of amino acid sequence, function and three-dimensional structures of the enzymes, Critical reviews in Microbiology 41(2) (2015) 172-189.

[80] J. Wu, R.W. Woodard, New insights into the evolutionary links relating to the 3-deoxy-D-arabino-heptulosonate 7-phosphate synthase subfamilies, Journal of Biological Chemistry 281(7) (2006) 4042-4048.

[81] L.R. Schofield, M.L. Patchett, E.J. Parker, Expression, purification, and characterization of 3-deoxy-D-arabino-heptulosonate 7-phosphate synthase from Pyrococcus furiosus, Protein expression and purification 34(1) (2004) 17-27.

[82] I.A. Shumilin, R.H. Kretsinger, R.H. Bauerle, Crystal structure of phenylalanine-regulated 3-deoxy-D-arabino-heptulosonate-7-phosphate synthase from Escherichia coli, Structure 7(7) (1999) 865-875.

[83] V. König, A. Pfeil, G.H. Braus, T.R. Schneider, Substrate and metal complexes of 3-deoxy-D-arabino-heptulosonate-7-phosphate synthase from Saccharomyces cerevisiae provide new insights into the catalytic mechanism, Journal of molecular biology 337(3) (2004) 675-690.

[84] P.J. Cross, A.L. Pietersma, T.M. Allison, S.M. Wilson-Coutts, F.C. Cochrane, E.J. Parker, Neisseria meningitidis expresses a single 3-deoxy-d-arabino-heptulosonate 7-phosphate synthase that is inhibited primarily by phenylalanine, Protein Science 22(8) (2013) 1087-1099.

[85] H. Nagano, H. Zalkin, Tyrosine-inhibited 3-deoxy-d-arabino-heptulosonate 7-phosphate synthetase: Properties of the partially purified enzyme from Salmonella typhimurium, Archives of biochemistry and biophysics 138(1) (1970) 58-65.

[86] P. Hoffmann, C. Doy, D. Catcheside, The separation of three allosterically inhibitable 3-deoxy-D-arabino-heptulosonate 7-phosphate synthases from extracts of Neurospora crassa and the purification of the tyrosine inhibitable isoenzyme, Biochimica et Biophysica Acta (BBA)-Enzymology 268(2) (1972) 550-561.

[87] P.J. Cross, E.J. Parker, Allosteric inhibitor specificity of Thermotoga maritima 3-deoxy-d-arabino-heptulosonate 7-phosphate synthase, FEBS letters 587(18) (2013) 3063-3068.

[88] I.A. Shumilin, R. Bauerle, J. Wu, R.W. Woodard, R.H. Kretsinger, Crystal structure of the reaction complex of 3-deoxy-D-arabino-heptulosonate-7-phosphate synthase from Thermotoga maritima refines the catalytic mechanism and indicates a new mechanism of allosteric regulation, Journal of molecular biology 341(2) (2004) 455-466.

[89] L.R. Schofield, B.F. Anderson, M.L. Patchett, G.E. Norris, G.B. Jameson, E.J. Parker, Substrate ambiguity and crystal structure of Pyrococcus furiosus 3-deoxy-D-arabino-heptulosonate-7-phosphate synthase: an ancestral 3-deoxyald-2-ulosonate-phosphate synthase?, Biochemistry 44(36) (2005) 11950-11962.

[90] S.H. Light, A.S. Halavaty, G. Minasov, L. Shuvalova, W.F. Anderson, Structural analysis of a 3-deoxy-D-arabino-heptulosonate 7-phosphate synthase with an N-terminal chorismate mutase-like regulatory domain, Protein Science 21(6) (2012) 887-895.

[91] A.R. Nazmi, E.J. Lang, Y. Bai, T.M. Allison, M.H. Othman, S. Panjikar, V.L. Arcus, E.J. Parker, Interdomain conformational changes provide allosteric regulation en route to chorismate, Journal of Biological Chemistry 291(42) (2016) 21836-21847.

[92] S. Pratap, A. Dev, V. Kumar, R. Yadav, M. Narwal, S. Tomar, P. Kumar, Structure of Chorismate Mutase-like Domain of DAHPS from Bacillus subtilis Complexed with Novel Inhibitor Reveals Conformational Plasticity of Active Site, Scientific reports 7(1) (2017) 6364.

[93] N.J. Blackmore, S. Reichau, W. Jiao, R.D. Hutton, E.N. Baker, G.B. Jameson, E.J. Parker, Three sites and you are out: ternary synergistic allostery controls aromatic amino acid biosynthesis in Mycobacterium tuberculosis, Journal of molecular biology 425(9) (2013) 1582-1592.

[94] R.J. Whitaker, M.J. Fiske, R.A. Jensen, Pseudomonas aeruginosa possesses two novel regulatory isozymes of 3-deoxy-D-arabino-heptulosonate 7-phosphate synthase, Journal of Biological Chemistry 257(21) (1982) 12789-12794.

[95] G. Gosset, C.A. Bonner, R.A. Jensen, Microbial origin of plant-type 2-keto-3-deoxy-D-arabino-heptulosonate 7-phosphate synthases, exemplified by the chorismate-and tryptophan-regulated enzyme from Xanthomonas campestris, Journal of bacteriology 183(13) (2001) 4061-4070.

[96] F.L. Henriquez, S.J. Campbell, B.K. Sundararaj, A. Cano, S.P. Muench, C.W. Roberts, The Acanthamoeba shikimate pathway has a unique molecular arrangement and is essential for aromatic amino acid biosynthesis, Protist 166(1) (2015) 93-105.

[97] B. Silakowski, B. Kunze, R. Müller, Stigmatella aurantiaca Sg a15 carries genes encoding type I and type II 3-deoxy-D-arabino-heptulosonate-7-phosphate synthases: involvement of a type II synthase in aurachin biosynthesis, Archives of microbiology 173(5-6) (2000) 403-411.

[98] J. Wu, D.L. Howe, R.W. Woodard, Thermotoga maritima 3-Deoxy-D-arabino-heptulosonate 7-Phosphate (DAHP) Synthase the ancestral eubacterial dahp synthase?, Journal of Biological Chemistry 278(30) (2003) 27525-27531.

[99] O.K. Park, R. Bauerle, Metal-catalyzed oxidation of phenylalanine-sensitive 3-deoxy-D-arabino-heptulosonate-7-phosphate synthase from Escherichia coli: inactivation and destabilization by oxidation of active-site cysteines, Journal of bacteriology 181(5) (1999) 1636-1642.

[100] C.J. Webby, W. Jiao, R.D. Hutton, N.J. Blackmore, H.M. Baker, E.N. Baker, G.B. Jameson, E.J. Parker, Synergistic allostery, a sophisticated regulatory network for the control of aromatic amino acid biosynthesis in Mycobacterium tuberculosis, Journal of Biological Chemistry 285(40) (2010) 30567-30576.

[101] L. Zhou, J. Wu, V. Janakiraman, I.A. Shumilin, R. Bauerle, R.H. Kretsinger, R.W. Woodard, Structure and characterization of the 3-deoxy-D-arabino-heptulosonate 7-phosphate synthase from Aeropyrum pernix, Bioorganic chemistry 40 (2012) 79-86.

[102] P.J. Cross, R.C. Dobson, M.L. Patchett, E.J. Parker, Tyrosine latching of a regulatory gate affords allosteric control of aromatic amino acid biosynthesis, Journal of Biological Chemistry 286(12) (2011) 10216-10224.

[103] P.J. Cross, T.M. Allison, R.C. Dobson, G.B. Jameson, E.J. Parker, Engineering allosteric control to an unregulated enzyme by transfer of a regulatory domain, Proceedings of the National Academy of Sciences 110(6) (2013) 2111-2116.

[104] B. Keith, X. Dong, F.M. Ausubel, G.R. Fink, Differential induction of 3-deoxy-D-arabino-heptulosonate 7-phosphate synthase genes in Arabidopsis thaliana by wounding and pathogenic attack, Proceedings of the National Academy of Sciences 88(19) (1991) 8821-8825.

[105] R. Sharma, M. Jain, R.K. Bhatnagar, N. Bhalla-Sarin, Differential expression of DAHP synthase and chorismate mutase in various organs of Brassica juncea and the effect of external factors on enzyme activity, Physiologia Plantarum 105(4) (1999) 739-745.

[106] R. Entus, M. Poling, K.M. Herrmann, Redox regulation of Arabidopsis 3-deoxy-D-arabino-heptulosonate 7-phosphate synthase, Plant Physiology 129(4) (2002) 1866-1871.

[107] R.J. Ganson, R.A. Jensen, Response of cytosolic-isozyme and plastid-isozyme levels of 3-deoxy-D-arabino-heptulosonate 7-phosphate synthase to physiological state of Nicotiana silvestris in suspension culture, Plant physiology 83(3) (1987) 479-482.

[108] J.L. Rubin, R.A. Jensen, Differentially regulated isozymes of 3-deoxy-D-arabino-heptulosonate-7-phosphate synthase from seedlings of Vigna radiata [L.] Wilczek, Plant physiology 79(3) (1985) 711-718.

[109] R.J. Ganson, T.A. d'Amato, R.A. Jensen, The two-isozyme system of 3-deoxy-D-arabino-heptulosonate 7-phosphate synthase in Nicotiana silvestris and other higher plants, Plant physiology 82(1) (1986) 203-210.

[110] J. Costerton, J. Ingram, K. Cheng, Structure and function of the cell envelope of gram-negative bacteria, Bacteriological reviews 38(1) (1974) 87.

[111] C.R. Raetz, Biochemistry of endotoxins, Annual review of biochemistry 59(1) (1990) 129-170.

[112] X. Wang, P.J. Quinn, Lipopolysaccharide: Biosynthetic pathway and structure modification, Progress in lipid research 49(2) (2010) 97-107.

[113] M. Osborn, R. Munson, [67] Separation of the inner (cytoplasmic) and outer membranes of gram-negative bacteria, Methods in enzymology, Elsevier1974, pp. 642-653.

[114] T.J. Silhavy, D. Kahne, S. Walker, The bacterial cell envelope, Cold Spring Harbor perspectives in biology 2(5) (2010) a000414.

[115] H. Nikaido, Molecular basis of bacterial outer membrane permeability revisited, Microbiology and molecular biology reviews 67(4) (2003) 593-656.

[116] M.P. Bos, V. Robert, J. Tommassen, Biogenesis of the gram-negative bacterial outer membrane, Annu. Rev. Microbiol. 61 (2007) 191-214.

[117] H. Tokuda, S.-i. Matsuyama, Sorting of lipoproteins to the outer membrane in E. coli, Biochimica et Biophysica Acta (BBA)-Molecular Cell Research 1693(1) (2004) 5-13.

[118] C.R. Raetz, C. Whitfield, Lipopolysaccharide endotoxins, Annual review of biochemistry 71(1) (2002) 635-700.

[119] K. Zeth, M. Thein, Porins in prokaryotes and eukaryotes: common themes and variations, Biochemical Journal 431(1) (2010) 13-22.

[120] O. Holst, H. Brade, Chemical structure of the core region of lipopolysaccharides, Endotoxin in health and disease 1 (1999) 115-154.

[121] C.R. Raetz, C.M. Reynolds, M.S. Trent, R.E. Bishop, Lipid A modification systems in gram-negative bacteria, Annu. Rev. Biochem. 76 (2007) 295-329.

[122] A. Silipo, M.R. Leone, R. Lanzetta, M. Parrilli, G. Lackner, B. Busch, C. Hertweck, A. Molinaro, Structural characterization of two lipopolysaccharide O-antigens produced by the endofungal bacterium Burkholderia sp. HKI-402 (B4), Carbohydrate research 347(1) (2012) 95-98.

[123] C. Alexander, E.T. Rietschel, Invited review: bacterial lipopolysaccharides and innate immunity, Journal of endotoxin research 7(3) (2001) 167-202.

[124] S. Akira, K. Takeda, Toll-like receptor signalling, Nature reviews immunology 4(7) (2004) 499.

[125] M.G. Netea, M. van Deuren, B.J. Kullberg, J.-M. Cavaillon, J.W. Van der Meer, Does the shape of lipid A determine the interaction of LPS with Toll-like receptors?, Trends in immunology 23(3) (2002) 135-139.

[126] R. Bone, Pathophysiology of sepsis, Ann Intern Med 115(6) (1991) 457-469.

[127] R.C. Bone, C.J. Grodzin, R.A. Balk, Sepsis: a new hypothesis for pathogenesis of the disease process, Chest 112(1) (1997) 235-244.

[128] M. Caroff, D. Karibian, Structure of bacterial lipopolysaccharides, Carbohydrate research 338(23) (2003) 2431-2447.

[129] S.G. Wilkinson, Bacterial lipopolysaccharides—themes and variations, Progress in lipid research 35(3) (1996) 283-343.

[130] C. galanos, O. lüderitz, E.T. rietschel, O. westphal, H. Brade, L. Brade, M. Freudenberg, U. Schade, M. Imoto, H. Yoshimura, Synthetic and natural Escherichia coli free lipid A express identical endotoxic activities, The FEBS Journal 148(1) (1985) 1-5.

[131] C. Galanos, M. Freudenberg, Bacterial endotoxins: biological properties and mechanisms of action, Mediators of inflammation 2(7) (1993) S11-S16.

[132] J.Y. Homma, M. matsuura, S. Kanegasaki, Y. kawakubo, Y. kojima, N. shibukawa, Y. kumazawa, A. yamamoto, K.-i. Tanamoto, T. Yasuda, Structural requirements of lipid A

responsible for the functions: a study with chemically synthesized lipid A and its analogues, The Journal of Biochemistry 98(2) (1985) 395-406.

[133] S. Kotani, H. Takada, M. Tsujimoto, T. Ogawa, I. Takahashi, T. Ikeda, K. Otsuka, H. Shimauchi, N. Kasai, J. Mashimo, Synthetic lipid A with endotoxic and related biological activities comparable to those of a natural lipid A from an Escherichia coli re-mutant, Infection and immunity 49(1) (1985) 225-237.

[134] A. Steimle, I.B. Autenrieth, J.-S. Frick, Structure and function: lipid A modifications in commensals and pathogens, International Journal of Medical Microbiology 306(5) (2016) 290-301.

[135] B.M. Plötz, B. Lindner, K.O. Stetter, O. Holst, Characterization of a Novel Lipid A Containingd-Galacturonic Acid That Replaces Phosphate Residues THE STRUCTURE OF THE LIPID A OF THE LIPOPOLYSACCHARIDE FROM THE HYPERTHERMOPHILIC BACTERIUM AQUIFEX PYROPHILUS, Journal of Biological Chemistry 275(15) (2000) 11222-11228.

[136] M. Caroff, C. Deprun, J. Richards, D. Karibian, Structural characterization of the lipid A of Bordetella pertussis 1414 endotoxin, Journal of bacteriology 176(16) (1994) 5156-5159.

[137] U. Zähringer, Y. Knirel, B. Lindner, J. Helbig, A. Sonesson, R. Marre, E.T. Rietschel, The lipopolysaccharide of Legionella pneumophila serogroup 1 (strain Philadelphia 1): chemical structure and biological significance, Progress in clinical and biological research 392 (1995) 113-139.

[138] A. Moran, E.T. Rietschel, T. Kosunen, U. Zähringer, Chemical characterization of Campylobacter jejuni lipopolysaccharides containing N-acetylneuraminic acid and 2, 3-diamino-2, 3-dideoxy-D-glucose, Journal of bacteriology 173(2) (1991) 618-626.

[139] U.R. Bhat, L.S. Forsberg, R.W. Carlson, Structure of lipid A component of Rhizobium leguminosarum bv. phaseoli lipopolysaccharide. Unique nonphosphorylated lipid A containing 2-amino-2-deoxygluconate, galacturonate, and glucosamine, Journal of Biological Chemistry 269(20) (1994) 14402-14410.

[140] A. Aderem, R.J. Ulevitch, Toll-like receptors in the induction of the innate immune response, Nature 406(6797) (2000) 782.

[141] R. Medzhitov, C. Janeway Jr, Innate immunity, New England Journal of Medicine 343(5) (2000) 338-344.

[142] B. Beutler, A. Cerami, Tumor necrosis, cachexia, shock, and inflammation: a common mediator, Annual review of biochemistry 57(1) (1988) 505-518.

[143] C.A. Dinarello, Interleukin-1 and interleukin-1 antagonism, Blood 77(8) (1991) 1627-1652.

[144] S.I. Miller, R.K. Ernst, M.W. Bader, LPS, TLR4 and infectious disease diversity, Nature Reviews Microbiology 3(1) (2005) 36.

[145] R. Shimazu, S. Akashi, H. Ogata, Y. Nagai, K. Fukudome, K. Miyake, M. Kimoto, MD-2, a molecule that confers lipopolysaccharide responsiveness on Toll-like receptor 4, Journal of Experimental Medicine 189(11) (1999) 1777-1782.

[146] A. Visintin, K.A. Halmen, E. Latz, B.G. Monks, D.T. Golenbock, Pharmacological inhibition of endotoxin responses is achieved by targeting the TLR4 coreceptor, MD-2, The Journal of Immunology 175(10) (2005) 6465-6472.

[147] M. Gangloff, N.J. Gay, MD-2: the Toll 'gatekeeper'in endotoxin signalling, Trends in biochemical sciences 29(6) (2004) 294-300.

[148] T. Drake, J. Cheng, A. Chang, F. Taylor Jr, Expression of tissue factor, thrombomodulin, and E-selectin in baboons with lethal Escherichia coli sepsis, The American journal of pathology 142(5) (1993) 1458.

[149] A. Li, A.C. Chang, G.T. Peer, L.B. Hinshaw, J.F. Taylor, Comparison of the capacity of rhTNF-alpha and Escherichia coli to induce procoagulant activity by baboon mononuclear cells in vivo and in vitro, Shock (Augusta, Ga.) 5(4) (1996) 274-279.

[150] D. Golenbock, R. Hampton, N. Qureshi, K. Takayama, C. Raetz, Lipid A-like molecules that antagonize the effects of endotoxins on human monocytes, Journal of Biological Chemistry 266(29) (1991) 19490-19498.

[151] K. Takayama, N. Qureshi, B. Beutler, T. Kirkland, Diphosphoryl lipid A from Rhodopseudomonas sphaeroides ATCC 17023 blocks induction of cachectin in macrophages by lipopolysaccharide, Infection and immunity 57(4) (1989) 1336-1338.

[152] Y.-C. Lu, W.-C. Yeh, P.S. Ohashi, LPS/TLR4 signal transduction pathway, Cytokine 42(2) (2008) 145-151.

[153] Y. Nagai, S. Akashi, M. Nagafuku, M. Ogata, Y. Iwakura, S. Akira, T. Kitamura, A. Kosugi, M. Kimoto, K. Miyake, Essential role of MD-2 in LPS responsiveness and TLR4 distribution, Nature immunology 3(7) (2002) 667.

[154] T.L. Gioannini, A. Teghanemt, D. Zhang, N.P. Coussens, W. Dockstader, S. Ramaswamy, J.P. Weiss, Isolation of an endotoxin–MD-2 complex that produces Toll-like receptor 4-dependent cell activation at picomolar concentrations, Proceedings of the National Academy of Sciences 101(12) (2004) 4186-4191.

[155] D. Heumann, T. Roger, Initial responses to endotoxins and Gram-negative bacteria, Clinica chimica acta 323(1-2) (2002) 59-72.

[156] N. Suzuki, S. Suzuki, G.S. Duncan, D.G. Millar, T. Wada, C. Mirtsos, H. Takada, A. Wakeham, A. Itie, S. Li, Severe impairment of interleukin-1 and Toll-like receptor signalling in mice lacking IRAK-4, Nature 416(6882) (2002) 750.

[157] T.W. Kim, K. Staschke, K. Bulek, J. Yao, K. Peters, K.-H. Oh, Y. Vandenburg, H. Xiao, W. Qian, T. Hamilton, A critical role for IRAK4 kinase activity in Toll-like receptor–mediated innate immunity, Journal of Experimental Medicine 204(5) (2007) 1025-1036.

[158] P. Sperandeo, A.M. Martorana, A. Polissi, Lipopolysaccharide biogenesis and transport at the outer membrane of Gram-negative bacteria, Biochimica et Biophysica Acta (BBA)-Molecular and Cell Biology of Lipids 1862(11) (2017) 1451-1460.

[159] L. Steeghs, R. den Hartog, A. den Boer, B. Zomer, P. Roholl, P. van der Ley, Meningitis bacterium is viable without endotoxin, Nature 392(6675) (1998) 449.

[160] M.S. Anderson, C.E. Bulawa, C. Raetz, The biosynthesis of gram-negative endotoxin. Formation of lipid A precursors from UDP-GlcNAc in extracts of Escherichia coli, Journal of Biological Chemistry 260(29) (1985) 15536-15541.

[161] M.S. Anderson, C. Raetz, Biosynthesis of lipid A precursors in Escherichia coli. A cytoplasmic acyltransferase that converts UDP-N-acetylglucosamine to UDP-3-O-(R-3-hydroxymyristoyl)-N-acetylglucosamine, Journal of Biological Chemistry 262(11) (1987) 5159-5169.

[162] M. Anderson, H. Bull, S. Galloway, T. Kelly, S. Mohan, K. Radika, C. Raetz, UDP-N-acetylglucosamine acyltransferase of Escherichia coli. The first step of endotoxin biosynthesis is thermodynamically unfavorable, Journal of Biological Chemistry 268(26) (1993) 19858-19865.

[163] A.H. Williams, C.R. Raetz, Structural basis for the acyl chain selectivity and mechanism of UDP-N-acetylglucosamine acyltransferase, Proceedings of the National Academy of Sciences 104(34) (2007) 13543-13550.

[164] T.J. Wyckoff, S. Lin, R.J. Cotter, G.D. Dotson, C.R. Raetz, Hydrocarbon rulers in UDP-N-acetylglucosamine acyltransferases, Journal of Biological Chemistry 273(49) (1998) 32369-32372.

[165] K. Young, L.L. Silver, D. Bramhill, P. Cameron, S.S. Eveland, C.R. Raetz, S.A. Hyland, M.S. Anderson, The envA permeability/cell division gene of Escherichia coli encodes the second enzyme of lipid A biosynthesis UDP-3-O-(R-3-hydroxymyristoyl)-N-acetylglucosamine deacetylase, Journal of Biological Chemistry 270(51) (1995) 30384-30391.

[166] J.E. Jackman, C.R. Raetz, C.A. Fierke, UDP-3-O-(R-3-hydroxymyristoyl)-N-acetylglucosamine deacetylase of Escherichia coli is a zinc metalloenzyme, Biochemistry 38(6) (1999) 1902-1911.

[167] H.R. Onishi, B.A. Pelak, L.S. Gerckens, L.L. Silver, F.M. Kahan, M.-H. Chen, A.A. Patchett, S.M. Galloway, S.A. Hyland, M.S. Anderson, Antibacterial agents that inhibit lipid A biosynthesis, Science 274(5289) (1996) 980-982.

[168] T. Kline, N.H. Andersen, E.A. Harwood, J. Bowman, A. Malanda, S. Endsley, A.L. Erwin, M. Doyle, S. Fong, A.L. Harris, Potent, Novel in Vitro Inhibitors of the Pseudomonas a eruginosa Deacetylase LpxC, Journal of medicinal chemistry 45(14) (2002) 3112-3129.

[169] A.L. McClerren, S. Endsley, J.L. Bowman, N.H. Andersen, Z. Guan, J. Rudolph, C.R. Raetz, A slow, tight-binding inhibitor of the zinc-dependent deacetylase LpxC of lipid A biosynthesis with antibiotic activity comparable to ciprofloxacin, Biochemistry 44(50) (2005) 16574-16583.

[170] T. Kelly, S. Stachula, C. Raetz, M. Anderson, The firA gene of Escherichia coli encodes UDP-3-O-(R-3-hydroxymyristoyl)-glucosamine N-acyltransferase. The third step of endotoxin biosynthesis, Journal of Biological Chemistry 268(26) (1993) 19866-19874.

[171] S.M. Galloway, C. Raetz, A mutant of Escherichia coli defective in the first step of endotoxin biosynthesis, Journal of Biological Chemistry 265(11) (1990) 6394-6402.

[172] M. Vaara, Eight bacterial proteins, including UDP-N-acetylglucosamine acyltransferase (LpxA) and three other transferases of Escherichia coli, consist of a six-residue periodicity theme, FEMS microbiology letters 97(3) (1992) 249-254.

[173] L. Buetow, T.K. Smith, A. Dawson, S. Fyffe, W.N. Hunter, Structure and reactivity of LpxD, the N-acyltransferase of lipid A biosynthesis, Proceedings of the National Academy of Sciences 104(11) (2007) 4321-4326.

[174] K.J. Babinski, S.J. Kanjilal, C.R. Raetz, Accumulation of the lipid A precursor UDP-2, 3-diacylglucosamine in an Escherichia coli mutant lacking the lpxH gene, Journal of Biological Chemistry 277(29) (2002) 25947-25956.

[175] K.J. Babinski, A.A. Ribeiro, C.R. Raetz, The Escherichia coli gene encoding the UDP-2, 3-diacylglucosamine pyrophosphatase of lipid A biosynthesis, Journal of Biological Chemistry 277(29) (2002) 25937-25946.

[176] D.N. Crowell, M.S. Anderson, C. Raetz, Molecular cloning of the genes for lipid A disaccharide synthase and UDP-N-acetylglucosamine acyltransferase in Escherichia coli, Journal of bacteriology 168(1) (1986) 152-159.

[177] T.A. Garrett, J.L. Kadrmas, C.R. Raetz, Identification of the Gene Encoding the Escherichia coli Lipid A 4′-Kinase Facile phosphorylation of endotoxin analogs with recombinant LpxK, Journal of Biological Chemistry 272(35) (1997) 21855-21864.

[178] T. Clementz, C. Raetz, A gene coding for 3-deoxy-D-manno-octulosonic-acid transferase in Escherichia coli. Identification, mapping, cloning, and sequencing, Journal of Biological Chemistry 266(15) (1991) 9687-9696.

[179] K.A. Brozek, C. Raetz, Biosynthesis of lipid A in Escherichia coli. Acyl carrier protein-dependent incorporation of laurate and myristate, Journal of Biological Chemistry 265(26) (1990) 15410-15417.

[180] C. Belunis, C. Raetz, Biosynthesis of endotoxins. Purification and catalytic properties of 3-deoxy-D-manno-octulosonic acid transferase from Escherichia coli, Journal of Biological Chemistry 267(14) (1992) 9988-9997.

[181] M.K. Vorachek-Warren, S. Ramirez, R.J. Cotter, C.R. Raetz, A triple mutant of Escherichia coli lacking secondary acyl chains on lipid A, Journal of Biological Chemistry 277(16) (2002) 14194-14205.

[182] C. Whitfield, N. Kaniuk, E. Frirdich, Molecular insights into the assembly and diversity of the outer core oligosaccharide in lipopolysaccharides from Escherichia coli and Salmonella, Journal of endotoxin research 9(4) (2003) 244-249.

[183] W.T. Doerrler, H.S. Gibbons, C.R. Raetz, MsbA-dependent translocation of lipids across the inner membrane of Escherichia coli, Journal of Biological Chemistry 279(43) (2004) 45102-45109.

[184] G. Samuel, P. Reeves, Biosynthesis of O-antigens: genes and pathways involved in nucleotide sugar precursor synthesis and O-antigen assembly, Carbohydrate research 338(23) (2003) 2503-2519.

[185] N. Ruiz, D. Kahne, T.J. Silhavy, Transport of lipopolysaccharide across the cell envelope: the long road of discovery, Nature Reviews Microbiology 7(9) (2009) 677.

[186] P. Sperandeo, G. Dehò, A. Polissi, The lipopolysaccharide transport system of Gram-negative bacteria, Biochimica et Biophysica Acta (BBA)-Molecular and Cell Biology of Lipids 1791(7) (2009) 594-602.

[187] E. Freinkman, S.-S. Chng, D. Kahne, The complex that inserts lipopolysaccharide into the bacterial outer membrane forms a two-protein plug-and-barrel, Proceedings of the National Academy of Sciences 108(6) (2011) 2486-2491.

[188] S.B. Falconer, E.D. Brown, New screens and targets in antibacterial drug discovery, Current opinion in microbiology 12(5) (2009) 497-504.

[189] U. Amineni, D. Pradhan, H. Marisetty, In silico identification of common putative drug targets in Leptospira interrogans, Journal of chemical biology 3(4) (2010) 165-173.

[190] C.-E. Chong, B.-S. Lim, S. Nathan, R. Mohamed, In silico analysis of Burkholderia pseudomallei genome sequence for potential drug targets, In silico biology 6(4) (2006) 341-346.

[191] D. Barh, A. Kumar, In silico identification of candidate drug and vaccine targets from various pathways in Neisseria gonorrhoeae, In silico biology 9(4) (2009) 225-231.

[192] B.E. Coggins, A.L. McClerren, L. Jiang, X. Li, J. Rudolph, O. Hindsgaul, C.R. Raetz, P. Zhou, Refined Solution Structure of the LpxC− TU-514 Complex and p K a Analysis of an Active Site Histidine: Insights into the Mechanism and Inhibitor Design, Biochemistry 44(4) (2005) 1114-1126.

[193] R.P. Emptage, K.D. Daughtry, C.W. Pemble, C.R. Raetz, Crystal structure of LpxK, the 4′-kinase of lipid A biosynthesis and atypical P-loop kinase functioning at the membrane interface, Proceedings of the National Academy of Sciences 109(32) (2012) 12956-12961.

[194] J. Zhang, L. Zhang, X. Li, W. Xu, UDP-3-O-(R-3-hydroxymyristoyl)-N-acetylglucosamine deacetylase (LpxC) inhibitors: a new class of antibacterial agents, Current medicinal chemistry 19(13) (2012) 2038-2050.

[195] J.E. Jackman, C.A. Fierke, L.N. Tumey, M. Pirrung, T. Uchiyama, S.H. Tahir, O. Hindsgaul, C.R. Raetz, Antibacterial agents that target lipid a biosynthesis in gram-negative bacteria inhibition of diverse UDP-3-O-(R-3-hydroxymyristoyl)-N-acetylglucosamine deacetylases by substrate analogs containing zinc binding motifs, Journal of Biological Chemistry 275(15) (2000) 11002-11009.

[196] S. Normark, H.G. Boman, E. Matsson, Mutant of Escherichia coli with anomalous cell division and ability to decrease episomally and chromosomally mediated resistance to ampicillin and several other antibiotics, Journal of bacteriology 97(3) (1969) 1334-1342.

[197] J.E. Jackman, C.R. Raetz, C.A. Fierke, Site-directed mutagenesis of the bacterial metalloamidase UDP-(3-O-acyl)-N-acetylglucosamine deacetylase (LpxC). Identification of the zinc binding site, Biochemistry 40(2) (2001) 514-523.

[198] C.P. McClure, K.M. Rusche, K. Peariso, J.E. Jackman, C.A. Fierke, J.E. Penner-Hahn, EXAFS studies of the zinc sites of UDP-(3-O-acyl)-N-acetylglucosamine deacetylase (LpxC), Journal of inorganic biochemistry 94(1-2) (2003) 78-85.

[199] D.A. Whittington, K.M. Rusche, H. Shin, C.A. Fierke, D.W. Christianson, Crystal structure of LpxC, a zinc-dependent deacetylase essential for endotoxin biosynthesis, Proceedings of the National Academy of Sciences 100(14) (2003) 8146-8150.

[200] M. Hernick, H.A. Gennadios, D.A. Whittington, K.M. Rusche, D.W. Christianson, C.A. Fierke, UDP-3-O-((R)-3-hydroxymyristoyl)-N-acetylglucosamine deacetylase functions

through a general acid-base catalyst pair mechanism, Journal of Biological Chemistry 280(17) (2005) 16969-16978.

[201] L. Buetow, A. Dawson, W.N. Hunter, The nucleotide-binding site of Aquifex aeolicus LpxC, Acta Crystallographica Section F: Structural Biology and Crystallization Communications 62(11) (2006) 1082-1086.

[202] A.W. Barb, L. Jiang, C.R. Raetz, P. Zhou, Structure of the deacetylase LpxC bound to the antibiotic CHIR-090: time-dependent inhibition and specificity in ligand binding, Proceedings of the National Academy of Sciences 104(47) (2007) 18433-18438.

[203] K.E. Cole, S.G. Gattis, H.D. Angell, C.A. Fierke, D.W. Christianson, Structure of the metal-dependent deacetylase LpxC from Yersinia enterocolitica complexed with the potent inhibitor CHIR-090, Biochemistry 50(2) (2010) 258-265.

[204] I. Mochalkin, J.D. Knafels, S. Lightle, Crystal structure of LpxC from Pseudomonas aeruginosa complexed with the potent BB-78485 inhibitor, Protein Science 17(3) (2008) 450-457.

[205] B.E. Coggins, X. Li, A.L. McClerren, O. Hindsgaul, C.R. Raetz, P. Zhou, Structure of the LpxC deacetylase with a bound substrate-analog inhibitor, Nature Structural and Molecular Biology 10(8) (2003) 645.

[206] W. Wang, M. Maniar, R. Jain, J. Jacobs, J. Trias, Z. Yuan, A Fluorescence-Based Homogeneous Assay for Measuring Activity of UDP–3-O-(R-3-Hydroxymyristoyl)-N-acetylglucosamine Deacetylase, Analytical biochemistry 290(2) (2001) 338-346.

[207] P. Zhou, A.W. Barb, Mechanism and inhibition of LpxC: an essential zinc-dependent deacetylase of bacterial lipid A synthesis, Current pharmaceutical biotechnology 9(1) (2008) 9-15.

[208] B.E. Coggins, X. Li, O. Hindsgaul, C.R. Raetz, P. Zhou, Letter to the Editor: Assignment of the 1 H, 13 C and 15 N Resonances of the LpxC Deacetylase from Aquifex aeolicus in Complex with the Substrate-Analog Inhibitor TU-514, Journal of biomolecular NMR 28(2) (2004) 201-202.

[209] J.M. Clements, F. Coignard, I. Johnson, S. Chandler, S. Palan, A. Waller, J. Wijkmans, M.G. Hunter, Antibacterial activities and characterization of novel inhibitors of LpxC, Antimicrobial agents and chemotherapy 46(6) (2002) 1793-1799.

[210] X. Li, T. Uchiyama, C.R. Raetz, O. Hindsgaul, Synthesis of a carbohydrate-derived hydroxamic acid inhibitor of the bacterial enzyme (LpxC) involved in lipid A biosynthesis, Organic letters 5(4) (2003) 539-541.

[211] N. Anderson, J. Bowan, A. Erwin, E. Harvood, T. Kline, K. Mdluli, K. Pfister, R. Shawar, A. Wagman, A. Yabannavar, International Patent, WO 62601 (2004) 2004.

[212] C.-J. Lee, X. Liang, X. Chen, D. Zeng, S.H. Joo, H.S. Chung, A.W. Barb, S.M. Swanson, R.A. Nicholas, Y. Li, Species-specific and inhibitor-dependent conformations of LpxC: implications for antibiotic design, Chemistry & biology 18(1) (2011) 38-47.

[213] U.F. Mansoor, D. Vitharana, P.A. Reddy, D.L. Daubaras, P. McNicholas, P. Orth, T. Black, M.A. Siddiqui, Design and synthesis of potent Gram-negative specific LpxC inhibitors, Bioorganic & medicinal chemistry letters 21(4) (2011) 1155-1161.

[214] M.F. Brown, U. Reilly, J.A. Abramite, J.T. Arcari, R. Oliver, R.A. Barham, Y. Che, J.M. Chen, E.M. Collantes, S.W. Chung, Potent inhibitors of LpxC for the treatment of Gram-negative infections, Journal of medicinal chemistry 55(2) (2012) 914-923.

[215] L.A. McAllister, J.I. Montgomery, J.A. Abramite, M.F. Brown, J.M. Chen, R.A. Barham, Y. Che, S.W. Chung, C.A. Menard, M. Mitton-Fry, Heterocyclic methylsulfone hydroxamic acid LpxC inhibitors as Gram-negative antibacterial agents, Bioorganic & medicinal chemistry letters 22(22) (2012) 6832-6838.

[216] J.I. Montgomery, M.F. Brown, U. Reilly, L.M. Price, J.A. Abramite, J. Arcari, R. Barham, Y. Che, J.M. Chen, S.W. Chung, Pyridone methylsulfone hydroxamate LpxC inhibitors for the treatment of serious gram-negative infections, Journal of medicinal chemistry 55(4) (2012) 1662-1670.

[217] J.S. Warmus, C.L. Quinn, C. Taylor, S.T. Murphy, T.A. Johnson, C. Limberakis, D. Ortwine, J. Bronstein, P. Pagano, J.D. Knafels, Structure based design of an in vivo active hydroxamic acid inhibitor of P. aeruginosa LpxC, Bioorganic & medicinal chemistry letters 22(7) (2012) 2536-2543.

[218] D.V. Kalinin, R. Holl, LpxC inhibitors: a patent review (2010-2016), Expert opinion on therapeutic patents 27(11) (2017) 1227-1250.

[219] A. Dev, S. Tapas, S. Pratap, P. Kumar, Structure and function of enzymes of shikimate pathway, Current Bioinformatics 7(4) (2012) 374-391.

[220] R. Ducati, L. Basso, D. Santos, Mycobacterial shikimate pathway enzymes as targets for drug design, Current drug targets 8(3) (2007) 423-435.

[221] J.L. Báez-Viveros, N. Flores, K. Juárez, P. Castillo-España, F. Bolivar, G. Gosset, Metabolic transcription analysis of engineered Escherichia coli strains that overproduce L-phenylalanine, Microbial cell factories 6(1) (2007) 30.

[222] S. Bhattacharya, P. Kumar, An insilico approach to structural elucidation of 3-deoxy-d-arabino-heptulosonate 7-phosphate synthase from Arabidopsis thaliana: Hints for herbicide design, Phytochemistry 73 (2012) 7-14.

[223] S. Tapas, G.K. Patel, S. Dhindwal, S. Tomar, In Silico sequence analysis and molecular modeling of the three-dimensional structure of DAHP synthase from Pseudomonas fragi, Journal of molecular modeling 17(4) (2011) 621-631.

[224] S. Tapas, A. Kumar, S. Dhindwal, P. Kumar, Structural analysis of chorismate synthase from Plasmodium falciparum: A novel target for antimalaria drug discovery, International journal of biological macromolecules 49(4) (2011) 767-777.

[225] A. Dev, N. Bodra, P. Kumar, S. Pratap, P. Kumar, Homology modeling and functional characterization of three-dimensional structure of dahp synthase from brachypodium distachyon, Journal of Proteins & Proteomics 4(1) (2013).

[226] H. Kloosterman, G. Hessels, J. Vrijbloed, G. Euverink, L. Dijkhuizen, (De) regulation of key enzyme steps in the shikimate pathway and phenylalanine-specific pathway of the actinomycete Amycolatopsis methanolica, Microbiology 149(11) (2003) 3321-3330.

[227] G.E. Walker, B. Dunbar, H.G. Nimmo, J.R. Coggins, Evidence for a novel class of microbial 3-deoxy-D-arabino-heptulosonate-7-phosphate synthase in Streptomyces coelicolor A3 (2), Streptomyces rimosus and Neurospora crassa, Microbiology 142(8) (1996) 1973-1982.

[228] M.R. Birck, R.W. Woodard, Aquifex aeolicus 3-deoxy-D-manno-2-octulosonic acid 8-phosphate synthase: a new class of KDO 8-P synthase?, Journal of molecular evolution 52(2) (2001) 205-214.

[229] S.H. Light, W.F. Anderson, The diversity of allosteric controls at the gateway to aromatic amino acid biosynthesis, Protein Science 22(4) (2013) 395-404.

[230] J. Camakaris, J. Pittard, Purification and properties of 3-deoxy-D-arabinoheptulosonic acid-7-phosphate synthetase (trp) from Escherichia coli, Journal of bacteriology 120(2) (1974) 590-597.

[231] I. Dusha, G. Dénes, Purification and properties of tyrosine-sensitive 3-deoxy-D-arabino-heptolosonate-7-phosphate synthetase of Escherichia coli K12, Biochimica et Biophysica Acta (BBA)-Enzymology 438(2) (1976) 563-573.

[232] K. Helmstaedt, A. Strittmatter, W.N. Lipscomb, G.H. Braus, Evolution of 3-deoxy-D-arabino-heptulosonate-7-phosphate synthase-encoding genes in the yeast Saccharomyces cerevisiae, Proceedings of the National Academy of Sciences of the United States of America 102(28) (2005) 9784-9789.

[233] L.R. Schofield, B.F. Anderson, M.L. Patchett, G.E. Norris, G.B. Jameson, E.J. Parker, Substrate Ambiguity and Crystal Structure of Pyrococcus furiosus 3-Deoxy-d-arabino-heptulosonate-7-phosphate Synthase: An Ancestral 3-Deoxyald-2-ulosonate-phosphate Synthase?†, Biochemistry 44(36) (2005) 11950-11962.

[234] J.M. Sobota, M. Gu, J.A. Imlay, Intracellular hydrogen peroxide and superoxide poison 3-deoxy-D-arabinoheptulosonate 7-phosphate synthase, the first committed enzyme in the aromatic biosynthetic pathway of Escherichia coli, Journal of bacteriology 196(11) (2014) 1980-1991.

[235] M.J. Davies, Protein oxidation and peroxidation, Biochemical Journal 473(7) (2016) 805-825.

[236] M.J. Davies, The oxidative environment and protein damage, Biochimica et Biophysica Acta (BBA)-Proteins and Proteomics 1703(2) (2005) 93-109.

[237] H.C. Mahler, W. Friess, U. Grauschopf, S. Kiese, Protein aggregation: pathways, induction factors and analysis, Journal of pharmaceutical sciences 98(9) (2009) 2909-2934.

[238] M.J. Albert, K. Alam, M. Ansaruzzaman, M. Islam, A. Rahman, K. Haider, N. Bhuiyan, S. Nahar, N. Ryan, J. Montanaro, Pathogenesis of Providencia alcalifaciens-induced diarrhea, Infection and immunity 60(12) (1992) 5017-5024.

[239] G. Cornaglia, S. Frugoni, A. Mazzariol, E. Piacentini, A. Berlusconi, R. Fontana, Activities of oral antibiotics on Providencia strains isolated from institutionalized elderly patients with urinary tract infections, Antimicrobial agents and chemotherapy 39(12) (1995) 2819-2821.

[240] M. Mohammadi, V. Chalavi, M. Novakova-Sura, J.F. Laliberté, M. Sylvestre, Expression of bacterial biphenyl-chlorobiphenyl dioxygenase genes in tobacco plants, Biotechnology and bioengineering 97(3) (2007) 496-505.

[241] M. Mohammadi, M. Sylvestre, Resolving the profile of metabolites generated during oxidation of dibenzofuran and chlorodibenzofurans by the biphenyl catabolic pathway enzymes, Chemistry & biology 12(7) (2005) 835-846.

[242] V.E. Fadouloglou, M. Kokkinidis, N.M. Glykos, Determination of protein oligomerization state: two approaches based on glutaraldehyde crosslinking, Analytical biochemistry 373(2) (2008) 404-406.

[243] A. Shevchenko, H. Tomas, J. Havli, J.V. Olsen, M. Mann, In-gel digestion for mass spectrometric characterization of proteins and proteomes, Nature protocols 1(6) (2006) 2856-2860.

[244] E. Gasteiger, C. Hoogland, A. Gattiker, S.e. Duvaud, M.R. Wilkins, R.D. Appel, A. Bairoch, Protein identification and analysis tools on the ExPASy server, Springer2005.

[245] C. Doy, K. Brown, Control of aromatic biosynthesis: The multiplicity of 7-phospho-2-oxo-3-deoxy-d-arabino-heptonate d-erythrose-4-phosphate-lyase (pyruvate-phosphorylating) in Eschetichia coli W, Biochimica et Biophysica Acta (BBA)-General Subjects 104(2) (1965) 377-389.

[246] H. Motulsky, A. Christopoulos, Fitting models to biological data using linear and nonlinear regression: a practical guide to curve fitting, Oxford University Press2004.

[247] L. Whitmore, B. Wallace, DICHROWEB, an online server for protein secondary structure analyses from circular dichroism spectroscopic data, Nucleic acids research 32(suppl 2) (2004) W668-W673.

[248] K. Glover, Y. Mei, S.C. Sinha, Identifying intrinsically disordered protein regions likely to undergo binding-induced helical transitions, Biochimica et Biophysica Acta (BBA)-Proteins and Proteomics 1864(10) (2016) 1455-1463.

[249] S. Sinha, Y. Mei, A. Ramanathan, K. Glover, Z. Yang, C. Colbert, Conformational Flexibility Enables Function of a BECN1 Region Essential for Starvation-Mediated Autophagy, The FASEB Journal 30(1 Supplement) (2016) 1062.6-1062.6.

[250] M. Amor-Mahjoub, J.-P. Suppini, N. Gomez-Vrielyunck, M. Ladjimi, The effect of the hexahistidine-tag in the oligomerization of HSC70 constructs, Journal of Chromatography B 844(2) (2006) 328-334.

[251] A. Goel, D. Colcher, J.-S. Koo, B.J. Booth, G. Pavlinkova, S.K. Batra, Relative position of the hexahistidine tag effects binding properties of a tumor-associated single-chain Fv construct, Biochimica et Biophysica Acta (BBA)-General Subjects 1523(1) (2000) 13-20.

[252] A. Chant, C.M. Kraemer-Pecore, R. Watkin, G.G. Kneale, Attachment of a histidine tag to the minimal zinc finger protein of the Aspergillus nidulans gene regulatory protein AreA causes a conformational change at the DNA-binding site, Protein expression and purification 39(2) (2005) 152-159.

[253] F. Song, A study of noncovalent protein complexes by matrix-assisted laser desorption/ionization, Journal of the American Society for Mass Spectrometry 18(7) (2007) 1286-1290.

[254] E. Stadtman, Oxidation of free amino acids and amino acid residues in proteins by radiolysis and by metal-catalyzed reactions, Annual review of biochemistry 62(1) (1993) 797-821.

[255] L. Mouls, E. Silajdzic, N. Haroune, C.M. Spickett, A.R. Pitt, Development of novel mass spectrometric methods for identifying HOCl-induced modifications to proteins, Proteomics 9(6) (2009) 1617-1631.

[256] M.D. Griffin, R.C. Dobson, F.G. Pearce, L. Antonio, A.E. Whitten, C.K. Liew, J.P. Mackay, J. Trewhella, G.B. Jameson, M.A. Perugini, Evolution of quaternary structure in a homotetrameric enzyme, Journal of molecular biology 380(4) (2008) 691-703.

[257] A.R. Nazmi, L.R. Schofield, R.C. Dobson, G.B. Jameson, E.J. Parker, Destabilization of the homotetrameric assembly of 3-deoxy-D-arabino-heptulosonate-7-phosphate synthase from

the hyperthermophile Pyrococcus furiosus enhances enzymatic activity, Journal of molecular biology 426(3) (2014) 656-673.

[258] S. Arya, A. Kumari, V. Dalal, M. Bhattacharya, S. Mukhopadhyay, Appearance of annular ring-like intermediates during amyloid fibril formation from human serum albumin, Physical Chemistry Chemical Physics 17(35) (2015) 22862-22871.

[259] K.K. Sweers, K.O. van der Werf, M.L. Bennink, V. Subramaniam, Atomic force microscopy under controlled conditions reveals structure of C-terminal region of α-synuclein in amyloid fibrils, ACS nano 6(7) (2012) 5952-5960.

[260] A. Stirpe, M. Pantusa, B. Rizzuti, L. Sportelli, R. Bartucci, R. Guzzi, Early stage aggregation of human serum albumin in the presence of metal ions, International journal of biological macromolecules 49(3) (2011) 337-342.

[261] S.M. Kelly, T.J. Jess, N.C. Price, How to study proteins by circular dichroism, Biochimica et Biophysica Acta (BBA)-Proteins and Proteomics 1751(2) (2005) 119-139.

[262] M. Abidi, A. Iram, M. Furkan, A. Naeem, Secondary structural alterations in glucoamylase as an influence of protein aggregation, International journal of biological macromolecules 98 (2017) 459-468.

[263] A.K. Thakur, M. Jayaraman, R. Mishra, M. Thakur, V.M. Chellgren, I.-J.L. Byeon, D.H. Anjum, R. Kodali, T.P. Creamer, J.F. Conway, Polyglutamine disruption of the huntingtin exon 1 N terminus triggers a complex aggregation mechanism, Nature Structural and Molecular Biology 16(4) (2009) 380.

[264] R. Mishra, M. Jayaraman, B.P. Roland, E. Landrum, T. Fullam, R. Kodali, A.K. Thakur, I. Arduini, R. Wetzel, Inhibiting the nucleation of amyloid structure in a huntingtin fragment by targeting α-helix-rich oligomeric intermediates, Journal of molecular biology 415(5) (2012) 900-917.

[265] S. Joshi, A.R. Singh, A. Kumar, P.C. Misra, M.I. Siddiqi, J.K. Saxena, Molecular cloning and characterization of Plasmodium falciparum transketolase, Molecular and biochemical parasitology 160(1) (2008) 32-41.

[266] B.S. Berlett, E.R. Stadtman, Protein oxidation in aging, disease, and oxidative stress, Journal of Biological Chemistry 272(33) (1997) 20313-20316.

[267] L. Redecke, M. von Bergen, J. Clos, P.V. Konarev, D.I. Svergun, U.E. Fittschen, J.A. Broekaert, O. Bruns, D. Georgieva, E. Mandelkow, Structural characterization of β-sheeted oligomers formed on the pathway of oxidative prion protein aggregation in vitro, Journal of structural biology 157(2) (2007) 308-320.

[268] G. Kim, S.J. Weiss, R.L. Levine, Methionine oxidation and reduction in proteins, Biochimica et Biophysica Acta (BBA)-General Subjects 1840(2) (2014) 901-905.

[269] G. Sancataldo, V. Vetri, V. Foderà, G. Di Cara, V. Militello, M. Leone, Oxidation enhances human serum albumin thermal stability and changes the routes of amyloid fibril formation, PloS one 9(1) (2014) e84552.

[270] P. Lasch, T. Petras, O. Ullrich, J. Backmann, D. Naumann, T. Grune, Hydrogen peroxide-induced structural alterations of RNAse A, Journal of Biological Chemistry 276(12) (2001) 9492-9502.

[271] J. Ravi, A.E. Hills, E. Cerasoli, P.D. Rakowska, M.G. Ryadnov, FTIR markers of methionine oxidation for early detection of oxidized protein therapeutics, European Biophysics Journal 40(3) (2011) 339-345.

[272] M. Narayan, E. Welker, W.J. Wedemeyer, H.A. Scheraga, Oxidative folding of proteins, Accounts of chemical research 33(11) (2000) 805-812.

[273] E. Welker, M. Narayan, W.J. Wedemeyer, H.A. Scheraga, Structural determinants of oxidative folding in proteins, Proceedings of the National Academy of Sciences 98(5) (2001) 2312-2316.

[274] Q. Luo, M.K. Joubert, R. Stevenson, R.R. Ketchem, L.O. Narhi, J. Wypych, Chemical modifications in therapeutic protein aggregates generated under different stress conditions, Journal of Biological Chemistry 286(28) (2011) 25134-25144.

[275] D. Hu, Z. Qin, B. Xue, A.L. Fink, V.N. Uversky, The effect of methionine oxidation on structural properties, conformational stability, and aggregation of immunoglobulin light chain LEN, Biochemistry 47(33) (2008) 8665.

[276] Y.Q. Wong, K.J. Binger, G.J. Howlett, M.D. Griffin, Methionine oxidation induces amyloid fibril formation by full-length apolipoprotein AI, Proceedings of the National Academy of Sciences 107(5) (2010) 1977-1982.

[277] T. Koudelka, F.C. Dehle, I.F. Musgrave, P. Hoffmann, J.A. Carver, Methionine oxidation enhances κ-casein amyloid fibril formation, Journal of agricultural and food chemistry 60(16) (2012) 4144-4155.

[278] W.R. Markesbery, Oxidative stress hypothesis in Alzheimer's disease, Free Radical Biology and Medicine 23(1) (1997) 134-147.

[279] W.R. Markesbery, J.M. Carney, Oxidative alterations in Alzheimer's disease, Brain pathology 9(1) (1999) 133-146.

[280] G. Yamin, C.B. Glaser, V.N. Uversky, A.L. Fink, Certain metals trigger fibrillation of methionine-oxidized α-synuclein, Journal of Biological Chemistry 278(30) (2003) 27630-27635.

[281] J. Dong, C.S. Atwood, V.E. Anderson, S.L. Siedlak, M.A. Smith, G. Perry, P.R. Carey, Metal binding and oxidation of amyloid-β within isolated senile plaque cores: Raman microscopic evidence, Biochemistry 42(10) (2003) 2768-2773.

[282] M.I. Elmallah, U. Borgmeyer, C. Betzel, L. Redecke, Impact of methionine oxidation as an initial event on the pathway of human prion protein conversion, Prion 7(5) (2013) 404-411.

[283] H.C. Altmeppen, J. Prox, B. Puig, F. Dohler, C. Falker, S. Krasemann, M. Glatzel, Roles of endoproteolytic α-cleavage and shedding of the prion protein in neurodegeneration, The FEBS journal 280(18) (2013) 4338-4347.

[284] V.N. Uversky, G. Yamin, P.O. Souillac, J. Goers, C.B. Glaser, A.L. Fink, Methionine oxidation inhibits fibrillation of human α-synuclein in vitro, FEBS letters 517(1-3) (2002) 239-244.

[285] L. Hou, I. Kang, R.E. Marchant, M.G. Zagorski, Methionine 35 oxidation reduces fibril assembly of the amyloid Aβ-(1–42) peptide of Alzheimer's disease, Journal of Biological Chemistry 277(43) (2002) 40173-40176.

[286] S.D. Maleknia, N. Reixach, J.N. Buxbaum, Oxidation inhibits amyloid fibril formation of transthyretin, FEBS Journal 273(23) (2006) 5400-5406.

[287] W. Wang, Protein aggregation and its inhibition in biopharmaceutics, International journal of pharmaceutics 289(1) (2005) 1-30.

[288] J. Mukherjee, M.N. Gupta, Protein aggregates: Forms, functions and applications, International journal of biological macromolecules 97 (2017) 778-789.

[289] P. Singh, M. Kumar Singh, V. Chauhan, P. Gupta, R. Kumar Dhaked, Prevention of aggregation and autocatalysis for sustaining biological activity of recombinant BoNT/A-LC upon long-term storage, Protein and peptide letters 18(12) (2011) 1177-1187.

[290] M.F. Khalil, C. Valenzuela, D. Sisniega, R. Skouta, M. Narayan, ER protein processing under oxidative stress: Implications and prevention, Cell biochemistry and biophysics 74(2) (2016) 213-220.

[291] C.M. Dobson, Protein folding and misfolding, Nature 426(6968) (2003) 884-890.

[292] A.M. Bhattacharyya, A.K. Thakur, R. Wetzel, Polyglutamine aggregation nucleation: thermodynamics of a highly unfavorable protein folding reaction, Proceedings of the National Academy of Sciences 102(43) (2005) 15400-15405.

[293] W.J. Wedemeyer, E. Welker, M. Narayan, H.A. Scheraga, Disulfide bonds and protein folding, Biochemistry 39(15) (2000) 4207-4216.

[294] M. Stefani, C.M. Dobson, Protein aggregation and aggregate toxicity: new insights into protein folding, misfolding diseases and biological evolution, Journal of molecular medicine 81(11) (2003) 678-699.

[295] K.S. Vassilenko, V.N. Uversky, Native-like secondary structure of molten globules, Biochimica et Biophysica Acta (BBA)-Protein Structure and Molecular Enzymology 1594(1) (2002) 168-177.

[296] A. Hawe, M. Sutter, W. Jiskoot, Extrinsic fluorescent dyes as tools for protein characterization, Pharmaceutical research 25(7) (2008) 1487-1499.

[297] M.S. Borana, P. Mishra, R.R. Pissurlenkar, R.V. Hosur, B. Ahmad, Curcumin and kaempferol prevent lysozyme fibril formation by modulating aggregation kinetic parameters, Biochimica et Biophysica Acta (BBA)-Proteins and Proteomics 1844(3) (2014) 670-680.

[298] G. Burra, A.K. Thakur, Inhibition of polyglutamine aggregation by SIMILAR huntingtin N-terminal sequences: Prospective molecules for preclinical evaluation in Huntington's disease, Peptide Science 108(4) (2017).

[299] D. Rehders, B. Claasen, L. Redecke, A. Buschke, C. Reibe, N. Jehmlich, M. von Bergen, C. Betzel, B. Meyer, Peptide NMHRYPNQ of the Cellular Prion Protein (PrPC) Inhibits Aggregation and Is a Potential Key for Understanding Prion–Prion Interactions, Journal of molecular biology 392(1) (2009) 198-207.

[300] A. Sharma, V. Kumar, A. Chatrath, A. Dev, R. Prasad, A.K. Sharma, S. Tomar, P. Kumar, In vitro metal catalyzed oxidative stress in DAH7PS: Methionine modification leads to structure destabilization and induce amorphous aggregation, International journal of biological macromolecules 106 (2018) 1089-1106.

[301] M. Winn, A. Ashton, P. Briggs, C. Ballard, P. Patel, Ongoing developments in CCP4 for high-throughput structure determination, Acta Crystallographica Section D: Biological Crystallography 58(11) (2002) 1929-1936.

[302] T. Kashav, R. Nitharwal, S.A. Abdulrehman, A. Gabdoulkhakov, W. Saenger, S.K. Dhar, S. Gourinath, Three-dimensional structure of N-terminal domain of DnaB helicase and helicase-primase interactions in Helicobacter pylori, PLoS One 4(10) (2009) e7515.

[303] W. Minor, D. Tomchick, Z. Otwinowski, Strategies for macromolecular synchrotron crystallography, Structure 8(5) (2000) R105-R110.

[304] I. Nagpal, I. Raj, N. Subbarao, S. Gourinath, Virtual screening, identification and in vitro testing of novel inhibitors of O-acetyl-L-serine sulfhydrylase of Entamoeba histolytica, PLoS One 7(2) (2012) e30305.

[305] C.P. Collaborative, The CCP4 suite: programs for protein crystallography, Acta crystallographica. Section D, Biological crystallography 50(Pt 5) (1994) 760.

[306] I.A. Shumilin, R. Bauerle, R.H. Kretsinger, The high-resolution structure of 3-deoxy-D-arabino-heptulosonate-7-phosphate synthase reveals a twist in the plane of bound phosphoenolpyruvate, Biochemistry 42(13) (2003) 3766-3776.

[307] G.N. Murshudov, A.A. Vagin, E.J. Dodson, Refinement of macromolecular structures by the maximum-likelihood method, Acta Crystallographica Section D: Biological Crystallography 53(3) (1997) 240-255.

[308] M. Goel, D. Jain, K.J. Kaur, R. Kenoth, B.G. Maiya, M.J. Swamy, D.M. Salunke, Functional Equality in the Absence of Structural Similarity an added dimension to molecular mimicry, Journal of Biological Chemistry 276(42) (2001) 39277-39281.

[309] P.D. Adams, P.V. Afonine, G. Bunkóczi, V.B. Chen, I.W. Davis, N. Echols, J.J. Headd, L.-W. Hung, G.J. Kapral, R.W. Grosse-Kunstleve, PHENIX: a comprehensive Python-based system for macromolecular structure solution, Acta Crystallographica Section D: Biological Crystallography 66(2) (2010) 213-221.

[310] P. Emsley, K. Cowtan, Coot: model-building tools for molecular graphics, Acta Crystallographica Section D: Biological Crystallography 60(12) (2004) 2126-2132.

[311] D. Jain, V. Lamour, Computational tools in protein crystallography, Computational Biology, Springer2010, pp. 129-156.

[312] R.A. Laskowski, M.W. MacArthur, D.S. Moss, J.M. Thornton, PROCHECK: a program to check the stereochemical quality of protein structures, Journal of applied crystallography 26(2) (1993) 283-291.

[313] W.L. DeLano, The PyMOL molecular graphics system, http://pymol. org (2002).

[314] E.J. Dodson, M. Winn, A. Ralph, [32] Collaborative computational project, number 4: Providing programs for protein crystallography, Methods in enzymology, Elsevier1997, pp. 620-633.

[315] A. Vagin, A. Teplyakov, Molecular replacement with MOLREP, Acta Crystallographica Section D: Biological Crystallography 66(1) (2010) 22-25.

[316] A.J. McCoy, Solving structures of protein complexes by molecular replacement with Phaser, Acta Crystallographica Section D: Biological Crystallography 63(1) (2007) 32-41.

[317] T.C. Terwilliger, R.W. Grosse-Kunstleve, P.V. Afonine, N.W. Moriarty, P.H. Zwart, L.-W. Hung, R.J. Read, P.D. Adams, Iterative model building, structure refinement and density modification with the PHENIX AutoBuild wizard, Acta Crystallographica Section D: Biological Crystallography 64(1) (2008) 61-69.

[318] M.C. Cavalier, M.I. Ansari, A.D. Pierce, P.T. Wilder, L.E. McKnight, E.P. Raman, D.B. Neau, P. Bezawada, M.J. Alasady, T.H. Charpentier, Small molecule inhibitors of Ca2+-S100B reveal two protein conformations, Journal of medicinal chemistry 59(2) (2016) 592-608.

[319] J.L. Jensen, A. Balbo, D.B. Neau, S. Chakravarthy, H. Zhao, S.C. Sinha, C.L. Colbert, Mechanistic implications of the unique structural features and dimerization of the cytoplasmic domain of the Pseudomonas sigma regulator, PupR, Biochemistry 54(38) (2015) 5867-5877.

[320] U. Das, V. Pogenberg, U.K.T. Subhramanyam, M. Wilmanns, S. Gourinath, A. Srinivasan, Crystal structure of the VapBC-15 complex from Mycobacterium tuberculosis reveals a two-metal ion dependent PIN-domain ribonuclease and a variable mode of toxin–antitoxin assembly, Journal of structural biology 188(3) (2014) 249-258.

[321] G.N. Murshudov, P. Skubák, A.A. Lebedev, N.S. Pannu, R.A. Steiner, R.A. Nicholls, M.D. Winn, F. Long, A.A. Vagin, REFMAC5 for the refinement of macromolecular crystal structures, Acta Crystallographica Section D: Biological Crystallography 67(4) (2011) 355-367.

[322] M.A. Silvers, S. Pakhomova, D.B. Neau, W.C. Silvers, N. Anzalone, C.M. Taylor, G.L. Waldrop, Crystal structure of carboxyltransferase from Staphylococcus aureus bound to the antibacterial agent moiramide B, Biochemistry 55(33) (2016) 4666-4674.

[323] A.A. Perederina, M.N. Vassylyeva, I.A. Berezin, V. Svetlov, I. Artsimovitch, D.G. Vassylyev, Cloning, expression, purification, crystallization and initial crystallographic analysis of transcription elongation factors GreB from Escherichia coli and Gfh1 from Thermus thermophilus, Acta Crystallographica Section F: Structural Biology and Crystallization Communications 62(1) (2006) 44-46.

[324] I.A. Shumilin, C. Zhao, R. Bauerle, R.H. Kretsinger, Allosteric inhibition of 3-deoxy-D-arabino-heptulosonate-7-phosphate synthase alters the coordination of both substrates, Journal of molecular biology 320(5) (2002) 1147-1156.

[325] C.T. Walsh, J. Liu, F. Rusnak, M. Sakaitani, Molecular studies on enzymes in chorismate metabolism and the enterobactin biosynthetic pathway, Chemical Reviews 90(7) (1990) 1105-1129.

[326] W. Holms, The central metabolic pathways of Escherichia coli: relationship between flux and control at a branch point, efficiency of conversion to biomass, and excretion of acetate, Current topics in cellular regulation, Elsevier1986, pp. 69-105.

[327] S. Sasso, M. Ökvist, K. Roderer, M. Gamper, G. Codoni, U. Krengel, P. Kast, Structure and function of a complex between chorismate mutase and DAHP synthase: efficiency boost for the junior partner, The EMBO journal 28(14) (2009) 2128-2142.

[328] J. Wu, G.Y. Sheflyan, R.W. Woodard, Bacillus subtilis 3-deoxy-D-arabino-heptulosonate 7-phosphate synthase revisited: resolution of two long-standing enigmas, Biochemical Journal 390(2) (2005) 583-590.

[329] M. Othman, Characterisation and Control of 3-Deoxy-D-arabino-heptulosonate 7-phosphate Synthase from Geobacillus sp, (2014).

[330] N. Bijari, S. Ghobadi, H. Mahdiuni, R. Khodarahmi, S.A. Ghadami, Spectroscopic and molecular modeling studies on binding of dorzolamide to bovine and human carbonic anhydrase II, International journal of biological macromolecules 80 (2015) 189-199.

[331] M. Biasini, S. Bienert, A. Waterhouse, K. Arnold, G. Studer, T. Schmidt, F. Kiefer, T.G. Cassarino, M. Bertoni, L. Bordoli, SWISS-MODEL: modelling protein tertiary and quaternary structure using evolutionary information, Nucleic acids research 42(W1) (2014) W252-W258.

[332] B. Webb, A. Sali, Protein structure modeling with MODELLER, Protein Structure Prediction, Springer2014, pp. 1-15.

[333] R. Chenna, H. Sugawara, T. Koike, R. Lopez, T.J. Gibson, D.G. Higgins, J.D. Thompson, Multiple sequence alignment with the Clustal series of programs, Nucleic acids research 31(13) (2003) 3497-3500.

[334] D. Eisenberg, R. Lüthy, J.U. Bowie, [20] VERIFY3D: Assessment of protein models with three-dimensional profiles, Methods in enzymology, Elsevier1997, pp. 396-404.

[335] S.C. Lovell, I.W. Davis, W.B. Arendall, P.I. De Bakker, J.M. Word, M.G. Prisant, J.S. Richardson, D.C. Richardson, Structure validation by Cα geometry: ϕ, ψ and Cβ deviation, Proteins: Structure, Function, and Bioinformatics 50(3) (2003) 437-450.

[336] C. Colovos, T. Yeates, ERRAT: an empirical atom-based method for validating protein structures, Protein Sci 2 (1993) 1511-1519.

[337] M. Wiederstein, M.J. Sippl, ProSA-web: interactive web service for the recognition of errors in three-dimensional structures of proteins, Nucleic acids research 35(suppl_2) (2007) W407-W410.

[338] G. Morris, D. Goodsell, M. Pique, W. Lindstrom, R. Huey, S. Forli, W. Hart, S. Halliday, R. Belew, A. Olson, AutoDock 4.2 with AutoDockTools, 2009.

[339] G.M. Morris, D.S. Goodsell, R.S. Halliday, R. Huey, W.E. Hart, R.K. Belew, A.J. Olson, Automated docking using a Lamarckian genetic algorithm and an empirical binding free energy function, Journal of computational chemistry 19(14) (1998) 1639-1662.

[340] W.L. DeLano, The PyMOL user’s manual, DeLano Scientific, San Carlos, CA 452 (2002).

[341] I. Wiegand, K. Hilpert, R.E. Hancock, Agar and broth dilution methods to determine the minimal inhibitory concentration (MIC) of antimicrobial substances, Nature protocols 3(2) (2008) 163.

[342] C. Dichroism, Principles and Applications, Nakanishi, K (2000).

[343] N.J. Greenfield, G.D. Fasman, Computed circular dichroism spectra for the evaluation of protein conformation, Biochemistry 8(10) (1969) 4108-4116.

[344] S.M. Kelly, N.C. Price, The use of circular dichroism in the investigation of protein structure and function, Current protein and peptide science 1(4) (2000) 349-384.

[345] G. Holzwarth, P. Doty, The ultraviolet circular dichroism of polypeptides1, Journal of the American Chemical Society 87(2) (1965) 218-228.

[346] L. Whitmore, B. Wallace, DICHROWEB, an online server for protein secondary structure analyses from circular dichroism spectroscopic data, Nucleic acids research 32(suppl_2) (2004) W668-W673.

[347] G.-Z. Chen, X.-Z. Huang, J.-G. Xu, Z. Zheng, Z. Wang, The methods of fluorescence analysis, Science, Beijing 112 (1990).

[348] B.R. Masters, Principles of fluorescence spectroscopy, Journal of Biomedical Optics 13(2) (2008) 029901.

[349] M. Eftink, C. Ghiron, Fluorescence quenching of indole and model micelle systems, The Journal of Physical Chemistry 80(5) (1976) 486-493.

[350] C. Li, Y. Liu, Y. Fu, T. Huang, L. Kang, C. Li, The antiproliferative activity of di-2-pyridylketone dithiocarbamate is partly attributed to catalase inhibition: detailing the interaction by spectroscopic methods, Molecular BioSystems 13(9) (2017) 1817-1826.

[351] T.I. Chandel, G. Rabbani, M. Khan, M. Zaman, P. Alam, Y. E. Shahein, R. Hasan Khan, Binding of anti-cardiovascular drug to serum albumin: an insight in the light of spectroscopic and computational approaches, Journal of Biomolecular Structure and Dynamics 36(1) (2018) 54-67.

[352] H.F. Crouse, E.M. Petrunak, A.M. Donovan, A.C. Merkle, B.L. Swartz, S. Basu, Static and dynamic quenching of tryptophan fluorescence in various proteins by a chromium (III) complex, Spectroscopy Letters 44(5) (2011) 369-374.

[353] A. Velazquez-Campoy, E. Freire, Isothermal titration calorimetry to determine association constants for high-affinity ligands, Nature protocols 1(1) (2006) 186.

[354] P. Gouet, E. Courcelle, D.I. Stuart, F. M√© toz, ESPript: analysis of multiple sequence alignments in PostScript, Bioinformatics (Oxford, England) 15(4) (1999) 305-308.

[355] V. Srivastava, A. Kumar, B.N. Mishra, M.I. Siddiqi, Molecular docking studies on DMDP derivatives as human DHFR inhibitors, Bioinformation 3(4) (2008) 180.

[356] N. Singh, M.I. Siddiqi, Computational evaluation of glutamine synthetase as drug target against infectious diseases: molecular modeling, substrate-binding analysis, and molecular dynamics simulation studies, Medicinal Chemistry Research 26(2) (2017) 450-460.

[357] A. Coates, Y. Hu, R. Bax, C. Page, The future challenges facing the development of new antimicrobial drugs, Nature reviews Drug discovery 1(11) (2002) 895.

[358] H. Yoneyama, R. Katsumata, Antibiotic resistance in bacteria and its future for novel antibiotic development, Bioscience, biotechnology, and biochemistry 70(5) (2006) 1060-1075.

[359] T. Rodrigues, D. Reker, P. Schneider, G. Schneider, Counting on natural products for drug design, Nature chemistry 8(6) (2016) 531.

[360] A. Ganesan, The impact of natural products upon modern drug discovery, Current opinion in chemical biology 12(3) (2008) 306-317.

[361] R. Tamimi, P. Lagiou, H.O. ADAMI, D. Trichopoulos, Prospects for chemoprevention of cancer, Journal of Internal Medicine 251(4) (2002) 286-300.

[362] X. Zhu, H. Zhang, R. Lo, Phenolic compounds from the leaf extract of artichoke (Cynara scolymus L.) and their antimicrobial activities, Journal of Agricultural and Food Chemistry 52(24) (2004) 7272-7278.

[363] E.J. Goldstein, T.F. Murphy, G.I. Parameswaran, Moraxella catarrhalis, a human respiratory tract pathogen, Clinical Infectious Diseases 49(1) (2009) 124-131.

[364] S.B.U. Shaikh, Z. Ahmed, S.A. Arsalan, S. Shafiq, Prevalence and resistance pattern of Moraxella catarrhalis in community-acquired lower respiratory tract infections, Infection and drug resistance 8 (2015) 263.

[365] V. Kumar, A. Sharma, S. Pratap, P. Kumar, Characterization of isoflavonoids as inhibitors of β-hydroxyacyl-acyl carrier protein dehydratase (FabZ) from Moraxella catarrhalis: Kinetics, spectroscopic, thermodynamics and in silico studies, Biochimica et Biophysica Acta (BBA)-General Subjects (2017).

[366] H. Shaban, I. Na, A.A. Kislichkina, S.V. Dentovskaya, A.P. Anisimov, V.N. Uversky, Effect of natural polymorphism on structure and function of the Yersinia pestis outer membrane porin F (OmpF protein): a computational study, Journal of Biomolecular Structure and Dynamics 35(12) (2017) 2588-2603.

[367] R.P. Darveau, Lipid A diversity and the innate host response to bacterial infection, Current opinion in microbiology 1(1) (1998) 36-42.

[368] E. Lien, T.K. Means, H. Heine, A. Yoshimura, S. Kusumoto, K. Fukase, M.J. Fenton, M. Oikawa, N. Qureshi, B. Monks, Toll-like receptor 4 imparts ligand-specific recognition of bacterial lipopolysaccharide, The Journal of clinical investigation 105(4) (2000) 497-504.

[369] T.J. Wyckoff, C.R. Raetz, J.E. Jackman, Antibacterial and anti-inflammatory agents that target endotoxin, Trends in microbiology 6(4) (1998) 154-159.

[370] S. Pratap, P. Kesari, R. Yadav, A. Dev, M. Narwal, P. Kumar, Acyl chain preference and inhibitor identification of Moraxella catarrhalis LpxA: Insight through crystal structure and computational studies, International journal of biological macromolecules 96 (2017) 759-765.

[371] D. Pradhan, V. Priyadarshini, M. Munikumar, S. Swargam, A. Umamaheswari, A. Bitla, Para-(benzoyl)-phenylalanine as a potential inhibitor against LpxC of Leptospira spp.: homology modeling, docking, and molecular dynamics study, Journal of Biomolecular Structure and Dynamics 32(2) (2014) 171-185.

[372] A.L. Erwin, Antibacterial drug discovery targeting the lipopolysaccharide biosynthetic enzyme LpxC, Cold Spring Harbor perspectives in medicine 6(7) (2016) a025304.

[373] M.C. Pirrung, L.N. Tumey, C.R. Raetz, J.E. Jackman, K. Snehalatha, A.L. McClerren, C.A. Fierke, S.L. Gantt, K.M. Rusche, Inhibition of the antibacterial target UDP-(3-O-acyl)-N-acetylglucosamine deacetylase (LpxC): isoxazoline zinc amidase inhibitors bearing diverse metal binding groups, Journal of medicinal chemistry 45(19) (2002) 4359-4370.

[374] S. Ding, R.-Y. Dai, W.-K. Wang, Q. Cao, L.-F. Lan, X.-L. Zhou, Y.-S. Yang, Design, synthesis and structure-activity relationship evaluation of novel LpxC inhibitors as Gram-negative antibacterial agents, Bioorganic & medicinal chemistry letters 28(2) (2018) 94-102.

[375] A.P. Tomaras, C.J. McPherson, M. Kuhn, A. Carifa, L. Mullins, D. George, C. Desbonnet, T.M. Eidem, J.I. Montgomery, M.F. Brown, LpxC inhibitors as new antibacterial agents and tools for studying regulation of lipid A biosynthesis in Gram-negative pathogens, MBio 5(5) (2014) e01551-14.

[376] S. Sengyee, N. Saiprom, S. Paksanont, D. Limmathurotsakul, V. Wuthiekanun, N. Chantratita, Susceptibility of Clinical Isolates of Burkholderia pseudomallei to a Lipid A Biosynthesis Inhibitor, The American journal of tropical medicine and hygiene 97(1) (2017) 62-67.

[377] S. Sengyee, N. Saiprom, S. Paksanont, D. Limmathurotsakul, V. Wuthiekanun, N. Chantratita, The American Society of Tropical Medicine and Hygiene, Am. J. Trop. Med. Hyg 97(1) 62.

[378] S. Cristobal, A. Zemla, D. Fischer, L. Rychlewski, A. Elofsson, A study of quality measures for protein threading models, BMC bioinformatics 2(1) (2001) 5.

[379] E.F. Pettersen, T.D. Goddard, C.C. Huang, G.S. Couch, D.M. Greenblatt, E.C. Meng, T.E. Ferrin, UCSF Chimera—a visualization system for exploratory research and analysis, Journal of computational chemistry 25(13) (2004) 1605-1612.

[380] S.K. Pawar, R. Punith, R.S. Naik, J. Seetharamappa, Spectroscopic and molecular modeling approaches to investigate the binding of proton pump inhibitors to human serum albumin, Journal of Biomolecular Structure and Dynamics 35(15) (2017) 3205-3220.

[381] A. Velazquez-Campoy, E. Freire, Isothermal titration calorimetry to determine association constants for high-affinity ligands, Nature Protocols 1 (2006) 186.

[382] J.E. Ladbury, G. Klebe, E. Freire, Adding calorimetric data to decision making in lead discovery: a hot tip, Nature reviews Drug discovery 9(1) (2010) 23.

[383] C.-J. Lee, X. Liang, R. Gopalaswamy, J. Najeeb, E.D. Ark, E.J. Toone, P. Zhou, Structural basis of the promiscuous inhibitor susceptibility of Escherichia coli LpxC, ACS chemical biology 9(1) (2013) 237-246.

[384] A.S. Abdelhameed, P. Alam, R.H. Khan, Binding of janus kinase inhibitor tofacitinib with human serum albumin: multi-technique approach, Journal of Biomolecular Structure and Dynamics 34(9) (2016) 2037-2044.